

AD-A254 135



DTIC
ELECTE
JUN 18 1992
S C D



THE MICROPHYSICS OF SURFACES: BEAM-INDUCED PROCESSES

Sponsored by
Optical Society of America
In cooperation with
American Vacuum Society

1991 TECHNICAL DIGEST
SERIES VOLUME 3

February 11-13, 1991
Santa Fe, New Mexico

DISTRIBUTION STATEMENT A
Approved for public release.
Distribution Unlimited

REPORT DOCUMENTATION PAGE

Form Approved
OMB NO 0704-0188

Public reporting burden for this collection of information is estimated to average 1.75 hours per response, including the time for reviewing instructions, searching existing data sources, gathering and maintaining the data needed, and completing and reviewing the collection of information. Send comments regarding this burden estimate or any other aspect of this collection of information, including suggestions for reducing this burden, to Washington Headquarters Services, Directorate for Information Operations and Reports, 1215 Jefferson Davis Highway, Suite 1204, Arlington, VA 22202-4302, and to the Office of Management and Budget, Paperwork Reduction Project (0704-0188), Washington, DC 20503.

1. AGENCY USE ONLY (Leave blank)	2. REPORT DATE	3. REPORT TYPE AND DATES COVERED
	May 22, 1992	Final 1/1/91-12/31/91
4. TITLE AND SUBTITLE		5. FUNDING NUMBERS
Organization of the 1991 Optical Society of America Photonic Science Technical Meeting Series VOL 3		G - AFOSR-91-0176
6. AUTHOR(S)		
Jarus W. Quinn		
7. PERFORMING ORGANIZATION NAME(S) AND ADDRESS(ES)		8. PERFORMING ORGANIZATION REPORT NUMBER
Optical Society of America 2010 Massachusetts Ave. NW Washington, DC 20036		AFOSR-TR- 92 0015
9. SPONSORING/MONITORING AGENCY NAME(S) AND ADDRESS(ES)		10. SPONSORING/MONITORING AGENCY REPORT NUMBER
US Air Force Office of Scientific Research Department of the Air Force Bolling Air Force Base Washington, DC 20332-6448 Schlossberg		2305/A1
11. SUPPLEMENTARY NOTES		
12a. DISTRIBUTION/AVAILABILITY STATEMENT		12b. DISTRIBUTION CODE
Approved for public release Distribution unlimited		
13. ABSTRACT (Maximum 200 words)		
<p>Attach list of reports supported by Optical Society of America</p> <p>Photorefractive Materials, Effects, and Devices</p> <p>Integrated Photonics Research</p> <p>Nonlinear Guided Wave Phenomena</p> <p>Optical Amplifiers and Their Applications</p> <p>Optical computing</p> <p>Picosecond Electronics and Optoelectronics</p> <p>Quantum Optoelectronics</p> <p>Photonic Switching</p> <p>Microphysics of Surfaces: Beam Induced Processes</p> <p>Soft X-ray Projection Lithography</p> <p>Short Wavelength Coherent Radiation, Generation & Applications</p> <p>Persistent Spectral Hole-Buring: Science & Applications</p>		

14. SUBJECT TERMS	15. NUMBER OF PAGES
16. PRICE CODE	
17. LIMITATION OF ABSTRACT	
18. SECURITY CLASSIFICATION	19. SECURITY CLASSIFICATION
20. SECURITY CLASSIFICATION	21. SECURITY CLASSIFICATION

18. SECURITY CLASSIFICATION

19. SECURITY CLASSIFICATION

20. SECURITY CLASSIFICATION

21. SECURITY CLASSIFICATION

Summaries of papers presented at the
Microphysics of Surfaces: Beam-Induced Processes Topical Meeting

Microphysics of Surfaces: Beam-Induced Processes

1991 Technical Digest Series
Volume 3

CONFERENCE EDITION
February 11-13, 1991 — Santa Fe, New Mexico

•

Accession For	
NTIS	43161
DATA TAB	<input checked="" type="checkbox"/>
Unknown	<input type="checkbox"/>
Classification	
By	
Distribution/	
Availability Codes	
Dist	Avail and/or Special
A-1	

Cosponsored by
Optical Society of America
American Vacuum Society

Optical Society of America
2010 Massachusetts Avenue, NW
Washington, DC 20036

92-15744

92 6 1 1 1



Articles in this publication may be cited in other publications. In order to facilitate access to the original publication source, the following form for the citation is suggested:

Name of Author(s), "Title of Paper," in Technical Digest on The Micophysics of Surfaces: Beam-Induced Processes, 1991 (Optical Society of America, Washington, D.C., 1991), Vol. 3, pp.xx-xx.

ISBN Number

Conference Edition	1-55752-164-6 (softcover)
Postconference Edition	1-55752-165-4 (hardcover)
(Note: Postconference Edition includes postdeadline papers.)	
1991 Technical Digest Series	1-55752-192-1 (hardcover)

Library of Congress Catalog Card Number

Conference Edition	90-63035
Postconference Edition	89-63034

Copyright © 1991, Optical Society of America

Individual readers of this digest and libraries acting for them are permitted to make fair use of the material in it, such as to copy an article for use in teaching or research, without payment of fee, provided that such copies are not sold. Copying for sale is subject to payment of copying fees. The code 1-55752-192-1/91/\$2.00 gives the per-article copying fee for each copy of the article made beyond the free copying permitted under Sections 107 and 108 of the U.S. Copyright Law. The fee should be paid through the Copyright Clearance Center, Inc., 21 Congress Street, Salem, MA 01970.

Permission is granted to quote excerpts from articles in this digest in scientific works with the customary acknowledgment of the source, including the author's name and the name of the digest, page, year, and name of the Society. Reproduction of figures and tables is likewise permitted in other articles and books provided that the same information is printed with them and notification is given to the Optical Society of America. Republication or systematic or multiple reproduction of any material in this digest is permitted only under license from the Optical Society of America; in addition, the Optical Society may require that permission also be obtained from one of the authors. Address inquiries and notices to Director of Publications, Optical Society of America, 2010 Massachusetts Avenue, NW, Washington, DC 20036. In the case of articles whose authors are employees of the United States Government or its contractors or grantees, the Optical Society of America recognizes the right of the United States Government to retain a nonexclusive, royalty-free license to use the author's copyrighted article for United States Government purposes.

THE MICROPHYSICS OF SURFACES: BEAM-INDUCED PROCESSES

Sponsored by
Optical Society of America
In cooperation with
American Vacuum Society

1991 TECHNICAL DIGEST
SERIES VOLUME 3

February 11-13, 1991
Santa Fe, New Mexico

POSTDEADLINE PAPERS and ADDENDUM

TABLE OF CONTENTS

POSTDEADLINE PAPERS

PdP1	Site-specific reactivity of hydrogen on Ge(111):c(2x8):direct observation by STM and pseudopotential calculations of reaction-induced rest-atom to adatom charge exchange , T. Klitsner, J. S. Nelson, Sandia National Laboratory.....	175
PdP2	Reflection mass spectrometry (REMS) measurements of the reactivities of GaAs, AlAs, and InAs Surfaces during molecular beam epitaxy , T. M. Brennan, J. Y. Tsao, B. E. Hammons, Sandia National Laboratory.....	176
PdP3	Layer-by-layer sputtering and epitaxy of Si(100) , P. Bedrossian, J. E. Houston, J. Y. Tsao, E. Chason, S. T. Picraux, Sandia National Laboratory.....	177
PdP4	Nonlinear optical studies of electronic excitations and thermalization on a metal surface , L. E. Urbach, J. M. Hicks, K. P. Percival, E. W. Plummer, H. L. Dai, University of Pennsylvania.....	178

ADDENDUM

WC10	Laser induced polymerization of monolayer formaldehyde on silver , L. Fleck, W. Fehery, Z. C. Ying, H. L. Dai, University of Pennsylvania.....	179
------	---	-----

PdP1-1

SITE-SPECIFIC REACTIVITY OF HYDROGEN ON Ge(111):c(2X8): DIRECT OBSERVATION BY STM AND PSEUDOPOTENTIAL CALCULATIONS OF REACTION-INDUCED REST-ATOM TO ADATOM CHARGE EXCHANGE.

T. Klitsner and J.S. Nelson, Sandia National Labs, Albuquerque, NM 87185-5800.

Charge transfer induced by chemical reactions has previously been used to tailor the site-specific reactivity of various organic molecules. In this work we show that such reaction-induced localized charge transfer can also occur on semiconductor surfaces, which raises the possibility of using this as a new technique for producing tailored structures on these substrates. The equilibrium Ge(111):c2x8 surface has fairly complete charge transfer from adatom to rest-atom sites, and so is a good substrate on which to look for these effects. In this work we use dual polarity scanning tunneling microscope (STM) images to study the configuration of both occupied and unoccupied electronic states before and after hydrogen ion bombardment and annealing of the Ge(111):c2x8 surface. We also perform first principles self-consistent pseudopotential calculations on the unreacted and hydrogen-reacted surface. Before reaction with hydrogen, the STM images and the calculated charge densities show the unoccupied states localized on adatom sites, and the occupied states localized primarily around rest-atom sites. After hydrogen ion bombardment and annealing, the STM images show a reaction occurs preferentially at the rest-atom site and is accompanied by a dramatic charge transfer from this site to the neighboring adatom sites. Our calculations also show this hydrogen-induced charge transfer, in excellent agreement with the STM images. Specifically, the calculations show that after reaction with hydrogen, the occupied surface-state charge density has transferred from on top of the rest-atom, and is now primarily localized between the adatom and the underlying five-fold coordinated second-layer atom.

Reflection Mass Spectrometry (REMS) Measurements of the Reactivities of GaAs, AlAs and InAs Surfaces During Molecular Beam Epitaxy.

T. M. Brennan, J.Y. Tsao and B.E. Hammons
Sandia National Labs, Albuquerque, New Mexico 87185-5800

Our current understanding of the growth of binary compounds by Molecular Beam Epitaxy (MBE) is limited by the lack of growth compatible, real-time in-situ diagnostics. For example, the kinetic parameters that characterize the surface processes occurring during MBE growth are not currently well understood. We are developing a means of measuring those parameters in real MBE growth situations which can contribute significantly to our ability to understand and control the actual growth mechanisms.

Using Reflection Mass Spectrometry (REMS) we have measured the reactive sticking coefficients of As_4 on the group III rich surface of GaAs, and for the first time on the group III rich surfaces of AlAs and InAs. We find the As_4 sticking coefficient is 0.5 for all the systems measured near their optimum growth temperatures, but is temperature dependent approaching 1.0 at lower, suboptimal temperatures. The increase in the As_4 sticking coefficient is accompanied by various deviations from the metal rich (4x2) surface reconstruction commonly observed at the higher temperatures.

We also observed, for the first time, a dependence to the reactivity to the surface to As_4 on surface microstructure, i.e. on the roughness or smoothness of the surface. This dependence manifests itself as slight fluctuations in the As_4 incorporation rate that are periodic with the bilayer-by-bilayer growth cycle. The As_4 sticking coefficient is slightly lower on smooth surfaces and slightly higher on rough surfaces.

These "REMS" oscillations, together with our measurements of group V sticking coefficients, can provide very accurate real-time characterization of V/III flux ratios and group III growth rates independent of other techniques. Routine use of reflection mass spectrometry therefore offers the possibility of on-line feedback and control of the MBE process.

Thomas M. Brennan
Sandia National Laboratories
P.O. Box 5800, Division 1144
Albuquerque, New Mexico 87107-5800
(505) 846-8192 phone
(505) 844-3211 fax

Layer-By-Layer Sputtering and Epitaxy of Si(100).

P. BEDROSSIAN, J. E. HOUSTON, J. Y. TSAO, E. CHASON, and
S. T. PICRAUX, Sandia National Laboratory, Albuquerque, NM.

We report the observation of pronounced RHEED oscillations under sequential and simultaneous epitaxy and 200-250eV Xe bombardment of Si(100). Analysis of the relative phase relationships of growth- and ion-induced oscillations shows that ion bombardment can reverse the surface roughening resulting from previous epitaxy and can cancel the oscillations resulting from simultaneous epitaxy. These observations indicate that the ion-induced oscillations arise from simple layer-by layer removal of silicon. We will discuss these results in terms of models of possible ion processes, and the results of experiments on ion-assisted growth.

Peter J. Bedrossian
Division 1114
Sandia Nat. Laboratory
Albuquerque, NM 87185

NONLINEAR OPTICAL STUDIES OF ELECTRONIC EXCITATIONS AND THERMALIZATION ON A METAL SURFACE

L. E. Urbach, J. M. Hicks, K. P. Percival, E. W. Plummer, and H. L. Dai

Departments of Chemistry and Physics, University of Pennsylvania,
Philadelphia, Pennsylvania 19104

ABSTRACT

Resonant enhancement of second harmonic generation (SHG) due to a transition between two surface states on Ag(110) is observed. An increase in the nonlinear susceptibility, attributed to the coupling of the fundamental light with this transition, is proven by the energy dependence of the second harmonic signal and by the observed selection rules dictated by the symmetry of the surface states. The signal resonantly enhanced by the transition between surface states at 1.74eV exhibits a strong dependence on temperature and adsorbate coverage, in sharp contrast to the nonresonant signal.

On the same Ag(110) surface, a strong enhancement in SHG was also observed at the interband transition energy of 3.9eV in resonance with the second harmonic frequency. The SHG enhancement arises from increased nonlinear susceptibility and, primarily, the change in dielectric constants in this energy region. A strong temperature dependence in the SHG intensity was also observed here. This temperature dependence was used as a surface temperature calibration for probing the transient temperature jump induced by pulsed laser excitation of the silver surface. This SHG technique is surface sensitive, nonintrusive and has time resolution limited only by the probe laser pulselength. For the Ag(110) surface, a $> 10^{10}$ K/sec heating rate induced by a nanosecond IR excitation pulse was monitored. The much stronger temperature dependence observed in the SHG resonantly enhanced by the surface state transition can in principle be used for surface temperature measurements. This kind of surface temperature measurement method can be generally applied to metals, semiconductors and solids that have temperature dependent electronic transitions.

LASER INDUCED POLYMERIZATION OF MONOLAYER FORMALDEHYDE ON SILVER

L. Fleck, W. Fehery, Z. C. Ying, and H. L. Dai

Department of Chemistry, University of Pennsylvania,
Philadelphia, Pennsylvania 19104-6323

ABSTRACT

Formaldehyde (H_2CO), physisorbed at 90K with near saturation coverage, were found to polymerize on a $\text{Ag}(111)$ surface under UV irradiation. This polymerization is initiated by radicals generated in photoexcitation induced dissociation, $\text{H}_2\text{CO} \xrightarrow{h\nu} \text{H}_2\text{CO}^* \longrightarrow \text{H} + \text{HCO}$. H is identified by EELS detection of the Ag-H vibration at low formaldehyde coverage, at which dissociation of formaldehyde occurred but no polymerization was observed. The polymer was determined to be $-(\text{CH}_2\text{-O})_n-$ from comparison of the EELS spectrum with previously measured IR absorption spectrum of the polymer. Strong wavelength dependence in the dissociation and polymerization yields proved that the initiation of those processes is nonthermal and is most likely caused by resonant excitation of formaldehyde to its first electronic excited state.

Physisorbed formaldehyde were found to desorb at 120 K while the polymer pyrolyses on silver at about 210 K. Due to the higher chemical resistivity of the polymer, it is feasible to use light to induce polymerization on selected areas on the surface and protect these areas from surface treatments. Surface processing on submicron scale may thus be achieved this way.

CONTENTS

MA	Beam-Assisted Film Growth.....	1
MB	Initiation and Growth of Surface Layers.....	17
MC	Photon- and Hot-Electron-Induced Surface Reactions	31
TuA	Beam-Assisted Etching	51
TuB	Laser-Induced Desorption and Reaction	67
TuC	Processing and Applications.....	85
WA	Structure and Deposition of Metal Overlayers	93
WB	Surface Modification and Analysis.....	109
WC	Poster Session.....	127
WD	Nanoscale Structure and Lithography	161

SUNDAY, FEBRUARY 10, 1991

Anasazi Lobby

6:00 pm-9:00 pm Registration/
 Informal Reception

MONDAY, FEBRUARY 11, 1991

7:00 am-11:00 am Registration/Speaker Check-in
Anasazi North

7:00 am-8:00 am Breakfast Served
Anasazi South

8:00 am-8:10 am Opening Remarks, Richard B. Hall,
 *Exxon Research and Engineering,
 Conference Chair*

Anasazi South

8:10 am-9:30 am

MA, BEAM-ASSISTED FILM GROWTH

Frances A. Houle, *IBM Almaden Research Center,
 Presider*

8:10 am (Invited)

MA1 **Electron- and photon-beam-induced thin-film growth**, Ferenc Bozso, *IBM Research Division*. Low-temperature thin-film deposition with control over composition and thickness by using low-energy electron or UV photon beams to induce reactions in adsorbed molecular layers is reported. 2

8:40 am (Invited)

MA2 **Low-energy ion-surface interactions during vapor-phase film growth for manipulating microchemistry and microstructure at the atomic level**, J. E. Greene, *University of Illinois*. Low-energy (≤ 200 eV) ion irradiation from the vapor phase during crystal growth can be used to provide new chemical reaction pathways and to controllably modify film-growth kinetics. 6

9:10 am

MA3 **Coherent strain changes in Si-Ge alloys grown by ion-assisted molecular-beam epitaxy**, H. A. Atwater, C. J. Tsai, T. Vreeland, *California Institute of Technology*. Concurrent low-energy ion bombardment during epitaxy of coherent Si-Ge alloy layers results in large changes in layer strain. Implications for ion-surface interactions are discussed. 13

Anasazi North

9:30 am-9:45 am Coffee Break

Anasazi South

9:45 am-11:15 am
MB, INITIATION AND GROWTH OF SURFACE LAYERS
Daniel J. Ehrlich, *MIT Lincoln Laboratory, Presider*

9:45 am (Invited)
MB1 **Adsorbed layers in the process of chemical vapor deposition**, Jun-ichi Nishizawa, *Semiconductor Research Institute, Japan*. Photo-irradiation effect on the adsorption species and the surface reaction of GaAs growth were studied by using mass spectroscopy and by using our original epitaxial method. 18

10:15 am

MB2 **Elucidation of the mechanism of the initial stages of Si(111)-7 \times 7 oxidation using scanning tunneling microscopy**, Ph. Avouris, I.-W. Lyo, F. Bozso, B. Schubert, R. Hoffmann, *IBM Research Division*. We present scanning tunneling microscopy results, photoemission results, and theoretical calculations that allow us to elucidate the mechanism of the initial stages of Si(111)-7 \times 7 oxidation. 22

10:35 am

MB3 **Oxide layer growth on gallium arsenide using a high kinetic energy atomic oxygen beam**, M. A. Hoffbauer, J. B. Cross, J. D. Farr, V. M. Bermudez, *Los Alamos National Laboratory*. Oxide layers approximately 400 Å thick have been formed on (110) and (100)GaAs wafers by exposure to an ~2.8 eV atomic O beam and have been characterized by using x-ray photoemission spectroscopy and Raman spectroscopy. 26

10:55 am

MB4 **Electronically induced modifications of a-Si:H(P) films by scanning tunneling microscopy**, E. Hartmann, F. Koch, R. J. Behm, *University of Munich, Federal Republic of Germany*. We report on how to make local electronic modifications of phosphorus-doped, hydrogenated amorphous silicon films [a-Si:H(P)] on a nanometer scale using a scanning tunneling microscope. 29

11:15 am-7:30 pm Afternoon Free

Anasazi Lobby

6:45 pm-9:00 pm Registration/Speaker Check-in

Anasazi South

7:30 pm-9:30 pm
MC, PHOTON- AND HOT-ELECTRON-INDUCED SURFACE REACTIONS
Michael Stuke, *Max Planck Institute, Federal Republic of Germany, Presider*

7:30 pm (Invited)
MC1 Photochemistry at metal surfaces, J. M. White, *University of Texas, Austin*. Bond cleavage processes, driven by ultraviolet photons, have been investigated for a number of transition metal-small molecule systems with attention to mechanisms. 32

8:00 pm (Invited)
MC2 Interaction of low-energy electrons with adsorbed molecules: mechanisms of energy transfer and dissociation, Léon Sanche, *University of Sherbrooke, Canada*. The mechanisms by which low-energy electrons transfer energy to molecular adsorbates are discussed with emphasis on the formation of transient negative ions decaying into dissociative attachment. 35

8:30 pm
MC3 Bond orbital model of two-hole laser-induced desorption from GaP(110), Richard F. Haglund, Jr., Ken Hatton, Noriaki Itoh, Yasuo Nakai, *Vanderbilt University*. We use a bond orbital model of laser-induced bond breaking in compound semiconductors to describe recent experimental results in subband gap laser-induced desorption and ablation from GaP(110) through two-hole localization. 39

8:50 pm
MC4 Photoemission from Si(111) surfaces covered with thick overlayers of CaF₂, B. Quiniou, W. Schwarz, Z. Wu, R. M. Osgood, Jr., Q. Yang, J. Phillips, *Columbia University*. We report the observation of significant UV-photoemissive current through thick insulator layers: ~8000 Å on semiconductors. The implications for light-induced surface chemistry on insulators are discussed. 43

9:10 pm
MC5 Silicon atomic layer growth by laser beam Si₂H₆ adsorbates interactions, Y. Nagasawa, T. Tanaka, S. Miyazaki, M. Hirose, *Hirosshima University, Japan*. Si₂H₆ adsorbed on a cooled Si substrate was resonantly decomposed by ArF excimer laser and CO₂ laser irradiations to achieve silicon atomic layer growth. 47

TUESDAY, FEBRUARY 12, 1991**Anasazi Lobby**

7:00 am-11:00 am Registration/Speaker Check-in

Anasazi North

7:00 am-8:00 am Breakfast Served

Anasazi South

8:00 am-9:30 am
TuA, BEAM-ASSISTED ETCHING
Stuart J. C. Irvine, *Rockwell International Corporation, Presider*

8:00 am (Invited)
TuA1 Laser-induced reactions of semiconductor surfaces with chlorine, Qi-Zong Qin, Yu-Lin Li, Ping-He Lu, Zhuang-Jian Zhang, Zhong-Kao Jin, Qi-Ke Zheng, *Fudan University, China*. Laser-induced chemical reactions of semiconductor surfaces with halogen and halogen compounds have recently attracted attention because of their potential application to the fabrication of microelectronic devices. This paper will present our recent studies of laser-induced reactions of Ge(111), Si(111), GaAs(100), and InP(100) surfaces with Cl molecules under 355-, 560-, and 1064-nm laser irradiations. 52

8:30 am
TuA2 Mechanism of chemical etching of doped GaAs by Cl₂, F. A. Houle, *IBM Almaden Research Center*. Molecular-beam mass spectroscopy has been used to investigate the chemistry of thermal etching of GaAs. The relative importance of thermochemical and kinetic driving forces will be discussed. 55

8:50 am
TuA3 UV laser-induced interaction of Cl₂ with GaAs(110), G. Haase, V. Liberman, M. C. Shih, R. M. Osgood, Jr., *Columbia University*. An electron photoemission-initiated mechanism is proposed to explain AsCl₃ formation and time-of-flight distributions of ejected chlorine species on UV-laser illumination of chlorine-covered 85 K GaAs(110). 58

9:10 am
TuA4 Pulsed UV induced etching of silicon: a time-of-flight study, Carlotta Paulsen-Boaz, Thor Rhodin, *Cornell University*. Mechanisms of pulsed UV laser-induced chlorination of silicon (111) were studied as a function of laser influence and sample doping using primarily time-of-flight mass spectroscopy. Electronic mechanisms are clearly observable only at very low power levels (<150 mJ/cm²/pulse). 62

Anasazi North

9:30 am-9:45 am Coffee Break

Anasazi South

9:45 am-11:25 am

TuB, LASER-INDUCED DESORPTION AND REACTION

Richard B. Hall, *Exxon Research and Engineering, Presider*

9:45 am

TuB1 State-specific studies of the laser-induced desorption of NO from Si(111), L. J. Richter, S. A. Bunting, D. S. King, R. R. Cavanagh, *National Institute of Standards and Technology*. The substrate photoexcitation responsible for laser-induced desorption of NO changes with NO coverage, resulting in strongly coverage-dependent state population distributions for the desorbed molecules. 68

10:05 am

TuB2 Adsorption and desorption kinetics for Si(C₂H₅)₂H₂ on Si(111) 7 × 7, P. A. Coon, M. L. Wise, S. M. George, *Stanford University*. Diethylsilane is a promising candidate for silicon atomic layer epitaxy. Adsorption and desorption kinetics for diethylsilane on Si(111) 7 × 7 were studied by using laser-induced desorption techniques. 72

10:25 am

TuB3 Absorption of 1.17 eV photons by Al₂O₃ (1120), M. A. Schildbach, A. V. Hamza, *Lawrence Livermore National Laboratory*. Multiphoton absorption of 1.17 eV photons by Al₂O₃(1120) is evidenced by the induced desorption of aluminum atoms with $\langle E_k \rangle = 7.9 \pm 0.4$ eV and the presence of surface states in the band gap. 76

10:45 am

TuB4 Photon-induced desorption of adsorbed water clusters, Joachim Dirks, Wolfgang Drachsel, Jochen H. Block, *Fritz-Haber-Institute of the Max-Planck-Gesellschaft, Federal Republic of Germany*. We use synchrotron radiation to study the photon-induced desorption of water clusters from water multilayers in the presence of a high electric field. 80

11:25 am-7:00 pm Afternoon Free

Anasazi Lobby

6:30 pm-9:00 pm Registration/Speaker Check-in

Anasazi South

7:00 pm-9:00 pm

TuPdP, Postdeadline Session

Thomas Mayer, *Sandia National Laboratory, Presider*

9:00 pm-10:00 pm

TuC, PROCESSING AND APPLICATIONS

Richard M. Osgood, *Columbia University, Presider*

9:00 pm (Invited)

TuC1 Laser-induced deposition of amorphous silicon: relations between chemical processing and performance, Peter Hess, *University of Heidelberg, Federal Republic of Germany*. The relations between gas phase and surface chemistry, growth rate and film structure, and properties will be discussed for aSi:H deposited by IR and UV lasers. 86

9:30 pm (Invited)

TuC2 cw laser-induced chemical reactions with integrated circuits, Geoffroy Auvert, *Centre National d'Etudes des Télecommunications, France*. The interaction of a focused cw laser beam with integrated circuits leads to various chemical reactions, depending on the nature of the irradiated interface or the surrounding atmosphere. The main possibilities of such an interaction, which is widely used for micrometer-size features, are cutting interconnections, etching of insulator layers, and depositing new connections. 88

WEDNESDAY, FEBRUARY 13, 1991

Anasazi Lobby

7:00 am-11:00 am Registration/Speaker Check-in

Anasazi North

7:00 am-8:00 am Breakfast Served

Anasazi South

8:00 am-9:40 am

WA, Structure and Deposition of Metal Overlays

Thor Rhodin, *Cornell University, Presider*

8:00 am (Invited)

WA1 STM studies on the growth and structure of thin metallic films on metal substrates, R. J. Behm, *Universität München, Federal Republic of Germany*. STM measurements are shown to give detailed information on the periodic defect structure of epitaxially grown metal films and on the kinetics and thermodynamics of their growth. 94

8:30 am	
WA2 Photochemical production of metallic gallium on cleaved GaAs surfaces: time-resolved measurements using laser and synchrotron radiation, S. S. Goldenberg, J. P. Long, M. N. Kabler, <i>Naval Research Laboratory</i> . The growth of metallic Ga islands, induced by 1-mJ/cm ² laser pulses on cleaved GaAs, is documented by photoemission spectroscopy and scanning electron microscopy.	98
8:50 am (invited)	
WA3 Surface chemistry of the selective-area deposition of metals, Marcel Widmer, Patrik Hoffmann, Baudouin Lecohier, Herbert Solka, Jean-Michel Philippoz, Hubert van den Bergh, <i>Ecole Polytechnique Fédérale de Lausanne, Switzerland</i> . Recent results obtained when using three different experimental approaches to fast <i>in situ</i> surface metallization are presented.	102
9:20 am	
WA4 Metal-semiconductor contacts: surface morphology and ballistic electron emission microscopy, R. Ludeke, M. Prietsch, A. Samavar, <i>IBM T. J. Watson Research Center</i> . Schottky barriers on cleaved GaP(110) are investigated by using ballistic electron emission microscopy. The surface morphology of the metal is the determining factor for image contrast.	104
Anasazi North	
9:40 am–10:00 am	COFFEE BREAK
Anasazi South	
10:00 am–11:20 am	
WB, SURFACE MODIFICATION AND ANALYSIS M. Hirose, <i>Hirosima University, Japan</i> , Presider	
10:00 am	
WB1 Chemical imaging of surface using the surface analysis by laser ionization technique, Lorenza Moro, Simon P. Mouncey, Christopher H. Becker, <i>Istituto per la Ricerca Scientifica e Tecnologica, Italy</i> . SALI has been developed to provide quantitative chemical images with ~0.1- to 1.0-μm spatial resolution. Significant advantages over SIMS and scanning AES are realized.	110
10:20 am	
WB2 Rotationally anisotropic second-harmonic generation studies of the structure and thermal stability of Cu(110), Mark A. Hoffbauer, Victoria J. McVeigh, Michael J. Zuerlein, <i>Los Alamos National Laboratory</i> . A large decrease in the rotationally anisotropic SH response from a Cu(110) surface with increasing temperature has been measured, and the results are related to changes in surface disorder.	114
10:40 am	
WB3 Vibrational spectroscopy of competitive adsorption at a liquid–solid interface using IR-visible sum-frequency generation, J. Miragliotta, R. S. Polizzotti, P. Rabinowitz, R. B. Hall, <i>Exxon Research and Engineering Company</i> . Molecular adsorption at a hydroxylated ZrO ₂ surface in contact with a binary liquid is reported. Results include equilibrium adsorption isotherms for a variety of solutions.	118
11:00 am	
WB4 Etching of SiO ₂ film by synchrotron radiation in hydrogen and its application to low-temperature surface cleaning, Yasuo Nara, Yoshihiro Sugiat, Noriaki Nakayama, Takashi Ito, <i>Fujitsu Laboratories Ltd., Japan</i> . SiO ₂ film is etched by using synchrotron radiation in a hydrogen atmosphere at 500 °C and is applied to low-temperature surface cleaning prior to epitaxial growth.	122
11:20 am–4:30 pm	Afternoon Free
Anasazi Lobby	
4:00 pm–8:00 pm	Registration/Speaker Check-in
Anasazi North	
4:30 pm–6:30 pm	
WC, POSTER SESSION Steven M. George, <i>Stanford University</i> , Presider	
WC1 Electronic energy transfer between donor and acceptor adlayers on single-crystal surfaces: distance and coverage dependence, D. R. Haynes, A. Tokmakoff, S. M. George, <i>Stanford University</i> . Electronic energy transfer between model donor/acceptor adlayers was studied on Al ₂ O ₃ by using laser-induced fluorescence techniques. The results versus distance and coverage were compared with Förster theory.	128
WC2 Arsenic passivation of silicon by photo-assisted metalorganic vapor-phase epitaxy, D. C. Rodway, K. J. Mackey, P. C. Smith, A. W. Vere, <i>Royal Signals & Radar Establishment, UK</i> . Arsenic-passivated silicon surfaces have been produced by photo-assisted deposition at 25–350 °C, significantly improving <i>in situ</i> substrate preparation prior to gallium arsenide growth.	132
WC3 Reflection electron energy loss spectroscopy during molecular-beam epitaxy, H. A. Atwater, C. C. Ahn, S. Nikzad, <i>California Institute of Technology</i> . We introduce and discuss applications of reflection electron energy loss spectroscopy as a powerful <i>in situ</i> probe of surface structure and composition during molecular-beam epitaxy.	134
WC4 XPS studies of halogen atom beam interactions with electronic materials, Andrew Freedman, Charter D. Stinespring, <i>Aerodyne Research, Inc.</i> XPS studies of halogen atom beam (fluorine and chlorine) interactions with diamond (100) and GaAs(100) surfaces will be presented.	138

WC5 Oriented aluminum films on silicon by direct ion-beam deposition, R. A. Zehr, T. E. Haynes, *Oak Ridge National Laboratory*. Crystalline Al films, which are oriented with respect to single-crystal Si substrates in spite of the 25% lattice mismatch, have been formed at room temperature by direct deposition from low-energy (30–120 eV) mass-analyzed ion beams. 139

WC6 Study of structural properties of non-stoichiometric zinc oxide films deposited by electron-beam evaporation technique, Rui-yu Chen, Chang-sheng Yuan, Qi-he Wang, *Nanjing University, China*. In this paper we discuss the effects of various temperatures of substrates and annealings on the structural properties of nonstoichiometric zinc oxide films. . . . 142

WC7 Scanning scattering microscope: a novel optical technique for imaging surface microtopography, Denes Marton, Joseph Fine, *National Institute of Standards and Technology*. Quantitative imaging of nanometer-high variations in surface microroughness can be obtained with a novel optical scanning technique that we have developed and patented. 146

WC8 Formation of submicrometer carbonaceous islands during SEM examination of thin GaAs layers on Si substrates, G. W. Turner, P. M. Nitishin, *MIT Lincoln Laboratory*. Carbonaceous islands with controllable diameters to ~2500 Å have been formed during SEM examination of very thin GaAs layers deposited by molecular-beam epitaxy on Si substrates. 149

WC9 Excitonic mechanism of photon-stimulated desorption of excited alkali atoms from alkali halides, Patrick H. Bunton, Richard F. Haglund, Jr., Dengfa Liu, Norman H. Tolk, *Austin Peay State University*. Recent measurements of photon-stimulated desorption of excited alkali atoms from alkali halides excited at both valence-band and core-level energies suggest that this process is driven not by two-hole localization but by the excitonic optical response of the material. 157

Zia Ballroom

6:30 pm–8:00 pm Conference Reception

Anasazi South

8:00 pm–9:15 pm
WD, NANOSCALE STRUCTURE AND LITHOGRAPHY
Phaedon Avouris, *IBM T. J. Watson Research Center*, Presider

8:00 pm (Invited)
WD1 Scanning tunneling microscopy studies of silicon molecular-beam epitaxy, M. G. Lagally, Y. W. Mo, *University of Wisconsin–Madison*. Scanning tunneling microscopy is used to investigate quantitatively kinetic processes in epitaxy, including diffusion, accommodation, coarsening, and transport over steps as well as their directional anisotropies. 162

8:30 pm (Invited)
WD2 Nanolithography, R. Fabian Pease, *Stanford University*. Our ability to fashion pattern with features below 100 nm is being put to good use for the microfabrication of devices and even circuits. Achieving economic throughput together with the precision required for sub-100-nm features is an enormous challenge. 166

9:15 pm–9:30 pm

Closing Remarks and Awards

TECHNICAL PROGRAM COMMITTEE

Richard B. Hall, Chair
Exxon Research and Engineering

Phaedon Avouris
IBM Thomas J. Watson Research Center

Daniel J. Ehrlich
MIT Lincoln Laboratory

Steven M. George
Stanford University

M. Hirose
Hiroshima University, Japan

Frances A. Houle
IBM Almaden Research Center

Stuart J. C. Irvine
Rockwell International Corporation

Richard M. Osgood
Columbia University

Thor Rhodin
Cornell University

Michael Stuke
Max Planck Institute, Federal Republic of Germany

Monday, February 11, 1991

Beam-Assisted Film Growth

MA 8:10am-9:30am
Anasazi South

Frances A. Houle, *Presider*
IBM Almaden Research Center



Electron and Photon-Beam Induced Thin-Film Growth

Ferenc Bozso

IBM Research Division, Thomas J. Watson Research Center
Yorktown Heights, N.Y. 10598

The small dimensions of novel electronic and optoelectronic device structures and their abruptly and unconventionally changing material compositions require high levels of spatial and kinetic control of the surface chemical reactions which are involved in the materials' growth or modification. These requirements exclude high temperature processes based on thermally activated chemical reactions. Directed energetic beams (electrons, photons, ions), however, can induce reactions at low temperatures, as well as provide for spatial and kinetic control in micro-fabrication processes. Electrons and photons of sufficient energy can cause fragmentation and desorption of adsorbed molecules or fragments of them, by inducing electronic excitations to dissociative states¹. The surface species after such excitations are mostly of highly reactive radical character, which readily react with the substrate and with other radical or molecular species in the adsorbed layer. The formation of such reactive surface species in a controlled way can provide a basis for non-thermal selective area film growth.

Here we use ultraviolet and X-ray photoemission spectroscopy (UPS and XPS) to study the adsorption and photon/electron-beam induced reactions of oxygen and disilane on Si(111)-7x7 substrate at 100 K. Since in this study the photon and electron-beams had similar effects, we limit the discussion to photo-induced reactions. The photon source used in this study was a 30 W deuterium lamp (with a UV spectral distribution down to 115 nm) mounted inside the vacuum system.

In Fig. 1a and 1b we show UPS spectra of oxygen and disilane adsorbed Si(111)-7x7 surfaces before and after UV-exposure at 100K. In Fig. 1a spectrum (2) shows that at 100 K oxygen adsorbs to a large extent in a negatively charged (O₂) molecular precursor state^{2,3}. Spectrum (3) shows that following 600 sec UV-exposure the oxygen is completely dissociated. In Fig. 1b curve (2) shows that at 100 K disilane adsorbs mainly in molecular form, while curve (3) and (4) show that upon UV-exposure disilane, as well, undergoes dissociation⁴.

Following the results which demonstrate the photo-induced dissociation of molecularly adsorbed species at a monolayer level, we show that in case of continuous flux of molecules and UV-exposure the photo-assisted reactions go beyond the monolayer level. In Fig. 1b, curve (5) is obtained after an originally oxidized silicon surface was exposed at 100 K to 1x10⁻⁷ torr Si₂H₆ and UV-beam. The UPS spectrum corresponds to that of an amorphous hydrogenated silicon film, which grows under the above conditions at a rate of ~.02 monolayer/sec as determined by the attenuation of the O(1s) XPS signal from the underlying oxide film. Upon rapid thermal annealing, the amorphous hydrogenated silicon converts into epitaxial film.

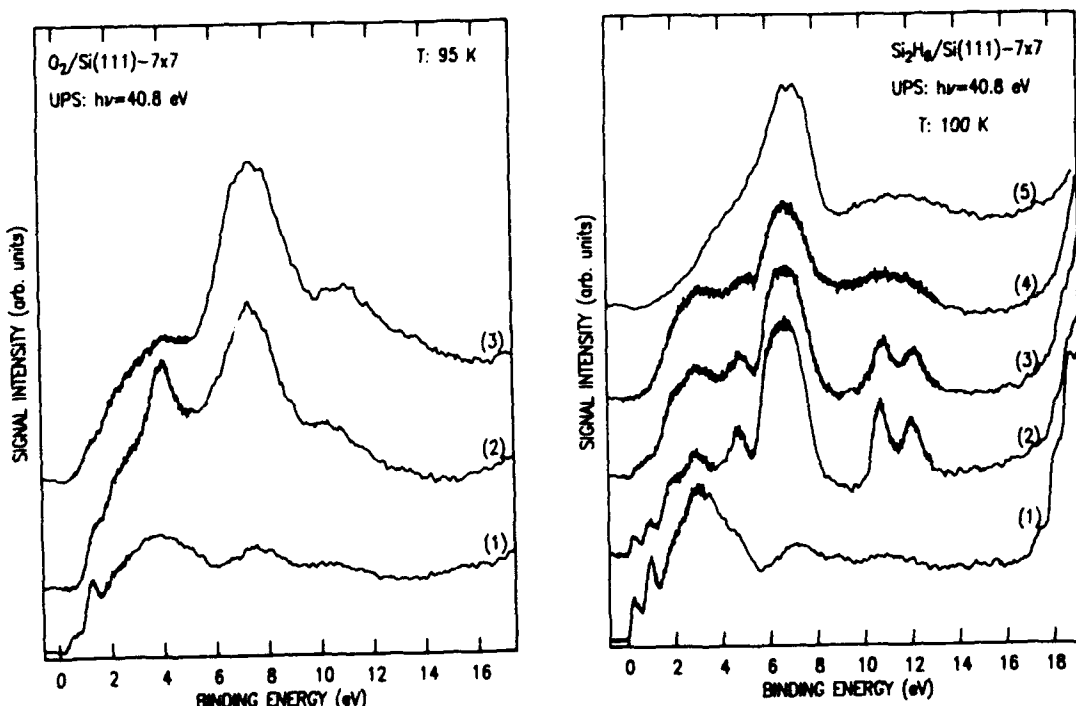


Fig. 1a. He II ($h\nu=40.8$ eV) UPS spectra of (1) clean Si(111)-7x7, (2) after 0.4L O_2 exposure at 100 K, (3) after 600 sec UV exposure of the oxygen-adsorbed surface at 100 K.

Fig. 1b. He II ($h\nu=40.8$ eV) UPS spectra of (1) clean Si(111)-7x7, (2) after 2L Si_2H_6 exposure at 100 K, (3) and (4) after 100 sec and 600 sec UV-exposure of the disilane adsorbed surface at 100 K, (5) after 1200 sec 1×10^{-7} torr Si_2H_6 and UV exposure at 100 K.

Fig. 2 shows oxygen uptake at 100 K in 5×10^{-7} torr O_2 on a clean Si(111)-7x7 and on a boron doped B:Si(111)- $\sqrt{3}\times\sqrt{3}$ surface in dark and under UV-exposure. The dashed curve shows that at 100 K in dark the clean Si(111)-7x7 surface adsorbs oxygen with high sticking probability up to a monolayer coverage, after which the adsorption virtually stops. Under UV-exposure, however, the oxygen uptake continues beyond the monolayer level at a considerable rate. The right panel of Fig. 2 shows UPS spectra after oxygen exposure in dark and under UV-illumination. The apparent band gap opening in the latter shows the effect of UV-enhanced oxidation extending beyond the surface silicon layer. The oxygen uptake curve of the B:Si(111)- $\sqrt{3}\times\sqrt{3}$ surface, however, shows a much slower oxidation rate both in dark and under UV-exposure. In such a surface a delta-doped boron layer is formed in the third atomic plane which, via charge-transfer, results in emptying the dangling-bond surface states³. It has been proposed that the sticking of oxygen is dominated by electron transfer from surface states in a harpooning process⁴. On a B-doped surface with diminished dangling-bond occupancy, the harpooning to form O_2^- is suppressed and the adsorption, as well as both thermal and photochemical silicon oxidation are greatly reduced.

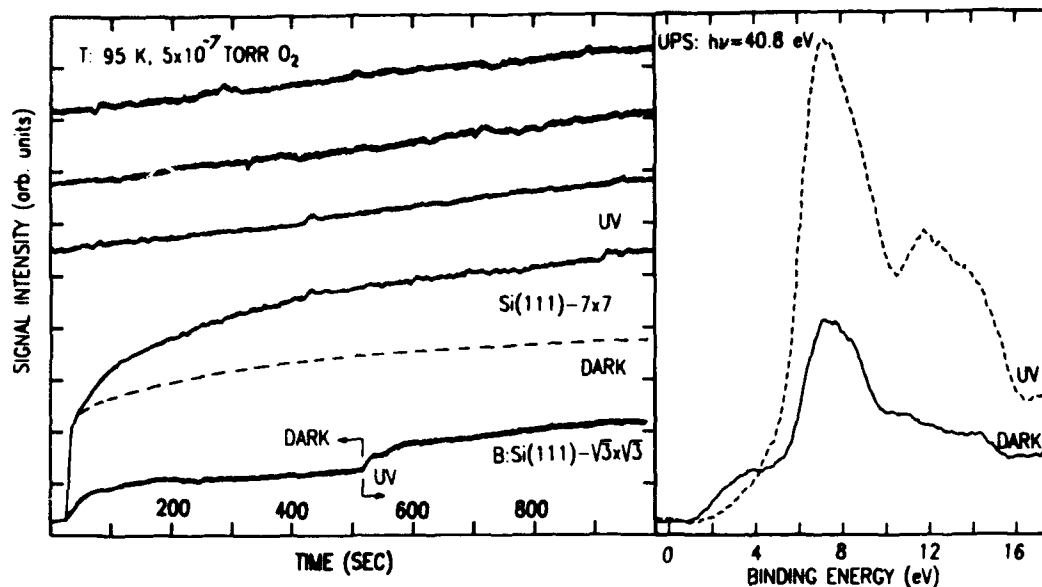


Fig. 2. Left panel: Oxygen uptake at 100 K in 5×10^{-7} torr O_2 , monitored by UPS intensity at 7.5 eV binding energy. Dashed curve: clean Si(111)-7x7 surface in dark. Upper solid curves: UV-exposed Si(111)-7x7. Bottom solid curve: B:Si(111)- $\sqrt{3} \times \sqrt{3}$ in dark and UV-exposed from time marked by arrows.

Right panel: He II ($h\nu=40.8$ eV UPS spectra of oxygen-exposed Si(111)-7x7 after treatments as in left panel.

Following the study of UV-induced oxidation and hydrogenated silicon film growth from single component adsorbed molecular layers, we turn to reactions in a co-adsorbed oxygen-disilane layer and to oxide film growth. In an ambient 1×10^{-7} torr Si_2H_6 and 2×10^{-6} torr O_2 under UV-exposure, an oxide film growth of ~ 0.02 monolayer/sec was observed at 100 K. Upon rapid thermal annealing to 1200 K, the UPS and XPS spectra of this film showed the characteristics of SiO_2 .

The mechanism of the photo-induced reactions in the co-adsorbed layer is too complicated to solve at present because of the great variety of possible photo-generated surface species. Here we focus only on one of them, i.e. on O_2 . In Fig. 1, curve (2) showed oxygen adsorption in form of O_2 molecular precursor. A high reactivity, and therefore a possible role of such photo-generated oxygen species in UV-induced SiO_2 film growth is indicated by its instantaneous reaction with disilane at 100 K, as it was observed by UPS.

Finally, we note that besides oxygen and disilane a number of other adsorbed molecules, such as NH_3 , NO , PH_3 and $B_{10}H_{14}$, have exhibited UV- or electron-beam-induced dissociation on silicon surfaces under similar conditions and silicon nitride, oxinitride and highly-doped silicon films have been grown at cryogenic temperatures.

References

1. Ph. Avouris and R. Walkup, *Ann. Rev. Phys. Chem.* **94**, 173 (1989).
2. P. Morgen, U. Hoefer, W. Wurth and E. Umbach, *Phys. Rev. B.* **39**, 3720 (1989); U. Hoefer, P. Morgan, W. Wutrh and E. Umbach, *Phys. Rev. B.* **40**, 1130 (1989).
3. Ph. Avouris, I.-W. Lyo and F. Bozso, *J. Vac. Sci. Technol. A.* in press and to be published.
4. Ph. Avouris and F. Bozso, *J. Phys. Chem.* **94**, 2243 (1990).
5. I.-W. Lyo, E. Kaxiras and Ph. Avouris, *Phys. Rev. Lett.* **63** (1989).

Low-Energy Ion/Surface Interactions During Vapor-Phase Film Growth For Manipulating Microchemistry and Microstructure at the Atomic Level

J.E. Greene

Department of Materials Science, the Coordinated Science Laboratory, and the Materials Research Laboratory, University of Illinois, 1101 Springfield Ave., Urbana, Illinois 61801, USA

1. Introduction

Low-energy (≤ 200 eV) ion irradiation during crystal growth from the vapor phase can be used to provide new chemical reaction pathways, modify film-growth kinetics, and, hence, controllably alter the physical properties of films deposited by a variety of techniques. The latter includes sputter deposition, ion plating, plasma-assisted chemical vapor deposition (PA-CVD), primary-ion deposition (PID), and molecular-beam epitaxy (MBE) using accelerated beam sources. Ion/surface interaction effects such as ion-induced chemistry, trapping, recoil implantation, preferential sputtering, collisional mixing, enhanced diffusion, and alteration in segregation behavior are used to interpret and model experimental results concerning the effects of low-energy particle bombardment on nucleation and growth kinetics, elemental incorporation probabilities, compositional depth distributions, and the growth of metastable phases. Review articles on various aspects of ion irradiation during film growth including effects on nucleation and growth kinetics [1-4], microstructural evolution [4], preferred orientation and stress [2], elemental incorporation probabilities [1-3], dopant incorporation and depth distributions [5], and the synthesis of metastable semiconducting alloys [1-3,6] are available. Monte Carlo and molecular dynamics growth simulations have also been reviewed [4]. In this extended abstract, some of the key features of low-energy ion/surface interactions are outlined and new results are described.

2. Nucleation Kinetics

Low-energy ion bombardment of the substrate and growing film can lead, in addition to sputter cleaning,[7] to fundamental changes in nucleation kinetics. Examples of irradiation-induced effects include the production of defects in the substrate surface which can act as preferred adsorption sites (e.g., refs. 8,9), trapping or implanting of incident species in the near-surface region (e.g., ref. 10), the dissociation of small clusters during the early stages of growth (e.g., ref. 11), enhanced adatom diffusion (see discussion in ref. 11), and local electric fields due to charging. The effects which dominate in a given experiment depend upon the film/substrate combination, the energy E_i , flux J_i , and mass m_i of the incident particles, and the growth temperature T .

Hasan et al. [11] interpreted transmission electron microscopy (TEM) observations of apparent "enhanced" adatom diffusion during PID of In on Si_3N_4 substrates in ultra-high vacuum (UHV) as being due to the depletion of small clusters (incipient islands) by sputtering and ion-induced dissociation. As small clusters are reduced in size, they become more mobile on the surface and can diffuse to feed larger stable islands. The suppression of secondary nucleation in these experiments led, in turn, to significant differences in island coalescence kinetics, and, hence, island size distributions as a function of nominal overlayer thickness.

Several workers have reported substantial decreases in the epitaxial temperature T of MBE Si, Ge, and metal films by either ionizing a small fraction of the evaporant flux and accelerating it to the substrate or using a UHV, low-energy, mass-filtered ion beam deposition system [12-15].

Mechanisms, other than sputter cleaning [16,17], for ion-bombardment-induced enhancement in film epitaxy can be visualized using molecular dynamic (MD) simulations such as those by Müller (e.g., ref. 18) for metals and the recent work of Kitabatake et al. [19,20] for Si. The use of an accelerated incident growth flux increases the "impact mobility" [21] of adatoms resulting in an increase (of the order of a few lattice spacings in $T = 0$ K simulations) in the average distance between the point of first interaction with the substrate surface and the position where the atom is finally adsorbed. In addition, rearrangements occur during both the first few hundred femtoseconds (fs) following a bombardment event and during the subsequent relaxation period. In the case of covalently bonded semiconductors, bond bending forces play a strong role and collision sequences leading to direct and exchange epitaxial events have been observed in simulations initiated at high and low symmetry points in the Si(001)2x1 surface unit cell [19,20].

Tsao et al. [22] have recently carried out in-situ measurements of ion-irradiation effects during epitaxial film growth. The authors videotaped changes in reflection high-energy electron diffraction (RHEED) patterns resulting from the addition of 500 eV Ar^+ ion irradiation during MBE growth of Ge(100) at 550 °C. They proposed that the primary effect of ion irradiation in their initial experiments was to break up 3-D clusters to provide a smoother growth surface. Choi et al. [23] used RHEED to show that layer-by-layer growth of InAs on Si(001) could be prolonged by simultaneous Ar^+ irradiation with a flux of 4 ions per deposited atom.

Both experimental results and growth simulations show that low-energy ion bombardment during deposition can provide local atomic rearrangement allowing atoms to relax into lower energy sites. However, the question of residual ion damage still needs to be addressed in more detail. The growth of high-quality films with reduced epitaxial temperatures requires a balance between the beneficial effects of ion irradiation such as enhanced diffusion and minimizing residual damage by annealing out bombardment-induced defects during deposition (see, for example, refs. 24-27).

3. Film Growth Kinetics

During growth at low substrate temperatures ($T/T_s \sim 0.3$) for which the films are generally underdense with a columnar microstructure, have shown that the number density of voids and pores decreases dramatically with increasing ion energy and/or ion flux [28-31]. Monte Carlo (MC) and MD simulations of film growth under ion irradiation have also shown an increase in film density towards bulk values [18,21,32]. For example, in low-temperature growth simulations, the MC films had porous columnar structures in the absence of ion bombardment. However, accounting for ion irradiation effects using a modified version of the TRIM computer yielded quite different growth morphologies. Ion incorporation, sputtering, and recoil implantation resulted in a film density that increased almost linearly with the ion-to-vapor flux ratio J_i/J_v . The calculations also predicted that there should be an optimum ion energy E_i^* for densification. The optimization resulted from the fact that at $E_i < E_i^*$ the number of recoil events is small while at $E_i > E_i^*$ an increasing fraction of the ion energy is lost deeper in the lattice leaving vacancies which cannot be filled by arriving vapor species. In cases for which the computer simulations were compared to experimental data, good agreement was found [30,31].

While ion irradiation is useful for increasing the density and modifying the morphology of films deposited at low temperatures, other irradiation-induced effects occur simultaneously. For example, as the ion energy and ion flux are increased, atomic displacements produced in the collision cascades result in an increasing number of residual interstitials and vacancies. These point defects can, in turn, lead to an increased density of

extended defects such as dislocation loops and reduced grain sizes in polycrystalline films grown under low-energy ion irradiation [29,33-35].

At elevated growth temperatures, low-energy ion irradiation can, in contrast to the above low temperature results, have the opposite effect and actually reduce residual defect densities in as-deposited films. Direct evidence has recently been published by Hultman et al. [25,26] who used TEM analyses to investigate the dislocation structure in epitaxial TiN films grown on MgO(100) substrates at T_s between 550 and 850 °C by reactive magnetron sputtering in pure nitrogen discharges. (T_e in this case is \approx 525-550 °C). The primary defects in the TiN films were dislocation loops on (111) planes. The dislocation number density n_d in epitaxial TiN layers decreased by many orders of magnitude with increasing V_s at constant T_s until a minimum defect density was obtained at a specific voltage V_s^* . For $V_s > V_s^*$, n_d increased rapidly and eventually the films became polycrystalline. J_i/J_v in these experiments ranged from \approx 1 to 1.4 and the energy per incident accelerated N atom was $\approx V_s/2$. Films grown at $T_s > 750$ °C and $V_s = V_s^*$ were essentially free of dislocation loops. XTEM micrographs of multilayer films in which sequential layers were grown with different values of V_s showed that ion bombardment effects were reversible [25].

Ion irradiation in the above experiments played at least two major roles. For the lower biases, the primary effect was to enhance adatom mobilities thereby accelerating the rate at which defects (both growth-related and ion-irradiation-induced) were annealed out during deposition. At higher bias voltages ($V_s > V_s^*$), the increased projected range of the impinging ions resulted in a larger fraction of the irradiation-induced defects being trapped in the growing film. Eventually, n_d became high enough that renucleation occurred during growth and polycrystalline films were obtained.

4. Elemental Incorporation Probabilities

Low-energy ion irradiation is often used during vapor-phase film growth to controllably alter the composition of as-deposited layers. Examples include preferential sputtering from the growing film during the deposition of alloys [36-39], enhanced reactive-gas incorporation during deposition of compounds [40-44], and increased dopant incorporation probabilities combined with better control of dopant depth distributions during the MBE growth of semiconductors (see discussion below). However, ion bombardment can also result in potentially deleterious effects such as rare-gas incorporation [45-47,48] leading to compressive stress in sputter-deposited coatings. Mechanisms associated with accelerated-particle/film interactions leading to changes in incorporation probabilities range from purely physical effects such as implantation and recoil processes to irradiation-assisted chemistry.

4.1 Incorporation of Non-Volatile Constituent Species

Ion bombardment during the deposition of alloys is commonly used to controllably modify the film composition through preferential resputtering. The first model for predicting the composition of alloy films deposited by bias sputtering was proposed by Winters et al. [36] in which they explicitly accounted for the surface area fraction of each species. Cuomo and Gambino [37] later derived useful empirical relationships between alloy film composition and the substrate bias during glow discharge sputtering.

One of the first systematic experimental studies in this area was carried out by Tarn and Wehner [38] using a triode Ar sputtering system mounted in one arm of an UHV analytical chamber equipped with facilities for Auger electron spectroscopy (AES). AES analyses showed that the composition of as-deposited $Ni_{1-x}Cu_x$ alloys could be varied from $x = 55$ at %, the target composition, to $x = 5$ at % by changing the negative applied substrate

potential from 0 to 100 V while maintaining the target voltage constant at -750 V. Similarly, Zilko and Greene [39] varied the Bi concentration in single-crystal $\text{InSb}_{1-x}\text{Bi}_x$ alloys by changing the Ar sputtering pressure, and hence the induced negative potential on the growing film, during rf glow-discharge sputtering from two targets, InSb and Bi. Dual ion-beam sputter deposition has also been employed to investigate preferential resputtering [49]. Much less work has been done on preferential sputtering during the deposition of compounds. However, the tendency appears to be that stoichiometry is favored as excess constituents are preferentially sputtered [50,51].

4.2 Incorporation of Volatile Constituent Species

The role of ion/surface interactions in altering the composition of compound and alloy films with volatile constituents is more complex and often involves a combination of trapping and ion-assisted chemistry in addition to preferential sputtering. In many cases, each of these effects is significant in determining the film condition.

An example for which preferential sputtering dominates is the growth of ZnO by reactive dc magnetron sputter deposition with an applied rf substrate bias in mixed Ar/O₂ atmospheres [40]. With no substrate bias, the films were oxygen deficient. However, the O/Zn ratio increased rapidly with increasing V_s until nearly stoichiometric films were obtained at V_s = 100 V. Collisionally-induced dissociative chemisorption and trapping, i.e. low-energy implantation, of accelerated O₂⁺ ions contributed to the increase in oxygen concentration in the films. The dominant ion bombardment effect, however, was preferential resputtering of Zn.

An example of ion-assisted chemistry is the use of accelerated group-V beams for the growth of III-V compounds and alloys such as GaAs, InP, GaAs_{1-y}P_y, and In_{1-x}Ga_xAs_{1-y}P_y [41,42]. In the case of InP grown from thermal In and P₄ beams, for example, P₄/In flux ratios as high as 100 are used. However, Shimizu et al. [41] have recently demonstrated that with low-energy (100-200 eV) mass-separated As⁺ and P⁺ ion beams, stoichiometric GaAs and InP films could be grown using V/III flux ratios near unity. Photoluminescence spectra from GaAs films grown with E_{As} = 100 eV and T \geq 500 °C showed no indication of residual damage. The first high resistivity GaN single crystals have been grown recently using reactive-ion MBE (Ga chemisorbs atomic N, but not molecular N₂) in which the Ga flux is provided by an effusion cell while the nitrogen flux is obtained from a low-energy (typically 35 eV) N₂⁺ source. [52] The N vacancy concentration was decreased by more than 5 orders of magnitude (as judged by Hall measurements) through increases in the N₂⁺/Ga ratio by less than a factor of 8.

The examples given above where preferential sputtering favored stoichiometry all involved the deposition of "line compounds"; that is, materials for which the single-phase compound field in the equilibrium phase diagram is very narrow. The effect does not appear to be as strong in materials such as transition-metal nitrides which exhibit extended phase fields with stable vacancy structures. For example, Sundgren et al. [44] showed that TiN films with N/Ti ratios up to 1.2 could be obtained by increasing the negative substrate bias during reactive magnetron sputter deposition. The dominant ion irradiation effect in this case is the trapping of excess N.

4.3 Dopant incorporation

There is growing interest in the use of accelerated dopant beams in MBE. Most of the common dopants used in both Si and GaAs device technology present problems during film growth by MBE due to low incorporation probabilities σ and/or pronounced surface accumulation. Recently, Hasan et al. [53] have shown that with 200 eV In⁺ accelerated-ion doping of Si(001) films grown at 800 °C, σ is unity (an increase by > five orders of magnitude over

that obtainable using thermal In). Doping profiles in modulation-doped structures were abrupt to within the depth resolution of secondary-ion microscopy and two-dimensional δ doping profiles were achieved. $\sigma(E_i, T_s)$ has been determined for $E_i = 50-500$ eV and $T_s = 500-1100$ °C. Temperature-dependent electrical measurements and cross-sectional TEM studies carried out by Noël et al. [54] showed that the films exhibited no indication of residual ion damage with maximum theoretically allowed carrier mobilities, even at In concentrations well above equilibrium solid-solubility limits, and minority-carrier trap concentrations $\leq 2 \times 10^{13}$ cm⁻³. Similar results have been obtained for Sb⁺ ion doping [55,56]. Recently, Ni et al. [56] developed a multi-site transition-state model (including surface, bulk, and three intermediate sites) in which dopant surface segregation, incorporation, and bulk diffusion are accounted for by solving simultaneous transition-rate equations.

While no residual ion-induced damage was observed for ion doping with $E_i \leq 200$ eV and $T_s = 800$ °C, clearly at sufficiently high E_i and/or low T_s , residual ion damage will be detectable. This has been demonstrated by Noël et al. [26] using a combination of DLTS and PL to study As⁺ ion doping during Si(100) MBE. Films grown with $E_i \leq 500$ eV and $T_s \geq 650$ °C exhibited some of the best photoluminescence ever reported in MBE Si with no traps detectable by DLTS [26,27]. However, strong ion-damage related PL signatures and electron trap states ($\geq 10^{14}$ cm⁻³) were observed in all ion-doped films grown at 500 °C and in films grown at $T_s = 650$ °C with $E_i = 1000$ eV.

Acknowledgements

The financial support of the Joint Services Electronics Program, the Materials Science Division of the U.S. Department of Energy, the Semiconductor Research Corporation, the Space Vacuum Epitaxy Center funded by NASA during the course of this work is gratefully acknowledged.

References

1. J.E. Greene, T. Motooka, J.-E. Sundgren, D. Lubben, S. Gorbatkin, and S.A. Barnett, *J. Nucl. Instr. Methods* B27, 226 (1987).
2. J.E. Greene, S.A. Barnett, J.-E. Sundgren, and A. Rockett, *Low-Energy Ion/Surface Interactions During Film Growth from the Vapor Phase*, ed. by T. Itoh, (Elsevier, Amsterdam, 1988), Chapter 5.
3. J.E. Greene, S.A. Barnett, J.-E. Sundgren, and A. Rockett, "Low-Energy Ion/Surface Interactions During Film Growth from the Vapor Phase: Effects on Nucleation and Growth Kinetics, Defect Structure, and Elemental Incorporation Probabilities," ed. by O. Auciello, A. Gras-Marti, and D.L. Flamm, *Plasma Surface Interactions and Processing of Materials*, NATO ASI Series (Kluwer Academic Publ., Dordrecht, Netherlands, 1990), p.281.
4. J.E. Greene, "Nucleation, Growth, and Microstructural Evolution in Films Grown by Physical Vapor Deposition," in *Deposition Technologies for Films and Coatings, 2nd Edition*, ed. by R.F. Bunshaw (Noyes Publ., Park Ridge, NJ), in press.
5. J.-E. Sundgren, J. Knall, W.-X. Ni, M.-A. Hasan, L.C. Markert, and J.E. Greene, *Thin Solid Films* 183, 281 (1989).
6. J.E. Greene, *J. Vac. Sci. Technol. A5*, 1947 (1987).
7. T.J. Donahue and R. Reif, *Semiconductor International*, August, 142, (1985).
8. G.E. Lane and J.C. Anderson, *Thin Solid Films* 26, 5 (1975).
9. G.E. Lane and J.C. Anderson, *Thin Solid Films* 57, 277 (1979).
10. S.A. Barnett, H.F. Winters, and J.E. Greene, *Surf. Sci.* 181, 596 (1987).
11. M.-A. Hasan, S.A. Barnett, J.-E. Sundgren, and J.E. Greene, *J. Vac. Sci. Technol. A5*, 1883 (1987).

12. T. Narusawa, S. Shimizu, and S. Komiya, *J. Vac. Sci. Technol.* **16**, 366 (1979).
13. G.E. Thomas, L.J. Beckers, J.J. Vrakking, and B.R. de Koning, *J. Cryst. Growth* **56**, 257 (1982).
14. P.C. Zalm and L.J. Beckers, *Appl. Phys. Lett.* **41**, 167 (1982).
15. N. Herbots, T.S. Noggle, B.R. Appleton, and R.A. Zhur, *J. Vac. Sci. Technol.*, in press.
16. K. Yagi, S. Tamura, and T. Tokuyama, *Jpn. J. Appl. Phys.* **16**, 245 (1977).
17. T. Tokuyama, K. Yagi, K. Miyaki, M. Tamura, N. Natsuaki, and S. Tachi, *Nucl. Instr. Meth.* **182/183**, 241 (1981).
18. K.-H. Müller, *Phys. Rev.* **35**, 7906 (1987).
19. M. Kitabatake, P. Fons, and J.E. Greene, *J. Vac. Sci. Technol.* **A8**, 3726 (1990).
20. M. Kitabatake, P. Fons, and J.E. Greene, *J. Vac. Sci. Technol.*, in press.
21. K.-H. Müller, *Surf. Sci. Lett.* **184**, L375 (1987).
22. J.Y. Tsao, E. Chason, K.M. Horn, D.K. Brice, and S.T. Picraux, *Nucl. Instr. Meth.*, in press.
23. C.-H. Choi, L. Hultman, and S.A. Barnett, *J. Vac. Sci. Technol.* **A8**, 1587 (1990).
24. L. Hultman, U. Helmersson, S.A. Barnett, J.-E. Sundgren and J.E. Greene, *J. Appl. Phys.* **61**, 552 (1987).
25. L. Hultman, S.A. Barnett, J.-E. Sundgren, and J.E. Greene, *J. Crystal Growth* **92**, 639 (1988).
26. J.-P. Noël, J.E. Greene, N.L. Rowell, S. Kechang, and D.C. Houghton, *Appl. Phys. Lett.* **55**, 1525 (1989).
27. J.-P. Noël, J.E. Greene, N.L. Rowell, and D.C. Houghton, *Appl. Phys. Lett.* **56**, 265 (1990).
28. D.M. Mattox and G.J. Kominiak, *J. Vac. Sci. Technol.* **9**, 528 (1972).
29. G. Hakanssan, J.-E. Sundgren, D. McIntyre, J.E. Greene and W.-D. Münz, *Thin Solid Films* **153**, 55 (1987).
30. P.J. Martin, R.P. Netterfield, and W.G. Sainty, *J. Appl. Phys.* **55**, 235 (1984).
31. R.P. Netterfield, W.G. Sainty, P.J. Martin, and S.H. Sie, *Appl. Opt.* **24**, 2267 (1985).
32. K.-H. Müller, *Appl. Phys. A* **40**, 209 (1986).
33. T.C. Huang, G. Lim, F. Parmigiani, and E. Kay, *J. Vac. Sci. Technol. A* **3**, 2161 (1985).
34. B.O. Johansson, J.-E. Sundgren and U. Helmersson, *J. Appl. Phys.* **58**, 3112 (1985).
35. E. Kay, F. Parmigiani and W. Parrish, *J. Vac. Sci. Technol. A* **5**, 44 (1987).
36. H.F. Winters, D.L. Ramondi and D.E. Horne *J. Appl. Phys.* **40**, 2996 (1989).
37. J.J. Cuomo and R.J. Gambino, *J. Vac. Sci. Technol.* **12**, 79 (1975).
38. M.L. Tarng and G.K. Wehner, *J. Appl. Phys.* **42**, 2449 (1971).
39. J.L. Zilko and J.E. Greene, *J. Appl. Phys.* **51**, 1549 (1980).
40. M.J. Brett and R.R. Parsons, *Can. J. Phys.* **63**, 819 (1985).
41. S. Shimizu, T. Tsukakoshi, S. Komiya, and Y. Makita, "GaAs and Related Compounds" in *Inst. Phys. Conf. Series* **79**, 91 (1985), ed. by M. Fujimoto.
42. S. Maruno, Y. Morishita, T. Isu, Y. Nomura, and H. Ogata, *J. Electronic Mater* **17**, 21 (1988).
43. J.M.E. Harper, J.J. Cuomo, and H.T.G. Hentzell, *J. Appl. Phys.* **58**, 550 (1985).

44. J.-E. Sundgren, B.O. Johansson, A. Rockett, S.A. Barnett and J.E. Greene, "Chemistry and Physics of Hard Coatings" in *American Inst. Phys. Series Conf. Proc. 149*, 95 (1986), ed. by W. Sproul, J.E. Greene, and J.A. Thornton.
45. H.F. Winters and E. Kay, *J. Appl. Phys.* **38**, 3928 (1967).
46. D.W. Hoffman and J.A. Thornton, *J. Vac. Sci. Technol.* **20**, 355 (1982).
47. A. Pan and J.E. Greene, *Thin Solid Films* **153**, 78 (1981).
48. L. Hultman, L.C. Markert, J.-E. Sundgren and J.E. Greene, *Appl. Phys. Lett.* **53**, 1175 (1988).
49. See, for example, J.M.E. Harper and R.J. Gambino, *J. Vac. Sci. Technol.* **16**, 1901 (1979).
50. A.H. Eltoukhy, S.A. Barnett and J.E. Greene, *J. Vac. Sci. Technol.* **16**, 321 (1979).
51. J.L. Zilko, S.A. Barnett, A.H. Eltoukhy, and J.E. Greene, *J. Vac. Sci. Technol.* **17**, 595 (1980).
52. R.C. Powell, G.A. Tomasch, Y.-W. Kim, J.A. Thornton, and J.E. Greene, in *Wide Bandgap Semiconductors*, ed. by J.T. Glass, N. Fujimori, and R. Messier, MRS, Pittsburgh, in press.
53. M. Hasan, J. Knall, S.A. Barnett, J.-E. Sundgren, L.C. Markert, A. Rockett, and J.E. Greene *J. Appl. Phys.* **65**, 172 (1989).
54. J.-P. Noël, N. Hirashita, L.C. Markert, Y.-W. Kim, J.E. Greene, J. Knall, W.-X. Ni, M. Hasan, and J.-E. Sundgren, *J. Appl. Phys.* **65**, 1189 (1989).
55. P. Fons, N. Hirashita, L.C. Markert, Y.-W. Kim and J.E. Greene, *Appl. Phys. Lett.* **53**, 1732 (1988).
56. W.-X Ni, J. Knall, M.A. Hasan, G.V. Hansson, J.-E. Sundgren, S.A. Barnett, L.C. Markert, and J.E. Greene, *Phys. Rev. B* **40**, 10449 (1989).

Coherent Strain Changes in Si-Ge Alloys Grown By Ion-Assisted Molecular Beam Epitaxy

H.A. Atwater, C.J. Tsai and T. Vreeland
Thomas J. Watson Laboratory of Applied Physics
M.S. 128-95
California Institute of Technology
Pasadena, CA 91125

Introduction

Although low energy ion bombardment has been employed in various contexts during epitaxial growth, such as enhanced dopant incorporation[1], surface cleaning during plasma-enhanced chemical vapor deposition[2], and direct low energy ion beam deposition[3,4], key questions about the interaction of low energy ions with growing surfaces remain unanswered. Improved understanding of ion-surface interactions during growth may yield additional elements of control over epitaxial film structure, strain state, and composition. Of particular interest for high quality epitaxial films is the identification of the regime in which surface and near-surface processes, such as surface diffusion and incorporation at growth sites, can be enhanced at low temperatures while avoiding or controlling damage in the deposited films.

In this paper we address the question of beam-induced defect generation at an epitaxial growth surface with measurements of the systematic modification of perpendicular strain in *coherent* Ge and Si_xGe_{1-x} layers by concurrent molecular beam epitaxial growth and low energy ion bombardment. Layers are uniformly strained and contain no dislocations, suggesting that misfit strain is accommodated by free volume changes associated with injection of ion bombardment-induced point defects. The dependence of layer strain on ion energy, ion-atom flux ratio and temperature are consistent with the presence of a uniform dispersion of point defects at high concentration. The strain produced by ion-induced defects provides a sensitive experimental probe of the distinction between ion-surface interactions and ion-bulk interactions.

Experimental Configuration

Films were grown in a custom-designed molecular beam epitaxy system with a base pressure of 1×10^{-10} Torr, which was equipped with electron beam sources for molecular beam deposition of Si and Ge. Strain-modified films 100 nm thick were grown at constant rate in the range 0.1-0.7 nm/sec on (001) Ge substrates, following growth of a 50 nm buffer layer of pure Ge by conventional molecular beam epitaxy. Concurrent ion bombardment was accomplished using a Kaufmann-type ion source noble gas ion bombardment during growth at energies of 50-500 eV, and ion-atom flux ratios were typically in the range 1:10 - 1:100. Growth temperatures were in the range of 250 - 500 ° C. Films were analyzed *in-situ* using reflection high energy electron diffraction (RHEED), and following growth by double-crystal X-ray diffractometry using $Fe-K\alpha$ radiation, and cross-sectional

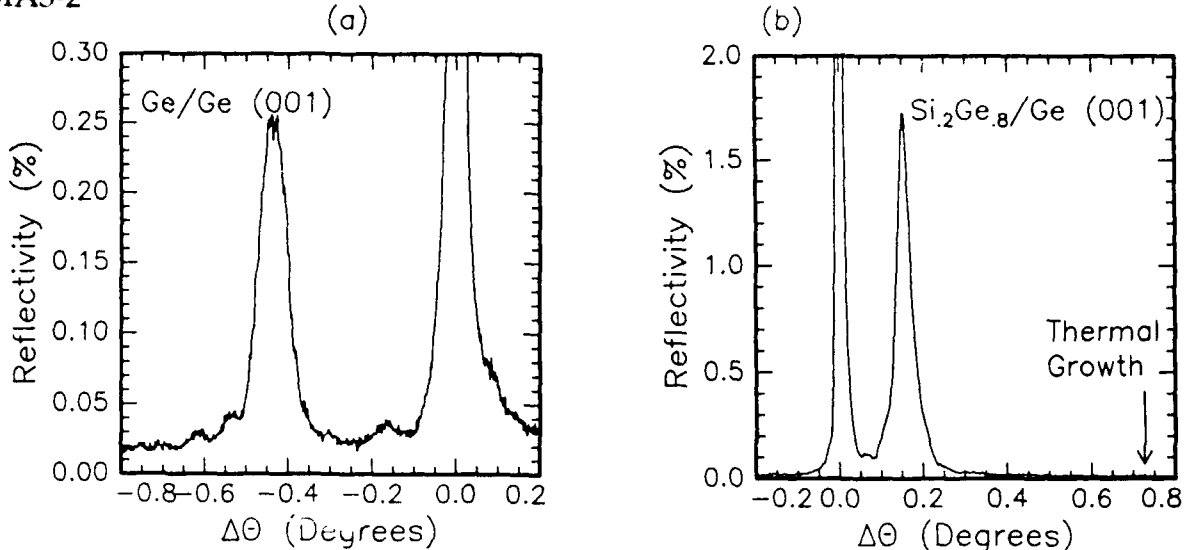


Figure 1: In (a), X-ray rocking curve around (400) Bragg peak for 100 nm Ge film grown on (001) Ge by IAMBE at $T = 360^\circ\text{C}$ for an ion/atom flux ratio $J_i/J_a = 0.03$, and incident Ar^+ ion beam energy $E_i = 200\text{ eV}$. In (b), X-ray rocking curve around (400) Bragg peak for similar growth conditions.

transmission electron microscopy.

Strain Changes During Ion-Assisted Epitaxial Growth

The strain state for a 100 nm thick Ge film on (001) Ge grown by IAMBE is illustrated by the X-ray rocking curves in Figure 1(a), taken around the (400) Bragg peak. The film was grown at $T = 360^\circ\text{C}$, at a growth rate of 0.3 nm/sec with an ion energy of $E_i = 200\text{ eV}$ and ion/atom flux ratio of $J_i/J_a = 0.03$. In the rocking curve scan around (400), a sharp Bragg peak of instrumentation-limited width is observed at angular shift of $\Delta\theta = -0.44^\circ$ from the substrate Bragg peak. The observations indicate the presence of a coherent film with perpendicular strain resulting in a tetragonal distortion such that $\epsilon_{\perp} = 0.82\%$. The observed RHEED pattern at 25 keV along a [110] azimuth indicated a smooth surface morphology with (2x1) reconstruction characteristic of a clean (001) Ge surface. Cross-sectional transmission electron microscopy indicated the 100 nm film to be free of misfit dislocations, threading dislocations and stacking faults, indicating that strain modification did not occur as a result of introduction of linear or planar defects.

Figure 1(b) shows an X-ray rocking curve scan for a Si₂Ge₈ layer grown at a rate of 0.25 nm/sec with an ion energy of $E_i = 200\text{ eV}$ and ion/atom flux ratio of $J_i/J_a = 0.03$. In the rocking curve scan around (400), the Bragg peak from the 100 nm film occurs $\Delta\theta = 0.2^\circ$ with respect to the substrate Bragg peak. It should be noted that a coherent film with this alloy composition grown by conventional MBE exhibits a Bragg peak at $\Delta\theta = 0.73^\circ$, with an associated strain of $\epsilon_{\perp} = -1.2\%$. The magnitude and sign of strain modification are nearly equal for the pure Ge film and Si₂Ge₈ alloy, strongly suggesting that the normally tensile strain in the Si₂Ge₈ alloy was compensated by point defects introduced by IAMBE growth.

The variation of perpendicular strain, ϵ_{\perp} , with ion/atom flux ratio J_i/J_a , for 100 nm thick Ge films grown on Ge (001) by IAMBE is shown in Fig. 2, for films grown at $T = 360^\circ\text{C}$ with an Ar ion energy of $E_i = 200\text{ eV}$. An approximately linear relationship

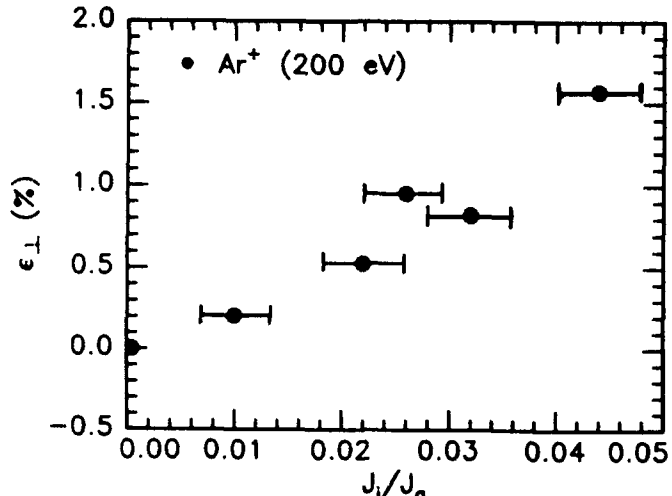


Figure 2: Variation of perpendicular strain, ϵ_{\perp} , with ion/atom flux ratio J_i/J_a , at the surface for 100 nm thick Ge films grown on Ge (001) by IAMBE at $T = 360^{\circ}\text{C}$. All films grown with Ar ion energy of $E_i = 200$ eV.

exists between perpendicular strain, ϵ_{\perp} and ion-atom flux ratio J_i/J_a in the range $J_i/J_a = 0 - 0.05$. For higher ion-atom flux ratios, no strain modification was observed. For ion-atom flux ratios above 0.06, the Bragg peak from the strain-modified film broadens and is reduced in intensity. For $J_i/J_a \geq 0.1$, the RHEED pattern is characterized by Bragg diffraction spots rather than rods, indicating qualitatively the development of a rough surface morphology.

Surface and Bulk Defect Kinetics

The variation of perpendicular strain, ϵ_{\perp} , with incident ion energy, E_i , for 100 nm thick Ge films grown on Ge substrates with ion-atom flux ratio of $J_i/J_a = 0.02$ at $T = 360^{\circ}\text{C}$ is illustrated in Fig. 3. Strain increases monotonically with incident ion energy in the energy regime $E_i = 70 - 300$ eV. For ion energies below 70 eV under these growth conditions, no detectable strain is observed. We believe that the present measurements of coherent perpendicular strain as a function of energy represent possibly *the most sensitive measurement to date* of the ion energy which demarcates the regimes for displacement of only surface atoms, and the displacement of bulk atoms as well as surface atoms. Brice, et. al. have suggested a conceptual framework for partitioning of surface and bulk displacements at low ion energies[5]. Interestingly, their calculations suggest that the surface-to-bulk displacement ratio, R , varies from $R = 1.6$ at $E_i = 100$ eV to $R = 8$ at $E_i = 50$ eV for Ar^+ ions incident on Ge surfaces. The close agreement between their calculations of the demarcation energy and strain modification in the present experiments may be fortuitous, but it illustrates that point that measurement of strain modification by injection of point defects into the bulk may be a powerful tool for delineation of this regime.

To elucidate the relative roles of native point defects and trapped gas in strain modification, another set of ion-assisted epitaxy experiments was performed. Rutherford backscattering spectrometry (RBS) was used to measure trapped gas concentration. To enhance the sensitivity of the measurements of gas concentration by RBS, 200 eV Xe^+

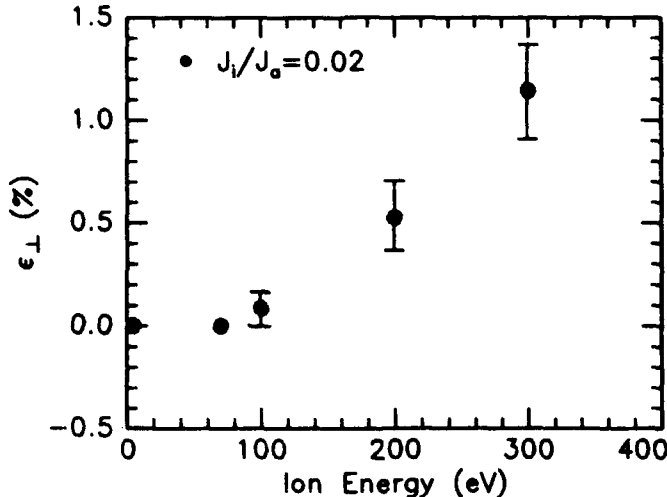


Figure 3: Variation of perpendicular strain, ϵ_{\perp} , with incident ion energy, E_i , for 100 nm thick Ge films grown on Ge substrates by IAMBE at $T = 360^{\circ}\text{C}$. Ion-atom flux ratio at the surface was fixed at $J_i/J_a = 0.02$. Error bars indicate the uncertainty introduced by possible variations in the ion-atom flux ratio, J_i/J_a .

ions were employed rather than Ar^+ . Briefly, for films grown using a Xe^+ ion beam, the strain was proportional to the concentration of Xe gas trapped in the film for concentrations up to approximately 0.5%. However, the change in strain with Xe concentration appears to be too large to be explained exclusively by interstitial accommodation of noble gas in the crystal, leading us to suggest that defect complex comprised of noble gas and native point defects is responsible for the observed strain modification.

This work was supported by the National Science Foundation P.Y.I.A. program (DMR-8958070) and the Materials Research Group program (DMR-8811795).

References

- [1] J.E. Greene, *CRC Critical Reviews in Solid State and Materials Science*, **2**, 47 (1983).
- [2] W.R. Burger and R. Reif, *J. Appl. Phys.* **62** 4255 (1987).
- [3] R.A. Zuhr, S.J. Pennycook, T.S. Noggle, N. Herbots T.E. Haynes, and B.R. Appleton, *Nucl. Instr. and Meth. B* **37/38**, 16 (1989).
- [4] P.C. Zalm and L.J. Beckers, *Appl. Phys. Lett.* **41** 167 (1982).
- [5] D.K. Brice, J.Y. Tsao and S.T. Picraux, *Nucl. Instrum and Methods* **44**, 68-78 (1989).

Monday, February 11, 1991

Initiation and Growth of Surface Layers

MB 9:45am-11:15am
Anasazi South

Daniel J. Erlich, *Presider*
MIT Lincoln Laboratory



ADSORBED LAYERS IN THE PROCESS OF CHEMICAL VAPOR DEPOSITION

Jun-ichi Nishizawa

Semiconductor Research Institute, Kawauchi, Aoba-ku, Sendai 980, Japan

Tel.: 022 (223) 7287

Introduction

In chemical vapor deposition, surface migration of adsorbed species is an important factor which limit the minimum crystal growth temperature, since high substrate temperature enhances the surface migration of the adsorbate. But, high temperature process produces defects in the crystal. Concerning this problem, photoepitaxy was proposed by the author in 1961 (1). It has been applied to Si (2) and GaAs vapor phase epitaxy (3), resulting in higher crystal quality at a lower growth temperature. Photochemical processes allow the possibility that each elemental process can be individually controlled among the competitive processes by using a specific wavelength.

Molecular layer epitaxy (MLE) is a crystal growth method using surface reactions of adsorption molecules and it is able to produce thin epitaxial films as accurate as a single atomic dimension (3). MLE of GaAs (3,4), Si (5) and AlGaAs were succeeded first in our experiments. It corresponds to the idea of atomic layer epitaxy using chemical reactants which was proposed by T. Suntola (6). In GaAs MLE, the material gases i.e. AsH_3 , TMG (or TEG) and dopant compound may adsorb on the specific site of the surface, when they are introduced onto the surface, alternately (7). Photo-excited process was also applied in MLE (8), the irradiation can be independently undertaken at different crystal growth steps.

Results and Discussion

Reaction mechanism of MLE had been measured by using mass spectroscopy and by measuring the growth thickness varying the growth condition. As a result, Ga compound which is made from TMG adsorbs on the surface, it may adsorb at monomolecular layer under the monolayer growth condition (7). When AsH_3 is injected onto the adsorption layer, the surface reaction of the adsorbate and AsH_3 occurs and the growth is performed.

Mass spectroscopic measurement during TMG injection were tried using some kinds of faces of GaAs substrates. Figure 1 (a)~(c) shows the intensity change of each species during TMG injection on (111)B, (100), and (111)A, respectively.

In the case of (111)B, at high temperature as 535°C , TMG may decompose quickly to Ga and CH_3 , but at lower temperature as 480°C , the increase of CH_3 needs 2~3 min. of TMG injection. It is supposed that when TMG is injected on the bare GaAs surface of (111)B, TMG decomposition is not easy to occur, but on Ga deposited (111)B surface TMG decomposition occur. The Ga deposition on that surface was identified by SEM topograph and AES. In MLE, we obtained the phenomenon of the self limiting growth on (111)B at 490°C , namely, the growth thickness per cycle is constant near monomolecular thickness in a wide range of TMG pressure. There is a possibility that the adsorbate in monomolecular growth condition is Ga or Ga compound, but a limiting effect for Ga deposition is exist.

In the case of (100), the reaction was quite different from the case of (111)B. TMG adsorption is caused at the beginning of the injection, and CH_3 desorbs at the same time. In Fig. 1-(b), the intensity difference between the first time exposure of TMG and the second time of it on (100) are shown. At the first time exposure, the surface may be bare, because AsH_3 was injected before TMG exposure. TMG adsorption occurred at the beginning of the injection, and it finished about 2 min. in our experimental conditions. At the same time of TMG adsorption CH_3 desorbed. We also tried the same measurement between the second

exposure and the third exposure, but the adsorption of TMG and the desorption of CH_3 was not observed.

In the case of (100), adsorption of excess TMG may be stopped after the adsorption layer is formed, and some methyl group desorbs during the formation of the adsorption layer. These phenomena correspond to the results of self-limit growth in MLE. To identify the species we need more experiments using XPS etc., these data will be published in another paper.

In the case of (111)A, during the exposure of TMG, the consumption of TMG (it corresponds to the intensity of amu 99) and the desorption of CH_3 and Ga compound amu 84 were observed. The intensity difference between the first exposure and the second exposure was also estimated, but any change was not observed except the adsorption phenomenon of TMG below 450°C. It was supposed that the reaction on (111)A occurred but the product was a volatile Ga compound. This result corresponds to the results of experiment in which no growth and no deposition of Ga occur on (111)A.

By the mass spectroscopic measurements, the difference of the adsorption and the reaction among various crystal faces were clarified. The difference may correspond to the difference of adsorbate.

The influence of the photoirradiation on the film growth by MLE was studied to prepare the perfect crystal thin film. As the experimental results, ultraviolet light irradiation improved the surface morphology of the film, but did not change the growth thickness. For GaAs MLE, AsH_3 as an arsenic source and TEG (or TMG) as a gallium source were used. These gaseous compounds were introduced alternately, but not simultaneously, and the evacuation was performed in between. The irradiation was independently undertaken at different crystal growth steps, e.g. the duration of the irradiation was synchronized with the time duration of AsH_3 feed, AsH_3 exhaust, TEG feed and TEG exhaust. As shown in Fig.2, the carrier concentration of the film was decreased and the Hall mobility was increased by the irradiation with 350 nm laser which was synchronized with AsH_3 or TEG feed. Whereas, they did not almost change the value when the irradiation was synchronized with AsH_3 and TEG exhaust. To consider about the improvement of the surface morphology and of the crystallinity by synchronized irradiation with AsH_3 and TEG feed, surface migration of adsorbate may be excited by photon energy, at least. Figure 3 shows the carrier concentration of the films obtained by the synchronized irradiation with excimer lasers. In the case of XeCl (308 nm) and XeF (350 nm), when the irradiation was synchronized with the AsH_3 feed and TEG feed, the carrier concentration decreased. On the other hand, when they are synchronized with the exhaust phase, the carrier concentration did not change. As mentioned, photodecomposition of TMG and AsH_3 occurs by the irradiation with 193 nm laser, and that of TMG occurs by the irradiation with 249 nm laser. It is supposed that when these wavelength lights are synchronized with AsH_3 feed and TEG feed duration, the carrier concentrations are increased by the photodecomposition. Then, the photo-effects in the case of 193 and 249 nm wavelength irradiation is quite different manner comparing the case of 308 and 350 nm irradiation.

Conclusion

Mass spectroscopic measurement during TMG injection were performed to investigate the surface reaction and the adsorbate on various GaAs surfaces. There was a limiting effect for TMG decomposition on bare GaAs surface on (111)B. In the case of (100), it was clarified that the adsorption of excess TMG after the formation of the adsorption layer (perhaps monomolecular layer), and some methyl group desorbs during the formation of the first adsorption layer. On (111)A, the reaction TMG may occur, but the product may be a volatile. To identify the adsorbate on each surface, more experiments using XPS is necessary.

In photoexcited MLE, the irradiation can be synchronized with the step of the gaseous injection sequence. The influences on the growing surface were revealed on the surface morphology and the electrical properties of the films. Namely, it is able to estimate which steps of the growth are effective for photoirradiation.

To consider about the improvement of the surface morphology and of the crystallinity, especially by the irradiation with 308 and 350 nm laser which were synchronized with AsH_3 and TEG feed. The irradiation effect may be concluded as the photoexcitation of the surface migration.

References

- (1) J. Nishizawa, Moletronics Program (I), J. Metal, 25, p. 149 (1961), Moletronics Program (II), J. Metal 25, p. 177 (1961).
- (2) M. Kumagawa, H. Sunami, T. Terasaki and J. Nishizawa, Jpn. J. Appl. Phys., 7 (11), 1332 (1969).
- (3) J. Nishizawa and Y. Kokubun, Extended Abstracts of 16th Int. Conf. on Solid State Devices and Materials, p. 1 (1984).
- (4) J. Nishizawa, H. Abe and T. Kurabayashi, J. Electrochem. Soc., 132, 1197 (1985).
- (5) J. Nishizawa, K. Aoki, S. Suzuki and K. Kikuchi, J. Crystal Growth 99, 502 (1990).
- (6) T. Suntola, Extended Abstracts of 16th Int. Conf. on Solid State Devices and Materials, p.647, Kobe, Japan (1984).
- (7) J. Nishizawa, T. Kurabayashi, H. Abe and A. Nozoe, Surface Science, 185, 249 (1987).
- (8) (a) J. Nishizawa and H. Abe, American Vacuum Society, 32nd National Symposium, Final Program, p. 109, Houston, Texas, Nov., 1985.
(b) J. Nishizawa, H. Abe, T. Kurabayashi, and N. Sakurai, J. Vac. Sci. Technol. A4, 706 (1986).
- (9) J. Nishizawa, T. Kurabayashi and J. Hoshina, J. Electrochem. Soc., 134, 502 (1987).
- (10) J. Nishizawa and T. Kurabayashi, J. Crystal Growth 99, 525 (1990).
- (11) J. Nishizawa and T. Kurabayashi, to be published in VACUUM, 41 (1990).

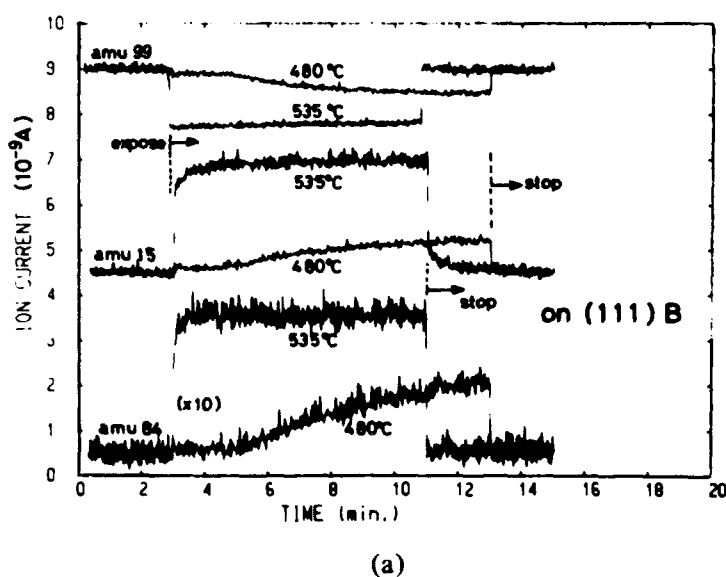


Fig.1 Mass spectrum intensity during TMG injection.
(a) (111)B.

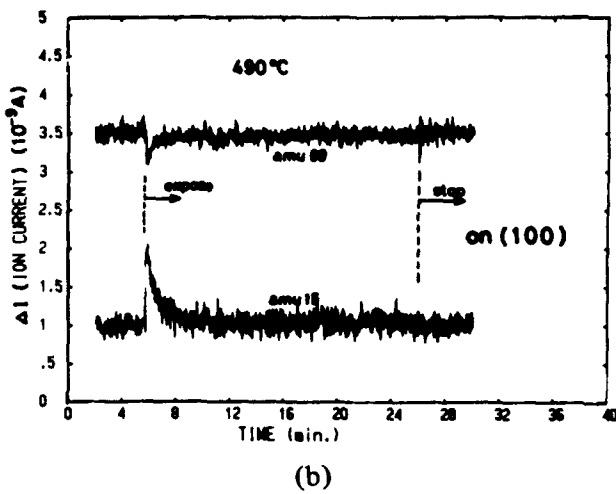


Fig.1 Mass spectrum intensity during TMG injection.

(b) (100), ΔI means the intensity difference between the first exposure of TMG and the second of it.

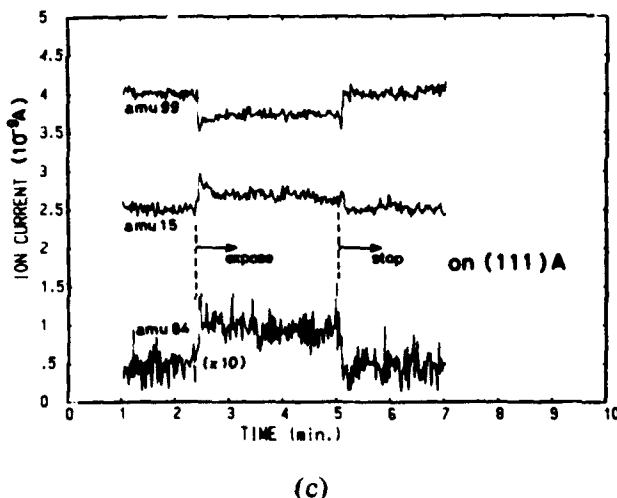


Fig.1 Mass spectrum intensity during TMG injection.

(c) (111)A.

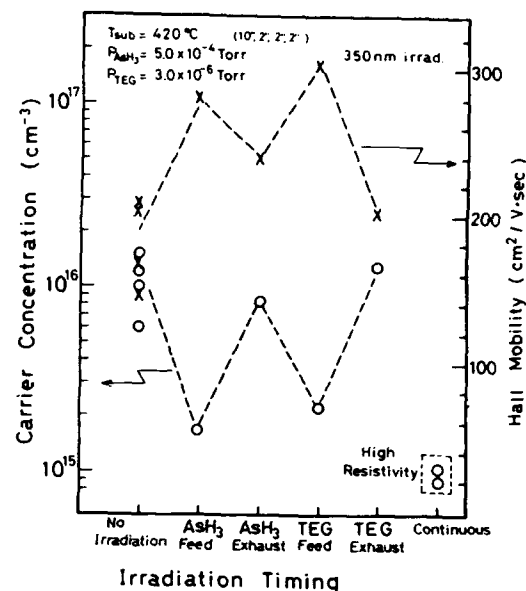


Fig.2 Carrier concentration and Hall mobility of the epitaxial films prepared by synchronized photo-excited MLE irradiated with XeF (350 nm) laser. The substrate is (100) of GaAs.

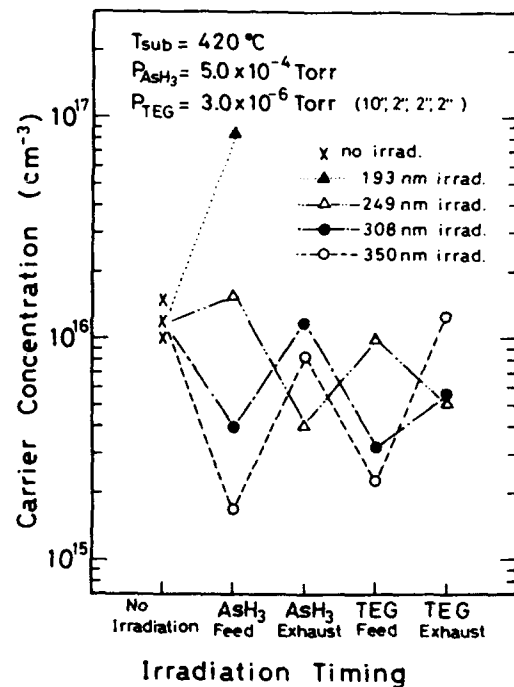


Fig.3 Carrier concentration of the epitaxial films prepared by synchronized photo-excited MLE irradiated with excimer lasers. The substrate is (100) of GaAs.

The Elucidation of the Mechanism of the Initial Stages of Si(111)-7x7 Oxidation Using Scanning Tunneling Microscopy

Ph. Avouris, I.-W. Lyo and F. Bozso
IBM Research Division, Watson Research Center
Yorktown Heights, NY 10598

B. Schubert and R. Hoffmann
Department of Chemistry and Materials Science Center
Cornell University, Ithaca, NY 14853

The capability of the scanning tunneling microscopy (STM) and spectroscopy (STS) to probe the topography and electronic structure of surfaces and adsorbate layers with atomic resolution makes it a powerful tool in the study of surface chemistry (1). Here we use STM, STS, ultraviolet photoemission spectroscopy (UPS) and electronic structure calculations to study the long-standing problem involving the nature of the initial stages of the oxidation of silicon. There have been a large number of studies on this issue utilizing a great variety of techniques. However, not only is the mechanism of oxidation still unclear, but there is not even agreement on what kind of product(s) is formed. Several different configurations have been proposed for the oxygen-containing sites in the early stages of the reaction (2). They involve oxygen atoms saturating the dangling-bonds of top-layer Si atoms, oxygen atoms inserted in back-bonds but leaving the dangling-bonds intact, or molecular forms of oxygen attached to surface atoms or bridging two surface Si atoms.

In Fig. 1 we show a topograph of the unoccupied states of a Si(111)-7x7 surface after an exposure to 0.2L of O₂ at 300K. A 7x7 unit cell is outlined. Two new types of sites are formed as a result of the exposure to O₂: (a) sites that appear darker than normal Si adatoms on the 7x7 surface and are labeled D, and (b) sites that appear brighter and are labeled B. There is a strong spatial selectivity in the distribution of these sites. Bright sites prefer corner-adatoms over center-adatoms by a factor of 4 and, even more remarkably, they prefer the faulted-half of the 7x7 unit cell over the unsfaulted half by about a factor of 8. Dark sites show the same trend but much smaller selectivity. From this difference in selectivity and because of their different behavior upon further O₂-exposure, we conclude that these two sites represent two different early products of the oxidation. As the O₂-exposure is increased towards the monolayer, the dark sites dominate. There is also a tendency for dark sites to aggregate to form dark islands. To help identify these sites we have obtained atom-resolved tunneling spectra such as those shown in Fig. 2. Spectra A, B and C are typical spectra obtained over unreacted restatom, corner-adatom and center-adatom sites, respectively. Spectrum D obtained over a dark site shows the absence of surface states. Spectrum E, over a bright site, is adatom-like but the occupied and unoccupied surface states are shifted by ~0.5eV from those of normal adatoms. Finally, spectrum F obtained over "gray" sites on the perimeter of dark islands is that of an adatom with an increased occupation of its dangling-bond Si surface state. We have performed tight-binding calculations of local density-of-states (3), which allow us to identify the bright site as involving an oxygen

atom inserted in an adatom back-bond, leaving the dangling-bond intact but empty. The occupied state at -0.8eV in spectrum E is an enhanced back-bond resonance. The identification of the dark site is more complex and involves UPS studies as a function of temperature and theoretical calculations. It is concluded that the dominant dark site involves an oxygen atom tying up the adatom dangling-bond and another atom inserted in one of the back-bonds. A negatively charged molecular precursor form is also identified by UPS at low temperatures (4). Comparison of the UPS spectra of the precursor with calculated spectra indicates that the precursor involves O₂ interacting with a single adatom site, not a bridged configuration as previously proposed. Detailed mechanisms by which molecular precursors decay to form the initial products and then SiO₄ structures are proposed.

Finally, we consider the issue of the site-selectivity of the initial stages of the oxidation process. Calculations (5) indicate that the molecular precursors are strongly bound to the Si surface so that once formed they will not diffuse but will decompose at the original site. Thus, the observed site distribution should reflect a site-selective sticking process of O₂ to form the molecular precursor - nominally O₂⁻. The faulted half of the unit cell and corner-adatom sites are both characterized by high electron occupation of the adatom S₁ dangling-bond state. We propose that the sticking is dominated by a O₂ harpooning process, involving electrons in the S₁ surface state (4). This suggestion is further supported by experiments in which we control the dangling-bond occupation by doping. Thus, by forming a δ -doped B layer in the 3rd atomic plane we empty by charge-transfer from the adatom dangling-bonds (6) and we find that no O₂⁻ is visible in UPS and that both the thermal and photochemical oxidation of Si are largely suppressed. The harpooning sticking mechanism also provides an explanation for the fast growth of dark islands. As we mentioned above in the perimeter of dark islands, "gray" sites (Fig. 2, spectrum F) with increased dangling-bond occupation are formed. Thus, the O₂ sticking probability at those sites should be increased leading to the expansion of the dark islands.

References

1. Ph. Avouris, J. Phys. Chem. **94**, 2246 (1990) and references cited therein.
2. P. Morgen, U. Hoefer, W. Wurth and E. Umbach, Phys. Rev. B **39**, 3720 (1989); U. Hoefer et al. Phys. Rev. B **40**, 1130 (1989), and references cited therin.
3. I.-W. Lyo, Ph. Avouris, B. Schubert and R. Hoffmann, J. Phys. Chem. **94**, 4400 (1990).
4. Ph. Avouris, I.-W. Lyo and E. Bozso, J. Vac. Sci. Technol. A, in press, and to be published.
5. B. Schubert, Ph. Avouris and R. Hoffmann, to be published.
6. I.-W. Lyo, E. Kaxiras and Ph. Avouris, Phys. Rev. Lett. **63**, 1261 (1989).

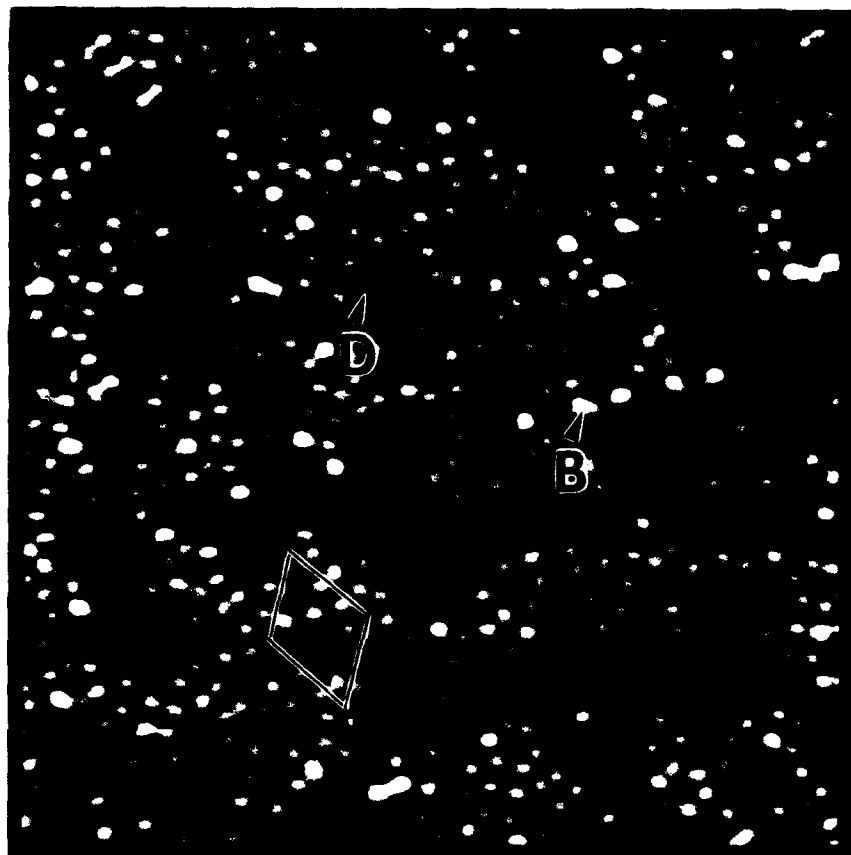


Figure 1. STM topograph of the unoccupied states of Si(111)-7x7 after exposure to 0.2 langmuir of O₂. A 7x7 unit cell is outlined. Oxygen-induced bright and dark sites are indicated by B and D, respectively.

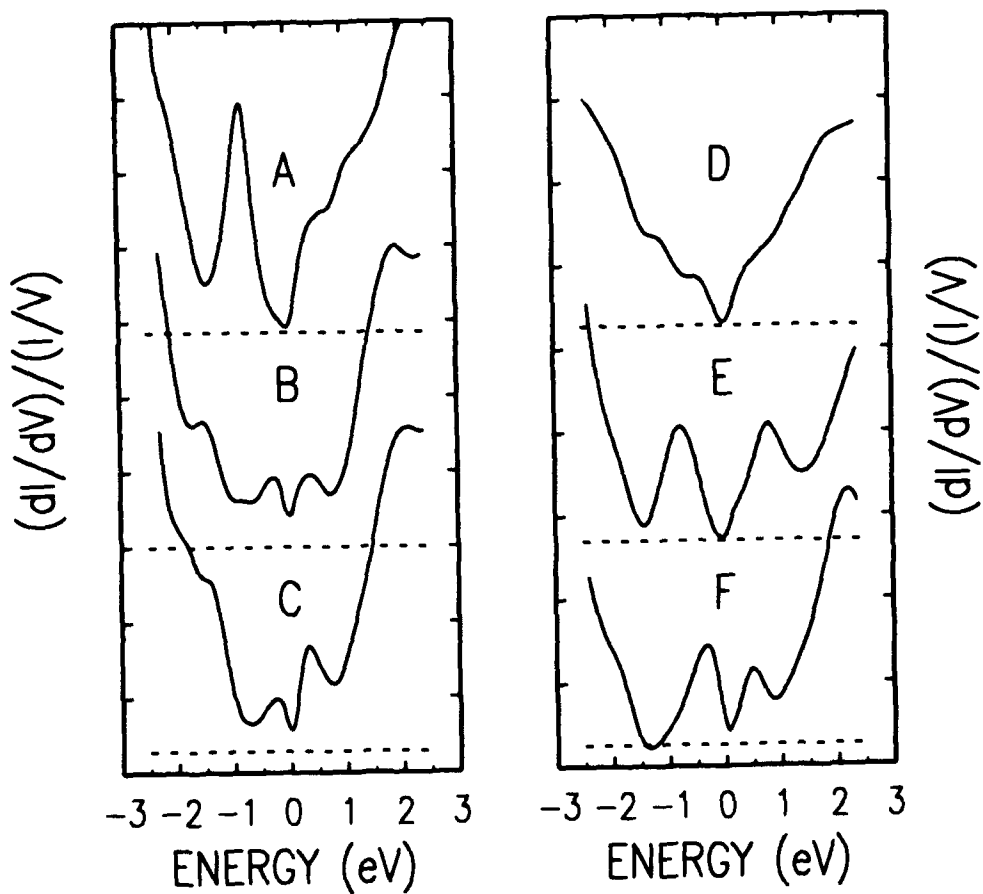


Figure 2. Atom-resolved tunneling spectra obtained over unreacted restatom (A), center-adatom (B), and corner-adatom (C) sites, and over O₂-induced dark (D), bright (E) and perturbed (gray) adatom sites.

Oxide Layer Growth on Gallium Arsenide Using a High Kinetic Energy Atomic Oxygen Beam

M.A. Hoffbauer, J.B. Cross, and J.D. Farr
Chemical and Laser Sciences Division, MS-G738

Los Alamos National Laboratory

Los Alamos, NM 87545

(505) 667-4878

and

V.M. Bermudez

Electronic Materials Branch, Code 6833

Naval Research Laboratory

Washington, DC 20375-5000

(202) 767-6728

The inherent theoretical advantages of GaAs electronic devices over those employing Si technology are severely limited in practice by the difficulty of forming passivating oxide layers.¹ Problems encountered with oxide stoichiometry, crystallinity, interface defects, and chemical stability have been the subjects of numerous studies over the last 15 years.²⁻⁸ One of the major factors contributing to these problems is the differing rates of oxidation of Ga and As and the volatility of the As₂O₃ and As₂O₅ products at temperatures above ~100 °C.

A number of different approaches to the growth of device-quality native oxides at low temperatures on GaAs have been attempted including: the use of ozone²; simultaneous O₂ and electron beam exposure³; photoexcitation of electron-hole pairs in the GaAs^{4,5}; the use of more reactive oxidizers,^{4,6} such as N₂O; photochemical excitation of the gas-phase molecular species⁶; addition of H₂O to the O₂⁷; excitation of O₂ with a hot filament³ or a Tesla discharge⁷; and plasma excitation⁸ of the O₂. Although, many of these techniques can greatly increase the rate of formation of the first few monolayers of oxide, they are generally unsuccessful in the growth of >100 Å thick oxide layers. Further, the oxidation reactions do not result in Ga or As in their highest formal oxidation state, and the resulting oxide is usually deficient in Ga or As.

Recently, we have begun investigating the oxidation of GaAs with a high kinetic energy beam of atomic oxygen and using x-ray photoemission (XPS) and Raman spectroscopies to characterize the thickness and stoichiometry of the oxide and to probe the oxide/GaAs interface. The energetic atomic O beam source is based on a laser sustained discharge described in detail elsewhere⁹. A 2.8 eV O-atom beam (FWHM of ~1.0 eV) and a flux of ~10¹⁷ atoms/cm²-sec (i.e. ~100 monolayers/sec) was used. The GaAs samples were (110)- or (100)-oriented wafers that were Si-doped (~2x10¹⁸/cm³) *n*-type or semi-insulating and were repolished in a freshly prepared 1% Br₂/methanol solution prior to use. The samples were exposed to the atomic O beam over an area of about 5x7 mm for periods of up to 5 hours, during which time the sample temperature was held constant. Following atomic O exposure, the samples were transferred in air to an ultra-high vacuum chamber for XPS analysis using Al K α excitation (h ν = 1487 eV). Ar⁺-ion sputter profiling used a 4.5 keV, 6 μ A/cm² beam at an estimated sputter rate of ~50 Å/min. Raman spectra were obtained in air using the 4880 Å line of an Ar-ion laser and a triple monochromator with a cooled optical multichannel analyzer (OMA) detector array in a backscattering geometry with either s- or p-polarization of the incident beam and no intentional polarization of the scattered beam.

A representative example of the Ga and As 3d core-level XPS data obtained at three distinct locations on an atomic O exposed sample held at 50 °C during oxidation are shown in Fig. 1. The As 3d binding energy (BE) shift, relative to that of the unexposed GaAs area, is about 3.2 eV at the edge of the O-exposed area and about 4.2 eV at the center. Reference to standard compounds^{10,11} shows that a 3.2 eV BE shift corresponds to As₂O₃ (3.2-3.4 eV), while a shift of 4.2 eV is approaching that of As₂O₅ (4.7-4.9 eV). Oxidation-induced BE shifts are generally smaller^{11,12} for Ga than for As 3d. At the center of the O-exposed area, the Ga 3d BE shift of 1.0 eV

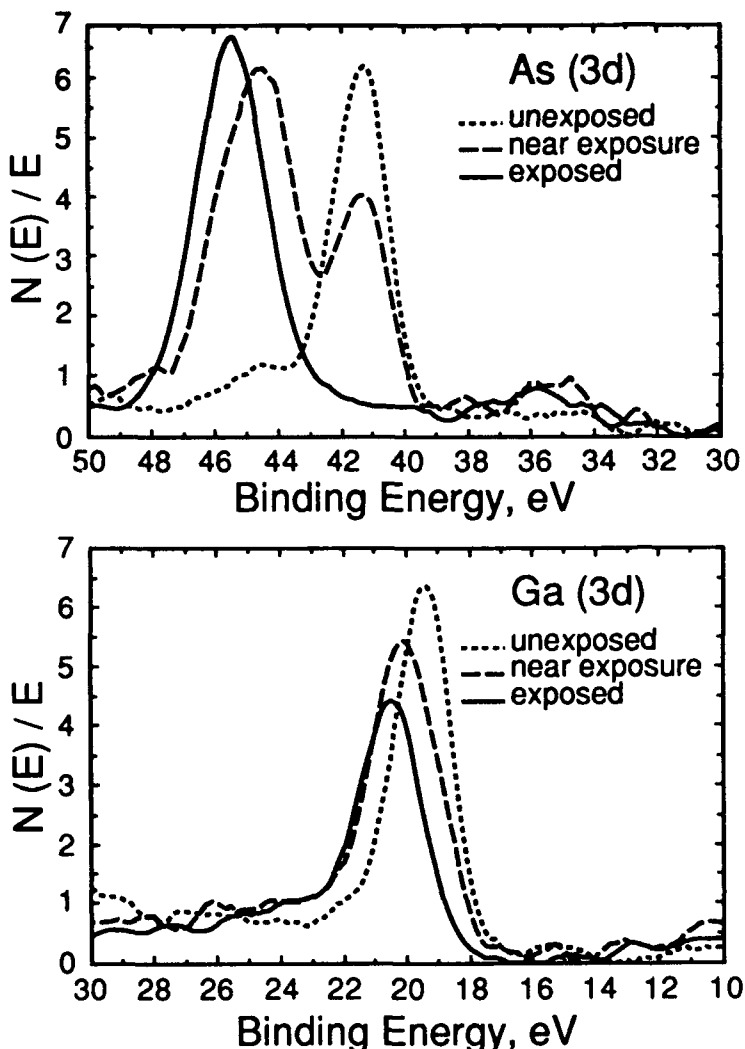


Figure 1. Ga and As 3d core-level XPS (Al K α excitation) for three regions of the GaAs(110) surface exposed to atomic oxygen at a substrate temperature of 50 °C. Dotted line-the unexposed area, dashed line-at the edge of the exposed area, and solid line-at the center of the exposed area. The relative intensities of the different spectra are not quantitative.

corresponds to that of Ga_2O_3 (0.9-1.4 eV), while the smaller shift at the edge indicates that the Ga is less than fully oxidized. It is worth noting that there is no sign of the "parent" (i.e., unoxidized) Ga or As 3d peaks at the center of the O-irradiated area. The attenuation length for 1400 eV photo-electrons in GaAs is estimated ¹² to be about 27 Å giving an effective sampling depth for the spectra in Fig. 1 of ~50 Å. Thus the substrate is completely reacted to at least the depth sampled.

Ar^+ -ion sputter profiling and XPS analysis were performed to evaluate the thickness and composition of the oxide layer. The raw data were converted to atomic percents and show an apparent excess of Ga at long sputter times in agreement with the observed preferential sputtering of As reported for oxide-free GaAs surfaces.¹³ However the Ga/As atomic ratio is similar to that of GaAs and shows only a small variation as sputtering progresses through the oxide and into the substrate, and there is no observed excess of either Ga or As at the oxide/substrate interface. The As 3d oxide satellite shows only a slight BE shift (from 4.2 to 4.0 eV) as profiling progressed through the oxide and the "parent" peak gained intensity. These results indicate that the oxide layer has a of a nearly uniform chemical composition. We tentatively conclude that the oxide layer is GaAsO_4 (gallium arsenate) but note that the BE shifts¹¹ for GaAsO_4 (estimated 4.7-5.0 eV) are not known with sufficient accuracy to permit a firm identification. From the estimated sputter rate of ~50 Å/min, the oxide thickness is ~ 400 Å for samples exposed at 50 °C and is significantly thicker for exposures at higher substrate temperatures. However, the oxide thicknesses obtained to date have not been sufficient to permit either x-ray diffraction analysis or detection of oxide lattice modes in the Raman spectra (see below) that could confirm the chemical composition of the oxide layer.

For oxidized III-V materials, several groups^{14,15} have discussed the use of Raman spectroscopy to detect oxidation-induced disorder and the accumulation of the elemental column-V species at the oxide-substrate interface. Raman data for the semi-insulating (100), *n*-type (110), and *n*-type (100) samples with and without exposure to the atomic O beam have been measured. For the (100) samples, the unoxidized area shows a strong GaAs LO phonon peak at about 290 cm⁻¹ with only a very weak, if any, TO phonon at about 270 cm⁻¹. The symmetry-forbidden TO mode can be made observable by the presence of residual strain, roughness or disorder in the substrate. For the O-exposed surface, there is no significant increase in the TO/LO relative intensity, indicating that oxidation has not perturbed the crystalline order of the substrate sufficiently to relax the Raman selection rules. Analogous results were obtained for the (110) samples where the TO mode is allowed and the LO forbidden. The O-exposed surface shows only a very slight increase in LO/TO relative intensity. These results contrast with those for thermal oxidation of (100) GaAs which show a strong "forbidden" TO peak as a result of substrate disorder¹⁴.

Raman spectra of thermal oxides on GaAs also show strong peaks at about 257 and 200 cm⁻¹ arising from the LO and TO phonons, respectively, of crystalline As at the oxide/GaAs interface. Amorphous As, if present, produces a broad band from about 200 to 250 cm⁻¹. For substrates exposed at 50 °C and 150 °C the O-exposed areas show none of these features. Apparently, oxidation by high kinetic energy atomic oxygen does not produce metallic As in either the oxide or at the oxide/GaAs interface. Previous work specifically aimed at detecting free As at native-oxide/GaAs interfaces is very limited. XPS chemical depth profiling¹⁶ has been used to study 30-40 Å thick native oxides on *n*-type (100) samples where a thin layer of free As was found at the interface but none within the oxide.

In summary, thick, uniform, and fully oxidized layers on GaAs have been formed by exposure to a high kinetic energy atomic O beam. The oxidation process has a minimal effect on the crystalline order of the substrate and results in no detectable levels of either crystalline or amorphous elemental As at the oxide-GaAs interface. The influence of surface orientation, carrier type and concentration, O-atom beam kinetic energy and flux, and sample temperature during exposure on the oxide layer formation kinetics are under study. Electrical characterizations of the oxide are in progress to establish whether the interface state density is sufficiently low to be competitive with that attainable in low-temperature chemical vapor deposition of passivating layers.

REFERENCES

1. M.H.Brodsky, *Scientific American* (Feb., 1990), p. 68
2. S.Ingrey, W.M.Lau and N.S.McIntyre, *J.Vac.Sci.Technol. A* 4, 984(1986)
3. I.López de Ceballos, M.C.Muñoz, J.M.Goñi and J.L.Sacedón, *J.Vac.Sci.Technol. A* 4, 1621(1986)
4. K.A.Bertness, T.T.Chiang, C.E.McCants, P.H.Mahowald, A.K.Wahi, T.Kendelewicz, I. Lindau and W.E.Spicer, *Surf.Sci.* 185, 544 (1987)
5. C.F.Yu, M.T.Schmidt, D.V.Podlesnik and R.M.Osgood Jr., *J.Vac.Sci.Technol. B* 5, 1087(1987)
6. P.A.Bertrand, *J.Electrochem. Soc.* 132, 973 (1985)
7. H.Iwasaki, Y.Mizokawa, R.Nishitani and S.Nakamura, *Japan.J.Appl.Phys.* 18, 1525(1979)
8. H.Sommer, W.John and A.Meisel, *Surf.Sci.* 178, 179 (1986)
9. J.B.Cross and N.C.Blais, *Prog. in Astronautics and Aeronautics* 116, 143 (1989); J.B.Cross and D.A.Cremers, U.S. Patent 4,780,608 (Oct. 25, 1988)
10. P.Pianetta, I.Lindau, C.M.Garner and W.E.Spicer, *Phys.Rev. B* 18, 2792 (1978)
11. G.P.Schwartz, G.J.Gualtieri, G.W.Kammlott and B.Schwartz, *J.Electrochem.Soc.* 126, 1737 (1979)
12. K.A.Bertness, J.-J.Yeh, D.J.Friedman, P.H.Mahowald, A.K.Wahi, T.Kendelewicz, I. Lindau and W.E.Spicer, *Phys.Rev. B* 38, 5406 (1988)
13. I.L.Singer, J.S.Murday, and L.R.Cooper, *Surf.Sci.* 108, 7(1981)
14. N.Levinsohn, R.Beserman, C.Cytermann, R.Brener, Y.L.Khait, G.K.Regel, J.Musolf, M.Weyers, A.Brauers and P.Balk, *Appl.Phys.Letts.* 56, 1131 (1990)
15. R.Martin and R.Braunstein, *J.Phys.Chem.Solids* 48, 1207 (1987)
16. P.J.Grunthaner, R.P.Vasquez and F.J.Grunthaner, *J.Vac.Sci.Technol.* 17, 1045 (1980)

**Electronically Induced Modifications of a-Si:H(P) Films by
Scanning Tunneling Microscopy**

E. Hartmann*, F. Koch*, and R. J. Behm

Inst. f. Kristallographie und Mineralogie, Universität
München, Theresienstr. 41, D-8000 München 2, F.R.G.

* Inst. f. Festkörper- und Technische Physik E16, Technische
Universität München, James-Franck-Str., D-8046 Garching,
F.R.G.

We report local electronic modifications of phosphorus-doped, hydrogenated amorphous silicon films [a-Si:H(P)], on a nm-scale, by use of a Scanning Tunneling Microscope.

High-quality a-Si:H(P) layers (5 at.% hydrogen) were deposited by rf glow discharge techniques on heavily doped p-type Si substrate material. The film was doped by adding 1 % PH_3 to the SiH_4 flux, resulting in a layer resistivity of 100 Ωcm . Film thicknesses ranged between 300 Å to 5000 Å.

Depending on the tunnel conditions, mainly tunnel current and tunnel voltage, the STM can be operated in an imaging mode ('read cycle') or in a surface modifying mode ('write cycle'). Under normal tunneling conditions, at + 3 V applied at the sample and 1 nA tunnel current, STM imaging does not alter the surface and the same area can be repeatedly scanned without any changes in the images. Tunneling at high voltages (+ 10 V) and currents (200-600 nA), however, lead to characteristic modifications of the amorphous film, which can be detected in topography images and/or in measurements of the effective barrier height. Three different types of modifications are distinguished:

- changes in the effective barrier height without noticeable changes in the apparent topography image
- changes in the effective barrier height together with creation of shallow depressions in the topography image
- changes in the effective barrier height combined with the formation of elevations in the apparent topography image.

We explain these modifications in terms of local changes in the layer conductivity, induced by the current, i. e. by an electronic rather than topographic modification of the layer. The conductivity is altered due to changes in the doping efficiency, e. g. by an autocompensation reaction /1/.

/1/ R. A. Street, Phys. Rev. Lett. 49, 1187 (1982);
G. Krötz, J. Wind, and G. Müller,
J. Non-Crystalline Solids 114, 663 (1989).

Monday, February 11, 1991

Photon- and Hot-Electron-Induced Surface Reactions

MC 7:30pm-9:30pm
Anasazi South

*Michael Stuke, Presider
Max Planck Institute,
Federal Republic of Germany*



Photochemistry at Metal Surfaces

J. M. White

Department of Chemistry

University of Texas

Austin, TX 78712

512-471-3704

Recently, photon-driven processes at adsorbate substrate interfaces has received considerable attention in the research community and for both fundamental and practical reasons. Among the most recent avenues being pursued is photochemistry at adsorbate-metal interfaces where bond breaking within the adsorbate, surface rearrangement, reaction with coadsorbates, and adsorbate desorption have all been observed in systems where thermal effects can be ruled out. Thus, the quenching of electronically excited states by metallic substrates does not always overwhelm, bond breaking processes.

The mechanisms by which these processes occur are of interest and include direct photon excitation of the adsorbate or adsorbate-substrate complex and photon excitation of the substrate followed by charge and/or energy transfer to the adsorbate. Examples of the latter include H_2O and O_2 on $Pd(111)$ and CH_3Cl on $Pt(111)$. An example of

the former is phosgene, Cl_2CO on Pt(111), provided the wavelength is less than 300 nm.

We have gathered experimental evidence regarding the mechanism in two ways: (1) measure the rates of photon-driven processes as a function of the polarization and incident angle of the light and (2) examine, for cases where photoelectrons are ejected, the relation between the photoelectron yield and the chemical rate.

For the case of CH_3Cl adsorbed either alone or on known coverages of H_2O on Pt(111), photoelectrons are produced by 5 eV photons and there is significant photon driven C-Cl bond cleavage even though neither adsorbate absorbs photons at this energy. Assuming that the bond cleavage is driven solely by photoelectrons and is first order in both electrons and CH_3Cl , we have extracted cross sections for bond cleavage as a function of the CH_3Cl coverage, for methyl chloride adsorbed alone, or as a function of H_2O coverage for a monolayer of methyl chloride adsorbed on water. In both cases, the cross section becomes independent of coverage for coverages greater than 2 monolayers, even though the electron flux through these drops by more than an order of magnitude. For CH_3Cl on H_2O the C-Cl bond cleavage cross-section increases between 1 and 2 monolayers of water coverage and the work function also rises. Detailed kinetic energy distribution measurements of the photoelectrons reflects this work function change; the average kinetic energy drops. Above 2 monolayers of water, the electron

yield drops but the energy distribution remains the same.

Thus, the cross section increase is interpreted as the result of a change in the kinetic energy of the photoelectrons; just as in the gas phase, electron attachment to methyl chloride leads to dissociation and the cross section maximizes below 0.4 eV kinetic energy.

For H_2O and O_2 on $Pd(111)$, the polarization measurements are all consistent with substrate excitation; the product formation rates for s- and p-polarized light faithfully track the absorptivity of the metal substrate. We have time-of-flight adsorbate desorption data, post-irradiation temperature-programmed desorption data and high resolution electron energy loss data all confirming this interpretation. For phosgene on $Pt(111)$, polarization data are consistent with substrate excitation for wavelengths longer, but not shorter, than 300 nm. The latter is a very interesting case since it is the only polarization data that is inconsistent with substrate excitation. We interpret this result in terms of direct adsorbate excitation, consistent with the known gas phase absorption of phosgene in this energy region.

INTERACTION OF LOW-ENERGY ELECTRONS WITH ADSORBED MOLECULES: MECHANISMS OF ENERGY TRANSFER AND DISSOCIATION

Leon Sanche.

MRC Group in the Radiation Sciences, University of Sherbrooke, QC, Canada J1H 5N4

1. INTRODUCTION

The chemical reactivity of molecules physisorbed or chemisorbed on solid surfaces is a topic of interest in many areas of applied physics and chemistry. A large portion of the activity in this field of research has been focused on the catalytic action of surfaces; however, the recent discoveries on the possibility to enhance, trigger and even control chemical reactions with photon and particle beams incident on surfaces are now starting to shift scientific interests toward studies of the dynamics involved in these non-thermal reactions. Particularly, photon and electron beam methods are expected to surpass present macroscopic methods (e.g., plasma etching) in the manufacture of microelectronic and micromechanical devices requiring fine-line lithography [1]. One class of such techniques involves the utilization of laser photons with energies ranging from 0.1 eV in the infrared to 6 eV in the ultraviolet [2]. Many of the laser-driven surface reactions are expected to be caused by the photogeneration of low-energy electrons which transfer energy to an adsorbate causing dissociation and desorption [3-7].

Low-energy electrons are also expected to play a dominant role in the basic physical and chemical mechanisms involved in microlithography techniques utilizing high-energy radiation such as direct writing with an electron beam and etching with laser- or synchrotron-generated X-rays [8]. In fact, both high-energy electrons and photons transfer most of their energy to the exposed material by producing a large quantity ($\sim 3 \times 10^4/\text{MeV}$) of secondary low-energy (0-70 eV) electrons having an average energy of about 10 eV [9]. These low-energy electrons scatter in the irradiated material and at its surface where they can interact with adsorbate molecules to produce highly reactive species including radicals, cations and anions. These intermediaries can subsequently react with the irradiated material in the vicinity of the surface and change its chemical nature within the spatial resolution of the instrument. The interaction of low-energy electrons with molecules condensed on surfaces must therefore be well understood in order to achieve a truly atomic and molecular description of the mechanisms involved in microlithographic surface modifications induced via particle beams and photons. Such a comprehension should improve our ability to produce chemical changes on a nanometer scale on materials of industrial interest.

2. INTERACTIONS OF LOW-ENERGY ELECTRONS WITH MOLECULES ON SURFACES

At low energies, the scattering of an electron by a molecule condensed on a surface can be described in terms of direct or resonant processes [10]. Electron resonances occur when the scattered electron resides in the neighborhood of the target atom or molecule for a time much longer than the usual scattering time. From a molecular orbital point of view, a resonant state may be considered as a transient negative ion formed by an incoming electron which temporarily occupies an orbital of the target molecule. When the projectile electron is temporarily captured by the target, it has an increased interaction time. This causes additional distortion of the target, the magnitude of which depends on the lifetime of the resonance. Consequently, the effect of a resonance on the magnitude of the scattering cross sections is dependent on the lifetime. Because of the uncertainty principle the transitory state has a width Γ in energy ($\Gamma \cdot \Delta t \approx \hbar$ where Δt is the resonance lifetime) which serves to characterize and identify the process in the energy dependence of the scattering cross sections or excitation functions. Thus, when resonances are short-lived ($\Delta t \ll 10^{-14}$ sec.) they produce broad peaks in their decay channels (i.e., in the specific excitation functions where they appear). Long-lived resonances ($\Delta t \geq 10^{-14}$ sec.) in molecules produce sharp peaks in

vibrational and electronic excitation cross sections. The main characteristics of a resonance occurring on a surface (i.e., symmetry, magnitude, lifetime and energy) depend not only on the nature of the target molecule but also on (1) the change in the symmetry of the scattering problem introduced by the presence of other nearby particles; (2) the polarization of these targets by the electron and the transient anion; (3) the fixed orientation of the molecule with respect to the solid surface and (4) the possible distortion and modification of the target molecule by the solid.

When the time-dependent amplitude of the projectile electron does not increase significantly in the vicinity of a particular molecular site at the surface, the scattering process is considered direct. In this case, insight into the physical phenomenon may still be gained from analysis of the interaction potential. In other words, by estimating the magnitude of the various terms in the expansion of this potential, it may be possible to sort out the dominant ones from which the main scattering mechanism may be deduced. For example, one possibility is to expand the electron-molecule potential around the equilibrium internuclear distance R_e as [11]

$$V = V(R = R_e) + (R - R_e) \left. \frac{\partial V}{\partial R} \right|_{R=R_e} + \dots \quad (1)$$

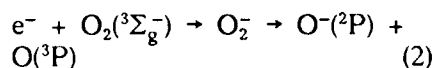
When only these two terms are considered and the molecule is assumed to be a harmonic oscillator, solving the problem within the Born approximation (which often corresponds to small momentum transfer) leads to the optical selection rule $\Delta v = 1$ for vibrational transitions. Thus, whenever this restrictive approximation applies, the electron behaves like broadband electromagnetic radiation. We can expect the electron-molecule potential described by equation (1) to be responsible for the magnitude of scattering cross sections which are large only for the excitation of the first vibrational energy level ($v = 1$) of the ground state of the molecule.

Direct and resonant electron scattering has been observed at submonolayer coverages of physisorbed as well as chemisorbed molecules into the various cross sections leading to vibrational and electronic excitation as well as molecular dissociation and desorption [10]. Resonance scattering has been found to be particularly effective in causing molecular dissociation in the low-energy range by dissociative attachment (DA). In this case, the transient anion dissociates into a neutral and a negative fragment (e.g., for a molecule AB: $e + AB \rightarrow AB^- \rightarrow A + B^-$). This decay channel can be observed by measuring a portion of the negative ions produced by electron impact on molecules condensed on a substrate with a mass spectrometer placed near its surface [12]. The apparatus can be operated in two modes: the ion-yield mode in which ions of a selected mass are detected as a function of incident electron energy and the ion-energy mode in which the ion current at a selected mass is measured for a fixed electron energy as a function of an ion retarding potential. DA is an effective mechanism to dissociate molecules with low-energy electrons [13] and induce and control specific ion-molecule reactions [14]. Examples of this process are given in the next section.

3. DISSOCIATIVE ATTACHMENT

Fig. 1 exhibits the energy dependence of the Cl^- yield produced by electron impact on a single layer of Cl_2 (lower curve) deposited on a polycrystalline Pt substrate [12]. The upper curve was recorded with a four-layer-thick film. The strong maximum which appears in both curves is due to the reaction $e + Cl_2 \rightarrow Cl_2^- ({}^2\Pi_u) \rightarrow Cl^- + Cl$. Decay of the Cl_2^- ${}^2\Pi_g$ state into the same dissociation limit is evidenced by the small "hump" around 2 eV shown in the inset. The structure at 11 eV is due to multiple electron scattering.

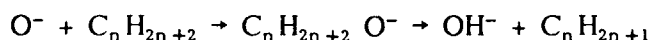
Another example of a DA reaction is illustrated by the two upper curves (a) and (b) in Fig. 2, which represent the energy dependence of the O^- current produced by electron impact on a multilayer film of O_2 [14]. Curve (b) was recorded discriminating anions having energies less than 1.8 eV with a retardation potential V_r . The broad peaks located around 8 and 13 eV in curves (a) and (b) have recently been ascribed to the DA reaction



The 8-eV peak arises from the decay of the $^2\Pi_u$ and $^2\Sigma_g^+$ transitory states of O_2^- whereas the 13-eV peak contains essentially contributions from the higher-energy symmetry-forbidden $^2\Sigma_u^-$ O_2^- state.

Curves (c) to (g) in the figure [14] represent the energy dependence of the OH^- yields produced by electron

impact on a 3-layer oxygen film covered by a monolayer of C_nH_{2n+2} molecules ($n = 1, 2, 4, 5$ and 6). At submonolayer alkane coverages, these OH^- yield functions exhibit the same characteristics but the signal is lower. In fact, in the submonolayer regime the magnitude of the OH^- signal is found to be directly proportional to the number of condensed hydrocarbon molecules. Similar results were also obtained for submonolayer coverages of O_2 on three-layer hydrocarbon films. Since no compound at the film surface contains both hydrogen and oxygen, OH^- ions cannot be produced by direct electron impact. They must arise from subsequent ion-molecule reactions. Here, the OH^- signal bears the signature of the O^- DA yield function from pure O_2 films which make it possible to ascribe the OH^- signal to the reaction



where the O^- ions are generated by DA of O_2 . This observation indicates the possibility of inducing with a low-energy electron beam a specific ion-molecule reaction.

REFERENCES

1. Scientific American 263, 98 (1990).
2. T.J. Chuang, J. Vacuum Sci. Technol. B1, 798 (1982) Mater. Res. Soc. Proc. 17, 45 (1983); 29, 185 (1984); and citations therein.
3. E.P. Marsh, T.L. Gilton, W. Meirer, M.R. Schneider, and J.P. Cowin, Phys. Rev. Lett. 61, 2725 (1988).

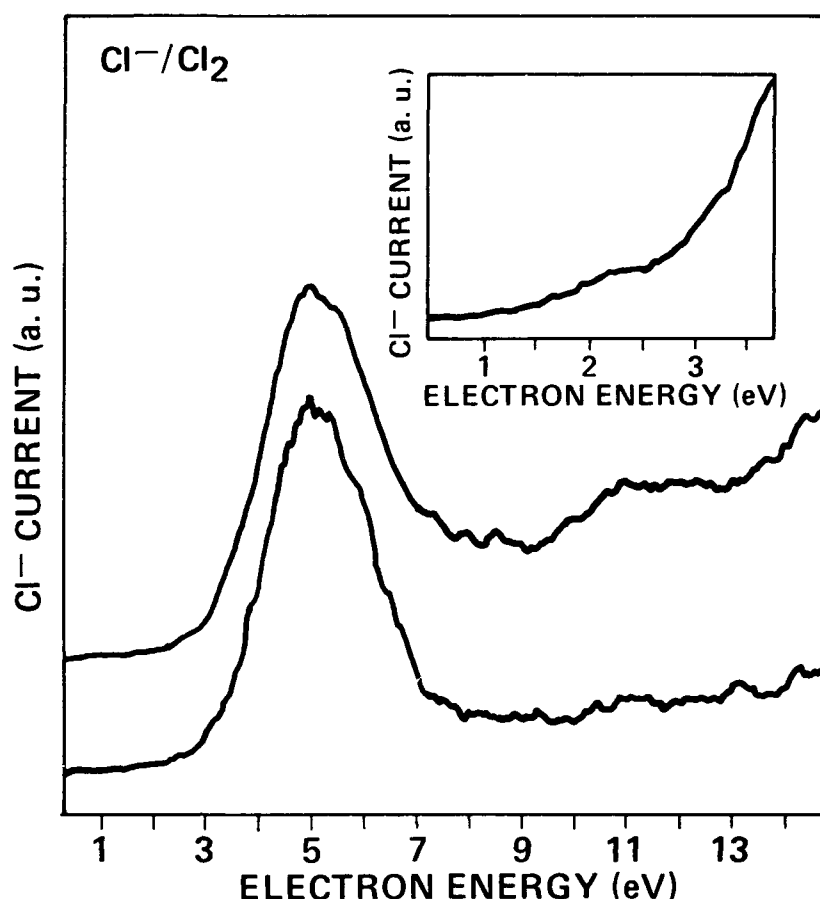


Fig. 1

4. E.P. March, F.L. Tabares, M.R. Schneider, T.L. Gilton, W. Meier, and J.P. Cowin, *J. Chem. Phys.* 92, 2004 (1990).
5. E. Hasselbrink, S. Jakubith, S. Netteshaim, M. Wolf, A. Cassuto, and G. Ertl, *J. Chem. Phys.* 92 3154 (1990).
6. S.R. Hatch, X.-Y. Zhu, J.M. White, and A. Campion, *J. Chem. Phys.* 92, 2681 (1990).
7. S.A. Buntin, Lee J. Richter, R.R. Cavanagh, and D.S. King, *Phys. Rev. Lett.* 61, 1321 (1988).
8. S.G. Anderson, T. Komeda, J.M. Seo, C. Capusso, G.D. Waddell, P.J. Benning, and J.H. Weaver, *Phys. Rev. B* 42 5082 (1990).
9. For a review of the role of low-energy electrons in Radiation Physics and Chemistry, see L. Sanche, *Radiat. Phys. Chem.* 32, 269 (1988).
10. For a review of low-energy electron scattering from molecules on surfaces, see L. Sanche, *J. Phys. B* 23, 1597 (1990).
11. K. Takayanagi, *Prog. Theor. Phys. Suppl. Japan* 40, 216 (1967).
12. R. Azria, L. Parenteau, and L. Sanche, *J. Chem. Phys.* 87, 2292 (1987).
13. H. Sambe, D.E. Ramaker, M. Deschenes, A.D. Bass, and L. Sanche, *Phys. Rev. Lett.* 64, 523 (1990).
14. L. Sanche and L. Parenteau, *Phys. Rev. Lett.* 59, 136 (1987).

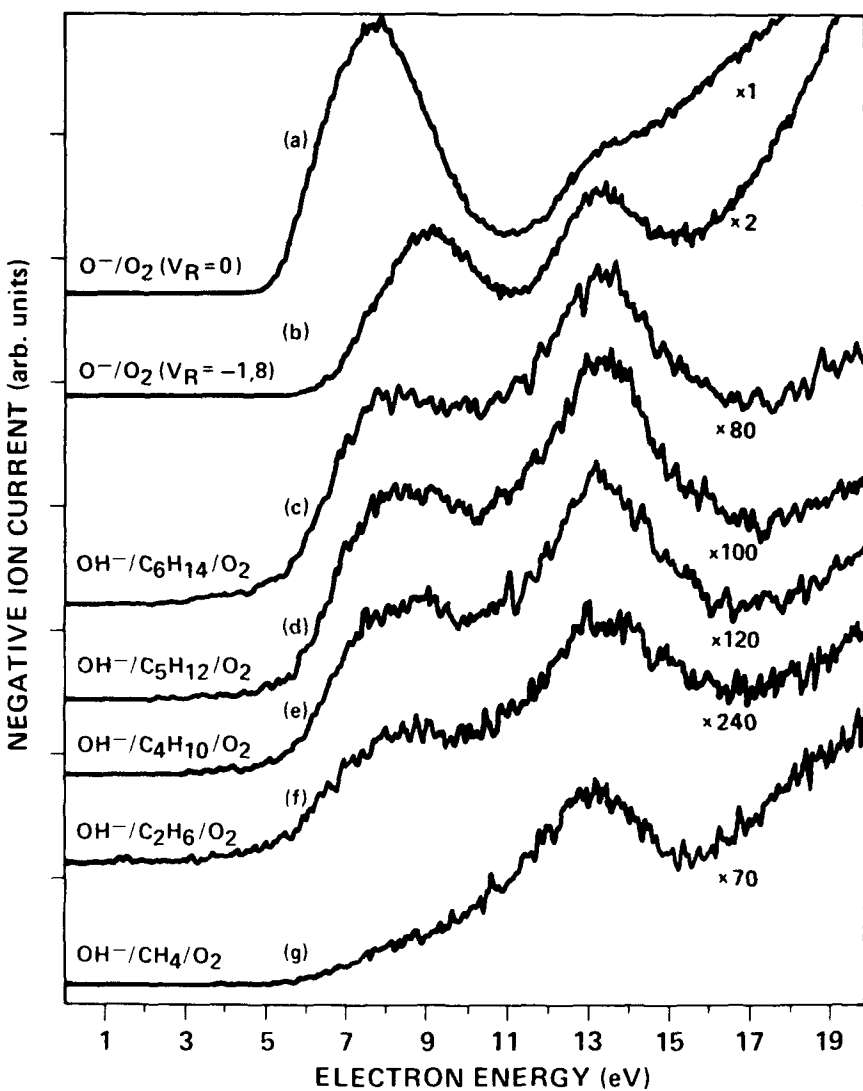


Fig. 2

Bond-Orbital Model of Two-hole Laser-Induced Desorption from GaP (110)

Richard F. Haglund, Jr.

Department of Physics and Astronomy
Vanderbilt University, Nashville, TN 37235 USA
Telephone 615-322-2828, Telefax 615-322-7623

Ken Hattori, Noriaki Itoh and Yasuo Nakai

Department of Physics, Nagoya University
Nagoya 464 Japan
Telephone 81-52-781-5111, Telefax 81-52-782-9794

The widespread application of lasers in semiconductor processing has produced a voluminous literature on the mechanisms of laser desorption and ablation. There are significant disagreements, however, about the extraordinarily complex physical mechanisms underlying laser desorption and ablation. Here we discuss recent experiments and a model of a particularly simple case: desorption of Ga^+ and Ga^0 by selective excitation of a surface electronic state on GaP (110). By choosing the electronic channel leading to desorption, and by monitoring the condition of the surface, one can determine accurately the threshold fluence above which the surface electronic structure is irreversibly altered by laser ablation. Below this threshold, desorption occurs at isolated defect sites and at perfect three-fold coordinated surface sites. This two-hole laser-induced desorption and ablation can be described by a bond-orbital model of electronic structure.

Pure crystalline n-type (S-doped) GaP (110) surfaces $10 \times 15 \text{ mm}^2$ were polished and etched according to a standard protocol, then sputter-cleaned and annealed to 500°C in ultrahigh vacuum (10^{-10} torr). The existence of a contamination-free 1×1 surface was verified by LEED and Auger spectroscopies. This surface of GaP, shown schematically in Fig. 1, has an unoccupied surface state about 2 eV above the valence-band edge.¹ This surface state was excited by an excimer-pumped dye laser tuned to 600 nm. A second dye laser tuned to the $^2\text{P}_{1/2} - ^2\text{D}_{3/2}$ transition of Ga^0 and the second harmonic of the 600 nm pump beam were used to excite and ionize, respectively, Ga^0 atoms desorbed by the pump for resonance ionization mass spectrometry (RIMS). Ga^+ ions were detected in the mass spectrometer by turning off the RIMS laser beams.

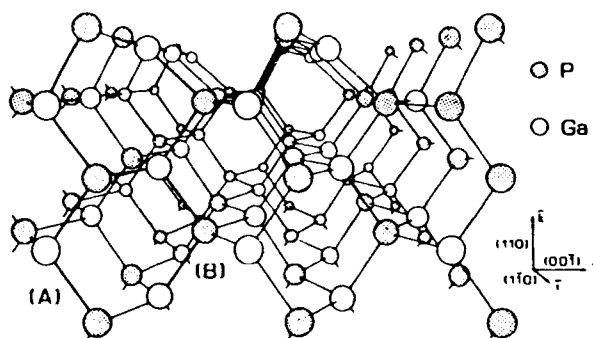


Figure 1. GaP (110) surface, showing the three-fold coordination of the Ga ions at perfect lattice sites. From Reference [1].

In our experiments, desorbed or ablated Ga ions and atoms were observed at pump laser fluences between 0.2 and $0.5 \text{ J} \cdot \text{cm}^{-2}$. Figures 2 and 3 show selected points along smooth curves drawn through hundreds of ion and neutral data at fluences below and above the ablation threshold, respectively. The trends shown in these curves are typical of results obtained under a variety of conditions and for several wavelengths below the photoionization threshold. Below the ablation threshold, the yield of Ga ions and atoms dropped sharply as a function of the number of laser shots to a plateau which was maintained for up to ten thousand shots. Under these conditions, LEED measurements following laser irradiation showed that the

GaP surface remained intact, suggesting laser-induced desorption from isolated defect or perfect lattice sites, rather than laser ablation of the surface. Above laser fluences of $0.4 \text{ J}\cdot\text{cm}^{-2}$, on the other hand, the yield of neutral Ga atoms increased rapidly with the number of laser shots, while the yield of Ga^+ decreased. Moreover, the ratio of neutral-to-ion yields inverts when one passes the ablation threshold: below threshold, ions predominate, while neutrals are the dominant ejected species above the ablation threshold. Above threshold, the surface sometimes showed significant damage - such as gross metallization - after only a few laser pulses.

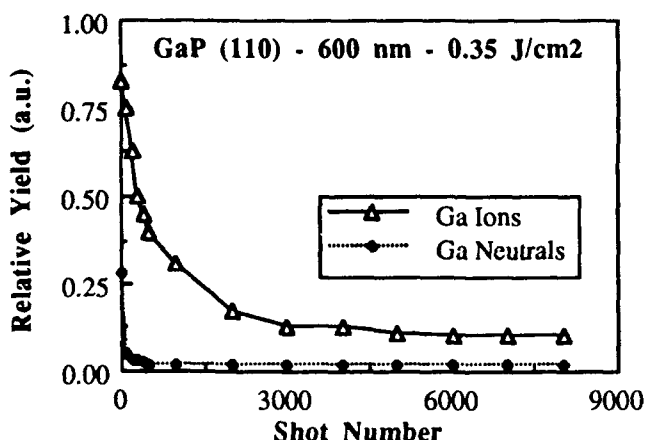


Figure 2. Smooth curves drawn through the measured yields of Ga^0 and Ga^+ from the GaP (110) surface at a laser fluence of $0.35 \text{ J}\cdot\text{cm}^{-2}$.

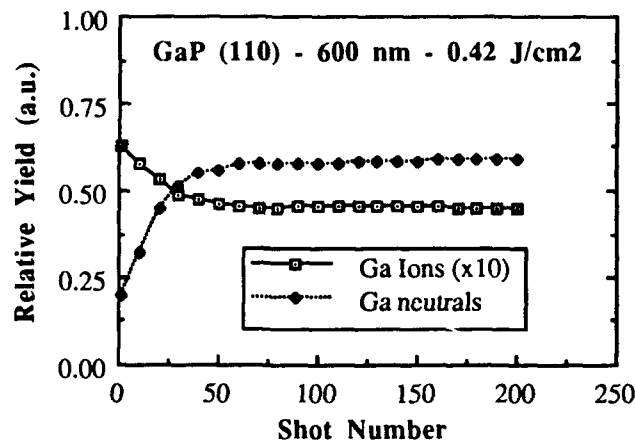


Figure 3. Smooth curves drawn through the measured yields of Ga^0 and Ga^+ from the GaP (110) surface at a laser fluence of $0.42 \text{ J}\cdot\text{cm}^{-2}$.

Several models have been proposed to describe nanosecond laser-induced sputtering of semiconductors, including desorption induced by creation of hole pairs,² bond softening followed by hole-stimulated desorption,³ and desorption induced by a phase change following the destabilization of the tetrahedral lattice.⁴ Of these models, only that of Ref. [2] relates desorption yields to microscopic parameters. However, none of the models takes into account the distinctive relaxation processes involved when semiconductors assimilate photo-excited electron-hole pairs. Moreover, all of these models are attempts to explain ablation, rather than desorption; thus they furnish little guidance about the connection between the desorption and ablation regimes.

We would thus like to find a model for the surface structure and dynamics of desorption from a defect site or a perfect lattice site which can be extrapolated to the ablation regime in a consistent way. We can assume that the desorption process is initiated by photon absorption and the creation of electron-hole pairs, the detailed properties of which depend on both the optical properties of the material and the laser wavelength. Desorption from individual lattice or defect sites occurs *via* a localized structural deformation that generates instability. There is a significant body of evidence suggesting that this localized lattice instability in compound semiconductors occurs by two-hole localization on a single lattice site.⁵ For specificity, we also assume that the laser photons have energies above the bandgap energy, but below the threshold for photoionization.

Below the threshold for laser ablation, the experimental data require that the model exhibit a mechanism with energetics favorable to desorption from a single site. We have calculated the available lattice relaxation energy from two-hole localization following the bond-orbital theory of Harrison.⁶ In spirit, the bond-orbital model is closely related to the bond-charge model of Phillips.⁷ The energy per bond in the perfect crystal is computed from the moment distribution of the density of states using linear combinations of atomic orbitals, and is given by⁸

$$E_{\text{pair}} = -n \left[M_2 - \frac{M_4 - M_2^2}{4 \cdot M_2} \right]^{1/2} + n \cdot V_0 + E_{\text{pro}} \quad (1)$$

where n is the coordination number; M_2 and M_4 are, respectively, the second and fourth moments of the electronic density of states (DOS); V_0 is the repulsive screening potential; and E_{pro} represents the energy required to create the appropriately hybridized sp^3 bonds for the covalent solid. The fourth moment is a function of the tetrahedral bond angle ϑ , and will, of course, be influenced by the dangling bonds and back-bonding required by surface reconstruction.

For GaP, the energy per pair in the surface bond can be calculated in first approximation assuming three-fold coordination. Computation of the energy per atom pair as a function of distance approximates one cut through the configuration coordinate space on a potential energy surface. Figure 4 shows how the radial dependence of the pair energy changes when first one hole and then two holes are produced in a semiconductor bond. In our computation, we have assumed that the local electronic excitation simply changes the population of electrons at the site, and does not significantly change the radial dependence of M_2 , M_4 or the screening potential V_0 . We also neglect changes in the angular dependence of M_4 due to the creation of the hole. Assuming that the creation of the holes is instantaneous in the sense of a Franck-Condon transition, the excess positive energy is available for lattice relaxation processes, including desorption. The parameters of the repulsive screening potential V_0 in Eq. (1) have been optimized for agreement with observed equilibrium inter-atomic spacing and bulk modulus for a three-fold-coordinated site, as in Ref. [8].

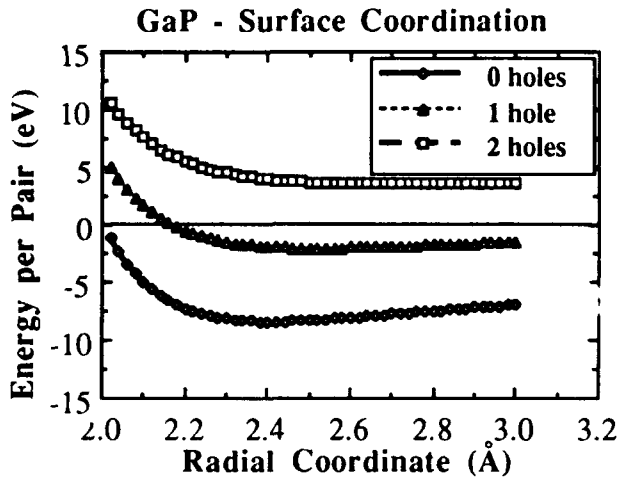


Figure 4. Bond-orbital model calculation of the energy per pair as a function of distance for GaP, for the unperturbed bond, one hole and two holes.

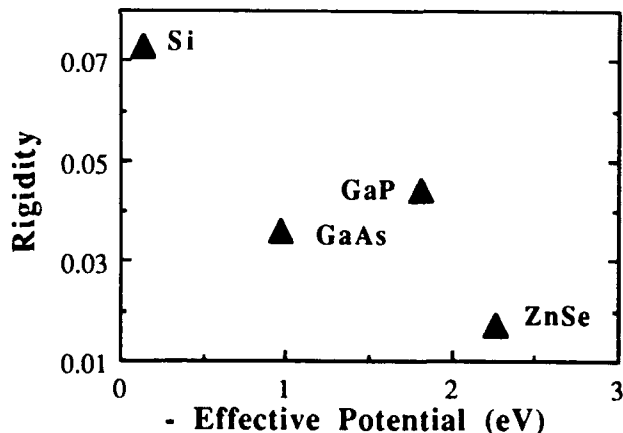


Figure 5. Calculation of the angular rigidity in the bond-orbital model for one-hole excitations in Si, GaAs, GaP and ZnSe, as a function of the calculated effective potential U_{eff} .

However, the existence of a large relaxation energy does not in itself guarantee that two-hole localization and desorption will occur. First of all, lattice relaxation must be energetically favorable over delocalization in a band; this implies that $E_{\text{LR}} > W$, where the bandwidth W is calculated from the second term in brackets in Eq. (1). The quantity which then determines the possibility of desorption is the effective potential

$$U_{\text{eff}} = U_{\text{screen}} - E_{\text{LR}} \quad (2)$$

where U_{screen} is the Coulomb barrier reduced by the Anderson "negative- U " screening potential.⁹ Desorption due to two-hole localization is energetically possible if the effective potential energy is negative. The desorption probability, at either a perfect lattice site or a defect, can thus be approached by computing the capture cross section for the second hole, using reasonable assumptions about the density of the laser-initiated electron-hole plasma in the near-surface absorption zone. We have discussed the details of this approach elsewhere (Reference [5]).

This same bond-orbital model also yields an *Ansatz* for laser ablation. Laser ablation is at least in part a collective phenomenon, as noted in Refs. 2-4; it is characterized by wholesale destruction of the surface, with a preponderant yield of neutrals and a smaller yield of ions created mostly by photoionization of the desorbing neutrals. For laser pulse energies or wavelengths which result in significant photoelectron production, there is also evidence¹⁰ that the surface undergoes an order-disorder transition prior to reconstruction. Here the bond-orbital model may provide significant clues to the structural precursors of the hydrodynamical behavior observed in the catastrophic phase of laser-induced sputtering.

This suggests that, at high laser fluence (high excitation densities), a bond-softening picture may be appropriate. With this in mind, we have used the bond-orbital model to calculate the angular rigidity parameter for a tetrahedral bond in a three-fold-coordinated site as defined in Ref. [6] for Si, GaAs, GaP and ZnSe, for the special case of a single electron-hole pair in a bond. Figure 5 shows the calculated rigidity parameter as a function of U_{eff} for these materials. It will be observed that the variation in the rigidity parameter for these materials roughly follows the trends in laser ablation thresholds for Group IV, III-V and II-VI semiconductors. Interestingly, these trends are *not* reproduced for the four-fold-coordinated bulk tetrahedron. Thus the bond-orbital approach appears to be effective in distinguishing surface from bulk phenomena as well as for predicting the general trends for laser ablation among the differing families of semiconductor materials.

This work was supported in part by the National Science Foundation Division of International Programs, Grant Number 89-16097, and by the Japan Society for the Promotion of Science.

References

- [1] F. Manghi, C. M. Bertoni, C. Calandra and E. Molinari, *Physical Review B* **24** (1981) 6029.
- [2] N. Itoh, T. Nakayama and T. A. Tombrello, *Physics Letters* **108A** (1985) 480.
- [3] Z. Wu, *Physics Letters* **131A** (1988) 486.
- [4] A. Namiki, S. Cho and K. Ichige, *Japanese Journal of Applied Physics* **26** (1987) 39.
- [5] Y. Nakai, K. Hattori, A. Okano, N. Itoh and R. F. Haglund, Jr., *Nuclear Instruments and Methods in Physics Research B*, to be published.
- [6] W. A. Harrison, *Electronic Structure and the Properties of Solids* (New York: Dover, 1989).
- [7] J. C. Phillips, *Bonds and Bands in Semiconductors* (New York: Academic Press, 1973)
- [8] W. A. Harrison, *Physical Review B* **41** (1990) 6008.
- [9] P. W. Anderson, *Physical Review Letters* **34** (1975) 953-955.
- [10] J. M. Moison and M. Bensoussan, *Journal of Vacuum Science and Technology* **21** (1982) 315.

**Photoemission from Si(111) Surfaces Covered with
Thick Overlays of CaF₂**

**B. Quiniou, W. Schwarz, Z. Wu, R.M. Osgood, Jr.
and Q. Yang**

**Columbia Radiation Laboratory
Columbia University
500 West 120th Street
New York, NY 10027
(212) 854-8449**

**J. Phillips
AT&T Bell Labs.
Murray Hill, NJ**

Recently, photoemitted electrons have been considered as a possible source of light-initiated surface reactions¹. In particular, for example, the photon energy, 6.4 eV, from an ArF laser, is known to exceed the work function of many materials used in laser processing, such as Si, GaAs, and Cu. In fact, space-charge limited photoemission has been reported by several groups doing illumination of surfaces of these materials².

In this talk we describe recent experiments which demonstrate that substantial photoelectron yields can be obtained even from UV illuminated semiconductor surfaces which are covered with thick insulating overlayers. Further, we show that by wavelength tuning of the UV source information about the relative band structure of the interfacial region can be obtained.

Our experiments were focused on Si(111) surfaces covered with thick epitaxial CaF₂ films. The CaF₂/Si(111) materials system was selected because of the quality of the overlying film and interface which can be achieved, its technological importance, and the amount of information already available on this system for its structure and its energy levels. Some measurements were also made on amorphous SiO₂ layers grown on Si(111) substrates.

For our experiments, CaF₂ layers were epitaxially deposited, in a MBE chamber, on n-type clean reconstructed Si(111) substrates with resistivities in the 5-25 Ω.cm range. During evaporation, the substrates temperatures were maintained at about 700° C. Further details on the growth of the CaF₂ layers are found in Ref. 3.

For the photoemission experiments, the samples were loaded in a separate UHV chamber equipped with standard surface preparation techniques and electron spectroscopies instruments. The photoelectron detection system consisted of an electrostatic energy analyzer with an energy resolution of 100 meV, a microchannel plate electron multiplier and a collecting electrode. Electrons emitted in a small solid angle normal to the surface of the samples were detected. The samples were biased at -5 volts relative to the spectrometer. Photons were provided by the frequency-doubled output of an excimer pumped dye laser. The focused laser beam was sent into the UHV chamber onto the sample, with an incidence angle of 67.5° and a spot size of 10⁻⁴ cm², and was allowed to exit the chamber without further reflection.

Before being studied the samples were heated up to 700° C for one hour and allowed to cool down. This heat treatment leaves the CaF₂ surface free of contaminants (C, O), as demonstrated by a separate XPS study, and is moderate enough to prevent the sublimation of CaF₂ molecules or the loss of F surface atoms. It also allows reproducible and stable results to be obtained. Although the previously described heat treatment is also believed to yield reproducible surface and bulk charge and defect rearrangement, the electrostatic charging of the insulator surface results in an ill-defined vacuum energy level at the surface of the CaF₂ layers.

We detected copious amounts of electrons photoemitted from our CaF₂/Si(111) when excited with laser radiation in the mid-UV range, typically 4.5 eV. We established that this emission phenomenon is observed for photons with energies above a threshold value. For all samples with CaF₂ layer thicknesses ranging from 30 to 800 nm, for photon energies above the threshold value and for sufficiently low laser intensities the total photoemission signal was found to exhibit an initial linear variation with the laser intensity and then saturation. Saturation at

higher laser intensities is ascribed to electronic space charge density formation in the insulator, which limits the emission in vacuum.

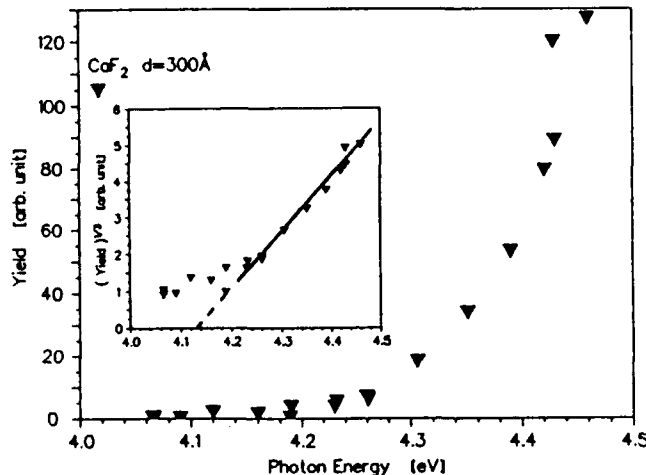


Fig. 1

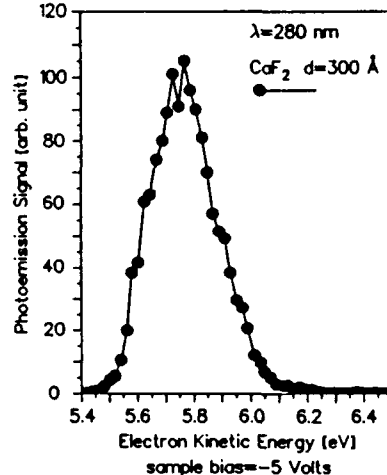


Fig. 2

In the linear regime, the photoemission yield was determined and found to increase with photon energies. Fig. 1 shows a plot of the yield against the photon energy in the case of a CaF₂ (d=300 Å)/Si(111) sample. The near threshold data was fitted to a third power law to yield a threshold value of 4.15 eV. The energy distribution curves, for electrons emitted in the vacuum from the insulator were obtained and analyzed. A typical energy distribution curve, showing the photoemission signal versus the photoelectron energies, is given in Fig. 2 for a CaF₂ (d=300 Å)/Si(111) sample and a photon wavelength $\lambda=280$ nm. For low laser intensities, we see photoelectrons emitted from energy levels up to about 0.2 eV below the Fermi level, which agrees with the position of the top of the valence energy band at the interface, as determined by Rieger *et al.*⁴, who evaluated the band bending at the CaF₂/Si(111) interface (for similar growth conditions) as a consequence of Fermi level pinning. At higher laser intensities, photoelectrons appear to originate from energy levels above the Fermi level, in other words, the width of the electron energy distribution curves increases. This effect is believed to be caused by space charge effects.

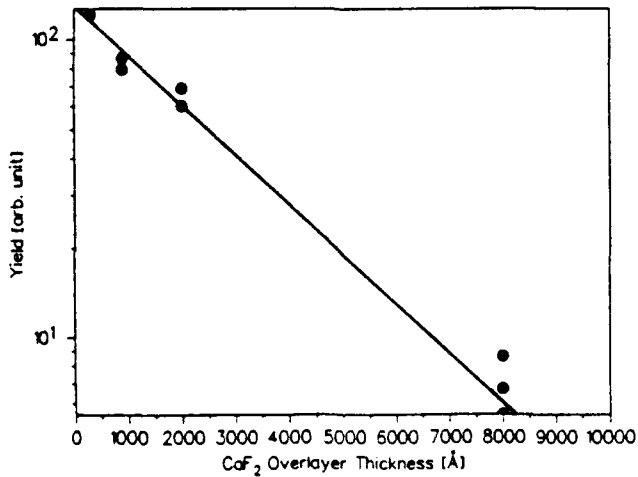


Fig. 3

Finally, together with the threshold behavior, the energy distribution curves are consistent with a picture in which electrons are excited by internal photoemission from the Si valence band to the CaF_2 conduction band. Emitted electrons are then able to travel in the CaF_2 layer with characteristic energy losses or scattering mechanisms. A comparative study of samples with different overlayer thicknesses has allowed us to determine a characteristic travel length for electrons in the insulating CaF_2 ; it was found to be approximately 2000 Å. This relatively high value is supported by the high electronic mobility of CaF_2 , the epitaxial quality of our overlayers as well as the low initial energy of the emitted electrons which screens them from most of the scattering mechanisms. Fig. 3 shows the photoemission yield at $\lambda=280$ nm plotted against the CaF_2 layer thickness. A similar long "untrapped length" for electrons in amorphous SiO_2 grown on Si(111) indicating that the phenomena is more general than just the $\text{CaF}_2/\text{Si}(111)$ system.

This work is supported by the Joint Services Electronics Program (JSEP), the Air Force Office of Scientific Research (AFOSR) and the Army Research Office (ARO).

References

1. T. L. Gilton, C.P. Dehubostel, M.P. Schneider, J.P. Cowin, *J. Chem. Phys.*, 91, 1937 (1989).
2. K. Giesen, F. Hage, W. Steinmann, *Ann. Iss. Phys. Soc.* 6, 446 (1984); J. O'Neill, Z. Wu and R.M. Osgood, Jr., *J. Vac. Sci. Technol.*, A6, 1426 (1988); T.L. Gilton, J.P. Cowin, G.D. Kubiak and, A.V. Hamza, *J. Appl. Phys.*, to be published.
3. T.P. Smith III, J.M. Phillips, W.M. Augustyniak and P.J. Stiles, *Appl. Phys. Lett.*, 45, 907 (1984); J.M. Phillips, L.C. Feldman, J.M. Gibson and M.L. McDonald, *Thin Solid Films*, 107, 217 (1983).
4. D. Rieger, F.J. Himpel, V.A. Karlsson, F.R. McFeely, J.F. Morar and J.A. Yarmoff, *Phys. Rev.*, B34, 7295 (1986).

**Silicon Atomic Layer Growth By Laser Beam/Si₂H₆
Adsorbates Interactions**

Y. Nagasawa, T. Tanaka, S. Miyazaki, M. Hirose

Department of Electrical Engineering, Hiroshima University
Higashi-Hiroshima 724, Japan

Abstract

Saturated monomolecular adsorption of Si₂H₆ on a silicon surface held at temperatures around -60°C and subsequent irradiation of a single shot of ArF excimer laser fully decomposes the adsorbed layer to promote the atomic layer growth of Si. TEA CO₂ laser irradiation at 10P6 line, which selectively excites the surface SiH₃ bond, significantly reduces the content of the bonded hydrogen in the silicon layer. Possible mechanisms for the silicon atomic layer growth and the hydrogen reduction are also discussed.

1. Experimental

The Si₂H₆ partial pressure, the substrate temperature, the excimer laser power and its repetition rate were maintained at 0.01Torr, -80°C, 21mJcm⁻²/shot and 0.67Hz, respectively. In a previous work[1], the Si growth kinetics has been systematically studied to achieve the atomic layer growth, and the deposition parameters have been optimized. TEA CO₂ laser beam from 10P6, 10P14 or 10P26 line was irradiated on the growth surface at a laser power of 22~42mJcm⁻²/shot and a repetition rate of 3.6Hz. Note that 10P6 line(956.1cm⁻¹) can excite the Si-SiH₃ bond-bending mode at 959cm⁻¹. 10P14 or 10P26 excites the asymmetric deformation mode of Si₂H₆ molecule. The experimental setup is schematically shown in Fig.1.

2. Results and Discussion

The silicon growth rate per laser pulse measured as function of reciprocal temperature(Fig.2) clearly shows a plateau which corresponds to the atomic layer thickness between Si(100) and Si(111) spacing since the deposited film is polycrystalline. To reveal the influence of the CO₂ laser irradiation, the growth rate and the hydrogen content were measured for 10P6, 10P14 and 10P26 lines as shown in Fig.3, where 10P6(956cm⁻¹) coincides with the absorption band of the bond-bending mode of Si-SiH₃ at 959cm⁻¹[2], and 10P14 and 10P26 lines are close to the absorption bands of Si₂H₆ molecule at 948cm⁻¹ and 937.5cm⁻¹, respectively. A little enhancement of the growth rate by 10P14 and 10P26 irradiation could be attributed to the disilane decomposition on the surface, while the 10P6 line causes the vibrationally excited desorption of hydrogen from the Si-SiH₃ surface bond, in consistence with the significant reduction of

hydrogen content in the 10P6 sample. The desorption of SiH_3 radicals from the surface is unlikely because the growth rate is nearly equal to the case without CO_2 laser irradiation. It is also interesting to note that the hydrogen content for the 10P14 sample is lower than the 10P26 one probably because the SiH_3 absorption band tail overlaps with 10P14 line.

To examine the thermal effect of the CO_2 laser irradiation, the laser power dependence of hydrogen content was measured as shown in Fig.4. The hydrogen content is almost unchanged above $20\text{mJcm}^{-2}/\text{shot}$, indicating that the CO_2 laser irradiation primarily induces the photochemical effect on the surface.

3. Possible Mechanism

The atomic layer growth must involve the self-limiting process in the reaction kinetics. It is shown in the previous paper[1] that the first monolayer of adsorbed Si_2H_6 on an Si surface is completely photodissociated by the ArF excimer laser irradiation in the power range of $20\text{~}50\text{mJcm}^{-2}/\text{shot}$. The self-limiting process arises from an extremely high dissociation rate of the monolayer Si_2H_6 . This also suggests that the growth surface is covered with hydrogen whose bonding configurations could be Si or SiH_3 for Si(111) plane and SiH_2 for Si(100). The vibrational frequency of Si-SiH₃ unit on the surface is calculated to be 959cm^{-1} [2], that is very close to the 10P6 line. Therefore, the 10P6 line irradiation promotes the hydrogen desorption from the growth surface because a significant fraction of silicon-hydrogen bonds is thought to be SiH_3 .

References

- [1] T. Tanaka, T. Fukuda, Y. Nagasawa, S. Miyazaki, M. Hirose: *Appl. Phys. Lett.*, 56(1990)1445.
- [2] J. C. Knights, G. Lucovsky and R. J. Nemanich: *Philos. Mag. B* 37(1978)4467.

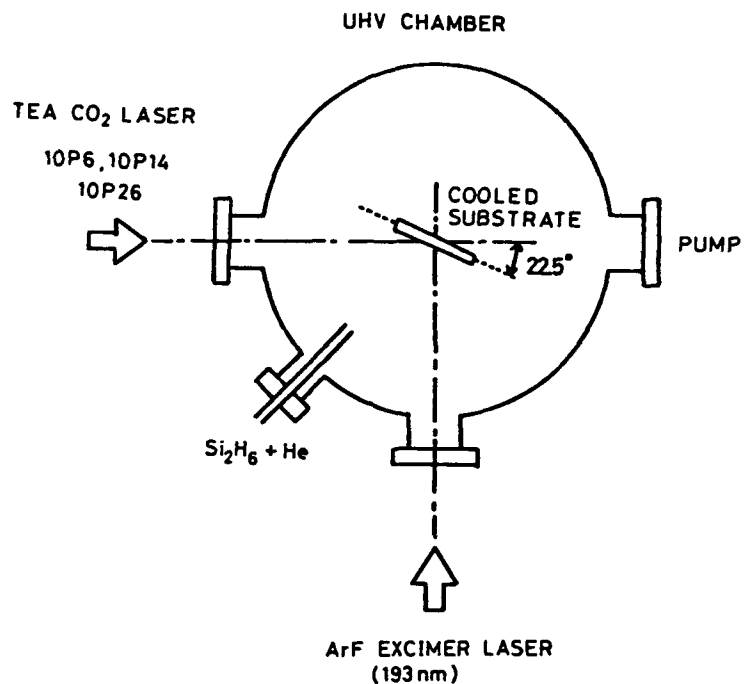


Fig. 1 Schematic illustration of experimental setup.

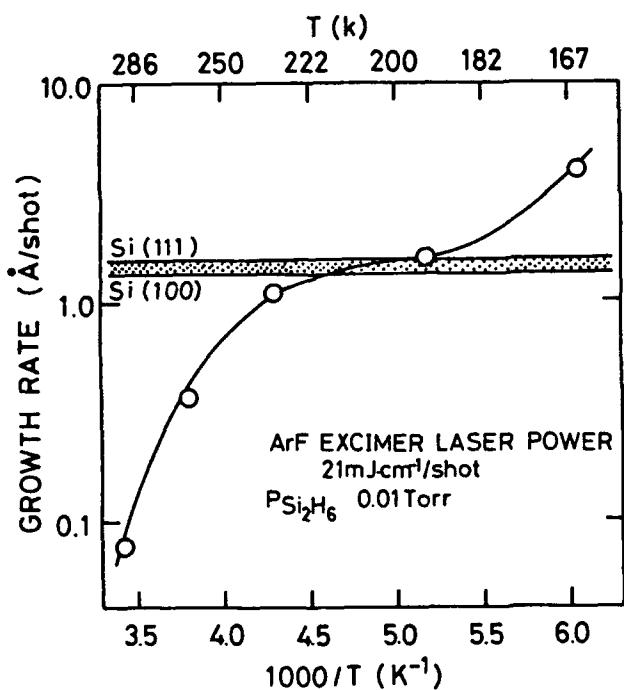


Fig. 2 Silicon growth rate versus reciprocal temperature.

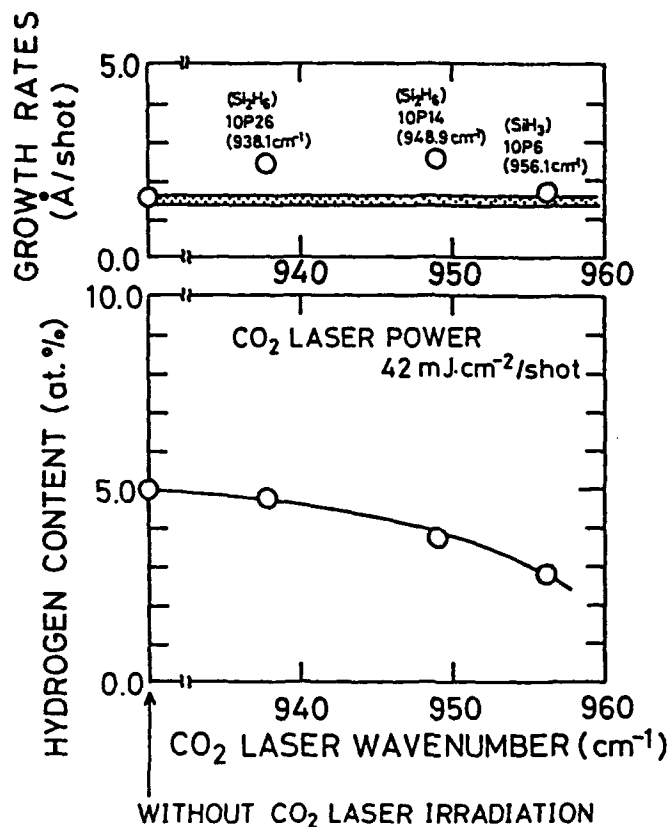


Fig. 3 Growth rates and hydrogen contents for different CO₂ laser lines.

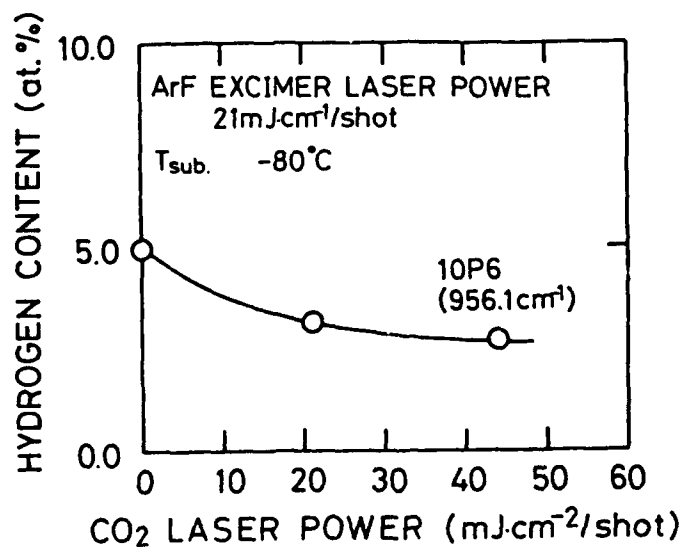


Fig. 4 CO₂ laser power dependence of hydrogen content in as grown silicon films.

Tuesday, February 12, 1991

Beam-Assisted Etching

TuA 8:00am–9:30am
Anasazi South

Stuart J. C. Irvine, *President*
Rockwell International Corporation



Laser-Induced Reactions of Semiconductor Surfaces with Chlorine

Qi-Zong Qin, Yu-Lin Li, Ping-He Lu, Zhuang-Jian Zhang,
Zhong-Kao Jin and Qi-Ke Zheng

Laser Chemistry Laboratory, Fudan University
Shanghai, P.R. China

Laser-induced chemical reaction of semiconductor with halogen and halogen compounds has attracted much attention in recent years due to its potential application in fabrication of microelectronic devices. We have reported UV and visible laser-induced reactions of Si and GaAs surfaces with chlorine using a CW molecular beam technique coupled with time-resolved mass spectrometry(1,2.). This paper will present recent studies in our laboratory on laser-induced reactions of Ge(111), Si(111), GaAs(100) and InP(100) surfaces with chlorine molecules under 355-, 560-, and 1064-nm laser irradiations. We are particularly interested in the use of near infrared (1064-nm) laser photons as well as the promotion of reaction by raising the incident chlorine molecules' translational energy. The objective is to achieve a better understanding of the mechanism of laser-induced reaction and its potential application in the chemical etching of semiconductor.

The details of the experimental setup have been described previously(2). A three-stage differentially pumped system is used and the monoenergetic chlorine molecular beam produced by an adiabatic expansion of 5% Cl₂ seeded in He, Ar or He/Ar mixture are varied from 10 to 60 kJ/mol by changing the seeding gas. The

laser beam is focused perpendicularly onto the semiconductor surface at the crossing point of the chlorine molecular beam and the surface. The reaction products desorbed from the surfaces pass through an orifice to a quadrupole mass spectrometer(QMS) where ionization is accomplished by 70 eV electron impact. The time of flight (TOF) spectra are measured with a transient recorder interfaced to an IBM PC/XT computer through a modified NIM controller. The data acquisition system is triggered synchronously with the laser pulse.

The TOF spectra of MCl_x^+ ($M=Ge, Si, Ga$ and $In, x=1,2,3$) ions have been measured for the reactions of Ge(111), Si(111), GaAs(100) and InP(100) surfaces with chlorine under 355-, 560-, and 1064-nm laser irradiations. The relative intensities of the ion signals are determined by integrating the observed TOF spectra. Results show that the MCl_1^+ signals are dominant and MCl_2^+ signals are of comparable intensities. Very weak MCl_3^+ signal is observed only for GaAs/Cl₂ system. As_n⁺ and P_n⁺ ($n=1,2,3$) are also detected, but none of ion signals corresponding to $AsCl_x^+$ and PCl_x^+ ($x=1,2,3$) is obtained. No obvious dependence of the mass distribution of the measured ion species on laser fluence and wavelength is observed for all the four systems, but the ion signal intensities for the 355-nm and 560-nm cases are stronger than that for the 1064-nm case at the same laser fluence.

Analysis of the shape and peak position of the TOF spectra shows that both MCl and MCl_2 are the major neutral products in the Si/Cl₂, GaAs/Cl₂ and InP/Cl₂ reaction systems. However, the similarity of the TOF spectra of $GeCl^+$ and $GeCl_2^+$ and the same values of their flight times at peak intensities(t_m) indicate that $GeCl^+$ ion may originate from the genuine desorbed species $GeCl_2$, thus $GeCl_2$ might be the only neutral desorbed product for Ge/Cl₂ reaction system. All the measured TOF spectra can be fitted with a Maxwell-Boltzmann distribution fairly satisfactorily when laser fluence is not very high.

The relative yields of MCl^+ has been examined as a function of laser fluence at 355-, 560- and 1064-nm. Obviously there exist laser fluence thresholds dependent on laser wavelength. The measured thresholds for the 1064-nm case is more higher than that for 560-nm and 355-nm cases. For instance, the threshold

fluences are 0.15, 0.035 and 0.02 J/cm² for Si/Cl₂ system at 1064-, 560-, and 355-nm, respectively. Above the thresholds the relative yields of MCl⁺ increase linearly with increasing laser fluence and saturate in the high laser fluence region.

A noticeable result of this study is the effect of the translational energy of the incident chlorine molecules on the laser-induced reactions. Experimental result shows that the yield of MCl⁺ ions increases rapidly with increasing the incident chlorine molecules' translational energy, and translational energy threshold for specific reaction system is independent on laser fluence and wavelength. A simplified dissociative chemisorption model, which is assumed that there is a barrier to dissociative chemisorption of chlorine molecule on the surface and the incident molecules' translational energy is effective in overcoming it, has been employed to interpret the enhancement of the chlorine molecules' translational energy on these laser-induced reactions.

The reaction mechanism can be described by a number of consecutive steps: (1) The dissociative chemisorption of chlorine molecule on the surface forms two absorbed Cl atom, when the incident chlorine molecules' translational energy is higher than its threshold. (2) The reaction of absorbed Cl atom with M(IV) or M(III) forms absorbed MCl and MCl₂ and the subsequent reactions between the absorbed Cl and chlorides take place on the surfaces. (3) The pulsed laser irradiation of the partially chlorinated surface leads the desorption of absorbed species. For the laser induced desorption with pulsed 355-nm and 560-nm photons the band-gap excitation is proposed for Si/Cl₂, GaAs/Cl₂ and InP/Cl₂ systems, as the energies of 355-nm and 560-nm photons are higher than the band-gap of Si, GaAs, and InP. For 1064-nm pulsed laser induced reactions, however, thermal heating process may play an important role in the desorption of the absorbed products.

References:

- (1) Q.Z.Qin, Y.L.Li, Z.K.Jin, Y.Y.Yang, W.J.Jia and Q.K.Zheng, Surf.Sci., 207(1988) 142.
- (2) Y.L.Li, Q.K.Zheng, Z.K.Jin, M.Yu, Z.K. Wu and Q.Z.Qin, J. Phys. Chem. 93(1989) 5531.

Mechanism of Chemical Etching of doped GaAs by Cl₂

E. A. Houle

IBM Research Division, Almaden Research Center

650 Harry Road, San Jose, CA 95120

(408) 927 2420

Consideration of product volatility and thermodynamic stability have been central to models developed for the thermal etching and deposition of GaAs by Cl₂.^{1,2} Mass spectrometric studies of the etching chemistry have tended to support some of the basic assumptions of these models: that the thermodynamically most stable product is formed and that product volatility controls the etch rate. Surface analyses, for example, have revealed the presence of a Ga-rich scale after etching, to be expected if the As chlorides are more volatile and desorb more readily.³⁻⁵ Consequently, models of beam modification of GaAs in the presence of Cl₂ have focussed on how energetic particles or light might perturb the thermal reaction. In this work the validity of the basis for these models has been examined by investigation of the etching chemistry of doped GaAs by molecular beam mass spectrometry and in situ Auger spectroscopy.

Experiments have been carried out using a spectrometer and experimental methods described in detail elsewhere.^{6,7} The instrument has been modified to include an ion gun and differentially pumped Auger spectrometer for sample cleaning and analysis, and a heated sample stage. GaAs(100) crystals doped n- and p-type (10^{16} cc⁻³) were etched side-by-side to ensure stability of reaction conditions. The Cl₂ flux was in the range of 10^{17} cm⁻²s⁻¹. Extensive calibrations have been carried out to determine cracking patterns of Ga and As reaction products.

Earlier studies have interpreted mass spectrometric data taken under similar conditions to show that GaCl₃, AsCl₃, and GaCl are the etch products. At high temperature the form of

As has been reported variously as AsCl and As₄.^{3,5} Analysis of the modulated waveforms measured in the present work does not completely support this interpretation. As shown in Fig 1 the etch products include GaCl₃, GaCl₂, GaCl, AsCl₃, AsCl₂ and various forms of elemental As. The branching ratios are sensitive to both temperature and doping, as indicated in Figs 1 and 2. These data indicate that the thermodynamically most stable products are not formed exclusively. Volatility is not a good criterion for predicting product desorption: the gallium chlorides form and desorb readily even though they are less volatile than As and its compounds, and Auger measurements show the surface of the crystal to be As rich under all conditions.

These results have important implications for models of GaAs etching in particular and semiconductor etching in general, whether thermal or beam-assisted. Although thermodynamic driving forces play an important role, they do not control product formation. The doping dependence in particular is most revealing, particularly when compared to similar behavior observed in Si.^{6,8} We suggest that microscopic aspects of the system such as local electron density are of critical importance, and must be considered explicitly in predicting reactivity for a particular semiconductor and crystallographic orientation.

References

1. S.C.McNevin, J. Vac. Sci. Technol. B4, 1216 (1986).
2. C. Chatillon and S. C. Bernard, J. Crystal Growth 71, 433 (1985).
3. M. Balooch, D. R. Olander and W. J. Sickhaus, J. Vac. Sci. Technol. B 4, 794 (1986).
4. N. Furuhata, H. Miyamoto, A. Okamoto and K. Ohata, J. Electron. Mater. 19, 201 (1990).
5. H. Hou, Z. Zhang, S. Chen, C. Su, W. Yan and M. Vernon, Appl. Phys. Lett. 55, 801 (1989).
6. E. A. Houle, J. Appl. Phys. 60, 3018 (1986).
7. E. A. Houle, J. Chem. Phys. 87, 1866 (1987).
8. E. A. Houle, Phys. Rev. B39, 10 120 (1989).

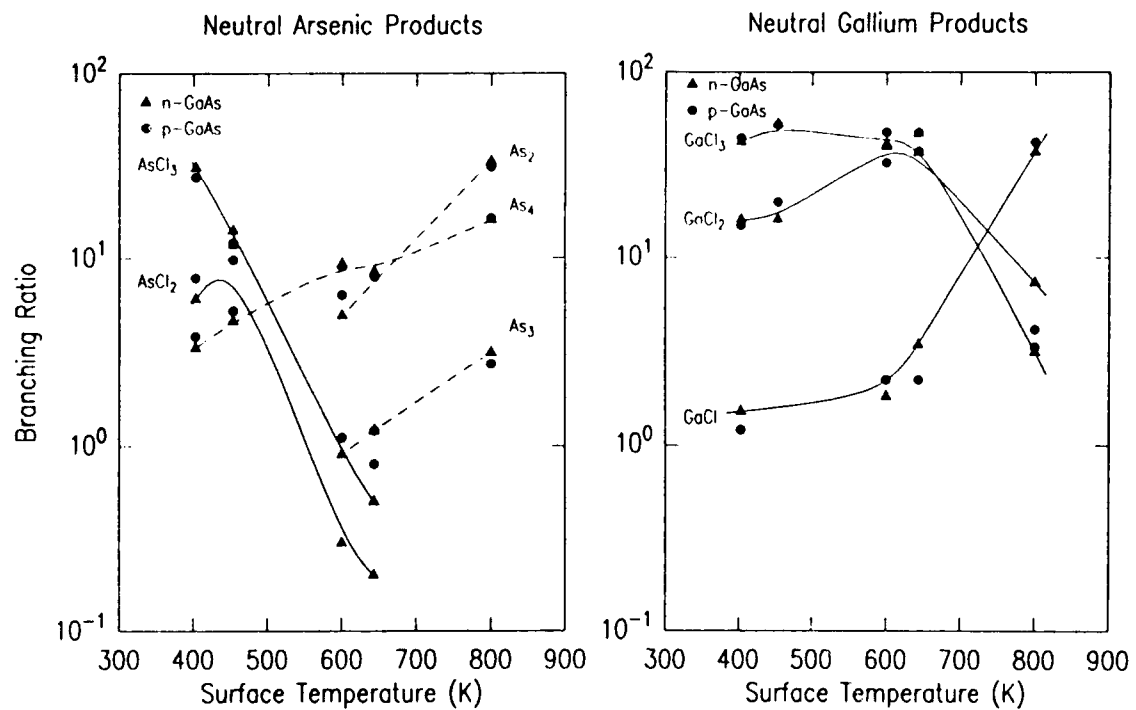


Figure 1 Branching ratios of neutral etch products (normalized to total Ga and As product signal) as a function of temperature for doped GaAs(100).

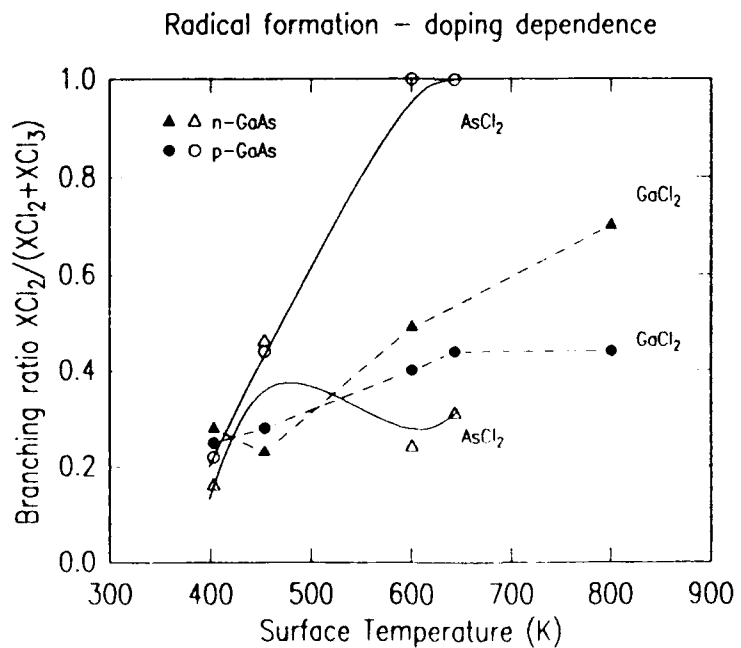


Figure 2 Influence of doping type on free radical formation.

UV Laser-Induced Interaction of Cl₂ with GaAs(110)

G. Haase, V. Liberman, M. C. Shih and R. M. Osgood, Jr.

Microelectronics Sciences Laboratories, Columbia University

500 W 120th St., New York, NY 10027

Tel: (212) 854-8449

We have studied the UV laser-induced interaction of molecular chlorine with a GaAs(110) surface under ultra-high vacuum (UHV) conditions. Unlike previous studies of this system [1,2,3], we concentrated on well-defined surfaces, known coverages and low laser fluences.

The experimental setup included a low energy electron diffraction apparatus, an Auger electron spectrometer and a differentially pumped mass spectrometer for thermal desorption spectra (TDS) and time-of-flight (TOF) measurements. Without illumination, chlorine was found to adsorb molecularly and dissociatively on *n*-GaAs(110) surfaces at 85 K. The laser experiments were done with a 193- and 351-nm excimer laser, at fluences below 5 mJ/cm². Illumination of a molecular chlorine-covered surface at 85 K with 193 nm excimer laser radiation led to the formation of AsCl₃, which desorbed at 180 K. Illumination with 351-nm radiation resulted in the formation of smaller amounts of arsenic chloride on the surface. Figure 1. presents a typical time-of-flight distribution of Cl₂ molecules and Cl atoms that were ejected by 193-nm excimer laser irradiation from condensed chlorine layer on an 85 K sample, while 351-nm light caused the ejection of Cl atoms exclusively. The desorption peak for mass 35 (Cl atoms, corrected for the Cl₂ dissociation in the mass spectrometer ionizer) in the 193-nm case was higher by a factor of ~20 than that produced by 351-nm radiation with twice the laser fluence.

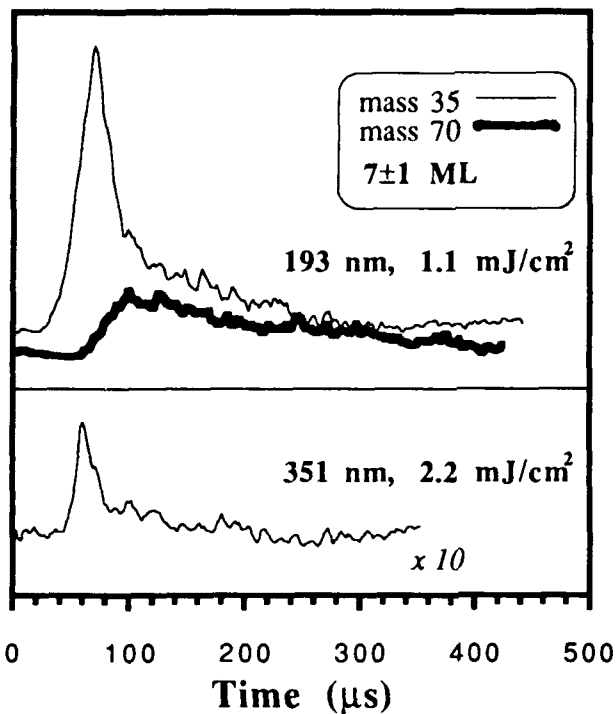


Fig 1. Time-of-flight distributions for 193-nm (1.1 mJ/cm^2) and 351-nm (2.2 mJ/cm^2) radiation. The TOF distributions are given for masses 35 (thin line) and 70 (thick line), at a chlorine coverage of $7\pm1 \text{ ML}$. The mass 35 signal is corrected for the contribution of the mass 70 fragmentation (see text) for the 193 nm irradiation. The time-of-flight is corrected for the time the ions spent in the mass spectrometer.

In order to check for electron-hole pair mechanism, we irradiated the surface with 535-nm laser light (photon energy of 0.9 eV above the GaAs direct band gap) at $6\text{-}80 \text{ mJ/cm}^2$. No new species were observed thus ruling out this mechanism. A thermal mechanism can also be ruled out due to the low fluences used in the UV laser experiments. At these fluences, the transient temperature peak was calculated not to exceed 5 K.

Direct absorption of the UV light by the condensed molecular Cl_2 can lead to dissociation, producing Cl atoms that will react with the substrate or be ejected into vacuum. A correlation between the amount of chlorine ejected and the AsCl_3 formation rate was indeed observed. Assuming that the UV absorption spectra of condensed chlorine is not significantly perturbed from that in the gas phase, one would expect a considerably higher reaction rate for the 351 nm than for the 193-nm radiation. Since we saw the opposite trend in our

experiment, this mechanism clearly cannot explain the data for the two UV wavelengths examined.

Fig.2 shows the integrated arsenic chloride TPD peak as a function of the number of molecular chlorine monolayers on the 85 K GaAs(110) surface. Note that 300 pulses of 351-nm laser light at 2 mJ/cm² were required to achieve an AsCl₃ coverage comparable to what 100 pulses of 193 nm at 0.8 mJ/cm² have produced. For the 193 nm case, the first Cl₂ layer contributed to >40% of the arsenic chloride signal. Additional layers, beyond the 10th layer, did not play any role in forming more product. On comparison to the 351-nm curve, we propose that for the 193-nm radiation, chlorine was dissociated next to the GaAs/Cl₂ interface by attachment of photoemitted electrons. Evidence of such a mechanism was presented by Cowin *et al* for methyl halides [4,5] and by others [6, 7].

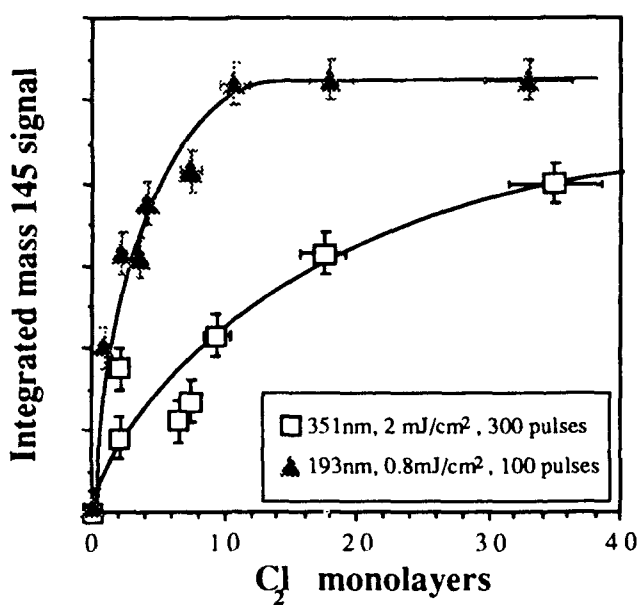


Fig 2. Integrated TPD spectra at mass 145 (AsCl₂) as a function of the number of molecular-chlorine monolayers at 85 K, after illumination with 100 excimer laser pulses of 193 nm, 0.8 mJ/cm² (solid triangles) and 300 pulses of 351 nm, 2 mJ/cm² (open squares). The solid lines are for guidance only.

In conclusion, we have studied the mechanisms leading to AsCl₃ formation as well as chlorine atom and molecule ejection from a Cl₂-covered 85 K GaAs(110) surface by UV laser. While direct photodissociation of Cl₂ molecules

may explain the results for the 351-nm laser, dissociative attachment of photoemitted electrons is proposed to initiate the reaction with 193-nm radiation.

References

1. S. C. McNevin and G. E. Becker, *J. Appl. Phys.* **58**, 4670 (1985).
2. M. Balooch, D. R. Olander and W. J. Siekhaus, *J. Vac. Sci. Technol. B* **4**, 794 (1986).
3. Q. Z. Qin, Y. L. Li, Z. K. Jin, Z. J. Zhang, Y. Y. Yang, W. J. Jia and Q. K. Zheng, *Surf. Sci.* **207**, 142 (1988)
4. M. R. Schneider, C. P. Dehnboestel, T. L. Giltonand and J. P. Cowin, *To be published* (1990).
5. T. L. Gilton, C. P. Dehnboestel, M. P. Schneiderand and J. P. Cowin, *J. Chem. Phys.* **91**, 1937 (1989).
6. S. J. Dixon-Warren, J. C. Polanyi, C. D. Stannersand and G. Xu, *J. Phys. Chem.* **94** (1990).
7. S. K. Jo and J. M. White, *J. Phys. Chem.* **94**, 6852 (1990).

Pulsed UV Induced Etching of Silicon: A Time-of-Flight Study

Carlotta Paulsen-Boaz and Thor Rhodin, Department of Chemistry and School of Applied and Engineering Physics, Clark Hall Cornell University Ithaca, New York 14853, Tel: (607) 255-4068

Introduction:

Understanding the dynamics of the laser-induced chlorine etching of silicon requires clarification of the mechanisms by which the photons interact more or less concurrently with the reacting gas, the surface adsorbate and the silicon substrate. To clarify the etching mechanism it is generally recognized that it is desirable to separate the relative contributions from: excitation and dissociation of the reacting gas, Maxwell-Boltzmann heating of the substrate, formation of an altered surface, dissociation, formation and desorption of surface products, generation of electron-hole pairs in the subsurface and the stimulation of new quantum mechanical channels for reaction.¹ Although much work has been done on these effects, most of the studies with some exceptions, have not focused on surface characterization and have been carried out at relatively high laser fluences. Hence, the microstructure and composition of the target surfaces have not always been adequately defined. Interpretation of the reaction mechanisms tend to be obscured by thermal effects and the nature, time and energy features of the emitted products have not always been completely resolved. The objective of this work is to clarify some of these issues. The factors of laser fluence and sample doping are specifically addressed. With reference to our system we have chosen one in which there is no etching in the absence of the photon beam, and gas-photon interactions are minimized at the pressures used.

Experimental:

These experiments were carried out in an ultra high vacuum chamber (base pressure 1×10^{-10} torr). The quadrupole mass analyzer was located along the sample normal, while the laser beam entered and exited at 45 degrees to the normal. Time-of-flight scans were obtained by synchronization of the laser pulse with collection of the mass analyzer output by a multichannel scaler. A diffuse Cl₂ molecular beam provided effective surface pressures of 10^{-7} to 10^{-6} torr. Samples were cleaned by argon ion bombardment prior to etching. The samples being etched were single crystal Si (111) of varied doping (n⁺, n, p, p⁺). We have employed both a XeCl and a KrF excimer laser (308 and 248nm respectively). Photon beams are of 10ns pulses operated at a repetition rate of 10 Hertz.

Results and Discussion:

Our investigations began with a survey of laser power effects upon time-of-flight (TOF) scans and product distributions. In all cases the products found were primarily Si, SiCl, and SiCl₂. Very small amounts of SiCl₃ could be seen, but no SiCl₄ was detected under the conditions studied. Product ratios were observed to be altered by changes in both laser power and wavelength. (Typical results are shown in figure 1.) Under moderate to low laser powers the Si-TOF data evidenced two major peaks. Of these, the slower peak occurs simultaneous to, and in a constant ratio with the SiCl-TOF peak. We therefore attribute this peak to cracking of chlorinated species. Unlike the work of Jackman, Ebert, and Foord² on Si (100), under the range of chlorine pressures used, no evidence for spontaneous etching was found.

We have found that the TOF characteristics of our etching studies can be divided into three distinct regimes: a high power regime, $\approx 600\text{mJ/cm}^2/\text{pulse}$, a moderate power regime, 200-400mJ/cm²/pulse, and a low power regime, $\leq 150\text{mJ/cm}^2/\text{pulse}$.

At the high power end, the predominate etch product is Si⁺ (figure 2). Minor amounts of the neutrals Si, SiCl, and SiCl₂ were present as well. The relative lack of chlorinated products is attributed primarily to the severe depletion of chlorine on the surface produced by the intense photon fluxes. The Si ions were produced at very short times. Assuming a Maxwell-Boltzmann energy distribution, their translational temperature would be in excess of 10,000 Kelvin. (Maxwell-Boltzmann temperatures are given for comparative purposes only. Curves generated by MB calculations did not in general describe well the leading edge of the TOF data collected.) This strongly suggests that at this laser power a plasma has been created over the surface and is the dominate etch mechanism.

At more moderate laser powers (200-400mJ/cm²/pulse), SiCl is the major product. Its production, as well as that of SiCl₂, is linear in Cl₂ pressure. More interestingly, the TOF data for these two chlorinated species show shifts to shorter times with a rise in Cl₂ pressure (and hence Cl surface coverage). Maxwell-Boltzmann fits for both SiCl and

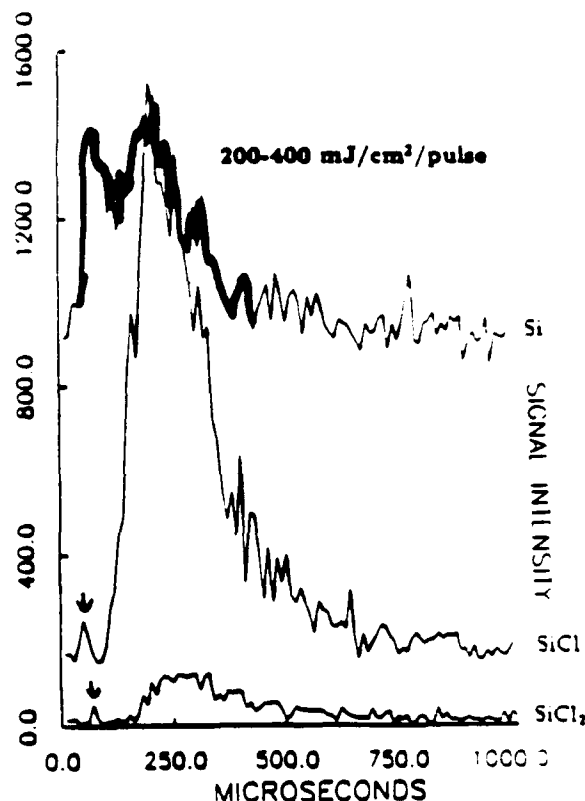


FIG. 1. Typical signal evolution with time. The slower of the Si peaks is due to cracking of chlorinated species. Small, fast peaks (marked with arrows) are tentatively attributed to photoejection. SiCl₃ signal is not shown as it would be flat on this scale. Laser pulse occurs at time zero.

SiCl_2 yield identical temperatures (typically on the order of 2-3000K, highly dependent on both chlorine pressure and laser power), while the Si peak evidences a distinctly higher temperature. No shift in the TOF peak positions of the various products was observed between the differently doped samples. These results are generally consistent with the earlier findings of Baller, Oosstra, de Vries, and van Veen.³ Minor peaks of Si, SiCl , and SiCl_2 at much shorter times may also be seen in figure 1. These are likely produced in a similar manner to the 'photoejection' peaks observed by Harrison, Polanyi, and Young⁴ in other surface adsorbate systems.

The results at significantly lower laser powers ($\leq 150\text{mJ/cm}^2/\text{pulse}$) for which TOF data has not been previously obtained, contrast markedly with the above data. While production of chlorinated species is still linear in Cl_2 pressure, the TOF peaks remain fixed in time with alterations in pressure. Furthermore, the SiCl and SiCl_2 peaks now evidence distinct temperatures. We additionally have enhanced production of the higher chlorinated species relative to SiCl , although SiCl production still dominates. The TOF data are characteristic of the dopant type and level of the samples. This has not previously been recorded for the Si/Cl_2 etch system. Heavily n-doped samples which are known to etch at higher rates produce TOF-peaks centered at distinguishably longer times than the n, p, or p^+ samples.

These general results hold for both the 308 and the 248nm excimer lines, though given similar conditions the 248 line gave more highly chlorinated products than the 308 line.

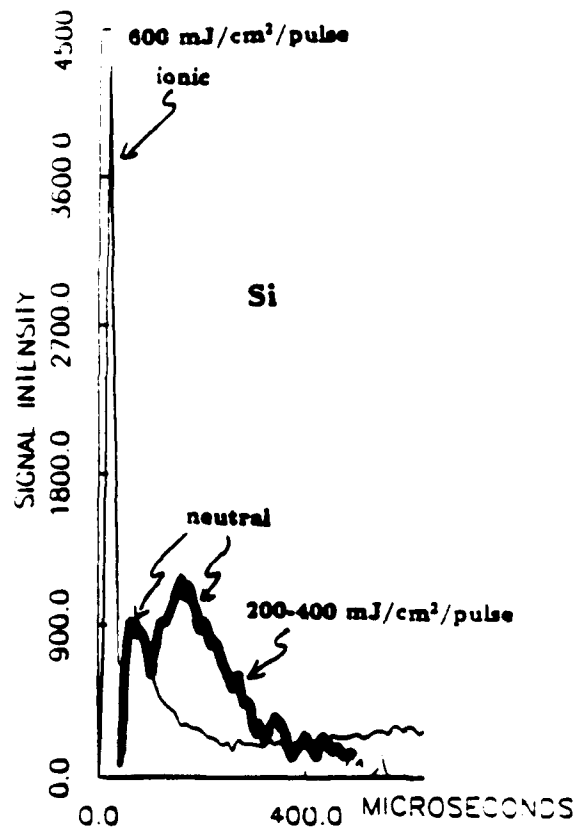


FIG. 2. Signal obtained under high power levels. Very fast, large peak is due to the evolution of Si^+ by a plasma mechanism. Also visible, the neutral Si peak falls at the same time as the peak seen in fig.1, which has been superimposed. Note the absence, on this scale, of the peak resulting from the cracking of chlorinated silicon species. Laser pulse occurs at time zero.

Conclusions:

Under very high laser fluences ($\approx 600\text{mJ/cm}^2/\text{pulse}$) a plasma mechanism dominates with Si^+ being the major product. At more moderate conditions (200-400 $\text{mJ/cm}^2/\text{pulse}$) TOF data are concluded to be partially thermalized. A photoejection process exists but produces only minor amounts of products. SiCl is the major product. At low laser powers ($\leq 150\text{ mJ/cm}^2/\text{pulse}$), an electronic process becomes visible. SiCl remains the major product. The results of the moderate laser power when contrasted with that of the lower power indicate that under the former conditions the burst of desorbed products from the crystal produces a localized high pressure which thermally averages the product energy distributions. Hence to obtain viable mechanistic information on the etching reaction from TOF data, measurements must be made while laser intensities are below the $150\text{mJ/cm}^2/\text{pulse}$ threshold: as such insight into the electronic mechanism only becomes accessible at very low power levels. These interpretations will be discussed in more detail in terms of our experimental results.

Acknowledgment: C. Paulsen-Boaz greatly acknowledges an IBM Manufacturing Research Fellowship. The research was funded by NSF grant DMR 87-05680. We would like to thank Professor T.A. Cool for his assistance and use of facilities.

1 T.J. Chuang, *J. Vac. Sci. Technol.*, 21(3) (1982) 798.

2 R.B. Jackman, H. Ebert, and J.S. Foord, *Surface Science*, 176 (1986) 183.

3 T. Boller, D.J. Oostra, A.E. de Vries, and G.N.A. van Veen, *J. Appl. Phys.*, 60 (1986) 2321.

4 I. Harrison, J.C. Polanyi, and P.A. Young, *J. Chem. Phys.*, 89 (1988) 1498.

Tuesday, February 12, 1991

Laser-Induced Desorption and Reaction

TuB 9:45am-11:25am
Anasazi South

Richard B. Hall, *Presider*
Exxon Research and Engineering



State-Specific Studies of the Laser-Induced Desorption of NO from Si(111)

L.J. Richter, S.A. Buntin, D.S. King, and R.R. Cavanagh

Center for Atomic, Molecular, and Optical Physics
 National Institute of Standards and Technology, Gaithersburg, MD 20899

A wide variety of chemical processes at semiconductor surfaces have been observed to be promoted by radiation. The possible mechanisms for the transfer of the initial photon energy to the reaction coordinate are many, including simple substrate heating, substrate carrier driven reactions, and localized adsorbate photoexcitation. State-resolved studies of laser-induced reaction products have proven extremely illuminating as they often allow the distinction and quantification of various competing excitation mechanisms.¹ We present the results of a state-resolved study of the laser-induced desorption (LID) of NO from Si(111) in which the energy partitioning in the desorbed NO is found to vary dramatically with the initial NO coverage due to the presence of competing excitation channels.

The experimental apparatus and principle procedures have been described earlier.¹ The Si samples were cleaned via Ne ion bombardment followed by thermal annealing at ≈ 950 K, a treatment which produces the 7x7 reconstruction as evidenced by sharp, bright 7th order low energy electron diffraction spots. Both 1.5 Ω -cm, B doped *p*-type and 0.5 Ω -cm, P doped *n*-type substrates were used. NO exposures via a directed array were performed with the substrate at ≈ 100 K. Detailed studies of the desorption were performed for two surface preparations: low coverage, which corresponds to ≈ 0.04 ML (1 ML = 7.8×10^{14} cm⁻²) of adsorbed NO, and saturation coverage, which corresponds to ≈ 0.6 ML of molecular adsorbates. The desorption-laser pulse was derived from a Q-switched Nd³⁺:yttrium-aluminum-garnet (YAG) laser and was incident normal to the crystal surfaces. Desorption-laser wavelengths, λ , of 1907, 1543, 532 and 355 nm were obtained by Raman shifting the fundamental or harmonic generation. The radiation exposure during an experiment was usually limited to produce no more than a 10% decrease in the observed NO photodesorption yield. After irradiation the substrate was subjected to an ion sputter/thermal anneal cycle to restore surface cleanliness and order. The desorbed NO was detected with quantum-state resolution by laser-induced-fluorescence as described previously.² Kinetic-energy distributions for a specific internal-state (vibration *v*; spin-orbit Ω ; rotation *J*) were extracted from optically detected time-of-flight (TOF) spectra obtained by varying the time delay between the firing of the desorption- and probe-lasers.

We will first discuss the results from the low coverage preparation. The flux-weighted average kinetic energy, $\langle E_k \rangle / 2k$, derived from TOF spectra recorded with $\lambda = 355$ nm were about 800 K. The kinetic energy distributions varied with the quantum state probed: $\langle E_k \rangle / 2k$ monotonically increased from ≈ 500 K to ≈ 1000 K as the rotational energy, E_{rot} , of the probed NO increased from 0 to 800 cm⁻¹. In Fig. 1 we present internal-state distributions derived from time integrals of TOF spectra. The data for the ground spin-orbit state ($\Omega = 1/2 \equiv F_1$) clearly lie on a common line, indicating that the rotational-level population distribution can be described by a Boltzmann distribution with a phenomenological rotational temperature, T_{rot} , of 230 ± 30 K. Additionally, a clear selectivity for desorption into the F_1 spin-orbit state is evident: the ratio of spin-orbit state populations: F_1/F_2 ($\Omega = 3/2 \equiv F_2$) is $\approx 9 \pm 1$, corresponding to a spin-orbit temperature of 80 K. A moderate degree of vibrational excitation was

observed, the $v=1/v=0$ state population ratio was 0.19 ± 0.08 . This would correspond to a vibrational temperature of 1600 K.

The various degrees of freedom of the desorbed NO are clearly not in equilibrium with each other. Combined with the fact that the calculated laser-induced surface temperature jump due to the 355 nm desorption-laser is less than 1 K and that the yield is linear with fluence, it is clear that the LID from low coverages is truly photochemical versus photothermal. The qualitative and quantitative aspects of the internal-state distributions for NO showed remarkably little dependence on either λ or substrate doping. All aspects of the NO($v=0$) distributions for 1064, 532, and 355 nm light on *n*- and *p*-type samples were indistinguishable. For 1907 and 1543 nm radiation on *p*-type samples, the qualitative variation of the kinetic energy distributions with E_{rot} , the Boltzmann nature of the F_1 states and the selectivity for the F_1 states were the same. However, T_{rot} was slightly cooler at 1543 and 1907 nm, ≈ 115 K. The insensitivity of the internal-state distributions to λ for the YAG harmonics establishes that a single desorption mechanism is responsible over the range 1064-355 nm. The qualitative similarity of the internal-state distributions for 1543 and 1907 nm suggests that the same mechanism is responsible for the entire range 1907-355 nm.

We have characterized the λ dependence of the yield per incident photon for NO($v=0$), arising from this common mechanism. On the *p*-type sample, the yields for 1907, 1543, 532, and 355 nm radiation relative to that at 1064 nm were $1.4(\pm 0.3) \times 10^{-4}$, $7(\pm 3) \times 10^{-3}$, $9(\pm 3) \times 10^{-1}$, and $15(\pm 2)$. The wavelength dependence of the yield (determined from the yields for 532 and 355 nm, relative to that of 1064 nm on *n*-type material) is independent of substrate doping. Experimental constraints make it difficult to accurately compare the absolute yields from the *n*- and *p*-type samples; however, they do not differ by more than an order of magnitude.

In earlier work², it was proposed that the photodesorption of NO from Si(111) at high coverages was driven by photogenerated hot carriers. The indirect gap at 100 K is 1.15 eV, therefore 1064 nm photons produce bulk carriers with only 15 meV excess energy. The significant yield we observe for LID of NO with 1064 nm incident light clearly rules out mechanisms involving hot photogenerated carriers at low initial coverages. Thermalized photogenerated carriers can also be excluded as important to the low coverage desorption channel based on the λ and doping dependence of the yield. The absorption depth of both 532 and 355 nm radiation is shorter than the thermal diffusion length during the laser pulse, therefore both the temporal and spatial evolution of the thermalized carriers generated at these two wavelengths are identical. The relative yields, 532:355 nm, of a photoprocess driven by thermalized carriers at these two wavelengths would be given by the relative optical absorption: $0.63:0.42 = 1.5:1$; however, the observed relative yield was $\approx 0.1:1$. Additionally, the absorption of 1064 nm light is sufficiently weak that at the fluences used (≈ 5 kW/cm²) the bands are not flattened by the pulse if they are assumed to be bent by their clean surface

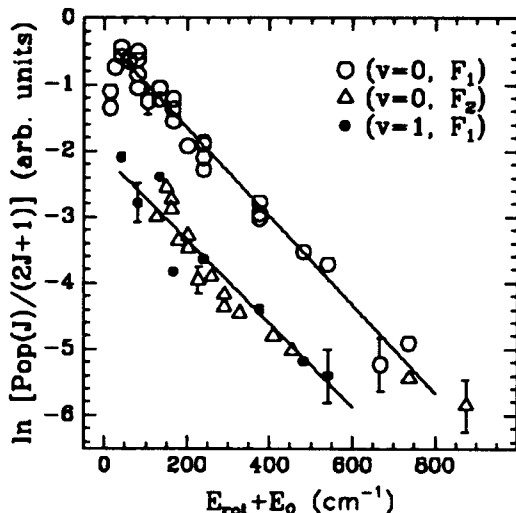


Figure 1 Boltzmann plot for LID from low coverages on *n*-type Si with 355 nm photons.

However, T_{rot} was slightly cooler at 1543 and 1907 nm, ≈ 115 K. The insensitivity of the internal-state distributions to λ for the YAG harmonics establishes that a single desorption mechanism is responsible over the range 1064-355 nm. The qualitative similarity of the internal-state distributions for 1543 and 1907 nm suggests that the same mechanism is responsible for the entire range 1907-355 nm.

values of ≈ 0.5 eV in the dark. Therefore, the yield due to a single band-edge carrier would be negligible for one of either n- or p-type doping, in contradiction with observation.

We have proposed that the LID from low coverages arises from photoproduction of a hole in the rest atom localized, S_2 , intrinsic surface state of the Si(111) 7x7 reconstruction.³ This is qualitatively consistent with the high yield at 1064 nm, the observable yield at 1907 and 1543 nm, and the quenching of the low coverage channel with increasing NO coverage. (During the initial stages of adsorption, NO preferentially quenches the adatom localized S_1 state, however at saturation coverage, both states are quenched.⁴) The role of the S_2 state is further supported by coadsorption experiments detailed in Fig. 2. NH_3 exposures quenched the yield, but did not alter the internal-state distributions significantly. NH_3 dissociatively adsorbs as NH_2 and H, preferentially bonding to rest atoms at low coverages, quenching the S_2 state.⁵ The effects of the coadsorption of O_2 , also shown in Fig. 2, confirm the role of the S_2 state and indicate that the S_1 state is not important. The adsorption of O_2 initially quenches the S_1 state, and subsequently quenches the S_2 state.⁶ Exposures of O_2 initially did not quench the low coverage NO LID; however, higher O_2 exposures did result in a decreased yield. Additional evidence that the S_1 state is not involved comes from the lack of any observable effect on the NO yield from the coadsorption of N_2O . N_2O interacts only with the adatom localized S_1 .⁴

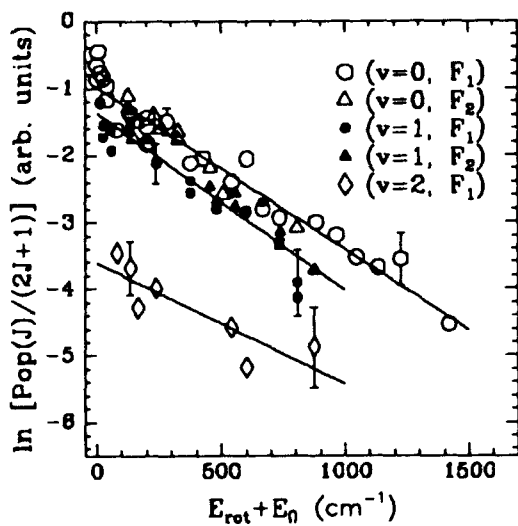


Figure 3 Boltzmann plot for LID from saturation coverages on n-type Si with 355 nm photons.

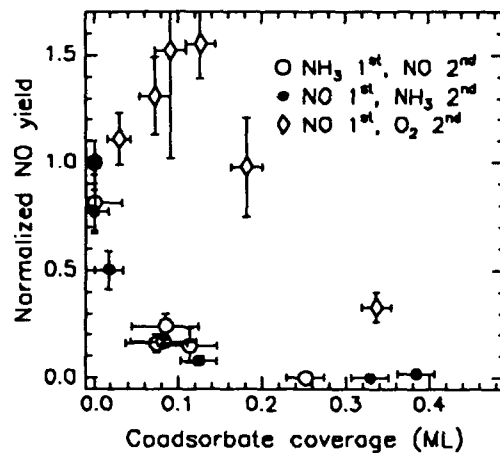


Figure 2 Yield for NO following coadsorption of either O_2 or NH_3 , relative to the yield with no coadsorbates.

When the NO coverage is increased above 0.04 ML, the NO begins to quench the S_2 state and the low coverage desorption channel shuts down. However, LID of NO still occurs due to the emergence of a second desorption channel. The $\langle E_k \rangle / 2k$ of this second channel at a desorption-laser wavelength of 355 nm were about 1100 K. Similar to the low coverage channel, the kinetic energy distributions varied with the quantum state probed: $\langle E_k \rangle / 2k$ monotonically increased from ≈ 700 K to ≈ 1400 K as E_{rot} of the probed NO increased from 0 to 1100 cm^{-1} . The internal state distributions for the high coverage channel (see Fig. 3) are dramatically different than those observed at low coverage. The effective T_{rot} was 590 ± 60 K and there was no spin-orbit selectivity: the spin-orbit population could be represented by a 'temperature' equal T_{rot} . Additionally, the degree of vibrational excitation observed at saturation coverage was significantly greater than at low

coverage. The vibrational-state population ratios were $(v=1):(v=0) = 0.57 \pm 0.24$ and $(v=2):(v=0) = 0.10 \pm 0.04$. The vibrational-state distribution was not well represented by a Boltzmann Distribution.

As mentioned above, earlier work implicated photogenerated hot carriers in the desorption mechanism from NO saturated Si(111) surfaces.² This postulate was motivated by the observation that the photodesorption yield essentially followed the bulk absorption coefficient for λ in the range 550-240 nm. Aspects of our state-resolved work are in qualitative agreement with the state-integrated studies, specifically the yield decreased by more than two orders of magnitude as the desorption wavelength was changed from 355 to 1064 nm. It has proven difficult to characterize the λ dependence of the energy partitioning in the LID at high coverages. However, it is clear that, unlike the observations at low coverage, the energy partitioning is sensitive to the desorption laser wavelength. At 1064 nm, the $\langle E_e \rangle / 2k$, T_{rot} , and vibrational excitation were all substantially cooler than observed at 355 nm.

It is interesting to conjecture what implications the observation of qualitatively different energy partitioning for desorption driven by the two substrate excitations, surface states and bulk carriers, may have for nonthermal processing. One aspect of the photogenerated carrier driven processes is their lack of selectivity. As an example, the photochemistry of NO on Si at high coverages is complex as at least three reactions occur: desorption of NO, dissociation of NO, and photosynthesis of N_2O . The different energy partitioning observed for the surface state and bulk carrier driven desorption reactions suggests that the two excitations may exhibit different chemistry. Therefore processing with below gap radiation, which will favor excitation channels due to surface states in cases where surface state and bulk channels compete, may give different results than with traditional visible and near UV wavelengths. Additionally, the observation of distinct photochemistry due to excitations of intrinsic surface states suggests that novel anisotropic surface processing may be possible by exploiting the differences in the electronic structure of various surface terminations.

This work was partially supported by the U.S. Department of Energy, Office of Basic Energy Sciences (D.E.-AIO5-84ER13150).

References

1. S.A. Buntin, L.J. Richter, R.R. Cavanagh, and D.S. King, Phys. Rev. Lett. **61**, 1321 (1988); J. Chem. Phys. **91**, 6429 (1989).
2. Z. Ying and W. Ho, Phys. Rev. Lett. **60**, 57 (1988).
3. L.J. Richter, S.A. Buntin, D.S. King, R.R. Cavanagh, Phys. Rev. Lett. **65**, 1957 (1990).
4. F. Bozso and Ph. Avouris, to be published.
5. Ph. Avouris and R. Wolkow, Phys. Rev. B **39**, 5091 (1989); F. Bozso and Ph. Avouris, Phys. Rev. B **38**, 3987 (1988).
6. G.V. Hansson, R.I.G. Uhrberg, and S.A. Flodström, J. Vac. Sci. Technol. **16**, 1287 (1979).

Adsorption and Desorption Kinetics for $\text{Si}(\text{C}_2\text{H}_5)_2\text{H}_2$ on $\text{Si}(111) 7\times 7$

P.A. Coon, M.L. Wise and S.M. George

Department of Chemistry
Stanford University
Stanford, CA 94305
(415) 725-0270

Diethylsilane (DES), $\text{Si}(\text{C}_2\text{H}_5)_2\text{H}_2$, is a promising candidate for the atomic layer epitaxy of silicon. Alkylsilanes are advantageous because they are less toxic and flammable than silanes. The reactions of organosilanes with silicon surfaces are also important both fundamentally and technologically. This study explored the adsorption and desorption kinetics for $\text{Si}(\text{C}_2\text{H}_5)_2\text{H}_2$ on $\text{Si}(111) 7\times 7$ using laser induced thermal desorption (LITD) and temperature programmed desorption (TPD) techniques.

Temperature programmed desorption (TPD) spectra obtained after DES adsorption on $\text{Si}(111) 7\times 7$ at 200 K were performed using a linear heating rate of $\beta = 9 \text{ K/s}$. The only species present in the TPD spectra following $\text{Si}(\text{C}_2\text{H}_5)_2\text{H}_2$ adsorption were C_2H_4 and H_2 at 700 and 810 K, respectively. TPD spectra for C_2H_4 and H_2 are shown below in Fig. 1.

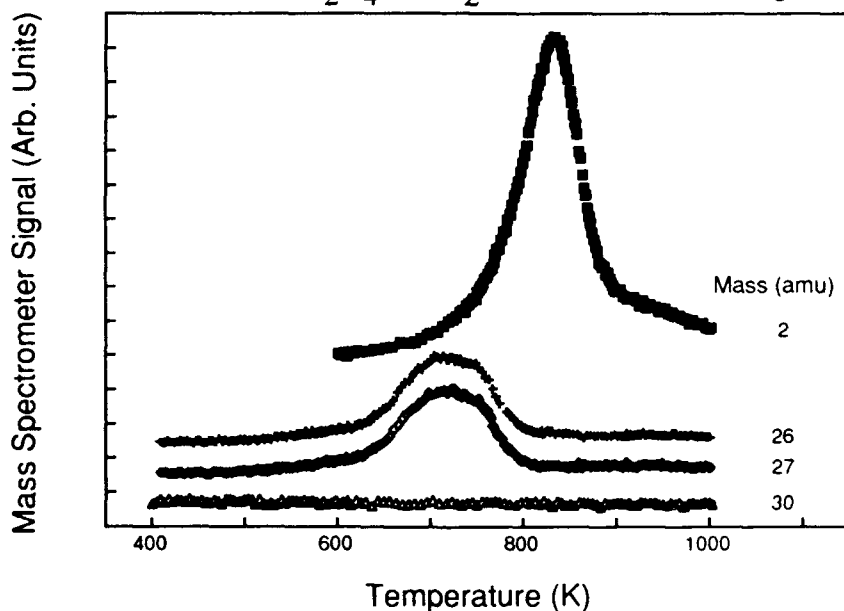


Fig. 1 TPD spectra at $\beta = 9 \text{ K/s}$ for C_2H_4 and H_2 after $\text{Si}(\text{C}_2\text{H}_5)_2\text{H}_2$ exposure on $\text{Si}(111) 7\times 7$.

Laser-induced thermal desorption (LITD) yields obtained after $\text{Si}(\text{C}_2\text{H}_5)_2\text{H}_2$ adsorption on $\text{Si}(111) 7\times 7$ at 200 K also contained only C_2H_4 and H_2 . Figure 2 shows the temperature-dependence of the H_2 and C_2H_4 LITD signals following a saturation $\text{Si}(\text{C}_2\text{H}_5)_2\text{H}_2$ exposure. The temperature was ramped linearly at $\beta = 2.1 \text{ K/s}$. The decreases in the C_2H_4 LITD signal between 600 - 750 K and the H_2 LITD signal between 750 - 810 K are consistent with the thermal desorption of C_2H_4 and H_2 as observed in Fig. 1.

Ethylene and hydrogen are the stable desorption species observed in both the LITD and TPD spectra from $\text{Si}(111) 7\times 7$ following $\text{Si}(\text{C}_2\text{H}_5)_2\text{H}_2$ adsorption. The presence of ethylene in the desorption yield suggests that the ethyl groups on the silicon surface decompose via a β -hydride elimination reaction. Although β -hydride elimination has been observed in the

thermal pyrolysis of gas-phase alkylsilanes (1), β -hydride elimination has not been observed from silicon atoms on silicon surfaces.

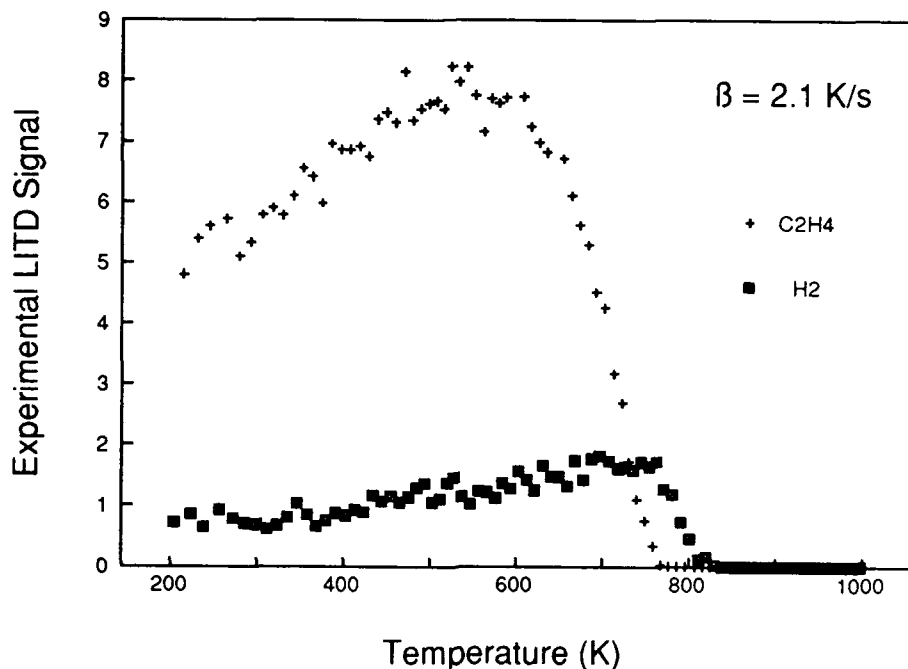


Fig. 2 Temperature dependence of the C_2H_4 and H_2 LITD signals following a saturation $\text{Si}(\text{C}_2\text{H}_5)_2\text{H}_2$ dose on $\text{Si}(111) 7\times7$.

The initial rate of $\text{Si}(\text{C}_2\text{H}_5)_2\text{H}_2$ adsorption on $\text{Si}(111) 7\times7$ was studied as a function of surface temperature. In these experiments, the clean $\text{Si}(111) 7\times7$ surface was maintained at a constant temperature while being exposed to $\text{Si}(\text{C}_2\text{H}_5)_2\text{H}_2$ through a capillary array doser. The capillary array doser was located directly above the ionizer of the quadrupole mass spectrometer. Consequently, adsorption kinetics of DES could be measured in real-time using LITD techniques.

The C_2H_4 LITD signals were proportional to the ethyl coverage on the $\text{Si}(111) 7\times7$ surface. The ethyl coverage was monitored during the $\text{Si}(\text{C}_2\text{H}_5)_2\text{H}_2$ exposure by measuring the C_2H_4 LITD signal from different surface positions at different times. The initial adsorption rate is proportional to the initial slope of the ethyl uptake curves versus time. Figure 3 shows that the initial rate of ethyl adsorption decreases as a function of increasing surface temperature.

The initial reactive sticking coefficients, S_0 , were obtained by dividing the initial adsorption rate by the $\text{Si}(\text{C}_2\text{H}_5)_2\text{H}_2$ flux. The results for the initial reactive sticking coefficient versus surface temperature are shown in Fig. 4. As expected from the uptake measurements, the initial sticking coefficients decrease as a function of surface temperature. Similar decreases in S_0 as a function of increasing surface temperature have been observed for O_2 (2), SiCl_4 (3) and SiCl_2H_2 (4) on $\text{Si}(111) 7\times7$, and O_2 on $\text{Si}(100)$ (5).

The temperature-dependence of the initial sticking coefficient of $\text{Si}(\text{C}_2\text{H}_5)_2\text{H}_2$ is consistent with a precursor-mediated adsorption model (6). In the precursor model, the first stage of adsorption involves the trapping of DES in a precursor state. The precursor species may either react to form chemisorbed species or desorb into the gas phase. Using this model,

the temperature dependence of the initial reactive sticking coefficient can be fit using the ratio of preexponential factors, k_d^0/k_r^0 , and the difference in the activation barriers, $E_d - E_r$, between the adsorption and desorption pathways. The solid line in Fig. 4 shows the fit using the parameters $k_d^0/k_r^0 = 1.2 \times 10^5$ and $E_d - E_r = 2.67$ kcal/mol.

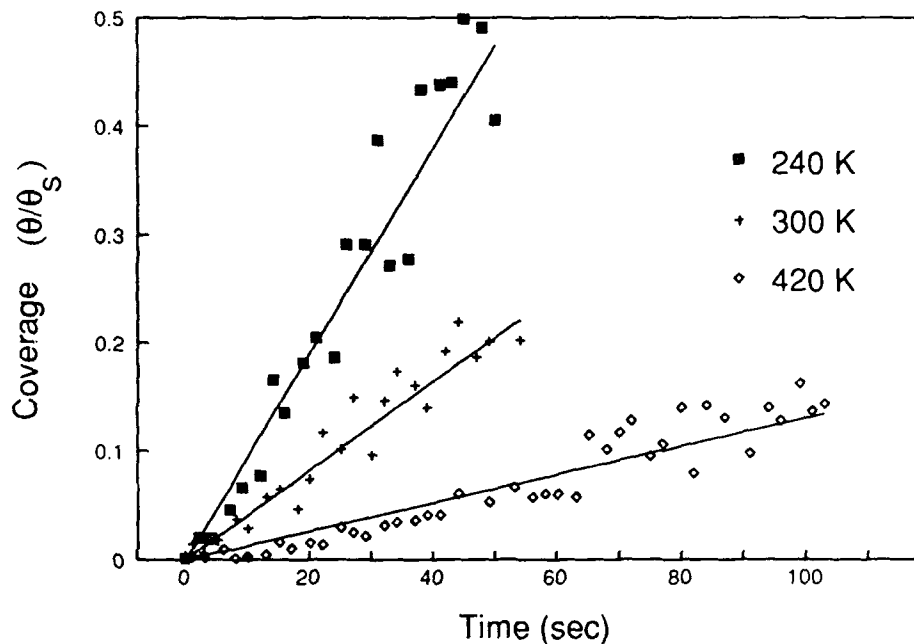


Fig. 3 Initial uptake of $\text{Si}(\text{C}_2\text{H}_5)_2\text{H}_2$ on $\text{Si}(111) 7\times 7$ at several surface temperatures. The ethyl coverage was measured by monitoring the C_2H_4 LITD signal versus time.

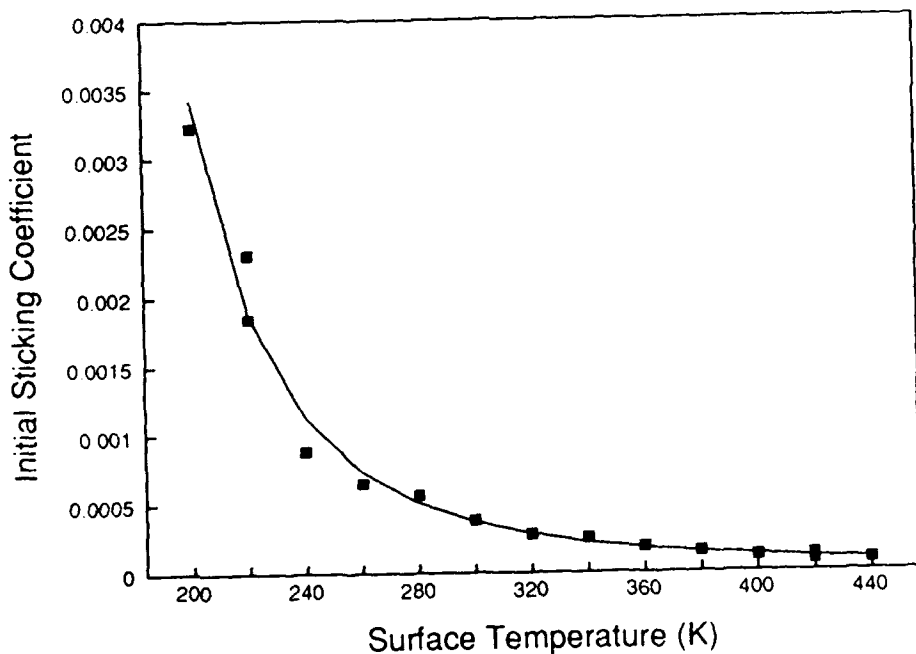


Fig. 4 Initial reactive sticking coefficient for $\text{Si}(\text{C}_2\text{H}_5)_2\text{H}_2$ on $\text{Si}(111) 7\times 7$. The solid line represents the fit of the precursor-mediated adsorption model to the data.

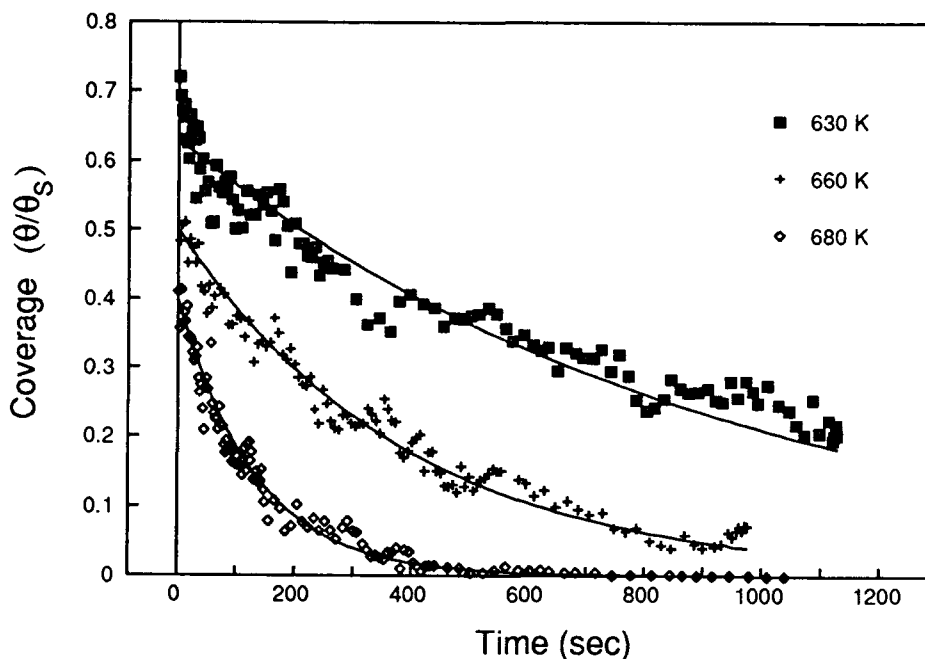


Fig. 5 Isothermal LITD measurements of the ethyl coverage versus time at three different surface temperatures. The solid lines represent first-order kinetic fits to the data.

The surface ethyl coverage versus time during β -hydride elimination of ethylene was monitored using isothermal C_2H_4 LITD measurements. LITD results at three surface temperatures are shown in Fig. 5. The ethyl coverages are all referenced to θ_s , the saturation ethyl coverage. First-order rate equations of the form $-d\theta/dt = k\theta^2$ were used to fit the isothermal data. An Arrhenius plot of the rate constants obtained from various isothermal LITD experiments yielded an activation barrier of $E_d = 36 \pm 1.5$ kcal/mol and a first-order desorption preexponential of $v_d = 2.7 \times 10^9 \text{ s}^{-1}$ for the β -hydride elimination of ethylene from ethyl groups on Si(111) 7x7.

Recent FTIR studies on high-surface-area porous silicon surfaces have verified the presence of ethyl groups and hydrogen on porous silicon following DES adsorption (7). These FTIR studies have confirmed the β -hydride elimination mechanism. There is also excellent agreement between the FTIR and LITD studies for the kinetics of β -hydride elimination and H_2 desorption.

References

1. S.F. Rickborn, M.A. Ring and H.E. O'Neal, *Int. J. Chem. Kinet.* **16**, 1371 (1984).
2. P. Gupta, C.H. Mak, P.A. Coon and S.M. George, *Phys. Rev. B* **40**, 7739 (1989).
3. P. Gupta, P.A. Coon, B.G. Koehler and S.M. George, *J. Chem. Phys.* **93**, 2827 (1990).
4. P. Gupta, P.A. Coon and S.M. George, in preparation.
5. M.P. D'Evelyn, M.M. Nelson and T. Engel, *Surf. Sci.* **186**, 75 (1987).
6. W.H. Weinberg, in *Kinetics of Interface Reactions*, edited by M. Grunze and H.J. Kreuzer (Springer-Verlag, New York, 1987), p. 94.
7. A.C. Dillon, M.B. Robinson, M.L. Han and S.M. George, in preparation.

The Absorption of 1.17 eV Photons by $\text{Al}_2\text{O}_3(11\bar{2}0)$

M. A. Schildbach and A. V. Hamza

Lawrence Livermore National Laboratory, L-357,
Livermore, California 94550
415-422-3073

Recently, it has been proposed that multiphoton absorption by wide band gap materials is an important mechanism for energy absorption on surfaces ultimately leading to laser-induced surface damage. Many authors have observed non-thermal, photon-stimulated desorption of particles with radiation at energies less than the band gap of the solid material sample.¹ The multiphoton nature of the process was gleaned either from the dependence of the particle yield on photon fluence or by the fact that the single photon energy was insufficient to excite electrons across the band gap. In cases where the number of photons required in the process is large (>3), the assistance of surface or defect states in the band gap has been proposed as the origin of photon absorption or as states that resonantly enhance the multiphoton absorption. However, the surfaces studied have not been sufficiently well-characterized to confirm the proposed mechanism.

We have attempted to discern the mechanism by which the surfaces of transparent materials absorb photons with energies significantly less than the band gap. Sapphire surfaces were chosen for study because of their importance in laser and optics technology, their large bulk-projected band gap, and the low threshold for secondary electron emission which allows the use of electron spectroscopies to characterize the surfaces. Our results for $\text{Al}_2\text{O}_3(11\bar{2}0)$ irradiated with 1.064 μm photons show that absorption by the surface is multiphoton in nature and that there are surface states present in the band gap that may participate in the photon absorption.

The experimental apparatus was an ultra high vacuum chamber with base pressure of 2×10^{-10} torr, equipped with reverse view low energy electron diffraction (LEED) optics and a double-pass cylindrical mirror analyzer (CMA) for surface structure and composition determination. Electron energy loss spectra (ELS) were obtained with the double-pass CMA as well. The 1064 nm, 8 ns output of a Nd:YAG laser was focused to a spot of size of 0.25 mm by 0.75 mm and incident at approximately 70° to the surface normal with the plane of incidence either parallel to the [1100] or the [0001] directions on the $\text{Al}_2\text{O}_3(11\bar{2}0)$ surface.

Time-of-flight (TOF) measurements were made with a quadrupole mass spectrometer using the laser pulse to trigger a transient digitizer with 1 μs per channel resolution. The flight distance from the sample to the ionizer was 25 cm. For increased sensitivity the quadrupole was oriented such that the desorbing flux passed down the centerline of the mass filter. Therefore, the flight time of the particles through the quadrupole was dependent on the velocity of the incident particles. The geometry of the mass filter was used to calculate the flight time of particles in the filter and the calculated flight times were confirmed by TOF measurements with supersonic expansions of helium, nitrogen and argon gas where the incident velocity of the particle was known.

$\text{Al}_2\text{O}_3(11\bar{2}0)$ samples were 0.5 by 0.5 by 0.040 inches. Tantalum strips were mounted between two samples to serve as resistive heaters as described by Chang² and Gignac *et al.*³ The temperature of the surface was monitored by a chromel-alumel thermocouple that was held in contact with the surface by a high temperature ceramic adhesive. The Ta strips were arranged so that the incident laser light could pass through the sapphire. The "as received" samples' only significant surface impurity was carbon. Cleaning of the surface was accomplished by heating to ~1100K and then sputtering the surface with Ar^+ ions to remove the residual carbon contaminant. After sputtering, annealing

to 1200K produced a (1x1) LEED pattern; further annealing to 1500 K produced a (3x1) pattern; and heating to 1700 K produced the equilibrium (12x4) pattern. After sputtering and subsequent annealing the Auger spectra showed no contaminants and a surface stoichiometry of two aluminum atoms to three oxygen atoms.

The (12x4) surface was exposed to a series of laser shots at $\sim 3.5 \text{ J/cm}^2$; the surface properties gradually changed such that after 50,000 pulses the LEED pattern had degraded to the point that fractional order diffraction beams were no longer detectable at any incident electron energy. Changes in the electronic properties of the surface were also observed after photon exposure. The clean and well-annealed surface exhibited stable LEED patterns down to incident electron energies of 80 eV, i.e. surface charging was negligible. Below 80 eV the sample charging caused deflection and defocusing of the diffracted beams, and at 60 eV the surface charged to the point that diffracted beams were no longer detected by the LEED optics. With increasing exposure to $1.064 \mu\text{m}$ photons the threshold electron energy for stable LEED patterns increased. After 50,000 pulses stable patterns could be observed only above 115 eV incident electron energy. Annealing of the laser-degraded surface to 1700 K was sufficient to restore the original (12x4) LEED pattern.

The exposure of the surface to 1.17 eV photons revealed the intimate relationship between atomic and electronic structure of the surface. The surface conductivity increases as the surface structure nears its equilibrium structure. Thus, a plausible explanation for the increased conductivity of the (12x4) surface may be delocalized surface electronic states that facilitate the removal of surface charge. Gignac *et al.*³ have observed a surface electronic state in the bulk band gap at $\sim 4 \text{ eV}$ below the conduction band minimum for $\text{Al}_2\text{O}_3(1102)$ and have suggested that the presence of this delocalized state may enable impinging electrons to flow rapidly away from the point of impact thereby reducing the charging of the surface.

ELS was performed to probe the surface for electronic states in the band gap. Figure 1 shows the EL spectrum for the $\text{Al}_2\text{O}_3(11\bar{2}0)$ -(12x4) surface.

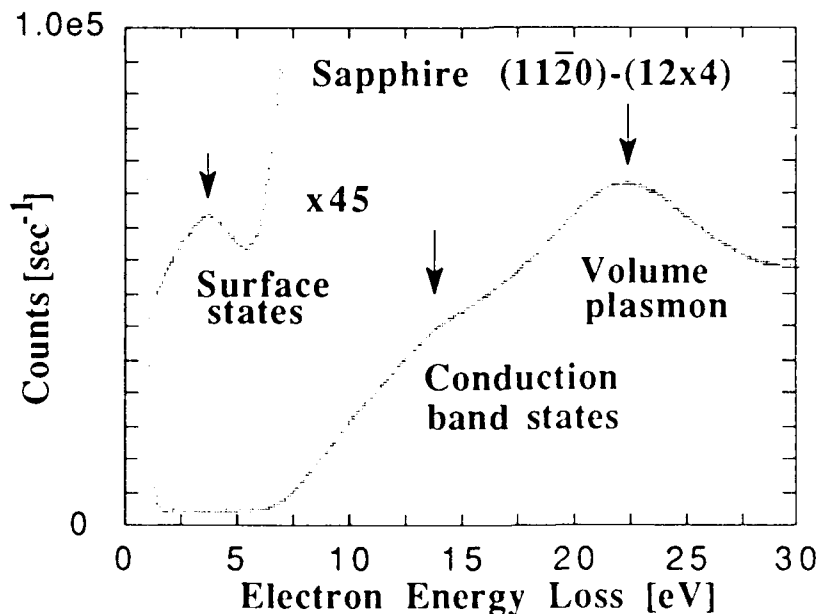


Figure 1. Electron energy loss spectrum for $\text{Al}_2\text{O}_3(11\bar{2}0)$ -(12x4). The 201.5 eV elastic peak registered 1.6×10^6 counts with a full width at half maximum of 0.8 eV. CMA pass energy was 50 eV.

The prominent loss features appear at 22 eV and 14 eV. The 22 eV loss is assigned to the excitation of the sapphire bulk plasmon. The observed energy loss agrees well with previous ELS measurements.^{3,4} The 14 eV loss feature is assigned to interband transitions from the valence band maximum (VBM) to empty states in the conduction band formed from empty aluminum 3s and 3p orbitals based on calculations by Ciraci and Batra.⁵ The enlargement of the bulk-projected band gap region reveals the presence of a broad loss feature in the band gap centered at 3.6 eV. This loss feature is assigned to either a transition from an occupied surface electronic state 3.6 eV below the conduction band minimum (CBM) to the CBM or a transition from the VBM to an unoccupied surface electronic state 3.6 eV above the VBM. Ciraci and Batra³ have also predicted the presence of a surface electronic state 3 eV above the VBM in the bulk-projected band gap for the Al₂O₃(0001) surface due to the s+p_z dangling bonds from the surface Al atoms. The surface state observed here may be derived from these same dangling bonds, since Al atoms on the (1120)-(12x4) surface may not be fully coordinated as well. However, since the loss feature is present in the absolute bulk band gap, surface electronic states are available to participate in a multiphoton absorption and in the conduction of electrons on the surface.

Desorption of aluminum (atoms and ions) was observed for laser fluences just below the visible damage threshold of 12 J/cm² (~10 J/cm²). Aluminum atoms were detected with the quadrupole mass spectrometer. Below the visible damage threshold no other desorbing species were observed. At fluences less than 10 J/cm² no desorbing flux was detectable. At fluences at which visible damage occurred dioxygen and aluminum desorption were observed. The catastrophic damage event was easily detectable because of the pressure burst in the UHV chamber. The characteristics of the particles produced during visible damage are complicated by laser-plume interactions and are not considered further here. Velocity distributions for the desorbing aluminum atoms during the pre-damage events were measured by time-of-flight. A typical time-of-flight distribution for neutral aluminum atoms is shown in figure 2.

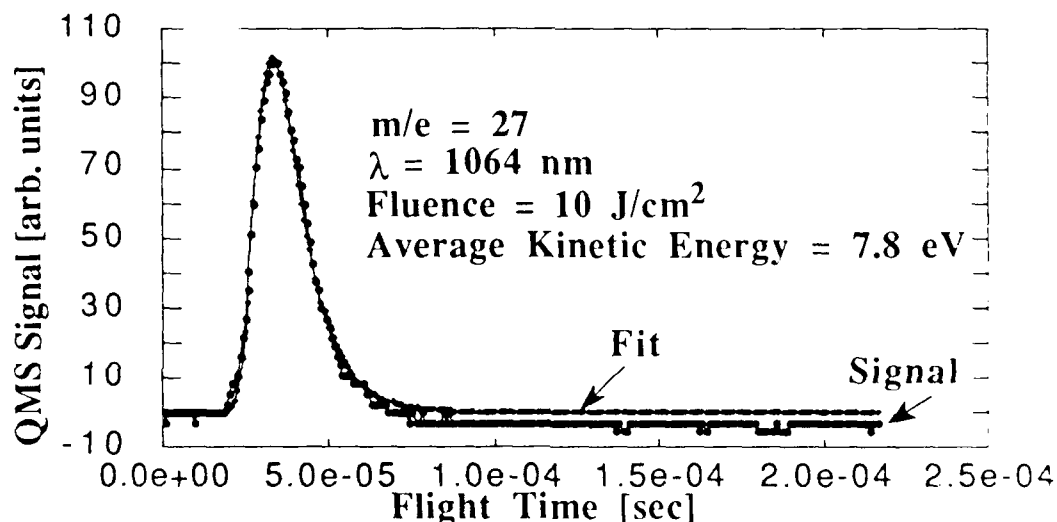


Figure 2. Aluminum time-of-flight distribution. Filled circles represent the quadrupole mass spectrometer signal at m/e=27. Filled diamonds represent the non-linear least squares fit to the data.

The measured time-of-flight distribution is fit to a density time-of-flight distribution, $n(t)$, of the following form:

$$n(t) = A_0 t^{-4} \exp\{-A_1 [(s/t) - A_2]^2\} \quad (\text{eq.1}),$$

where t is the flight time, s is the flight distance, A_0 is a normalization constant, A_1 is a measure of the width of the distribution, and A_2 is the stream velocity. If the stream velocity is zero and $A_1 = (m/2kT)$, where m is the mass of the particle, the velocity distribution would be a Maxwell-Boltzmann distribution at temperature T . The fit function is chosen as a matter of convenience from which to calculate the average velocity, the average kinetic energy, and the average variance. The most striking feature of the TOF distributions is the high kinetic energy of the desorbing aluminum. The second striking feature is the shot-to-shot stability of the TOF distribution. The average kinetic energy of the desorbing Al is 7.8 ± 0.4 eV for single laser shot distribution and 10 shot averaged distributions. The high average kinetic energy is indicative of a non-thermal desorption mechanism and, since the incident photon energy is only 1.17 eV, is also indicative of a multiphoton absorption process. Clues to the desorption mechanism can be gleaned from three main observations. First, only aluminum atoms (or ions) are desorbed; second, the kinetic energy of the desorbing aluminum is ~ 8 eV and is steady in the narrow range of fluences from $10-12$ J/cm²; and third, surface electronic states in the bulk-projected band gap are observed.

Desorption of particles with ~ 8 eV of energy requires a surface excitation of at least 8 eV. Sapphire exhibits an exciton that is bound by approximately 1 eV^{6,7} and since the band gap of sapphire is ~ 9 eV, the exciton lies ~ 8 eV above the valence band maximum. Decay of the exciton would yield up to 8 eV of energy. In addition the exciton is localized on the aluminum atom and no oxygen centered excitons have been observed for sapphire^{4,6}, which is consistent with the desorption of predominantly aluminum particles. Thus, exciton decay at aluminum atoms at the surface could lead to the observed desorption energies of ~ 8 eV. Since the unaided absorption of seven 1.17 eV photons to excite the exciton is unlikely, the presence of surface electronic states in the band gap to resonantly enhance the absorption of photons makes the desorption mechanism plausible. If occupied, the surface electronic states could also be the origin of the photoabsorption, thereby reducing the number of photons required to produce the exciton.

This work was performed under the auspices of the Division of Material Sciences, Office of Basic Energy Sciences, U. S. Department of Energy, by Lawrence Livermore National Laboratory under contract No. W-7405-ENG-48.

REFERENCES

1. E Matthias, H. B. Nielsen, J. Reif, A. Rosen, and E. Westin, *Journal of Vacuum Science and Technology B* **5** (1987) 1415 and references therein.
2. C. C. Chang, *Journal of Vacuum Science and Technology*, **8** (1971) 500.
3. W. J. Gignac, R. S. Williams, and S. P. Kowalczyk, *Physical Review B* **32** (1985) 1237.
4. J. Olivier and R. Poirier, *Surface Science* **105** (1981) 347.
5. S. Ciraci and I. P. Batra, *Physical Review B* **28** (1983) 982.
6. A. Balzarotti, F. Antonangeli, R. Girlanda, and G. Martino, *Solid State Communications*, **44** (1982) 275.
7. I. A. Brytov and Y. N. Romashchenko, *Sov. Phys. Solid State* **20** (1978) 384.

Photon-Induced Desorption of Adsorbed Water Clusters

J. Dirks, W. Drachsel, and J.H. Block

Fritz-Haber-Institute of the Max-Planck-Gesellschaft

D-W-1000 Berlin 33, Federal Republic of Germany

Phone / Fax: + 30 8305 438 / 520

INTRODUCTION

High electric fields of the order of several V/nm influence the adsorption- and desorption-processes of molecules [1]. Because photons are not effected by an electric field, they are suitable for investigating the underlying excitation mechanisms in the presence of such high electric fields. The effect of the external field on the adsorption and desorption processes should be particularly distinct if a polar adsorbate (e.g. water) is used. Therefore, experiments with synchrotron light were carried out with field emitters exposed to water vapor.

EXPERIMENTAL SET-UP

The measurements were performed using synchrotron radiation from DESY storage ring with an energy between 6 and 30 eV. The metal field emitter tips (Ag, Ni, Rh) were etched electrochemically using standard etching procedures [1]. Triply distilled water was continuously dosed into the UHV-chamber at a background pressure of $5 \cdot 10^{-11}$ mbar. The experimental set-up, shown in fig. 1, consisted of a field ion microscope, where the tip to screen distance also served as the flight path for the time-of-flight analysis [2].

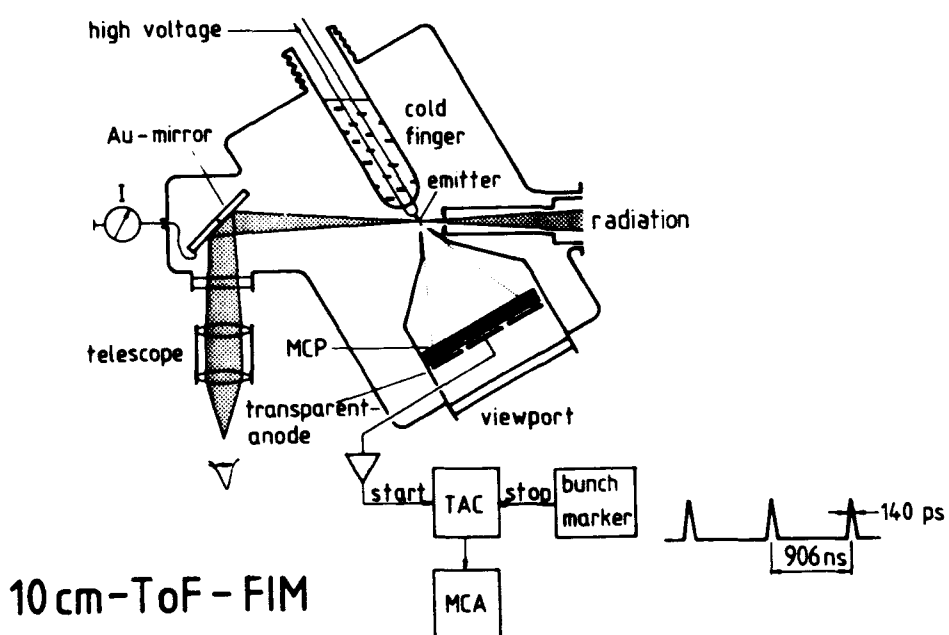


Fig. 1: Experimental set-up of the 10 cm time-of-flight field ion microscope

The light was focused onto the emitter tip. Because of the high repetition frequency of the synchrotron light, the flight time of the ions was measured in the reverse mode. The light intensity was monitored via the photo current of a gold-mirror and the desorption spectra were collected for at least 300 s.

RESULTS AND DISCUSSION

At a water pressure of 10^{-10} mbar and a surface temperature of 54 K, a submonolayer coverage of water is established on the emitter surface. In this case the spectra showed only a small amount of H_3O^+ and $(\text{H}_2\text{O})_2\cdot\text{H}^+$ ions. The occurrence of the latter ion indicated that even at this surface coverage the formation of dimers takes place on the surface. Increasing the dosing pressure to 10^{-8} mbar leads to the desorption of protonated water clusters $(\text{H}_2\text{O})_n\cdot\text{H}^+$, $n = 1, \dots, 15$, as can be seen in fig. 2.

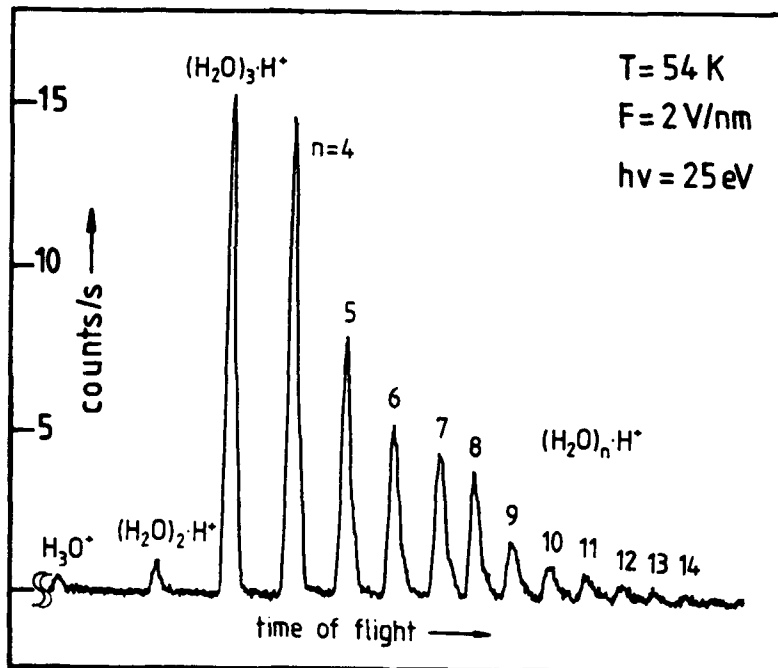


Fig. 2: Time-of-flight mass spectrum from a water covered Ag field emitter.

To investigate the underlying excitation, the photon energy was varied. We found that the desorption yield showed a steep onset at a photon energy of 7.1 eV for a field strength of 2 V/nm. This onset value was found to be independent of substrate material, water dosing pressure, and ion cluster size and shifted with increasing field strength towards lower threshold energy. The extrapolated value of 7.4 eV for zero field strength corresponds to the main absorption band of super-cooled water as discussed in ref. [3] and is attributed to an electronic excitation in the adsorbate due to a one-photon-excitation. This view was further confirmed in our experiments by the linear dependence of the desorption yield on the photon energy. Our experiments showed clearly that an external

electric field of several V/nm can significantly influence the energy levels of electronic states similar to the well known Stark-effect.

The measurements of the cluster distribution as a function of the substrate temperature showed that with increasing temperature the total ion yield decreased by nearly three orders of magnitude. This is explained by the enhanced thermal field desorption rate which results in a depletion of surface coverage at higher temperatures. However, above a surface temperature of 120 K the formation of larger clusters is much more favoured. The energy barrier for translational transport of a water molecule on the surface was found to be 9 meV. This value is significantly lower than diffusion barriers for the field free case (100 meV, [4]). Above 160 K no cluster ion formation is observed because of the decrease in the surface coverage.

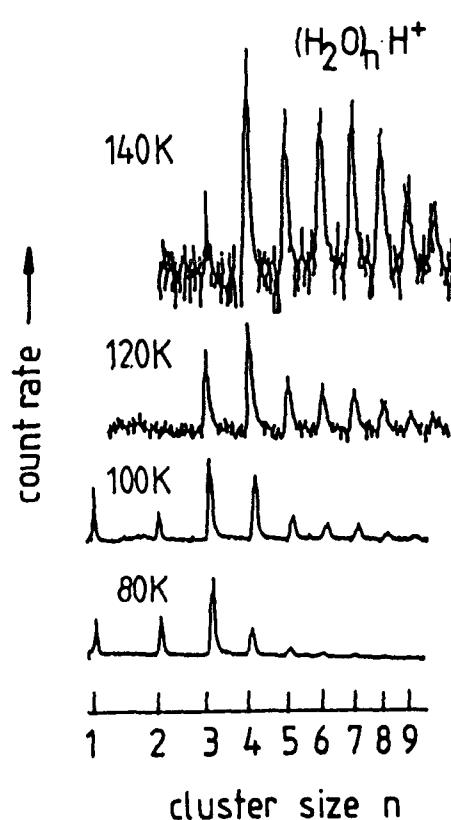


Fig. 3: ToF-MS for different surface temperatures. Yields normalized for the trimer.

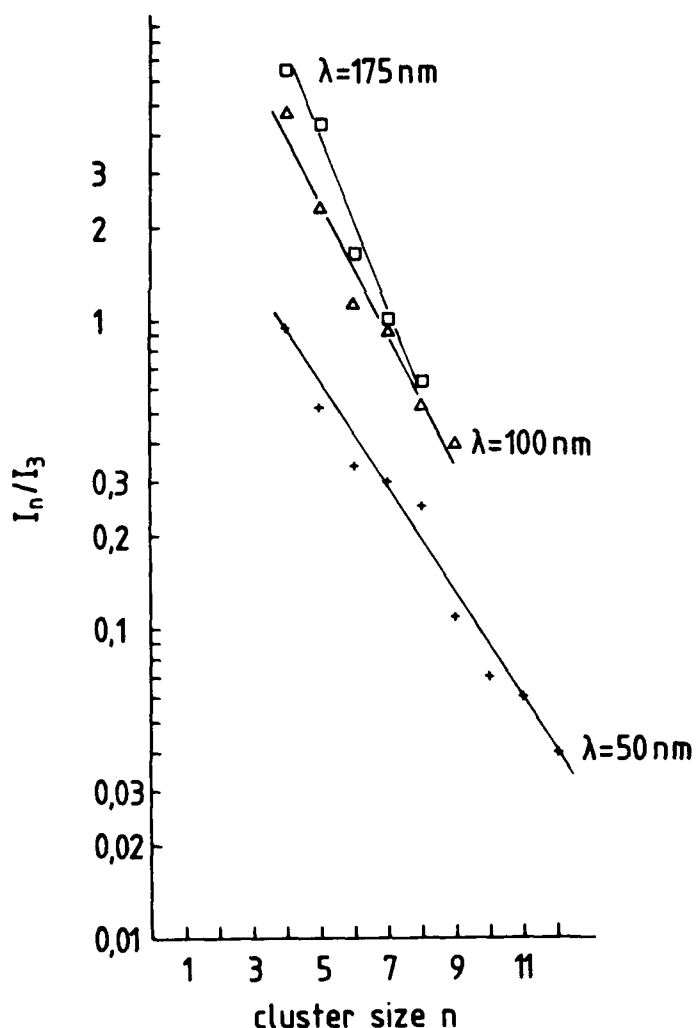
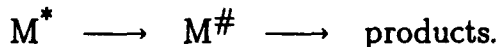


Fig. 4: Normalized cluster distribution at different photon energies.

The photon-induced desorption of water clusters is a rather complicated process. A general theory, applicable for this type of reaction was developed by Rice, Ramsperger, and Kassel (RRK) [5]. In the RRK-theory, the decomposition of the excited complex M^* proceeds via an activated state $M^\#$ according to the reaction:



In comparing this reaction scheme with our case, the electronic excitation in the adsorbate delivers the impact energy and leads to the excited complex M^* . After the redistribution of the impact energy into vibrational energy, localized in a subsystem of water molecules represented by $M^\#$, an ion complex is ejected. One consequence of the RRK-theory is that with increasing impact energy the yield of fragments in which more bonds have to be broken increases. This behaviour can be seen from fig. 4. A quantitative analysis of the experimental data reveals that the average impact energy per hydrogen bond at the threshold photon energy is 82 meV for a two-dimensional structure and 51 meV for a three-dimensional structure. As predicted by theory, these values increase with increasing photon energy. Both values agree well with a value for the H_2O / Cu system of 71 meV (2-dim.) obtained by Christiansen et al. [6].

In summary, the photon induced desorption of water clusters $(H_2O)_n \cdot H^+$ from different metal field emitters (Ag, Ni, Rh) exposed to water vapor can be understood as an emission of protonated water clusters. The clusters occur due to transfer of the impact energy to vibrational modes of the adsorbate. The RRK-theory give a good description of the experimental results.

REFERENCES

- [1] N. Ernst and G. Ehrlich; in *Topics in Current Physics* 40 (1986) 75
- [2] W. Drachsel, U. Weigmann, S. Jaenicke, and J. H. Block; in *Desorption Induced by Electronic Transitions DIET II*; W. Brenig and D. Menzel (eds.), Springer, Heidelberg (1985) 245
- [3] L. Painter, R. D. Birkhoff, and E. T. Arakawa; J. Chem. Phys. 51 (1969) 243
- [4] P. A. Thiel and T. E. Madey; Surf. Sci. Rep. 7 (1987) 211
- [5] O. K. Rice and H. C. Ramsperger; J. Am. Chem. Soc. 50 (1928) 617; L. S. Kassel; J. Phys. Chem. 32 (1928) 225
- [6] J. W. Christiansen and J. T. Tsong; J. Chem. Phys. 86 (1987) 4701

Tuesday, February 12, 1991

Processing and Applications

TuC 9:00pm-10:00pm
Anasazi South

Richard M. Osgood, *Presider*
Columbia University



Laser-Induced Deposition of Amorphous Silicon:
Relations between Chemical Processing and Performance

Peter Hess

Institute of Physical Chemistry, University of Heidelberg
Im Neuenheimer Feld 253, D-6900 Heidelberg, Germany
Tel: 6221/565205, Fax: 6221/563199

Hydrogenated, amorphous silicon (a-Si:H) is of great interest for thin film devices used, for example, for the transformation of photon energy and as semiconductor material. Important applications are thin film solar cells, thin film transistors for liquid crystal displays, photoreceptors for electrophotography and laser printing and image sensors. To improve and optimize the properties of the material for specific applications it is necessary to control the formation of the three dimensional network during the solidification process ("bandgap engineering"). Incorporation of hydrogen into the network reduces the density of defects near the middle of the bandgap ("gap states"). For optimal performance a specific binding configuration should be realized. Distortions in the metastable silicon network, especially in the bond angle, are believed to be responsible for the tail states at the bandgap edges. Since these defect states constitute traps for charge carriers and thus lower their mobilities it is necessary to reduce the density of these states. To achieve an efficient control of the deposition process in this direction, detailed molecular information on the dynamic processes leading to solidification and on the structure-performance relationship is needed.

Information on the processes occurring on the molecular scale can be obtained by a series of diagnostic techniques. This includes *in situ* detection of the gas phase chemistry employing a mass spectrometer and identification of surface species using IR spectroscopy. Results obtained for model systems such as single crystals are of great interest in elucidating the complicated reaction processes taking place at the surface. Important contributions can also be expected from STM and AFM techniques delivering pictures of real sur-

faces with atomic and molecular resolution. The performance of the deposited films is studied by measuring the optical, electrical, mechanical and chemical properties of the deposited material. The final goal is the development of a realistic model describing not only the transport processes, but also the reaction processes occurring in the gas phase and at the surface. In fact, such a model and detailed understanding is needed to select the deposition parameters and to control the deposition process.

The results obtained so far for the laser-induced deposition of a-Si:H from SiH_4 and Si_2H_6 as precursors employing cw CO_2 lasers and pulsed excimer lasers in parallel laser beam surface configuration will be reviewed. The processes occurring in the flow reactor under parallel illumination, where the laser radiation directly excites or heats only the gase above the surface, are far from equilibrium. Thus, the processes taking place in the gas phase e.g. the primary and secondary chemical reactions and the processes occurring at the surface determining the film structure and composition may be synergistic. The parallel configuration is ideal for studying the relationships between chemical pathways and functional structures. The progress made recently in this direction will be discussed in detail.

Deposition of a-Si:H with cw CO_2 lasers allows the soft growth of films via the lowest energy pathways of chemical transformation. For this simplest case a detailed model is available describing the gas phase chemistry and the interaction of active species with the surface. Important relations between laser-induced chemistry, growth rate and film properties can be detected by *in situ* and *ex situ* techniques. Details on the surface chemistry are derived from spectroscopic measurements and the analysis of well defined surfaces.

Chemical processing with UV photons gives access to higher energy channels and a manifold of reactive species. Some of these species modify the self-organization at the surface leading to the most stable surface structures and networks. This means that highly metastable structures near the limit of thermodynamic instability can be approached. In the case of a-Si:H the films processed under such energized conditions possess a superior performance. The chemical principles underlying these findings will be discussed.

CW laser induced chemical reactions with integrated circuits.

Geoffroy AUVERT

Centre National d'Etudes des Télécommunications
BP 98 - 38243 Meylan, France.

By focussing a CW laser on the surface of an integrated circuit, the temperature can be locally increased if the laser wavelength is adsorbed by the silicon of the circuit [1]. This is the case when using visible or UV wavelengths. When turning on the laser beam power, the laser induced temperature increases and reaches an equilibrium temperature in less than a tenth of a microsecond for a one micron laser spot diameter [2]. The equilibrium temperature strongly depends on the optical and thermal properties of the irradiated area and is lower when irradiating a metal, which has high lateral heat losses and high reflectivity, than a semiconductor, which has low thermal conductivity and low reflectivity.

Moreover, by using high power CW lasers, this temperature can be sufficiently high to induce a chemical reaction at or around the irradiated area. For example, at 1000°C, the silicon-silicon dioxide interface is unstable and volatile silicon mono-oxide molecules are produced leading to the cutting of the irradiated poly-silicon line [3]. By irradiating an aluminum line, a chemical reaction occurs at the aluminum melting temperature between the melt aluminum and the surrounding silicon oxide. This reaction leads to the formation of volatile compounds, namely silicon and aluminum mono-oxide, which evaporate from the hot zone. As aluminum is consumed, this chemical reaction leads to the cutting of the aluminum interconnection. In the same way, most interconnections used in integrated circuits can be cut allowing easy change of the electrical configuration of the circuit.

Another family of chemical reactions can be induced by a CW laser beam on an integrated circuit by placing the circuit in a chemical chamber. A circuit image is produced on a video screen as in a conventional microscope. The laser beam passing through the high

magnification objective is focussed on the surface of the circuit and appears as a bright spot on the video screen. After pumping the chamber at 10^{-3} Torr, it can be filled at a fixed pressure with a reactive gas. The laser beam power is then adjusted to an appropriate one and the laser spot is displaced on the surface of the circuit in order to draw one or several lines. Usually, the chemical reaction induced by the CW laser beam is a pyrolytic reaction and in the experimental set-up, the laser induced temperature at the window level must be kept low enough to avoid a reaction on the window surface. This is achieved by placing the window of the chemical chamber as far as possible from the circuit, where the laser beam is more than ten times wider than on the circuit surface [1].

When the reactive gas interacts in the high temperature area with the insulator layer of the circuit, an etching of this layer can be performed allowing the vias to be opened on top of a connection [4]. Using fluoride gas, silicon dioxide has been etched and vias above a refractory metal such as tungsten have been obtained. The chemical reactions of this family take place at temperatures above 1000°C and cannot be used to open vias above aluminum lines. For this underlying material, an etching reaction will be useful if it can take place at temperatures below 600°C.

When using nickel carbonyl molecules, the CW laser interaction with an integrated circuit leads to the deposition of nickel [5,6]. The thermal decomposition reaction of the molecules leads to the formation of the volatile CO molecule, leaving nickel atoms in the hot zone. The reaction takes place when using infrared (10.6 μm), visible (0.5 μm) or UV wavelengths (0.33 μm) and the deposition rate, which is independent of the gas pressure, is limited by a thermally activated process of about 12 eV. The limiting step seems to be the desorption of CO from the nickel surface. At a pressure below 0.4 Torr, a mass transport limited process occurs and the deposition rate is only determined by the number of carbonyl molecules impinging on the hot zone with a decomposition yield of 60%. The feasibility of nickel lines as narrow as 1.3 μm has been demonstrated and the deposited thickness is inversely proportional to the laser scan speed which can be as fast as 0.4 mm/s. Theoretically, the highest deposition rate for this compound is around 2 mm/s.

By reducing WF₆ molecules with hydrogen in the hot zone of a laser spot, deposition of nearly pure tungsten can be performed [7]. The chemical reaction occurring is complex and the nature of the limiting step depends on the hydrogen pressure used. At high pressure, the deposition rate varies as the square root of the hydrogen pressure and the corresponding limiting step is the dissociation reaction of the hydrogen molecules adsorbed on the tungsten surface. The highest deposition rate at 1400°C is about 2µm/s. At low hydrogen pressure, the tungsten deposition rate varies linearly with the hydrogen pressure and the limiting step seems to be the collisions of hydrogen molecules with the adsorbed species on the tungsten surface.

In order to draw a complex scheme of the interconnects on integrated circuit, it might be necessary to locally deposit an insulator. To day, this problem is being seriously studied, but does not seem to be completely solved. A possible chemical reaction is the oxidation of silicon when using a mixture of silane and N₂O. Unfortunately, in the hot zone, only silane mono-oxide molecules are formed and no deposition occurs in the laser spot area. This molecule diffuses around the laser spot, redeposits and is re-oxidized. Therefore, a silicon dioxide deposit is formed around the spot and extends as far as 50 µm. In order to use such a wide deposit, vias have to be opened and complex new interconnections can be drawn.

By using pyrolytic chemical reactions, induced by a CW laser beam in integrated circuits, existing connections can be interrupted and new connections can be performed. This technique allows us to rapidly change the electrical function and is of great interest for prototype repair and personalisation of circuits. As CW laser beams can be focussed just under one micron, this technique can be used in present day chip fabrication.

- 1- G.Auvert, Applied Surface Science 43 (1989) p.47.
- 2- D.Tonneau, G.Auvert, Mat. Res. Soc. Symp. Proc. Vol.101 (1988) p.131.
- 3- G.Auvert, Proc. European Conf. on "Gravure seche" Ed. Societe Francaise du vide, Paris, 233 sup.(1986) p.135.
- 4- D.Tonneau, G.Auvert, Y.Pauleau, Journal de Physique,n5, T50, (1989) p.C5-637.
- 5- D.Tonneau, Y.Pauleau, G.Auvert, J. Appl. Phys. 64 (1988) p.5189.
- 6- D.Tonneau, Y.Pauleau, G.Auvert, J. Appl. Phys. 66 (1989) p.165.
- 7- G.Auvert,Y.Pauleau, D.Tonneau, Mat.Res. Soc.Symp. Proc. V. 158 (1989) p.155.
- 8- G.Auvert, In "Reduced Thermal Processing for ULSI" Ed. R.Levy, (Plenum Pub. Corp. 1989) p.227.

Wednesday, February 13, 1991

Structure and Deposition of Metal Overlayers

WA 8:00am–9:40am
Anasazi South

Thor Rhodin, *Presider*
Cornell University



**STM studies on the growth and structure of thin metallic films
on metal substrates**

R.J.Behm

Institut für Kristallographie und Mineralogie, Univ. München
Theresienstr. 41, D-8000 München 2, Fed. Rep. Germany

The structure and growth of thin, epitaxially grown metal films vapor-deposited on metallic substrates have been studied by a variety of integrating techniques over many years [1]. On the theoretical side detailed predictions exist on both the structure and growth of these films, which were derived from considerations of the lattice mismatch between the respective materials and from their thermodynamical properties [2,3]. The verification of these predictions, however, requires an exact knowledge of the local structure and the topography of these films which was accessible only indirectly from these data. Scanning tunneling microscopy (STM) studies can provide direct information on these properties due to the local nature of the measurement which will be demonstrated in different examples.

In the interface region the lattice must transform from the that of the substrate to the bulk lattice of the deposited material. This occurs in a more or less gradual transition between subsequent layers. The misfit between the respective lattices can lead to the formation of complex superstructures in the different film layers [2]. This has already been

verified by diffraction methods [1,2] and by electron microscopy [4]. STM observations give direct access to structural details of these 'reconstructions', as was demonstrated recently for Cu/Ru(0001) [5] and Au/Ru(0001) [6]. In the first case a uni-directional contraction of the second adlayer leads to a structure very much like that of the reconstructed Au(111) surface [7-9]. In the latter system the larger Au atoms are accommodated in a uni-directionally expanded structure. In this case, the transition occurs already in the first adlayer. The STM measurements could also resolve characteristic local defects in the periodic structure of the film, which are formed due to kinetic limitations and dissolve upon annealing. These metastable structures can hardly be detected by integrating methods because of their very low density [5].

The characterization of the two- and three-dimensional film growth by STM is particularly informative and allows direct comparison with theoretical predictions [3,10]. This is demonstrated for the growth of a thin Au film on a Ru(0001) substrate [11]. Upon deposition at room temperature Au atoms are preferentially condensed at step edges, i.e. heterogeneous nucleation at step edges prevails. On sufficiently large terraces Au islands of one monolayer thickness are also nucleated in the middle of the terraces. Both types of islands exhibit a strongly dendritic shape which is consistent with the diffusion limited aggregation model of Witten and Sander and implies a reduced mobility of Au atoms along the edges of

the islands [12]. The two-dimensional growth of these islands with increasing coverage and the collapse of their dendritic shape upon annealing could also be observed by STM.

The transition from two-dimensional to three-dimensional growth is initiated by the nucleation of second layer islands on top of first-layer Au areas. STM measurements on Au/Ru(0001) show that in this case the onset of second and high layer nucleation depends strongly on the deposition temperature and that higher layers can be removed by annealing [11]. These observations demonstrate that the coexistence of several Au layers at nominal coverages of 1-2 monolayers results from kinetic effects and that under thermodynamically controlled conditions Au films grow layer by layer at least up to two layers on this substrate.

These and other already published examples demonstrate that STM studies provide detailed information on the microscopic structures and processes that occur during deposition of thin metal films on metallic substrates.

References

- 1] E. Bauer, *Applic. Surface Sci.* 11/12, 479 (1982).
- 2] E. Bauer and J.H. van der Merwe, *Phys. Rev. B* 33, 3657 (1986).
- 3] E. Bauer, *Z. Krist.* 110, 372 (1958).
- 4] K. Yagi, K. Tobayashi, Y. Tanishiro, and T. Takanayagi, *Thin Solid Films*, 126, 95 (1985).
- 5] G.O. Pötschke and R.J. Behm, *Phys. Rev. B* (subm.).
- 6] J. Schröder, C. Günther, R.Q. Hwang, and R.J. Behm, to be publ.
- 7] U. Harten, A.M. Lahee, J.P. Tönnies, and C. Wöll, *Phys. Rev. Lett.* 54, 2619 (1985).
- 8] C. Wöll, S. Chiang, R.J. Wilson, and P.H. Lippel, *Phys. Rev. B* 39, 7988 (1989).
- 9] J.V. Barth, H. Brune, G. Ertl and R.J. Behm, *Phys. Rev. B* (in press).
- 10] S. Stoyanov and I. Markov, *Surface Sci.* 116, 313 (1982).
- 11] J. Schröder, C. Günther, R.Q. Hwang, and R.J. Behm, *Surface Sci.* (subm.).
- 12] T.A. Witten and L.M. Sander, *Phys. Rev. B* 27, 5686 (1983).

PHOTOCHEMICAL PRODUCTION OF METALLIC GALLIUM ON CLEAVED GaAs SURFACES: TIME-RESOLVED MEASUREMENTS USING LASER AND SYNCHROTRON RADIATION

S. S. Goldenberg, J. P. Long, M. N. Kabler

Code 4686

Naval Research Laboratory

Washington, D. C. 20375

Phone: (202) 767-4654

1. Introduction

In the course of investigations of electronic processes on laser excited semiconductor surfaces cleaved in ultrahigh vacuum, we have discovered the accumulation of Ga islands on GaAs (110) induced by laser pulse fluences far below those previously reported for irreversible surface modification.¹ We have characterized these islands by core and valence photoelectron spectroscopy and by scanning electron microscopy. The photoemission spectra show a satellite of lower binding energy in the Ga 3d spectra which grows along with a metallic edge in the band gap. Because the Ga islands can be produced at fluences as low as 1 mJ/cm², for which the lattice temperature rise is insignificant, as described below, it is evident that a photochemical decomposition of the GaAs surface is occurring.

2. Experiment

The experiments were performed at the National Synchrotron Light Source on the NRL soft x-ray beam line. Full instrumental details appear elsewhere². A copper vapor laser was operated at 510 nm and 6 kHz, a repetition rate which facilitated the accumulation of measurable Ga in relatively short times at low intensities. For this work, optical feedback added to the laser cavity³ produced 5-ns pulses, and a dichroic splitter suppressed the 578-nm laser line. Degenerately doped n- and p-type GaAs single-crystal bars were potted with indium into a water cooled block and were cleaved *in situ*. Angle integrated photoelectron spectra were obtained with a commercial double-pass cylindrical mirror analyzer. Selected laser exposed samples were examined in a standard scanning electron microscope (SEM) after transfer in air.

3. Results and Discussion

Figure 1 shows photoelectron energy distribution curves (EDC's) of the Ga 3d core level from an n-type sample just after cleavage and the growth of the low-binding-energy satellite for progressively larger laser doses at a constant fluence of 3 mJ/cm².

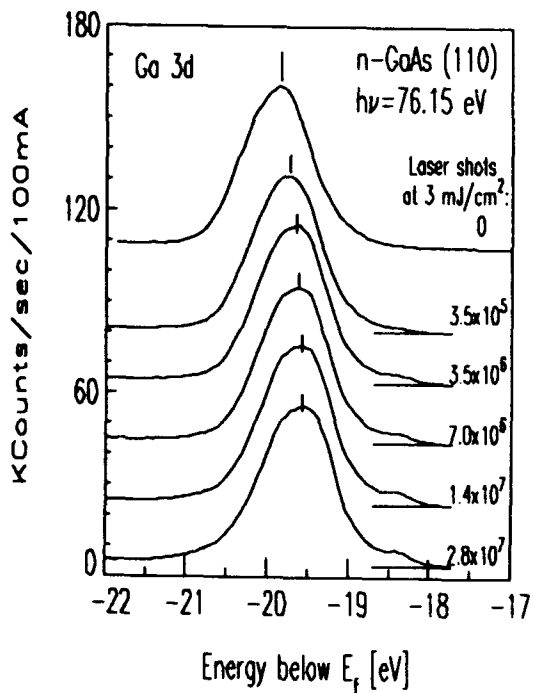


Fig. 1 EDC's showing the evolution of the Ga 3d line with laser exposure.

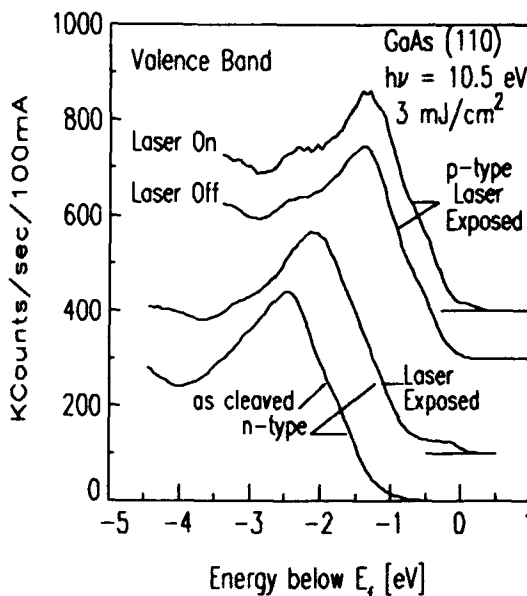


Fig. 2 Valence band EDC's showing metallic states from Ga islands on laser exposed surfaces. See text for explanation of p-type spectra.

Associated with the satellite are new states in the band gap which appear in the valence band spectrum, taken with $h\nu=10.5$ eV, seen in Fig. 2. As seen in Fig. 1, an increase in band bending accompanies laser exposure. Also evident is a characteristic decrease of growth rate of the island signal with exposure. Detailed measurements show that even though the growth rate decreases, the area occupied by Ga islands does not appear to saturate.

Metallic Ga on GaAs, whether created directly by evaporation⁴ or indirectly through either a replacement reaction with evaporated Al,⁵ or thermal decomposition,⁶ is known to form islands on the surface. The binding energy of the satellite in Fig. 1, which we measure explicitly as the energy difference between the satellite and the gold Fermi level, is 18.4 eV. This agrees well with the value of 18.4 ± 0.2 eV inferred by Skeath for metallic Ga evaporated on GaAs.⁵ The presence of islands at least several monolayers thick is inferred from escape depth arguments applied to core spectra. A quantitative analysis of Fig. 3, which compares Ga 3d EDC's spectra taken with ~ 6 Å and > 20 Å escape depths,⁷ yields an island thickness slightly larger than the escape depth of the 6-eV photoelectrons. Because the islands are thick, it follows that their fractional areal coverage may be determined from the relative intensities of satellite and substrate lines. Thus exposure to $\sim 10^7$ laser pulses at 3 mJ/cm² typically yields several percent areal coverage by islands.

An order-of-magnitude estimate of the efficiency with which laser exposure creates free Ga can be made by comparing our spectra to those of Cao, taken from surfaces on which calibrated amounts of

Ga were evaporated.⁴ The similarity of our spectra to Cao's for a 0.3 monolayer deposition gives a yield of 1 Ga atom per 10^8 incident laser photons. Note that this represents an initial yield, since as mentioned above, the rate of island growth falls off with laser exposure.

The presence of thick islands containing a total volume of metallic Ga consistent with the above yield (to within an order of magnitude) is supported by an initial analysis of SEM micrographs of a region exposed to 6 mJ/cm^2 . The Ga metal is organized in linear chains comprised of hemispheres several hundred angstroms in diameter. The chains are reminiscent of the 'ripples' widely reported in laser damage studies of metals and semiconductors conducted at much larger laser fluences.⁸ Indeed, the chains are aligned parallel to the optical electric field and the interchain spacing distribution function peaks near $\lambda/(1+\sin\theta)$,⁹ where λ and θ are the laser wavelength and angle of incidence, respectively, for the one angle so far studied. The pattern which the Ga hemispheres assume on the surface evidently depends on a variety of factors, since exposures at normal incidence to 15 mJ/cm^2 created a more uniform distribution, without obvious chains.

The creation of free Ga must occur through a process in which temperature plays, at most, an assisting role. The heating of the GaAs rods due to the average power of the laser pulse train has been measured with thermocouples. 3 mJ/cm^2 fluence gives a 10°C rise. At this fluence the instantaneous rise during the laser pulse is 30°C , determined with a numerical code which includes the temperature dependence of the material parameters.⁹ Scaling linearly to $\sim 1 \text{ mJ/cm}^2$, the smallest fluence for which islands have been observed, gives a maximum total temperature rise of only 13°C . This is small enough to rule out a thermal process. For comparison, total photoyield spectroscopy with $h\nu$ scanned through threshold, a technique especially sensitive to defect states, detects no spectral changes until temperatures reach 325°C .⁶

The island growth rate is superlinear in laser fluence. For example, for the same integrated dose of 1.3 kJ/cm^2 , no Ga islands are seen for exposure to 0.7 mJ/cm^2 fluence, but are readily observed for 7 mJ/cm^2 . Note, however, that the dose with the weaker fluence is sufficient to alter details in both the Ga and As 3d core spectra, most likely by disrupting surface order and hence introducing band bending.

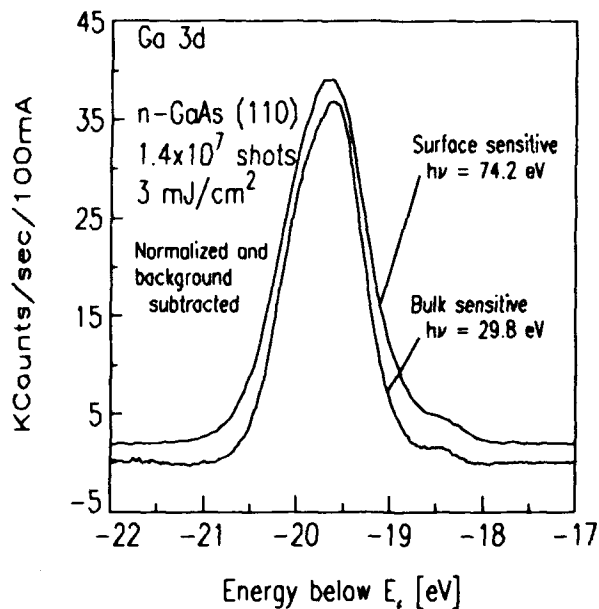


Fig. 3 Ga 3d core from laser saturated surface taken with bulk and surface sensitivity.

inhomogeneities.

Ga islands also form on p-type, but they are more difficult to observe. This is because both the metallic gap signal and the metallic Ga core level tend to be obscured by substrate valence and core emission, respectively, due to Fermi-level position and laser creation and filling of charged slow states which take up to 20 minutes to decay. However, by temporally overlapping synchrotron and laser pulses and recording time resolved spectra, we were able to observe metallic Ga on p-type. During the laser pulse, photoexcited carriers reduce band bending,¹⁰ and in particular even out inhomogeneously bent bands. This has the effect of moving the metallic features, beneath which the band bending is larger than the substrate regions, out to greater kinetic energies relative to the substrate, where they are more easily observed. The effect is demonstrated in Fig. 2, where metallic emission in the gap is observed during the laser pulse for a laser exposed p-type surface. Similar results are observed in the Ga 3d spectra. The duty-factor mismatch between laser and synchrotron pulse rates precludes such experiments except when the ring is operated in single bunch mode.

Quantitative comparison between n- and p-type island growth kinetics await detailed line fitting, which is underway. Preliminary comparisons suggest roughly comparable growth rates. Since the bands are nearly flat during the laser pulse, electrons and holes produced in the bulk by the laser have roughly equivalent access to the surface for n- and p-type. Thus the comparable growth rates for n- and p-type cannot be used to rule out a photochemical process involving bulk carriers.

4. References

1. B. Danielzik, P. Harten, T. Seeger, D. von der Linde, *Appl. Phys. Lett* **53**, 816 (88); T. Nakayama, M. Okigawa, N. Itoh, *Nucl. Intr. Methods* **B1**, 301 (84)
2. J. P. Long, *Nucl. Instr. Methods* **A266**, 673 (88).
3. Metalaser Technology, Inc., Pleasanton, CA, USA.
4. R. Cao, Dissertation, Dept. of E.E., Stanford Univ. (89).
5. P. Skeath, I. Lindau, P. Pianetta, P.W. Chye, C.Y. Su, W.E. Spicer, *J. Electr. Spectr.* **17**, 259 (79).
6. F. Proix, A. Akremi, Z.T. Zhung, *J. Phys. C* **16**, 5449 (83).
7. H. Gant, W. Mönch, *Surf. Sci.* **105**, 217 (81).
8. H. M. van Driel, J. E. Sipe, Jeff F. Young, *Phys. Rev. Lett.* **49**, 1955 (82).
9. Jerry Meyer, private communication.
10. J.P. Long, H.R. Sadeghi, J.C. Rife, M.N. Kabler, *Phys. Rev. Lett.* **64**, 1158 (90).

Fast In-Situ Metallization: A Comparison of Several Methods
with Possible Applications in High Density Multichip Interconnects

Marcel Widmer, Patrik Hoffmann, Baudouin Lecohier,
Herbert Solka, Jean-Michel Philippoz, Hubert van den Bergh

Laboratoire de Chimie Technique
Ecole Polytechnique Federale de Lausanne
CH-1015 Lausanne, Switzerland

Some recent results obtained using three quite different experimental approaches to fast in-situ surface metallization are presented. One of the goals is to make high density interconnects for multichip modules with metal contact width, height and pitch respectively of the order of 10, 5 and 25 μm . Direct writing speeds should be in excess of 1 cm/s. The first approach tried is to push classical pyrolytic laser chemical vapor deposition of copper from its bis-hexafluoroacetylacetone Cu(hfa)_2 to its limits. This is done by increasing the Cu(hfa)_2 vapor pressure and by seeding the transparent surface of our substrate with a thin layer of a strongly light-absorbing substance. Speeds in the order of a few mm/s have already been obtained with good electrical properties and adhesion. The second approach tested implies metallization by thermal in-situ decomposition of a metal complex layer on a surface with a laser beam. The precursors used in this work are metal cluster coordination complexes, in particular $\text{Au}_{55}(\text{P}\Phi_3)_{12}\text{Cl}_6$ (Φ stands for phenyl group $-\text{C}_6\text{H}_5$). Such molecules have a high metal content and advantageous thermal decomposition properties which enable writing speeds in excess of 1 cm/s while maintaining acceptable electrical properties of the metal lines. Finally, in a third approach, the fast in-situ step is limited to deposition of a thin metal line on the surface. These lines of only a few \AA height are then "developed" in a second step to much high (of the order of one μm) and better conducting metal lines. This second step may be relatively slow, as many devices which have been patterned on their surface with the thin metal "prenucleation" lines can subsequently be developed simultaneously in a parallel processing step. An example of this approach is surface seeding using

metals like Pt, W or Ir, followed by development by either selective low pressure CVD of copper from Cu(hfa)_2 , selective decomposition of a copper formate solid surface film, or selective electroless deposition from a copper bath. Possibilities of processing with much higher resolution using focussed charged particle beams are also briefly discussed.

Metal-Semiconductor Contacts: Surface Morphology and BEEM

R. Ludeke, M. Prietsch and A. Samsavar

IBM T.J. Watson Research Center,

P.O. Box 218, Yorktown Heights, N.Y. 10598. (914/945-2591)

Ballistic Electron Emission Spectroscopy (BEEM) is a promising new variant of STM spectroscopy that allows the determination of Schottky barrier heights with high lateral resolution for relatively thick ($\approx 100 \text{ \AA}$) metal overlayers.^{1,2} The technique encompasses the injection of electrons or holes with an STM, which then reach the interface without scattering (ballistically). At the interface they will be reflected unless sufficient bias is applied between the tunneling tip and the metal overlayer to overcome the Schottky barrier height (see Fig. 1). Once the electrons reach the conduction band of the semiconductor they will be detected as a collector current I_c . Representative I_c vs V_t , where V_t is the tip-to-metal bias, are shown in Fig. 2 for Ag and Au films on GaP(110). The Schottky barrier height is associated with the voltage threshold V_0 beyond which a current can be detected. Because of the "soft" turn on of I_c , V_0 is poorly defined unless the appropriate shape of the I-V curve is known from theoretical considerations. The imaging of the variations in I_c as a function of lateral position is referred to as a BEEM image, and has been associated with variations in Schottky barrier heights across the interface.^{1,3} We will show here that another and perhaps more dominant source of contrast in BEEM images is the surface topography, as surface gradients may result in current injections that reach the interface at angles substantially off-normal, a condition which drastically reduces the collector current intensities. The current variations in Fig. 2 are attributed to such variations in the injection angles. In order to quantify this notion we have also developed a model for the interface transport that includes non-classical transmission across the metal-semiconductor interface, as well as off-normal angles of incidence. An outline of these concepts will be presented here, as well as a quantitative comparison of the the model with topographic and BEEM data for several metals on GaP(110).

We have recently developed an UHV STM system with BEEM capability that includes provisions for cleavage, metal depositions and transfer to the STM chamber in UHV.⁴ Virgin n-type GaP(110) surfaces were prepared by cleaving a pre-notched $<110>$ oriented bar. Metal dots, 2 mm in diameter, were evaporated through a mask. Their thickness ranged from 30-200 \AA . Thus far we have investigated Au, Ag, Cu, Ni, Mg and Bi. After transfer to the STM, a Au contact wire was positioned with Burleigh Inchworms® onto the metal dot in order to apply the tip bias for BEEM I-V spectroscopy. I-V spectra were typically taken over a predetermined rectangular grid pattern consisting of 4x4 points across the surface. The following general observation were made: 1. threshold voltages varied negligibly ($\pm 0.01 \text{ V}$) across the sample surface for any given metal, although they varied by as much as 0.39 V between Mg and Au; 2. strong intensity variations were observed at different locations across the surface for all metals except Mg and Bi (Fig. 2); 3. current intensity fluctuations were frequently observed, as shown in Fig. 2a; and 4. intensity variations were correlated with topographic surface gradients, the steeper the gradient the smaller the observed collector current.

The physical origin of these current variations may be understood from an appropriate model of the injected current transport from the tunneling tip through the metal film and across the metal-semiconductor interface. The collector current density can be expressed by the following integral:

$$j_c = K \int_{E_{\min}}^{\infty} dE_x D(E_x) \int_{E_0}^{E_{\max}} dE_t f(E_x, E_t) T(E_x, E_t) E_0(E_{\max}, E_t) A(E_x, E_t) \quad (1)$$

The integration is over the energy variables with momentum vectors normal (E_x) and transverse (E_t) to the metal surface. The integration limits are given by $E_{\min} = E_F - e(V - V_o)$, $E_{\max} = r_m(E_x - E_{\min})$ and $E_\theta = \frac{1}{2}(eV + E_x) \sin^2\theta$, where V represents the applied tip-to-metal voltage, V_o the conduction threshold voltage (barrier height), E_F the Fermi energy of the metal tip relative to the bottom of its free-electron-like conduction band, and r_m the reduced electron mass ratio: $r_m = m_e/(m_e - m_s)$. $D(E_x)$ is the transmission factor for tunneling through the vacuum barrier and is assumed to be represented by planar tunneling theory over a rectangular barrier.⁵ $f(E_x, E_t)$ is the Fermi function and $\Lambda(E_x, E_t)$ is the probability that an electron traverses the metal film without scattering; we assume here that Λ is energy independent near threshold, and that any current reduction in the metal film is included in the scaling factor K . $F_\theta(E_{\max}, E_t) = (E_{\max} - E_t)^{1/2}/E_t^{1/2}$ and represents a coordinate transformation for off-normal angles of incidence.⁴ $T(E_x, E_t)$ is the quantum mechanical transmission across a one-dimensional potential step, and is proportional to $(1 - V_o/V)^{1/2}$ above V_o . Integration of eq. (1) leads to a power series, which in the vicinity of the threshold and to lowest order terms is:

$$j_c \propto \frac{(eV - eV_o)^{5/2}}{(E_F + eV_o)^{1/2}} - \frac{\sin |\theta|}{r_m^{1/2}} (eV - eV_o)^2 \quad (2)$$

Equation (2) predicts a 5/2 power law dependence of the current near threshold, which differs from the previously proposed "square" law dependence² by the 1/2 power contained in the transmission coefficient $T(E_x, E_t)$. Values of Schottky barrier heights from fits of eq. (2) to the experimental data are: 1.02 (Mg), 1.06 (Ni), 1.11 (Bi), 1.22 (Cu), 1.26 (Ag) and 1.41 eV (Au). Eq. (2) furthermore predicts a reduction of j_c for off-normal angles of incidence $\theta > 0$. Finite values of θ could arise during tunnel current injection as the tip scans over an area of the surface that is inclined relative to the interface plane. The injected electrons traverse the metal film ballistically and approach the interface at an angle that deviates on average from normal incidence by the inclination angle of the surface area at the point of injection. From our topographic images we have determined that for Ni, Cu, Ag and Au films grown on GaP(110), surface gradients corresponding to angles in the 5-10° range are commonplace. Examples of fits of BEEM I-V spectra with eq. (2) are shown in Fig. 2 as solid lines. For the Au case, the 8° fitted value corresponds well with the ≈ 10 ° value determined from the topographic images at the point of measurement. Such a reduction in j_c would manifest itself as a change of contrast in a BEEM image. These observations imply a new and dominant mechanism of image contrast due to surface topography for metals on GaP, as the variations in Schottky barrier heights, the previously acclaimed source of image contrast,^{2,3} is negligible for the six metals on n-type GaP(110) studied thus far by us. A clear manifestation of this contrast mechanism is shown in Fig. 3 for a 60 Å Mg film on GaP(110). All three images correspond to a 600×400 Å² area. The top image is the standard topography, with a contrast scale of 12 Å (white corresponds to high points). Image (b) is the computed gradient image of (a) with a contrast scale of 0-30%, with white representing the highest gradients observed at the grain boundaries. Curve (c) is the simultaneously acquired BEEM image, with a contrast scale based on collector current variations of 8-24 pA. Clearly there is an exact pattern match between the white regions of highest gradient in (b), and the dark areas of lowest collector current in (c). Finally, we would like to comment on the frequently observed current fluctuations, such as those shown in Fig. 2a. Their origin we attribute to drift during data acquisition (typically 30 sec) as the tip either samples different surface gradients, or changes its injection geometry, that is, different tip protrusions assume the tunneling process. It should be mentioned that the fluctuations can both increase and decrease in intensity, sometimes returning to the I-V trajectory followed prior to the fluctuations. In all cases the individual segments of a fluctuating I-V curve can be fitted by just varying θ in eq. (2), as was done for the fit of curve (a) in Fig. 2.

In conclusion, BEEM image contrast is largely derived from the surface topography of the metal, which may be the sole source for metal-semiconductor systems that do not exhibit posi-

tion dependent Schottky barriers, such as the metals on GaP(110) discussed here. Another potential image contrast source is roughness at the metal-semiconductor interface, which may arise from strongly reacting and intermixing components. Such a source has not yet been identified. I-V curves calculated with a new model that assumes an energy dependent transmission coefficient across the metal-semiconductor interface, as well as average off-normal angles of incidence of the injected electrons reaching the interface, agree well with experimental observations for several metals on n-type GaP(110) surfaces.

REFERENCES

1. W.J. Kaiser and L.D. Bell, Phys. Rev. Lett. **60**, 1406 (1988).
2. L.D. Bell and W.J. Kaiser, Phys. Rev. Lett. **61**, 2368 (1988).
3. A.E. Fowell, R.H. Williams, B.E. Richardson and T.H. Shen, Semicond. Sci. Technol. **5**, 348 (1990).
4. M. Prietsch and R. Ludeke, to be published.
5. E.L. Wolf, **Principles of Electron Tunneling Spectroscopy** (Oxford NY 1985) Ch. 2.

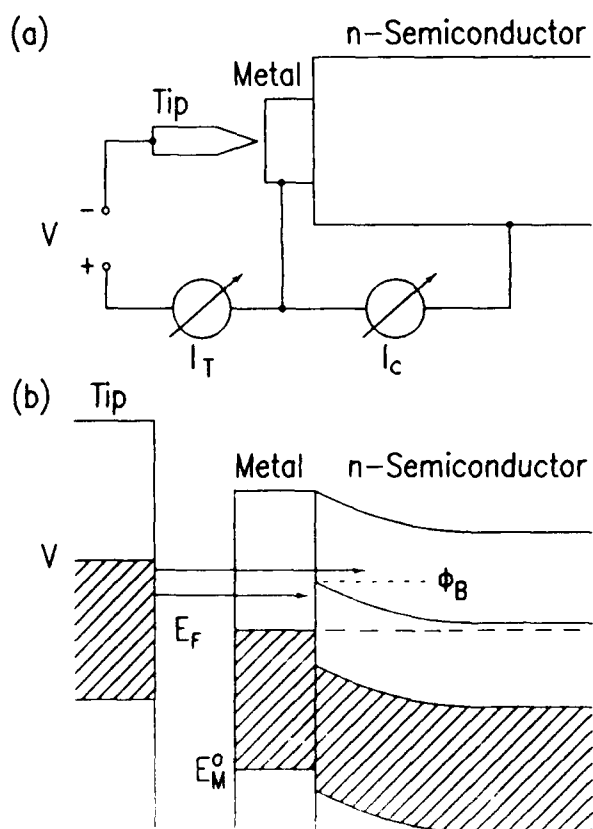


Fig. 1. Schematic view (a) and energy diagram (b) of a BEEM experiment. E_M^0 marks the bottom of the conduction band of the metal, E_F is the Fermi energy and ϕ_B is the Schottky barrier height.

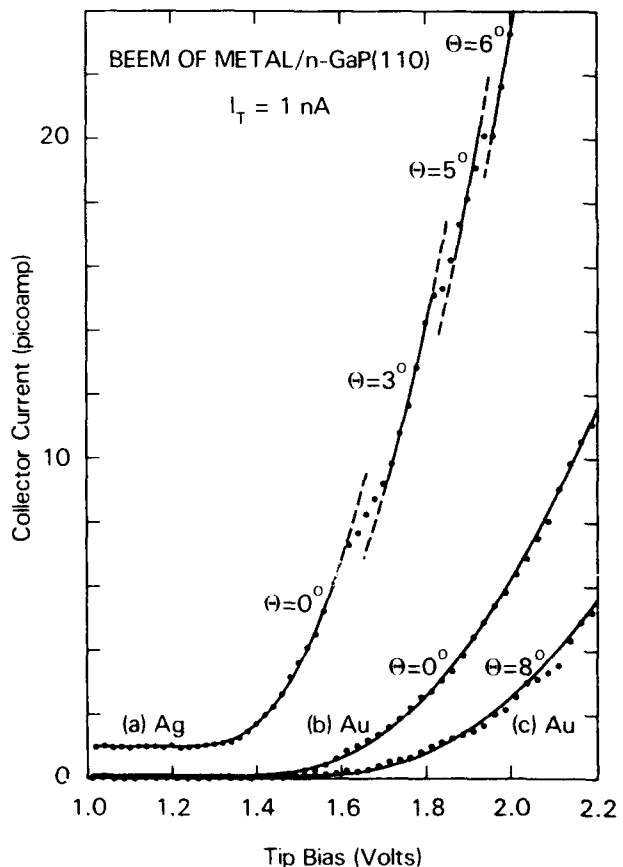


Fig. 2. Frequently observed current fluctuations in BEEM I-V spectra (dots) and their fits (lines) through variation of θ in eq. (2) for: (a) 200 Å Ag film, (b) and (c): 120 Å Au film.

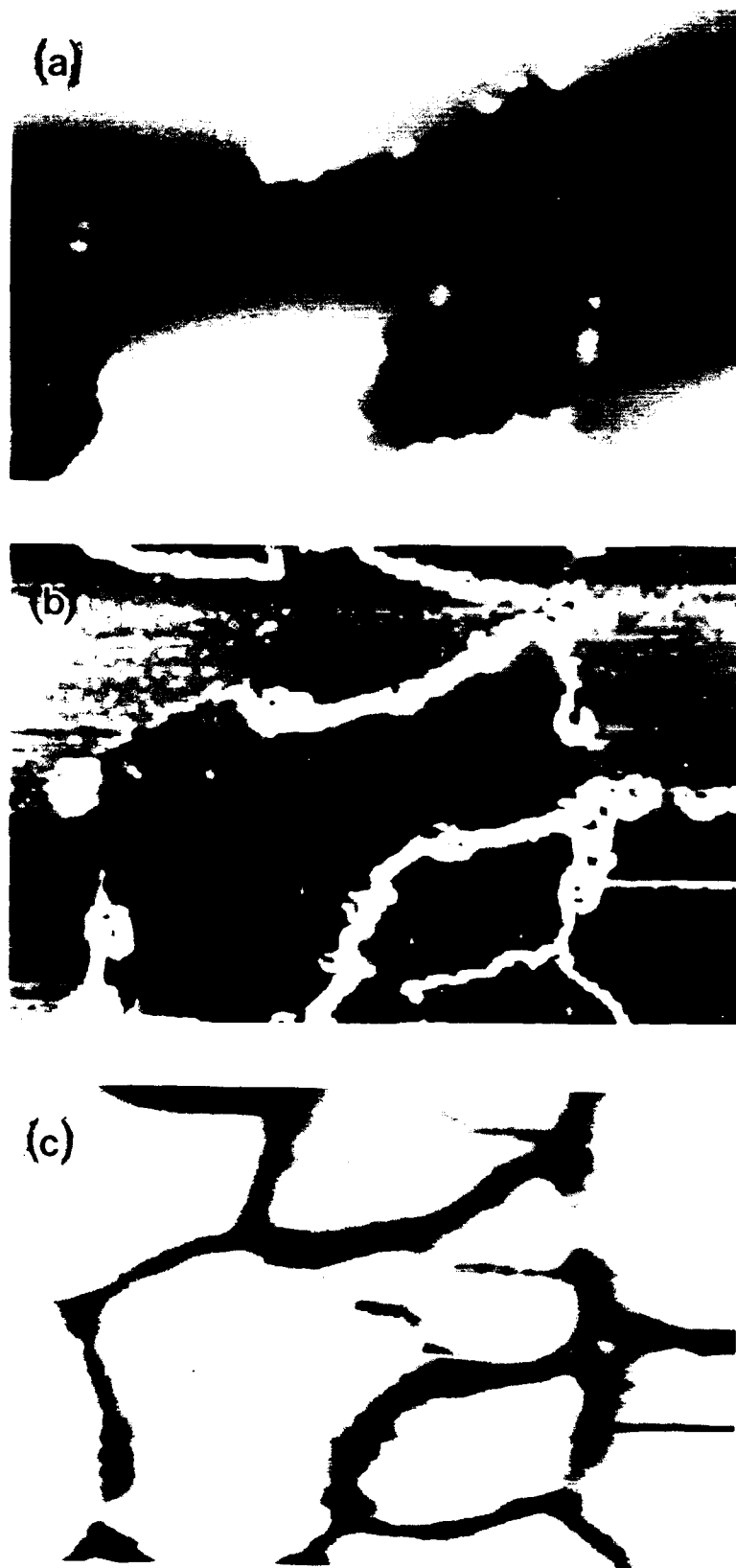


Fig. 3. 60 Å Mg film on GaP(110): (a) topographic image of $600 \times 400 \text{ \AA}^2$ area, (b) gradient image of (a), and (c) simultaneously collected BIELM image. $V = 2.5$ volt, tip current $I_t = 1 \text{ nA}$. Black-white contrast scale: (a) 12 Å, (b) 0-30%, (c) 8-28 pA.

Wednesday, February 13, 1991

Surface Modification and Analysis

WB 10:00am-11:20am
Anasazi South

M. Hirose, *Presider*
Hiroshima University, Japan



Chemical Imaging of Surfaces Using the Surface Analysis by Laser Ionization (SALI) Technique

Lorenza Moro, Istituto per la Ricerca Scientifica e Tecnologica, I 38050 Trento/Povo, Italy

Simon P. Mouncey, Dept. of Physics, Queens University of Belfast, Belfast, Northern Ireland BT6 0DG

Christopher H. Becker, Molecular Physics Laboratory, SRI International, Menlo Park, CA 94025, USA, telephone (415) 859-5130

The determination of the lateral distributions of chemical species on surfaces is of constantly increasing technological importance in many applications, such as integrated circuit manufacturing. The only two tools which have been available are scanning Auger electron spectroscopy (AES) and secondary ion mass spectrometry (SIMS) (in scanning or microscope modes). The AES technique is the most widespread but generally is considered to be of lesser sensitivity than SIMS, at least for spatial resolutions (defined by the primary beam diameter, d) of approximately $\geq 0.1 \mu\text{m}$. Nominal sensitivities for AES are ~2 to 3% concentrations for $d \geq 1 \mu\text{m}$, and 3 to 10 % for d ranging from $1.0 \mu\text{m}$ to $0.1 \mu\text{m}$, respectively.¹ Also, scanning AES can be very problematic for insulators and electron sensitive materials, although it undoubtedly will continue to be a major tool.

The sensitivities for SIMS are extremely variable, depending on both the species of interest and the local chemical matrix (so-called matrix effects). Quantitation is very problematic because of matrix effects and because on the microchemical scale associated with chemical imaging the notion of closely matched reference materials is essentially irrelevant. In the microscope mode, SIMS spatial resolutions are generally limited to about $1\mu\text{m}$. In the scanning mode, liquid metal ion guns (notably Ga^+) have been used with some success but are somewhat unsatisfactory because these guns are not effective for increasing secondary ion yields. The sensitivity for scanning SIMS can range, for example, from 0.01% to 10% at $d = 1\mu\text{m}$, and 1% to undetectable at $d = 0.1\mu\text{m}$.¹

By examining the sputtered neutral particles (the majority channel) using nonselective photoionization and time-of-flight mass spectrometry (TOF-MS), SALI generates a relatively uniform sensitivity with semiquantitative raw data.² Estimates for sensitivities as a function of lateral spatial resolution for a commercial liquid metal (Ga^+) ion gun range, for example, from approximately 5% for $d=0.1\mu\text{m}$ to 0.4% for $d=1.0\mu\text{m}$. These numbers, as above, are nominal values assuming reasonable data acquisition times.

The main criticism SALI has faced concerns data acquisition times. Because pulsed lasers are used and these have limited repetition rates the data acquisition rates are likewise limited. Below it is shown that this is not an overriding concern because even with the 100 Hz laser used, reasonable data acquisition times are achieved, and of course, data is recorded for all masses simultaneously owing to the mass multiplex advantage of TOF-MS.

Several laser manufacturers now sell excimer lasers operating above 500 Hz.

These initial experiments were performed on an existing SALI apparatus using a FEI Co. Ga^+ ion gun for sputtering and an excimer laser operating at 248 nm focused to approximately 10^{10} W/cm^2 running at 100 Hz. The Ga^+ ion gun has a changeable internal aperture which for this initial work was chosen to give $d = 1.0 \mu\text{m}$. The ion beam was at 20 keV at 60° incidence from normal. The Ga^+ beam can be pulsed with pulse widths well below $1 \mu\text{s}$, but for the initial imaging work the beam was operated in a dc mode. Data was collected in analog fashion using a transient digitizer operating at 100 MHz. Future work will use a Ga^+ beam diameters $\leq 0.2 \mu\text{m}$ and digital data collection with a multistop time-to-digital converter.

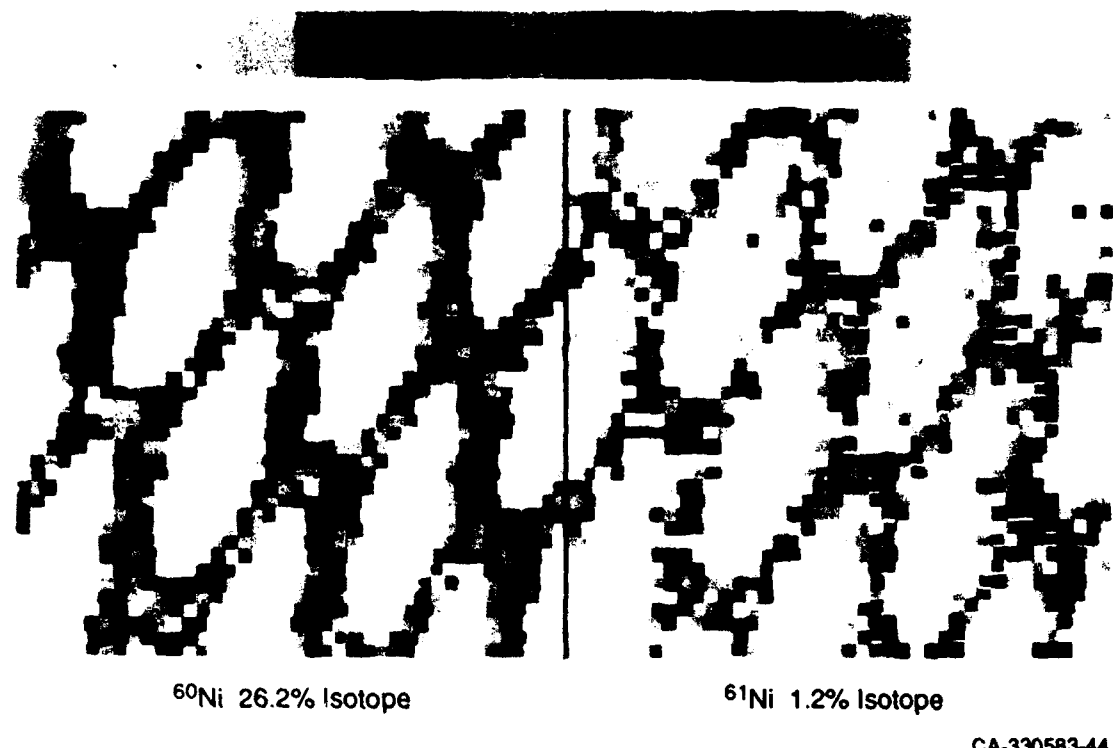
Figure 1 shows images taken of a TEM grid made of Ni with $6 \mu\text{m}$ wide bars. The color scale is linear with normalization for each mass. The skewing of the grid pattern in this figure is due to the angle of mounting of the grid and the angle of incidence of the Ga^+ beam. The data was taken in approximately 20 minutes, with 50 mass spectra (50 laser pulses) summed for each picture element, or "pixel." All of the Ni isotopes of course were recorded, and the ^{61}Ni isotope (1.2% abundance) shown demonstrates the dynamic range in the measurement. The sensitivity for this SALI measurement would be equivalent if the grid were made, for example, from Al, Cu, or Au--unlike for a SIMS measurement.

Figure 2 is an image taken from a test integrated circuit (IC) in the vicinity of an Al contact pad that is $140 \mu\text{m}$ across, showing a larger field of view than for Figure 1. The acquisition time was also about 20 minutes. The IC was earlier briefly dipped in HF acid to remove a passivation layer over the entire circuit. This resulted in partial fluorination of the surrounding SiO_2 . Note that the detection of small molecules in addition to elements provides additional chemical bonding information.

Further work beyond these initial experiments will be required to define the limits of sensitivity, lateral and depth resolutions, and degree of quantitation. However, this initial work clearly demonstrates the viability of using SALI for chemical imaging on a fine scale.

¹ D. G. Welkie, S. Daisser, and C. H. Becker, Vacuum (1990), in press.

² C. H. Becker, J. Vac. Sci. Technol. A5, 1181 (1987).



CA-330583-44

Figure 1. Chemical images of a Ni TEM grid with 6 μ m wide bars using Ga^+ sputtering and photoionization of the emitted neutrals at 248 nm.
Acquisition time approximately 20 minutes.

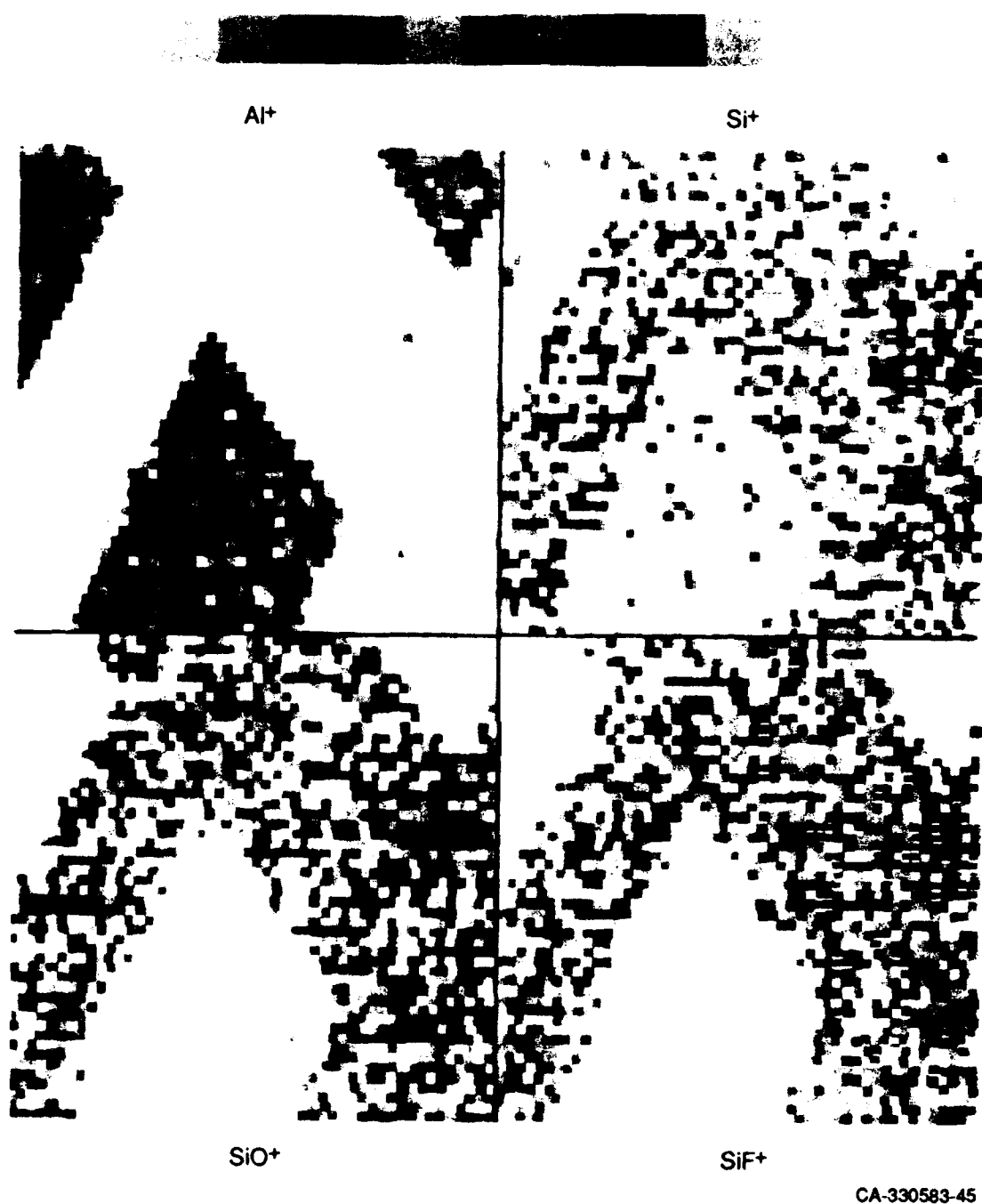


Figure 2. Chemical images from a test integrated circuit showing a 140 μm -wide aluminum contact pad.

The sample had been etched in HF acid resulting in partial silicon fluorination.
Sputtering with Ga^+ and 248 nm photoionization.

CA-330583-45

Rotationally Anisotropic Second-Harmonic Generation Studies of the Structure and Thermal Stability of Cu(110)

Mark A. Hoffbauer, Victoria J. McVeigh, and Michael J. Zuerlein
 Chemical and Laser Sciences Division, MS-G738
 Los Alamos National Laboratory
 Los Alamos, New Mexico 87545
 (505) 667-4878

The microscopic structure and thermal stability of interfaces are of fundamental importance in determining a variety of materials properties. Order-disorder transitions on surfaces have recently received considerable attention in the scientific literature since the dynamics of such processes can impose fundamental limits on material performance at elevated temperatures. Many high-index (11n) faces (where n>2) of single-crystal metal surfaces are known to undergo this type of phase-transition. By definition, roughening of an atomically clean surface consists of the proliferation of atomic steps by thermal means at a roughening temperature, T_R , where the surface free energy for creation of a step becomes zero. An unresolved question of fundamental importance is whether the roughening temperature of a low-index (110) surface can be lower than the bulk crystal melting temperature. For high index faces, a less stringent definition of roughening involving the proliferation of kinks on the already present step rows that can meander randomly has been suggested. The energy required for creation of a kink atom is lower than that required for generation of a step atom, thus roughening at temperatures lower than the bulk melting temperature can occur for stepped surfaces as opposed to low-index surfaces. Indeed, it has been shown both theoretically and experimentally that high-index faces of Cu, Ni, and other metals undergo roughening transitions well below the bulk melting temperatures.¹

Recent x-ray scattering data² suggest that the Cu(110) surface undergoes a distinct thermal roughening transition at temperatures above ~600 K. A sharp decrease in the scattered x-ray intensity above ~600 K was attributed to the migration of steps on the surface that form randomly shaped islands. However, an energy-resolved He-atom scattering experiment³ very recently found no evidence for the proliferation of steps up to 900 K. While the He-scattered intensity falls rapidly above ~550 K as in the x-ray scattering experiments, an increase in the number of surface steps that would be manifest by a broadening in the angular distribution of the He-atom beam was not observed. The results suggest that, rather than Cu(110) undergoing an order-disorder transition, the surface has an increased vibrational anharmonicity above ~550 K due to an anomalous increase in the mean-square displacement of the surface atoms.

Our experiments have examined the thermal behavior of Cu(110) using rotationally azimuthal surface second-harmonic generation (SHG). Owing to the inherent surface specificity of SHG, details regarding the temperature dependent surface structure and symmetry can be measured and changes in surface structure that occur on the picosecond time scale as a result of laser induced melting and recrystallization can be followed.^{4,5} It was anticipated from theoretical⁶ considerations that the rotational anisotropy from a Cu(110) surface with C_{2v} symmetry should have contributions predominantly from two-fold symmetry elements in the surface second-order nonlinear susceptibility tensor. However, it was not known if changes in the rotationally anisotropic surface SH intensity would be observed as the surface temperature increased that could be correlated with presumed thermally induced changes in the surface structure.¹⁻³

A UHV surface science chamber (base pressure $<2 \times 10^{-10}$ torr) equipped with instruments for making AES, LEED, and surface SHG measurements was used. A Cu(110) single crystal was mounted on a manipulator system that allowed heating to 1000 K and cooling to ~170 K. The Cu surface was cleaned by Ar^+ sputtering followed by annealing in UHV at 875 K. The surface was always checked for impurities using AES prior to SHG measurements and a sharp LEED pattern was confirmed. LEED measurements allowed a direct determination of the absolute surface azimuthal orientation to within $\pm 3^\circ$. SHG measurements were made using a 10 Hz pulsed

Nd:YAG laser at 1064 nm that provided ~10 nsec wide pulses with energies on the Cu surface of ~10 mJ. The laser was focussed to a spot size of ~3 mm in diameter at an incident angle of ~68°. The calculated laser-induced surface heating ⁷ was <30°C. Either p- or s-laser input polarization was selected and no polarization selection of the SH output signal was performed since the s-polarized signal is a factor of ~30 smaller than the predominantly p-polarized SH signal.⁸ The 532 nm SH output was separated from the fundamental with filters and detected using a photomultiplier tube. Typically, the SH signal was detected as the substrate was rotated over a fixed range of azimuthal angles (approximately -110° to 100° with respect to the rows of Cu surface atoms) with the substrate temperature held constant. Prior to measurements of the rotationally anisotropic SH intensity, the linear reflectivity at 532 nm was measured over the same range of angles and found to be constant to within 2%.

The SH intensity at fixed azimuthal angles of 0° and ~75° was measured as a function of the surface temperature. The projections of the input laser polarization relative to the azimuthal angles of the Cu(110) substrate correspond to 0° for p-polarization along the rows of Cu surface atoms in the [110] direction and ±90° for p-polarization across the rows in the [001] direction. A smooth nearly linear decrease in the SH intensity is observed at 0° azimuthal angle up to ~500 K after which the SH intensity starts to decrease rapidly with increasing temperature. This behavior very closely matches both the x-ray scattered intensity ² and the He-scattered intensity ³ as functions of surface temperature. At an azimuthal angle of ~75° a linear decrease in the SH intensity is observed up to ~700 K above which the SH intensity stops decreasing and remains constant. The observed temperature dependent behavior is completely reversible as the surface temperature is ramped up and down. Extensive checks were performed to see if the possibility of impurities segregating from the bulk could affect the SH signals and none were found.

In Figure 1 the rotationally anisotropic SH intensity as a function of substrate azimuthal angle at eight different fixed surface temperatures is shown. At the lower temperatures a large degree of anisotropy in the SH intensity is observed with a distinct minimum near 0° and a maximum at ±90°. The solid lines in Figure 1 are theoretical fits ⁶ to the data using an expression for the SH intensity as a function of the azimuthal angle, ϕ , of the form $I_{SH} = (A + B \cos(2\phi) + C \cos(4\phi))^2$ where the coefficients A, B, and C represent the isotropic, 2-fold anisotropic, and 4-fold anisotropic susceptibility elements for the Cu(110) surface. The rotationally azimuthal SH intensity shown in Figure 1 undergoes a rather dramatic decrease with increasing surface temperature. For the 177 K surface a very pronounced anisotropic two-fold SH response is observed superimposed on an isotropic background where B/A = -0.32 and C ~ 0. At 765 K, the anisotropy has nearly vanished (B/A = -0.085). Such a pronounced decrease in the anisotropic coefficients would be expected if the two-fold symmetry of the Cu(110) surface disappeared due to thermally induced "roughening" effects.

In a separate experiment, the clean Cu(110) surface held at 300 K was sputtered using 3.0 keV Ar⁺ (five minutes at ~20 mA). LEED measurements performed following sputtering indicated a very diffuse background with almost no evidence of surface order. The rotationally anisotropic SH response at 300 K was measured under identical conditions to those described above and found to be nearly identical to the data shown in Figure 1 at 765 K (i.e. B/A = -0.071). This result implies that the deliberately disordered sputtered Cu surface and the Cu(110) surface at 765 K have a similar overall SH response. This would be expected if a thermally induced surface phase transition occurred resulting in a significant degree of surface disorder.

To understand these results it is worth noting some differences intrinsic in the experimental techniques employed. First, consider the interaction times inherent in surface structural probes based on x-ray scattering ², He-atom scattering ³, and the present study using surface SHG. X-ray scattering predominantly involves the interaction of incident x-rays with the core electrons of near surface atoms. Such an interaction can be viewed as an instantaneous event involving an interaction time of <10⁻¹⁵ sec. Optical SHG involves the scattering of an incident photon from either the free or interband electrons of the surface atoms. The interaction time involved can again

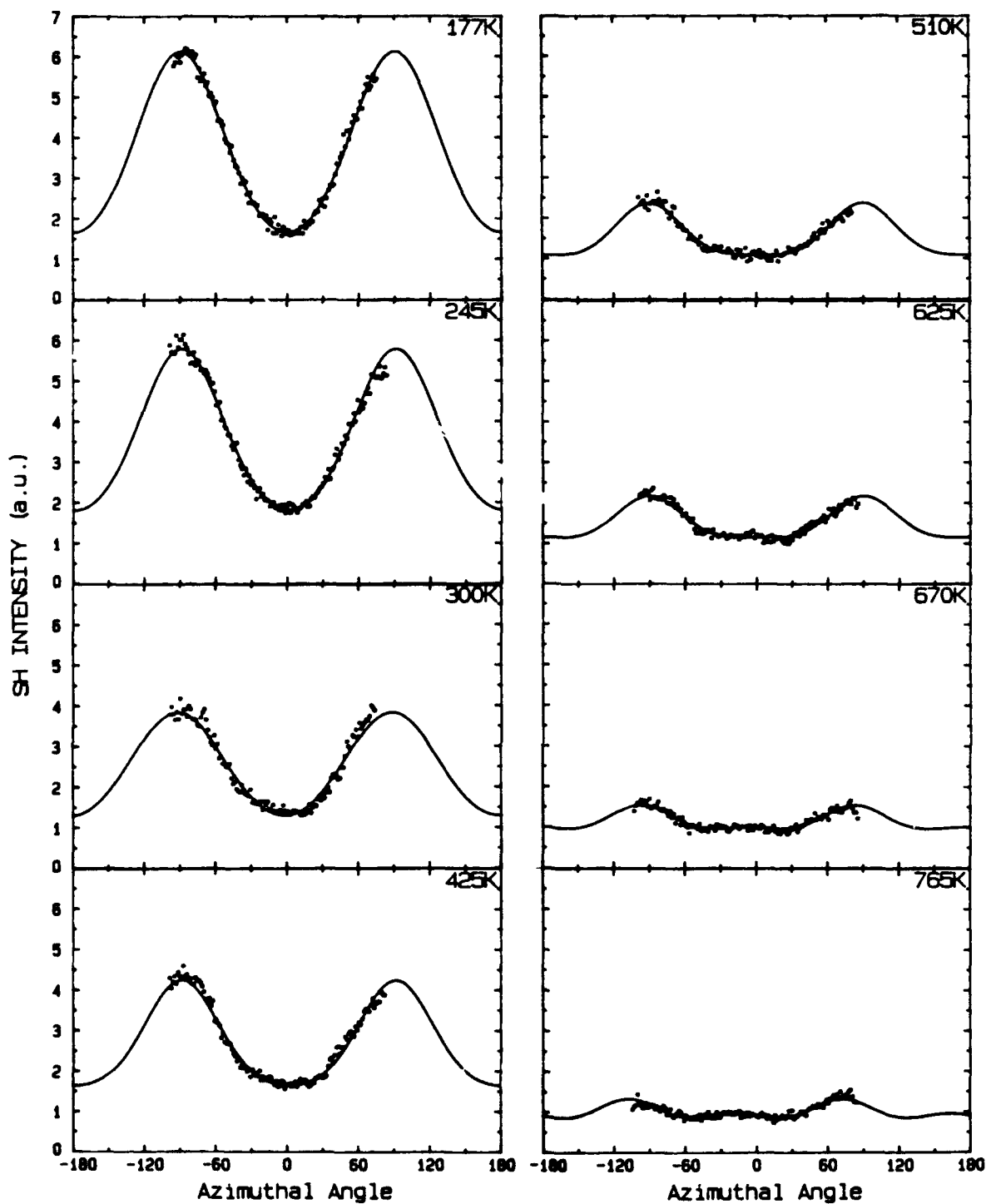


Figure 1. Rotationally azimuthal SH intensity as a function of Cu(110) surface azimuthal angle at the fixed surface temperatures indicated. The solid lines are fits to the data discussed in the text.

be viewed as instantaneous typically lasting $<10^{-15}$ sec. In the He-atom scattering experiments reported above³ the He-atom incident energy was ~ 18 meV which corresponds to an incident velocity of $\sim 10^5$ cm/sec. At such low collision energies the incident He-atom can be expected to interact with the electron density of the Cu surface atoms over a distance of ~ 5 Å on the incoming

and outgoing trajectory. The He-atom interaction time with the surface atoms is then $\sim 10^{-12}$ sec or approximately three orders of magnitude longer than that characteristic of x-ray scattering or optical SHG. Assuming that the Cu surface atoms at 300 K have a vibrational period of $\sim 10^{-13}$ sec, then it can be conjectured that He-atom scattering as an experimental probe measures the time averaged structure of the Cu(110) surface and, in a time averaged picture, the Cu surface atom positions are confined to the [110] rows over the temperature range of < 900 K. However, due to a large anharmonicity in the vibrational motion of the Cu surface atoms as a function of temperature, the instantaneous positions at elevated temperatures appear disordered. One can then envision a "1-D" type of disorder where the instantaneous Cu surface atom positions in the [110] rows appear to be highly kinked. It is this instantaneous position that is probed by both the x-ray scattering and the rotationally anisotropic SHG experiments reported in this study.

Over the temperature range of ~ 900 K a picture of the thermally induced changes in the surface structure that is consistent with all three experimental techniques is one where, on the time average, the surface looks like an ideal corrugated Cu(110) surface. However, an instantaneous snapshot of the surface would reveal a large amount of 1-D disorder where the rows of Cu atoms are highly kinked. This disorder increases sharply with increasing temperature. Support for this picture comes from the fixed azimuthal angle temperature dependence data measured at $\sim 75^\circ$. The smooth linear decrease with increasing temperature may be due to the increasing 1-D disorder in the rows of Cu atoms. The fact that the data appears to level off above ~ 700 K might suggest that either the anharmonicity associated with the 1-D disorder cannot increase further or that above this temperature the surface can be viewed as having truly disordered in a 2-D sense.

In summary, rotationally anisotropic SHG has been used to study the surface structure and thermal stability of a clean Cu(110) surface. The results show clear evidence of the surface structural sensitivity of the optical SHG diagnostic technique. The temperature dependence of the rotational anisotropy from Cu(110) is in agreement with other experiments performed using very different surface probes that indicate a temperature induced change in the Cu(110) surface structure and symmetry above ~ 600 K.^{2,3} We propose that a thermally induce 1-D disordering phenomena accounts for all of the experimental observations.

Experiments currently in progress using a tunable laser source will make it possible to determine the relative contributions of surface interband and free-electron transitions to the SH response and their possible temperature dependances. Theoretical lattice dynamics calculations should be very useful in understanding the thermally induced vibrational anharmonicity and the microscopic origins of the differences observed in the x-ray, He-atom, and surface SHG experiments. An extension of this work to the Cu(100) and Cu(111) surfaces which have very different thermal behavior will be useful in testing the generality of the conclusions drawn from this work.

REFERENCES

1. M. den Nijs, E. K. Riedel, E. H. Conrad, and T. Engel, Phys. Rev. Lett. 55, 1689(1985).
2. S. G. J. Mochrie, Phys. Rev. Lett. 59, 304(1987).
3. P. Zeppenfeld, K. Kern, R. David, and G. Comsa, Phys. Rev. Lett. 62, 63(1989).
4. Y. R. Shen, J. Vac. Sci. Technol. B 3, 1464(1985); Ann. Rev. Mater. Sci. 16, 69(1986); Nature 337, 519(1989).
5. G. L. Richmond, J. M. Robinson, and V. L. Shannon, Prog. Surf. Sci. 28, 1(1988).
6. J. E. Sipe, D. J. Moss, and H. M. van Driel, Phys. Rev. B 35, 1129(1987).
7. J. F. Ready (Academic, New York, 1971).
8. M. A. Hoffbauer and R. E. Muenchausen, in Photochemistry in Thin Films, T.F. George, Editor, Proc. SPIE 1056, 38(1989).

Vibrational Spectroscopy of Competitive Adsorption at a
Liquid/Solid Interface Using IR-Visible Sum-Frequency Generation

J. Miragliotta, R.S. Polizzotti, P. Rabinowitz, and R.B. Hall

Exxon Research and Engineering Co.

Rt. 22 East, Annandale, NJ 08801

(201) 730-2249

Optical IR-Visible sum-frequency generation (SFG), a surface vibrational spectroscopy, has been used to study competitive adsorption at a hydroxylated ZrO_2 surface in contact with a number of binary solutions. This technique is similar to surface second harmonic generation (SHG) in that it is forbidden (in the dipole approximation) in spatial regions possessing inversion symmetry. Therefore, systems consisting of an interface bound by centrosymmetric media give rise to a nonlinear response which is dominated by that of the interfacial region. In addition to being surface specific, the SFG signal from the liquid/solid interface can be resonantly enhanced when the incident IR laser source used in the generation process is tuned through a vibrational mode in the adsorbed species, provided the mode is both Raman and IR active. This vibrational information allows identification of the adsorbed molecule as well as measurements of surface coverage, molecular orientation, and adsorbate interactions for a number of the two-component liquid systems.

The present investigations are, to our knowledge, the first studies of competitive adsorption at a liquid/solid interface using SFG. The optical setup for the studies has been described elsewhere [1]. The ZrO_2 sample, transparent to both the IR ($2000-4000\text{ cm}^{-1}$) and visible laser sources, was designed so as to allow the incident excitation sources and the SFG signal to be internally reflected when the incident beams were transmitted through the ZrO_2 side of the interface. This allowed the use of a simple detection arrangement as well as providing a significant enhancement in the SFG signal with respect to an external reflection excitation geometry. In this optical configuration, typical signal levels at resonance (see Figure 1), were $\sim 500-1000$ photons/laser pulse. The ZrO_2 sample was prepared with a cleaning procedure so as to leave the surface hydroxylated. This was confirmed by the SFG response in the $3400-4000\text{ cm}^{-1}$ region, which showed vibrational resonances characteristic of surface hydroxyl groups ($3500-3800\text{ cm}^{-1}$ region).

Examples of the adsorbate information that can be obtained with SFG from the liquid/solid interface are shown in Figures 1-3. Figure 1 shows a series of SFG spectra from the ethanol:water/ ZrO_2 interface. As is evident from these results, the decrease in the peak intensities for the C-H stretches in the methyl group of the ethanol is due to the displacement of this molecule by the adsorbed water. At lower ethanol coverages, i.e., higher water concentrations, there is an apparent shift of the C-H symmetric stretch in the methyl group to lower frequencies. Although the origin of the shift is unknown at this time, it may be due to a change in the dipole-dipole coupling in the adsorbed layer. The integration of the SFG intensity for the C-H symmetric peak of the methyl group (2930 cm^{-1}) allows a determination of the relative surface coverage of ethanol since this intensity is proportional to the square of the surface coverage [2]. Figure 2 shows a plot of the square root of the SFG signal for the C-H symmetric stretch (data from Figure 1) versus the water concentration in the binary solution. The data is in good agreement to a simple Langmuir equilibrium adsorption isotherm for competitive adsorption [3] as shown by the solid line through

the data points in Figure 2.

In addition to determining adsorption isotherms, SFG is also capable of obtaining orientational information about the adsorbed layer. Figure 3 shows the SFG optical polarization dependence from the ethanol/ZrO₂ interface in the C-H stretching region. The variation in the intensity versus the input polarization of the excitation sources results from the average polar angle tilt of the surface dipole with respect to the surface normal. As shown by Shen's group [4], the ratio of the intensities for the C-H symmetric stretch in the methyl group allows a determination of this average tilt angle. For the example in Figure 3, the ratio of the SFG intensities (Figure 3b and d) showed the C-C bond direction in the ethanol to be tilted at 44° +/- 5° with respect to the surface normal.

In addition to this two-component liquid system, results of CH₃CN (acetonitrile) displacement by CH₃OH and CD₃OD at the ZrO₂ surface has also been investigated. Unlike the ethanol:water system, however, there appear to be inter-adsorbate interactions between the methanol and acetonitrile due to the similar vibrational frequencies of the two molecules in the C-H stretching region. A discussion of these interactions will be presented.

References

- [1] J. Miragliotta, R.S. Polizzotti, P. Rabinowitz, S.D. Cameron, and R.B. Hall, *Chem Phys.* 143 (1990) 123.
- [2] Y.R. Shen, *Principles of Nonlinear Optics* (Wiley, New York, 1984).
- [3] K.J. Laidler, *Chemical Kinetics* (McGraw-Hill, New York, 1965).
- [4] P. Guyot-Sionnest, J.H. Hunt, and Y.R. Shen, *Phys. Rev. Lett.* 59 (1987) 1597.

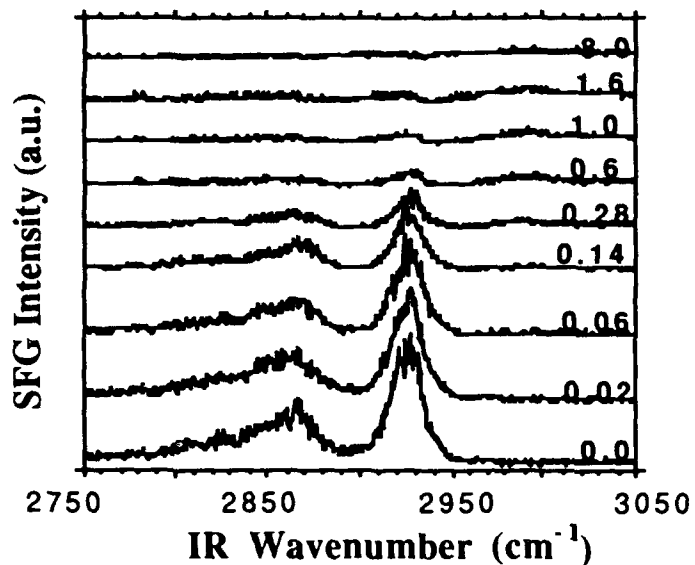


Fig. 1. SFG spectra from the ethanol:water/Zirconia interface for a number of ethanol:water mixtures. The numbers to the right of each spectrum represent the volume ratio of water-to-ethanol in the binary solutions.

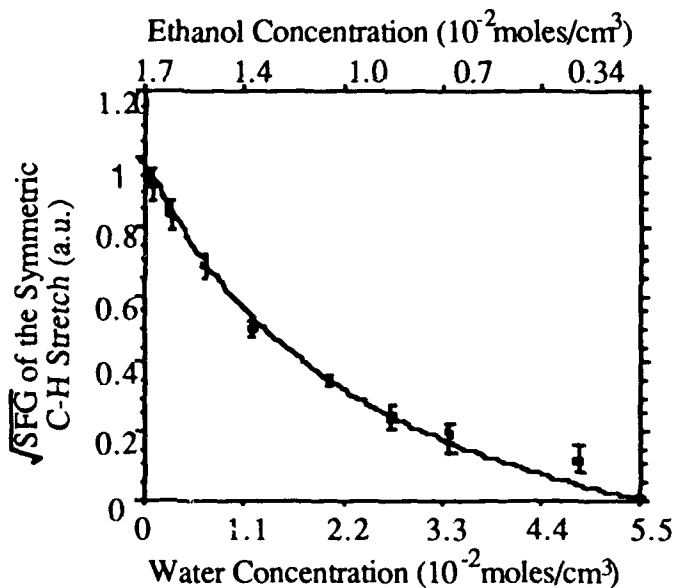


Fig. 2. Square root of the SFG intensity of the symmetric C-H stretch in the methyl group of the ethanol as a function of ethanol:water solution concentrations. Data points are from the spectra in Figure 1. Solid curve represents a fit to the data with a Langmuir equilibrium adsorption isotherm for competitive adsorption on Zirconia.

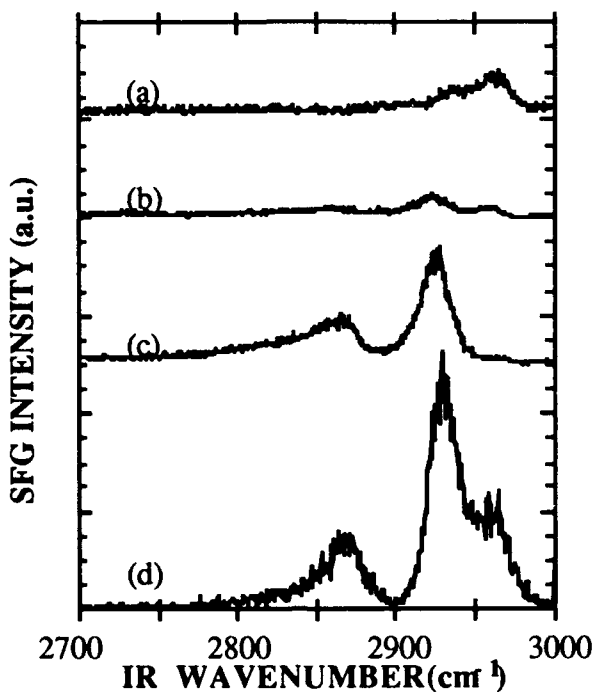


Fig. 3. SFG from ethanol adsorbed on Zirconia. (a) S-polarized visible and IR inputs. (b) P-polarized visible and S-polarized IR. (c) P-polarized visible and IR inputs.(d) S-polarized visible and P-polarized IR inputs.

Etching of SiO_2 film by synchrotron radiation in hydrogen and its application to low-temperature surface cleaning

Yasuo Nara, Yoshihiro Sugita, Noriaki Nakayama, and Takashi Ito

Fujitsu Laboratories LTD.

10-1 Morinosato-Wakamiya, Atsugi 243-01, Japan

Introduction

In order to grow silicon films with good crystal quality, it is important to remove oxygen and carbon contaminants on the surface and to obtain clean substrate surface immediately before growth. In conventional surface cleaning process, silicon substrate is heated up to about 1000°C and the surface contaminants are evaporated or gas-etched from the substrate surface. However, such high temperature treatment causes the redistribution of impurity atoms in the substrates and it makes difficult to fabricate fine structures. Recently, synchrotron radiation (SR) stimulated evaporation of SiO_2 film and its application to surface cleaning at 650°C have been reported¹⁾, and the usefulness of SR induced reactions for low-temperature process is being recognized.

In this paper, we report on new SiO_2 etching technique by the irradiation of SR in H_2 atmosphere and on the application of this process to the pretreatment of Si film deposition. It is revealed that the addition of H_2 gas during SR exposure is effective to increase the SiO_2 etching rate and to reduce the carbon contamination on the Si substrate at low-temperature of 500°C.

Experiment

We used the SR beam line 17B (BL-17B) at the Photon Factory in the National Laboratory for High Energy Physics. In this beam line, SR light from 2.5 GeV storage ring is reflected by Pt coated toroidal mirror which accepts 8 mrad horizontal and 1 mrad vertical divergence of SR. The incident angle of the toroidal mirror is fixed at 85°, so vacuum ultraviolet light with wavelength from 1 to 100 nm is utilized. The total photon flux of about 10^{16} photons/cm²/s is irradiated to the substrate surface at the storage current of 200 mA.

The schematic diagram of reaction chamber, which is located at the end of the beam line, is shown in Fig.1. For allowing the use of reaction gases at the reaction chamber, the differential pumping system is set between the beam line and the reaction chamber. This system allows a pressure of 10^3 Pa in the reaction chamber while the pressure in the beam

line is maintained on the order of 10^{-7} Pa.

The silicon substrate is set on a sample holder whose temperature is controlled up to 600°C. The base pressure of the reaction chamber is about 10^{-4} Pa. H_2 and SiH_4 (5% diluted in He) was introduced to the reaction chamber through a variable leak valve. SR is perpendicularly irradiated to the substrate.

Results and discussions

1. Etching characteristics of thermally grown silicon dioxide

Figure 2 shows the etching characteristics of thermally oxidized SiO_2 with the thickness of about 140nm. Etched SiO_2 thickness at the SR irradiated region, which is normalized by the SR exposure of 1000 A·s, is plotted against the substrate temperature with various H_2 pressure. In the low-temperature of 480-500°C, SiO_2 film is removed by only the SR irradiation and its etching rate is increased by the factor of more than 2 by the addition of H_2 . Since the substrate temperature increase by SR irradiation at around 500°C is estimated negligibly small, the etching reaction proceeds purely by the photochemical reaction. The effect of adding H_2 is found for the first time by our experiment.

Figure 3 shows the SiO_2 thickness distribution after 1 h SR exposure at 560°C. Etching is observed only the SR irradiated region with and without H_2 . This means the surface reaction such as photo stimulated desorption plays an important role in the etching reaction. The possible etching mechanism is as follows. Vacuum ultraviolet light in SR excites electronic states of Si and O at the SiO_2 substrate and the Si-O bonds are weakened. As a result, SiO and O desorb from the surface. Weakened Si-O bond by SR irradiation is also observed in the increase of etching rate of SiO_2 film by 10% HF solution by a factor of 2.7. By introducing H_2 gas, H radicals and/or ions are photochemically generated. Since these reactive species and the excited SiO_2 interact to produce volatile SiH_x ($x=1-4$) in addition to SiO and O generation, the etching rate is increased.

2. Application to the pretreatment of Si deposition

Possibility of the application of this new SiO_2 removal process to the low-temperature pretreatment for Si film deposition was examined. The silicon substrate with about 1nm native oxide was irradiated by SR at 560°C in 133 Pa H_2 ambient for 30 min. Immediately after this treatment, SiH_4 gas (partial pressure of 20 Pa) was introduced and the amorphous silicon film was deposited by SR irradiation at 160°C. The amount of the interface contaminants of oxygen and carbon was investigated by the secondary ion mass spectroscopy. The depth profiles of oxygen and carbon contaminants with and without SR irradiation are shown in Fig.4 (oxygen) and Fig.5 (carbon). Peaks in the secondary ion

signal are the interfaces between the deposited Si films and the Si substrates. The peak intensities of oxygen and carbon atoms has smaller values at the SR irradiated region than at the non-irradiated region. The effect of SR irradiation for contaminant removal is summarized in Table 1. The amount of interface oxygen is decreased to half value at the irradiated region compared with the non-irradiated region. Interface carbon, which is usually removed from silicon surface at 1200°C by the conventional heating treatment, is reduced to less than one-third at the SR irradiated region at 560°C. This means that SR irradiation in H₂ atmosphere is more effective for removing interface carbon than for oxygen. This is probably because the volatile CH_x (x=1-4) is efficiently produced by the excitation of substrate surface and hydrogen when SR is irradiated to the substrate.

Conclusion

It is experimentally demonstrated that the SiO₂ film is removed at relatively low-temperature of 500°C by irradiating SR to the substrate and that the etching rate increases when H₂ gas is added in this process. This process is applicable to the low-temperature surface cleaning prior to the epitaxial growth on the Si substrate because the interfacial contaminants such as oxygen and carbon are reduced.

References

- 1) H. Akazawa et. al., Extended abstract of 22nd International Conf. on Solid State Devices and Materials, Sendai, Japan, 1990, pp1171-1172.

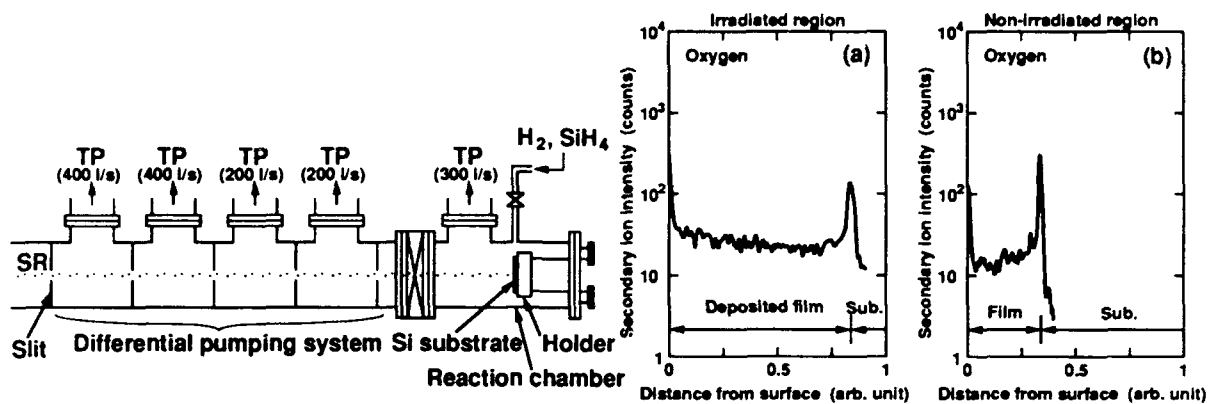


Figure 1 Schematic diagram of the reaction chamber. Differential pumping system and reaction chamber are evacuated by turbo molecular pumps (TP) and the SR beam is irradiated perpendicularly to the Si substrate.

Figure 4 SIMS depth profile of oxygen.

SR irradiated (a) and non-irradiated (b) regions are compared. Peaks in the figure is the interface between the deposited film and the substrate.

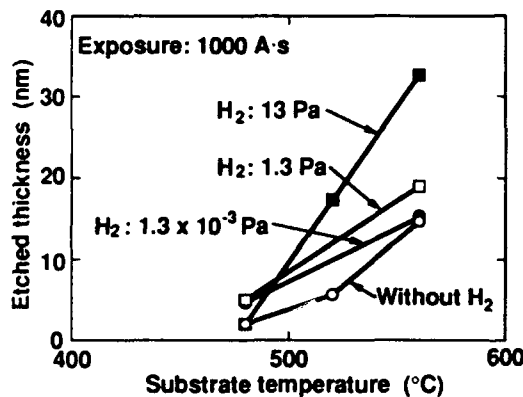


Figure 2 Substrate temperature dependence of the etched thickness of thermally oxidized silicon dioxide.

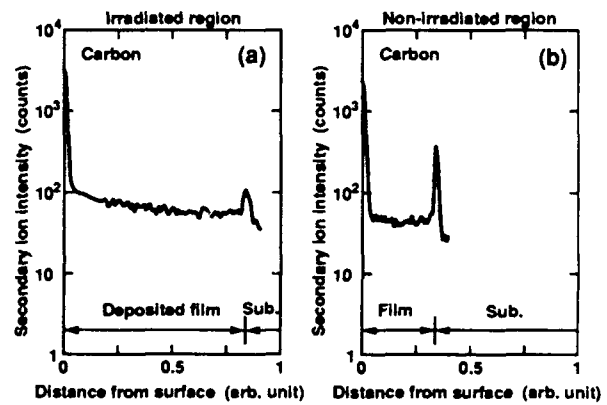


Figure 4 SIMS depth profile of carbon.

SR irradiated (a) and non-irradiated (b) regions are compared.

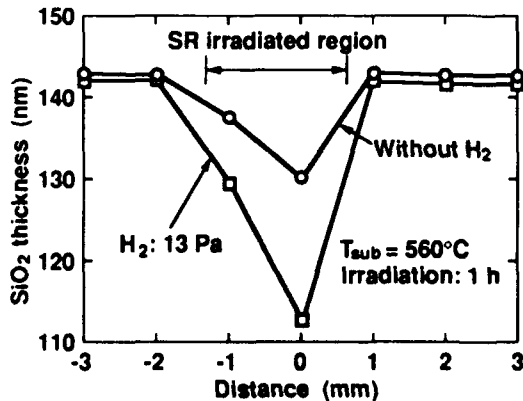


Figure 3 Silicon dioxide thickness distribution after the SR irradiation with and without H₂ introduction.

Table 1 Comparison of SIMS peak intensity between SR irradiated region and non-irradiated region.

	Non-irradiated region	Irradiated region
Oxygen	320	160
Carbon	390	120

(counts)

Wednesday, February 13, 1991

Poster Session

WC 4:30pm-6:30pm
Anasazi North

*Steven M. George, Presider
Stanford University*



Electronic Energy Transfer Between Donor and Acceptor Adlayers on Single-Crystal Surfaces: Distance and Coverage Dependence

D.R. Haynes, A. Tokmakoff and S.M. George

*Department of Chemistry
Stanford University
Stanford, CA 94305
(415) 725-0270*

Electronic energy transfer in surface adlayers is a mechanism of fundamental importance to surface photochemical processes. In this study, the electronic energy transfer from a donor p-terphenyl (TP) adlayer to an acceptor 9,10-diphenylanthracene (DPA) adlayer was studied using quantum yield measurements at 30 K and 85 K. These investigations employed an $\text{Al}_2\text{O}_3(0001)$ crystal surface as a two-dimensional support on which donor, spacer and acceptor adlayers could be sequentially adsorbed. The quantum yield measurements were performed in ultra high vacuum (UHV) utilizing laser induced fluorescence techniques.

To determine the distance dependence of electronic energy transfer, a butane adlayer was employed as a variable spacer to separate the donor and acceptor adlayers. Relative donor and acceptor fluorescence quantum yields were determined for a $\Theta = 10 \text{ \AA}$ coverage of TP donor separated by butane spacers from a $\Theta \approx 25 \text{ \AA}$ coverage of DPA acceptor on $\text{Al}_2\text{O}_3(0001)$. Butane spacers were varied from $d = 5 - 130 \text{ \AA}$. The experimental arrangement of the donor, spacer and acceptor adlayers is shown below in Figure 1.

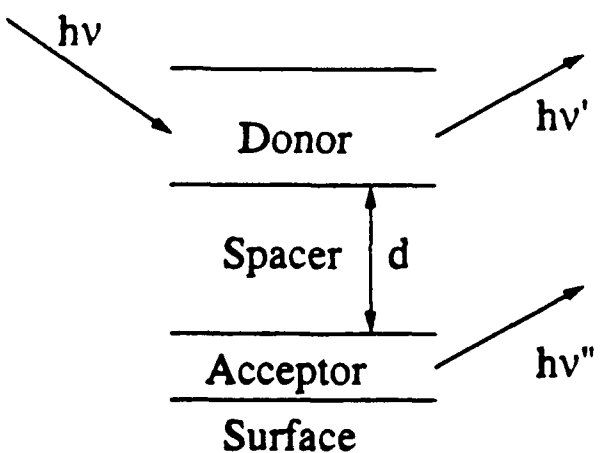


Figure 1. Arrangement of donor, spacer and acceptor adlayers.

The relative donor fluorescence quantum yield, Q_D , was defined as $Q_D = D/(D + A)$ where D is the donor fluorescence signal and A is the acceptor fluorescence signal. Fluorescence spectral measurements for various butane spacer thicknesses are shown in Fig. 2. The upper trace shown in each spectrum is the total fluorescence emitted by the TP and DPA at the given separation distance. The lower trace in each spectrum corresponds to the portion of the spectrum derived from TP donor fluorescence. Figure 2 reveals that the relative fraction of fluorescence from the donor increases as the butane spacer thickness is increased. This increase in the donor fluorescence signal is caused by the decreasing electronic energy transfer as a function of donor/acceptor separation distance.

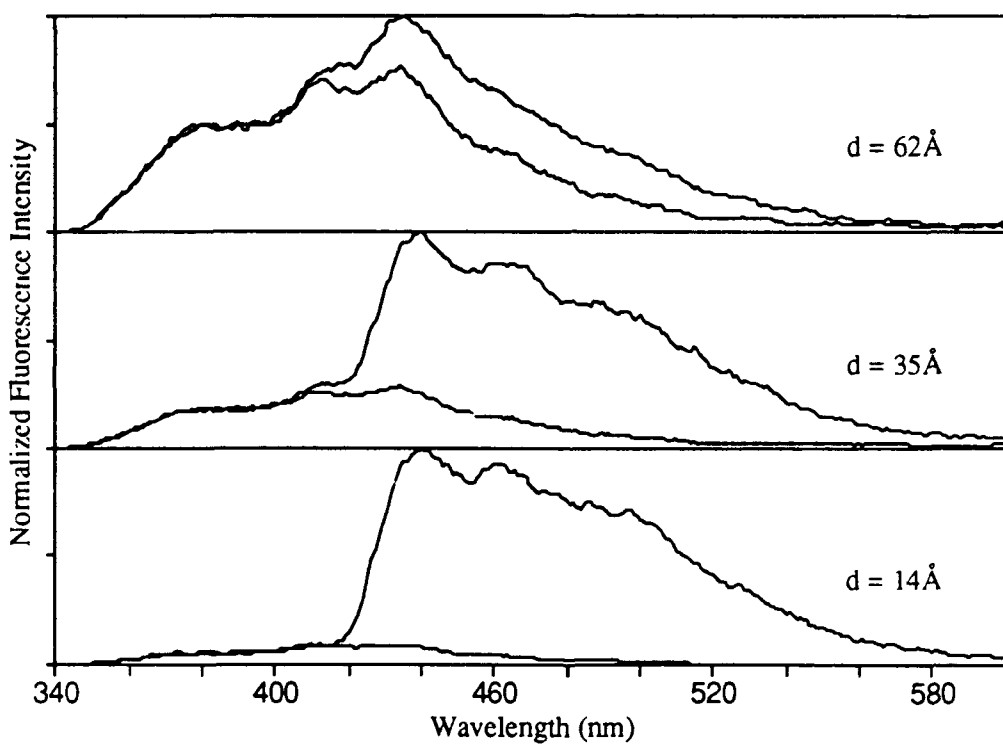


Figure 2. Fluorescence measurements versus butane spacer thickness.

The relative quantum yield results were fit to $1/d^3$ and $1/d^4$ functional forms corresponding with Förster energy transfer [1] to volume and surface acceptor arrays. These functional fits to the donor quantum yield are shown in Fig. 3. The results show that the $1/d^3$ functional fit is in excellent agreement with the data. The $1/d^3$ dependence suggests that electronic energy transfer is occurring from the excited donor adlayer to a three-dimensional acceptor array.

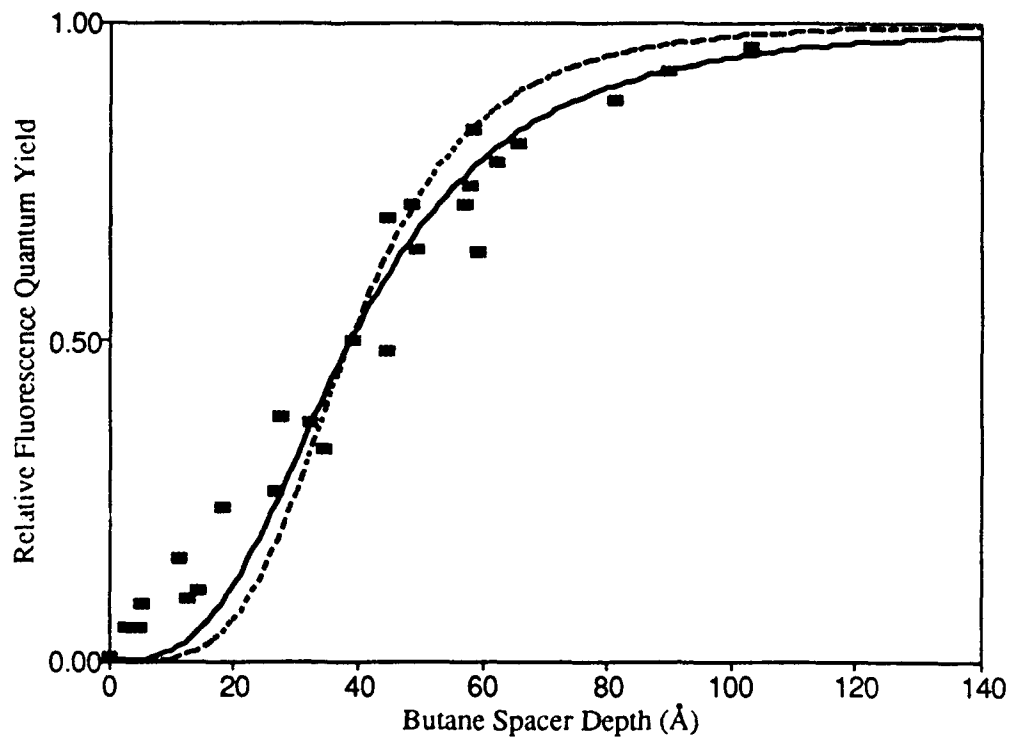


Figure 3. Relative donor quantum yield versus butane spacer thickness. Solid lines show $1/d^3$ and $1/d^4$ fits to quantum yield.

The critical energy transfer distance, d_0 , is defined as the donor/acceptor separation distance at which the donor \rightarrow acceptor electronic energy transfer rate is equal to the donor radiative relaxation rate. A critical energy transfer distance of $d_0 = 38 \pm 4 \text{ \AA}$ was observed at 30 K. In comparison, a critical energy transfer distance of $d_0 = 27 \pm 5 \text{ \AA}$ was obtained at 85 K. The change in d_0 with temperature was attributed to the red-shift in the TP donor fluorescence spectrum at higher temperatures. This red-shift reduces the overlap between the TP donor fluorescence and the DPA acceptor absorption spectra. Because this spectral overlap determines the efficiency of electronic energy transfer [1], the decreased spectral overlap at 85 K lowers the critical energy transfer distance.

The critical energy transfer distance can be calculated theoretically using the classical analysis developed by Kuhn [2]. This classical description is analogous to the quantum mechanical theory for electronic energy transfer described by Förster [1]. Theoretical values for the critical energy transfer distance of $d_0 = 39 \text{ \AA}$ at 30 K and $d_0 = 25 \text{ \AA}$ at 85 K were obtained employing the relevant spectral parameters. These theoretical values are in excellent agreement with the experimental observations.

To investigate electronic energy transfer within the donor adlayer, experiments

were performed in which the TP donor adlayer coverage was varied on the DPA acceptor adlayer. Relative donor and acceptor fluorescence quantum yields were measured for TP donor coverages between $\Theta = 5 - 250 \text{ \AA}$. The electronic energy transfer predicted by a simple summation model was then calculated from the results of the butane spacer experiments. The summation model assumed that no electronic energy migration occurred within the donor adlayer. The summation model results were then compared with the results versus donor coverage.

Figure 4 displays the results of the summation model compared with the relative quantum yield results obtained from experiments versus donor coverage. The summation model was in excellent agreement with the observed quantum yield versus donor coverage. This agreement indicates that there is no electronic energy migration within the donor adlayer. This absence of electronic energy transfer within the TP adlayer is also predicted from Förster theory because the spectral overlap between the TP fluorescence spectrum and TP absorption spectrum is negligible.

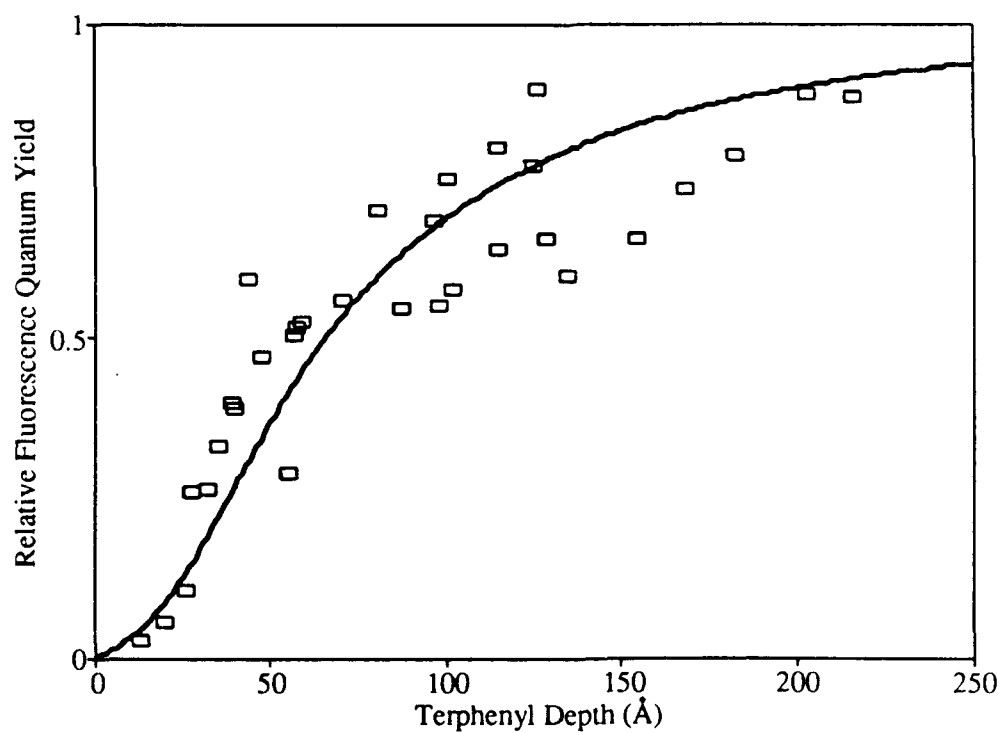


Figure 4. Relative donor quantum yield versus donor coverage. Solid line shows prediction from summation model.

1. Th. Förster, *Naturwissenschaften* 33, 166 (1946)
2. H. Kuhn, *J. Chem. Phys.* 53, 101 (1970)

Arsenic Passivation of Silicon by Photo-assisted Metalorganic Vapour Phase Epitaxy

D C Rodway, K J Mackey, P C Smith and A W Vere

Royal Signals & Radar Establishment, St Andrews Rd, Malvern, Worcs WR14 3PS, UK

The MOVPE deposition of semiconductors requires effective substrate surface preparation, especially where low temperature, photo-assisted growth is involved. Ideally this process should be achieved in situ in the growth reactor immediately prior to deposition. In a previous paper⁽¹⁾ we reported the in situ removal of carbon from Si and GaAs substrate surfaces using 193nm radiation in a 1 Torr O₂ ambient. This process generates a thin oxide which can then be removed by annealing at 850°C, although the process does not always go to completion. To protect the cleaned surface and to passivate the silicon substrate prior to deposition of GaAs we have explored the arsenic passivation techniques developed by Bringans et al^(2,3). The oxidation resistance of surfaces prepared this way is also sufficient to permit transfer between laboratories for collaborative studies.

In the work reported here an amorphous arsenic film is deposited on the pre-cleaned Si (111) surface⁽⁴⁾ of a 3" diameter substrate after loading into the photo-MOVPE reactor. This is achieved by using excimer laser radiation to decompose AsH₃ in the temperature range 25°C-350°C. When ArF* (193nm) radiation is used the decomposition occurs primarily in the gas phase leading to poor spatial delineation of the deposited area and a combination of layer deposition and physi-sorbed dust. The latter exhibits marked electrophoretic effects in the presence of the laser beam. By careful control of AsH₃ and hydrogen carrier gas flows and the total pressure in the reactor (typically 200-500mb) the gas phase reaction can be reduced to acceptable levels. Nishiwara et al have shown that at 248nm wavelength heterogeneous decomposition occurs on silicon surfaces but that gas-phase absorption does not occur⁽⁵⁾. We have found that superior quality layers can be produced at this wavelength due to the absorption-curve broadening associated with AsH₃ adsorption on the Si (111) surface. This heterogeneous reaction gives good spatial definition at acceptable deposition rates of 0.5μm hr⁻¹.

XPS data for As films grown at 193nm show that the directly irradiated area is covered by a thick film of elemental arsenic. Downstream from this directly illuminated area there is a distinct 'plume' of material deposited from the gas phase which is found to comprise particles of up to 2μm in diameter. XPS examination of this area shows that coverage is incomplete, the silicon substrate being clearly visible. The As 2p 3/2 peak at 1323.4eV BE is still present but a small secondary peak, shifted up approximately 3.5eV in energy is also observed. This energy shift is consistent with the binding of some of the As to residual oxygen on the substrate surface. The elemental As peak observed is probably attributable to the particles produced in the gas phase, whilst the shifted peak results from sub-monolayer growth at low illumination levels produced by multiple internal reflections of the primary beam in the chamber.

When 248nm radiation is used for the growth the downstream plume is absent. Again the directly illuminated area is covered by a thick film of elemental As whilst the weakly illuminated areas up and downstream show XPS peaks consistent with a mixture of elemental As and As oxide.

References

1. D C Rodway, K J Mackey, P C Smith and A W Vere
Tech Digest. Microphysics of Surfaces, Beams and Adsorbates Conf, Feb 27-Mar 1 (1989), 88-89
2. R D Bringans and M A Olmstead
J Vac Sci Technol B7(5) (1989) 1232-1235
3. R I C Uhrberg, R D Bringans, M A Olmstead, R Z Bachrach and J E Northrup
Phys Rev B35 (1987) 3945
4. D A Woolf, D I Westwood and R H Williams
Semicond Sci Technol 4 (1989) 1127-1134
5. J Nishiwara, T Kurabayashi and J Hoshina, J Electrochem Soc 134(2) (1987), 502-504

Acknowledgements

We would like to thank Mr P K Moores for assistance with the photodeposition experiments. The work described here is partially supported by the EEC Basic Research Programme No 3177 (Epioptics).

Copyright C HMSO, London, 1990

Reflection Electron Energy Loss Spectroscopy during Molecular Beam Epitaxy

H.A. Atwater, C.C. Ahn and S. Nikzad
Thomas J. Watson Laboratory of Applied Physics
California Institute of Technology
Pasadena, CA 91125

Introduction

Modern epitaxial crystal growth techniques have made it possible to tailor compositionally modulated thin films on an atomic level. However, further progress in control of epitaxial growth is limited by a relative lack of useful *in situ* techniques for surface analysis during growth. The most widely used *in situ* structural analysis technique for molecular beam epitaxial (MBE) growth is reflection high energy electron diffraction (RHEED). Its long working distance and high data rate have prompted investigations of RHEED oscillations and other RHEED dynamic features by many groups. However, there is currently no widely employed *in situ* chemical analysis technique that has the advantages of RHEED[1]. Hence, for example, the ability to perform real-time control of alloy composition in epitaxial films is limited.

Because of the availability of commercial instruments, electron energy loss spectroscopy has only been done previously at typical RHEED energies in transmission electron microscopes. Extensive work has established electron energy loss as a viable analytical tool at high energies in transmission mode, but very little work has been done using the reflection mode[2]. However, until two years ago, it was not clear that core loss information could even be extracted from reflection measurements[3].

In this paper we describe a promising new method for chemical analysis during epitaxial growth using core loss analysis by energy loss spectrometry of high energy electrons reflected from the surface, which we term reflection high energy electron diffraction with energy loss spectroscopy (RHEED/REELS)[4]. Since reflected electrons at RHEED energies are strongly forward scattered, the technique is compatible with much longer sample working distances than for competing techniques (e.g. Auger spectroscopy) and also with high data rates, both of which suggest that RHEED/REELS may have considerable potential as a *in situ* surface spectroscopy during molecular beam epitaxy.

Reflection Electron Energy Loss Spectroscopy during Ge Heteroepitaxy on Si

We have modified a RHEED-equipped Si MBE system in order to accomodate an electron energy loss spectrometer (typically used in an electron microscope) behind a 3 mm aperture in the RHEED screen. Structural analysis by RHEED at 30 keV with an emission current of 30 μ A was performed simultaneously with the REELS measurements. The spectrometer is a Gatan 607 second order corrected sector identical to that normally used in a transmission electron microscope. The object point of the spectrometer is the sample itself, located approximately 33 cm from the spectrometer entrance, giving a collection

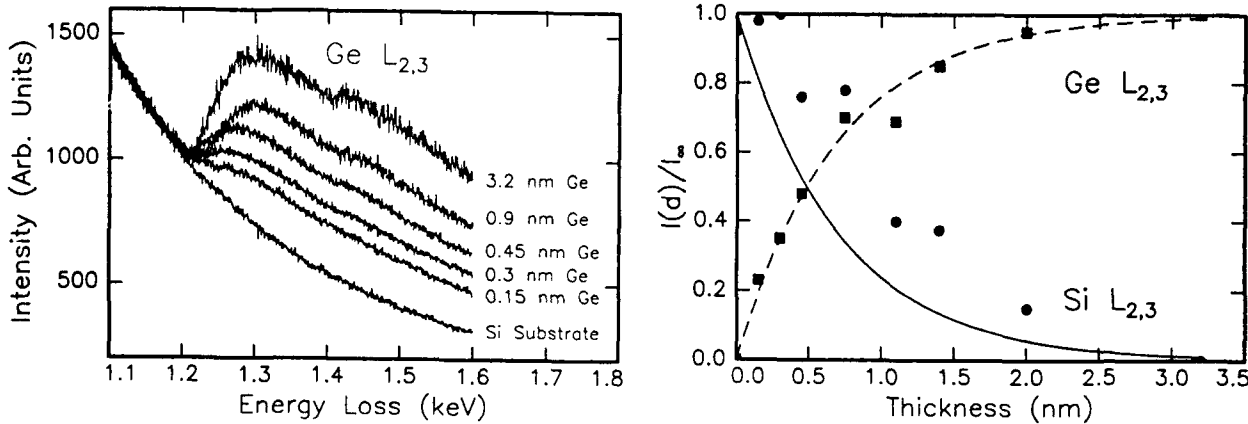


Figure 1: In (a) Normalized Ge $L_{2,3}$ intensity as a function of average layer coverage. Of special note is the fact that the presence of Ge can be adequately discerned after a monolayer of coverage, and that the much less intense Ge L_1 edge can be seen after several monolayers. In (b) normalized intensity variation with coverage for Ge and Si $L_{2,3}$ core losses. The solid lines are theoretical predictions from a simple model of grazing incidence electron scattering based on tabulated mean free path data for total electron scattering at 30 keV.

semi-angle of 5 mrad. The spectrometer energy resolution, calculated at 25 keV using the first order matrix coefficients[5] for this sector and an assumed 90 μm beam waist, is approximately 5 eV. Assuming an incident thermal beam spread of 1.5 eV, and high voltage power supply resolution of 3 eV, the energy resolution of the system is expected to be approximately 6 eV. Experimental measurements of the energy width of the through beam (i.e., the beam which does not strike the sample) indicated a system resolution of approximately 7 eV. While this is not a high energy resolution, it is more than adequate for quantitative analysis of core losses.

Initial experiments concentrated on characterizing the optimum scattering geometry for observation of core loss edge intensities for Si and Ge substrates. Several diffraction conditions were investigated: (i) specular reflection coincident with a Bragg peak of the substrate (in-phase), (ii) specular reflection not coincident with a substrate Bragg peak (out-of-phase), and (iii) a surface resonance condition, where the out-of-phase specular reflection intensity was enhanced by coincidence of an oblique Kikuchi line with the specular beam spot[6,7]. For Ge substrates, the Ge $L_{2,3}$ edge was observable in all three conditions, however better ratios of edge intensity to inelastic background intensity were obtained for conditions (ii) and (iii). It has been reported by Wang, et. al., that condition

(iii) scattering, corresponding to surface resonance is required to obtain acceptable ratios of core loss intensity to inelastic background intensity[8]. Little difference was observed in the ratio of edge intensity to inelastic background between conditions (ii) and (iii) above in the present work. However, it was determined qualitatively that surface sensitivity is strongly enhanced by adoption of surface resonant scattering conditions. For example, after growth of 0.3-0.5 nm of Si on a Ge (001) substrate, the Ge $L_{2,3}$ core loss intensity from the substrate was not observable. For nonresonant conditions, the substrate core loss intensity is still observable after growth of a 2.0-3.0 nm thick overlayer, as discussed below.

Following growth of a 300 nm Si buffer layer on a Si (001) substrate by molecular beam epitaxy, a streaked RHEED pattern with the Si 100-(2x1) reconstruction characteristic of clean surfaces was observed. Ge was grown at a rate of 0.84 nm/min on (001) Si substrates at a temperature of 410 °. Film thickness was measured using quartz crystal sensors which had been previously calibrated using Rutherford backscattering spectrometry. Growth was briefly interrupted to collect electron energy loss spectra. Energy loss spectra taken in scattering condition (ii) are shown in Figure 2(a) as a function of Ge thickness. The collection time for each spectrum was 40 sec. The appearance of the Ge $L_{2,3}$ edge is clearly visible in the electron energy loss spectrum at Ge thicknesses as small as 0.15 nm. For Ge thicknesses $d \geq 0.3$ nm, the Ge L_1 edge is also visible. It should be emphasized that the results in Fig. 2(a) are data from single spectra, and have not been averaged or otherwise processed, except to normalize the pre-edge background intensity. We expect the pre-edge intensity to remain constant, since the scattering geometry was unchanged during film growth. Figure 2(a) shows the Ge $L_{2,3}$ intensities for growth of 0.15 - 3.2 nm of Ge on Si(001), and Fig. 2(b) shows the dependence of normalized Si and Ge $L_{2,3}$ intensities as a function of nominal Ge overlayer thickness. The solid and dashed lines in Fig. 2(b) represent the predictions of a transmission model for grazing incidence electron scattering.

The normalized Ge $L_{2,3}$ and Si $L_{2,3}$ intensities shown in Fig. 2 were determined from power law background fits for 200 eV windows. These intensities vary gradually and in a complementary manner with coverage in the range $0 < d < 3.2$ nm. For nonresonant conditions, it is possible to interpret the changes in intensities with coverage as being due to electron energy loss at grazing incidence angle ϕ from thin uniform overlayer of thickness d , which is in most respects very similar to transmission electron energy loss, with a core loss scattering yield I_c from an elemental overlayer given by

$$I_c = I(\Delta E)\sigma(\Omega, \Delta E)N_{el}[\lambda(1 - e^{-d/\sin \phi \lambda})] \quad (1)$$

where $I(\Delta E)$ is the integrated low-loss intensity, and N_{el} is the elemental concentration of a given species in the overlayer. The integrated elemental scattering cross section, $\sigma(\Omega, \Delta E)$ is dependent on the collection semi-angle Ω , and the energy loss window for data collection ΔE . The effective thickness for electron scattering is equal to the projected overlayer thickness $d/\sin \phi$ for very thin overlayers of uniform thickness. In thicker overlayers, the effective thickness is limited by λ , the mean free path for total electron scattering. The solid line and dashed line in Fig. 2(b) are the intensities predicted using

this simple transmission model for Si and Ge respectively, assuming a uniform film thickness, and an electron mean free path at an energy of 30 keV of $\lambda \simeq 20$ nm[9]. Excellent agreement is obtained between the theoretical and experimental intensities for the Ge $L_{2,3}$ edge. The agreement between theoretical and experimental intensities for the Si $L_{2,3}$ edge is not as good, possibly due to multiple inelastic scattering in the low loss region, resulting in less accurate background fits. At an incidence angle of $\phi = 37$ mrad, the actual film thickness at which the projected thickness is equal to the total mean free path is $d = 0.74$ nm.

Considerable work remains to be done in assessing the resonance enhancement of surface sensitivity, absolute and relative chemical sensitivity, and effects due to multiple scattering in order to develop reflection electron energy loss spectroscopy for more general growth conditions. Considerable gains in data rate for deep core losses could also be realized by use of an electron energy loss spectrometer with parallel detection. Nonetheless, these initial experiments have demonstrated that the surface sensitivity, data rate and energy resolution are sufficiently high to suggest that reflection electron energy loss spectroscopy has great potential as a practical real time, *in-situ* probe of surface composition during epitaxial growth.

This work was supported by the National Science Foundation P.Y.I.A. program (DMR-8958070) and the Materials Research Group program (DMR-8811795).

References

- [1] A recently developed and promising technique, reflection mass spectrometry, does have some of these advantages, but its results are less direct and are confined to certain materials systems. See, for example, J. Y. Tsao, T. M. Brennan, and B. E. Hammons, *Appl. Phys. Lett.*, **53** (1988) 288.
- [2] R. F. Egerton, "Electron Energy Loss Spectroscopy in the Electron Microscope" (Plenum Press, New York, 1986).
- [3] Z. L. Wang and R. F. Egerton, *Surface Sci.*, **205** (1988) 25.
- [4] H. A. Atwater and C. C. Ahn, submitted to *Appl. Phys. Lett.*
- [5] K.L. Brown, *Adv. Part. Phys.*, **1**, 71 (1967).
- [6] E.G. McRae, *Rev. Mod. Phys.*, **51**, 541 (1979).
- [7] S. Miyake and K. Hayakawa, *Acta. Cryst.*, **A26**, 60 (1970).
- [8] Z. L. Wang and J. M. Cowley, *Surf. Sci.*, **193**, 501, (1988).
- [9] W. Brünger and W. Menz, *Zeit. Phys.*, **184**, 271 (1965).

**XPS Studies of Halogen Atom Beam Interactions
with Electronic Materials**

**Andrew Freedman, Charter D. Stinespring
Aerodyne Research, INC.**

**XPS studies of halogen atom beam (fluorine and chlorine) interactions with
diamond (100) and GaAs (100) surfaces will be presented.**

Oriented Aluminum Films on Silicon by Direct Ion Beam Deposition

R. A. Zuh and T. E. Haynes
Oak Ridge National Laboratory
P.O. Box 2008
MS 6057, Bldg. 3137
Oak Ridge, TN 37831-6057
Phone: 615-576-6722

The formation of metal films on Si at low temperatures is of fundamental interest in thin film physics, as well as a key step in the processing of integrated circuits for microelectronics. If grain size and uniformity could be controlled in the Al metallization used in semiconductor manufacturing, the reliability of such conductors, particularly during thermal cycling, could be greatly improved. One possible way to achieve such control is through the introduction of energy in the form of energetic ions during film growth. [1] The Al on Si system is especially interesting, not only because Al is presently the conductor of choice for microelectronics fabrication, but also because the system exhibits unusual interface properties. [2] It has been demonstrated that oriented crystalline Al films can be grown on Si(111) and Si(100) surfaces at room temperature by the technique of ionized cluster beam deposition (ICB), even though there is a large mismatch in the size of the respective lattices (25%). [3,4] It is important to determine whether similar oriented growth can be achieved by other thin film deposition techniques and to understand the significant deposition parameters. In this paper we will study the formation of oriented Al films on Si by direct deposition from a low-energy mass-analyzed ion beam.

Thin Al films were grown on Si substrates by the direct ion beam deposition (IBD) technique using the system developed at Oak Ridge National Laboratory (ORNL). This IBD system has been described previously. [5] The ions were extracted from the source at 35 keV and magnetically mass analyzed to provide beams of a single isotope of a single element. The analyzed beam was then passed through a trap to eliminate charge exchange neutrals, and through three stages of differential pumping to a UHV target chamber where it was decelerated to deposition energy immediately in front of the substrate by a four element electrostatic lens assembly. Ion current density was dependent on energy, but was typically on the order of 5 $\mu\text{A}/\text{cm}^2$ over the 3 cm^2 deposition area for energies in the range from 30 to 120 eV. The chamber was baked before deposition to give a base pressure of 2×10^{-9} Torr and pressures during deposition of 1×10^{-9} Torr.

Substrates cut from semiconductor grade single crystal Si were chemically cleaned immediately prior to introduction into the vacuum system. The final removal of the protective oxide was done in vacuum just before the deposition by reactive ion beam cleaning using O and Cl ions at 500°C. Temperatures were monitored during the cleaning procedure with an infrared pyrometer, and surface cleanliness was checked by in situ Auger spectroscopy before deposition. The characteristics of the completed samples were studied by 1.5 MeV He ion backscattering, scanning electron microscopy, optical microscopy, and x-ray diffraction using standard analysis techniques.

The quality of Al films formed on cleaned Si(111) substrates has been investigated as a function of ion energy, substrate temperature, and surface cleanliness. Initial investigations showed that cleanliness of the substrate and contamination from background gasses had a significant effect on film growth. Even in the low 10^{-9} Torr range where the ORNL deposition chamber operates during active beam deposition, bombardment by residual gasses, primarily water and hydrogen, can result in film contamination at a level which is sufficient to alter the growth properties. Improvements in the in situ sample cleaning procedure and baking of the chamber prior to each

deposition were necessary to achieve the formation of shiny, oriented Al films. Use of the reactive ion cleaning technique reduced the substrate surface contamination to less than 1% of C and O as measured by Auger spectroscopy, while baking decreased the total pressure enough to eliminate measurable effects of contamination in the films.

Scanning electron micrographs of three Al(111) films grown by IBD on ion beam cleaned Si(111) under these improved conditions are shown in Fig. 1. The films were grown with an ion energy of 120 eV at temperatures of 30 (left), 150 (center), and 300°C (right). The effects of elevated temperature are clear, the morphology of the surface roughens with increasing temperature, forming at 300°C a collection of micron size islands separated by a network of deep canyons. For the sample deposited at 150°C, the islands coalesce into a relatively smooth surface, with a network of depressions remaining where the deep canyons had been observed at 300°C. For room temperature deposition, the surface is smooth and featureless to the limit of resolution of the SEM. This can be understood in terms of the surface properties of Al on Si. The interface energy of Al/Si is high due to the large lattice mismatch, and the mobility of Al on Si is also quite high (surface diffusion energy = 0.3–0.6 eV depending on orientation). This results in conditions that are energetically favorable for the formation of clusters of Al. At temperatures above ambient, the surface diffusion increases and three-dimensional island growth predominates, resulting in the coarsely textured surface observed for the sample formed at 300°C.

The degree of crystallinity and orientation in these films can be determined from the 1.5 MeV He ion channeling spectra of Fig. 2. Interestingly, the minimum yield in the Al film, which is a direct measure of crystal quality and orientation, improves from 0.80 at room temperature to 0.40 at 150°C, and to 0.35 at 300°C. This would be expected if the primary driving force for crystal formation was thermal. X-ray scattering analysis confirms the improvement in crystal quality with temperature, indicating that the amount of twinning decreases from 25% in the 150°C sample to 10% in the 300°C sample. Thus, increased deposition temperature results in better crystalline quality, but rougher surface morphology in these ion beam deposited Al films.

The best Al films formed on Si(111) by IBD have been deposited at 30 eV and show a channeling minimum yield of 28%, [6] which is comparable to the best minimum yields achieved on this surface by ICB (22%). [7] It is thus clear that good quality epitaxial Al films can be formed on Si by methods other than ICB deposition, and that the quality of such films is a function of both incident energy and substrate temperature.



Fig. 1. Scanning electron micrographs of oriented Al films formed on Si(111) by IBD at 120 eV illustrate the changes in surface morphology that occur as a function of temperature. The surface changes from smooth at 30°C (left), through an intermediate stage at 150°C (center), to rough and islanded at 300°C (right).

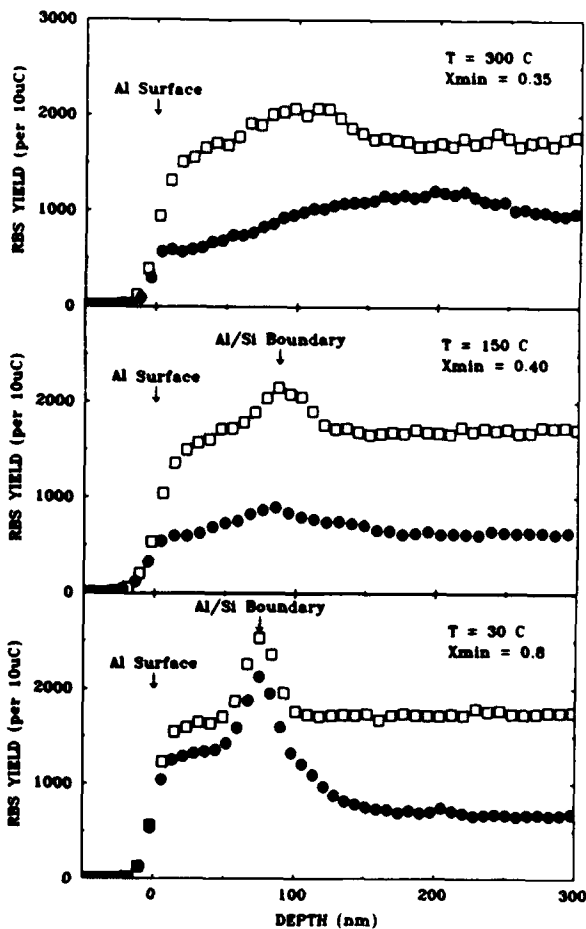


Fig. 2. Aligned <111> (●) and random (□) 1.5 MeV He ion scattering spectra for 120 eV IBD Al films deposited on Si(111) at substrate temperatures of 30°C (bottom), 150°C (center), and 300°C (top). The channeling minimum yield, X_{min} , decreases with increasing temperature, indicating improvement in crystal alignment of the films with temperature.

Research sponsored by the Division of Materials Science, U.S. Department of Energy under contract DE-AC05-84OR21400 with Martin Marietta Energy Systems, Inc.

References

1. G. K. Wolf and W. Ensinger, Proceedings of the 7th International Conference on Ion Beam Modification of Materials, September 9–14, 1990, Knoxville, TN, to be published.
2. T. M. Lu, P. Bai, A. S. Yapsir, P. H. Chang, and T. J. Shaffner, *Phys. Rev. B* **39**, 9584 (1989).
3. I. Yamada and T. Takagi, "Metallization of Ionized Cluster Beams," *IEEE Transactions on Electron Devices*, **ED-34**, No. 5, 1018 (1987).
4. I. Yamada, *Appl. Surf. Sci.* **43**, 23 (1989).
5. R. A. Zuhr, B. R. Appleton, N. Herbots, B. C. Larson, T. S. Noggle, and S. J. Pennycook, *J. Vac. Sci. and Technol. A* **5**, 2135 (1987).
6. R. A. Zuhr, T. E. Haynes, M. D. Galloway, S. Tanaka, A. Yamada, and I. Yamada, Proceedings of the 7th International Conference on Ion Beam Modification of Materials, September 9–14, 1990, Knoxville, TN, to be published.
7. I. Yamada, H. Inokawa, K. Fukushima, and T. Takagi, *Nucl. Inst. Meth. B* **7/8** 900 (1985).

A Study of Structural Properties of Non-stoichiometric Zinc Oxide Films Deposited by e-Beam Evaporation Technique

Rui-yu Chen, Chang-sheng Yuan and Qi-he Wang

Department of Physics, Nanjing University, Nanjing 210008

P.R.China . Telephone Number , 637651-2753 (Nanjing)

In this paper, we discuss the effects of various temperatures of substrates and annealings on the structural properties of non-stoichiometric zinc oxide films.

I. INTRODUCTION

Non-stoichiometric ZnO_x ($0.5 < x < 1$) films with different O / Zn composition ratios have been successfully deposited by e-beam evaporation technique under different conditions. Such zinc oxide films were analyzed using XPS method^[4-5]. X-ray diffraction was used to detect the crystallite orientation of ZnO_x films with various temperatures of the substrates^[1]. The thicknesses of the films were measured by an interferential Microscope. Van der Pauw method was used to measure the electrical resistivity of the films^[6]. Zinc oxide films have been widely studied recently. As one of the functional films, they take much more advantages over other similar films^[6]. The (002) line for zinc oxide films is more stronger than every line observed for indium oxide films and some other films. Zinc oxide has extremely low vapor pressure, and zinc oxide films seem to be more stable than other similar films^[7].

II. EXPERIMENTAL DETAILS

Here the samples of non-stoichiometric ZnO_x films were manufactured by e-beam evaporation technique . The substrates of K₂ glass were accepted . The samples with the purity of 99.99% are powdery ZnO , and they were sintered in order to prevent the sputters of ZnO particles during the evaporation procedure .

ZnO is a sublimate material ($> 1975^{\circ}\text{C}$) . It disintergrated into atoms of zinc and oxygen during the preparations, then the atoms of zinc and oxygen are combined into zinc oxide films on the surfaces of the substrates . Non-stoichiometric ZnO_x films were always obtained beacuse of the loss of oxygen atoms , so extra oxygen atoms should be given in order that ZnO of approximate stoichiometry should be produced during the preparations. At first , we pumped the vaccum system to the pressure of magnitude about 10^{-3} Torr, then O₂ were introduced into the vaccum system to the pressure of magnitude about 10^{-2} Torr , and pumped it to 10^{-3} Torr again . The temperatures of the substrates were controlled at $70^{\circ}\text{C}-350^{\circ}\text{C}$. The zinc oxide films under such conditions were to be colded in vaccum room for a period of time , and post-deposition heat treatment in air at temperature $200^{\circ}\text{C}-350^{\circ}\text{C}$ was used to remove the stress of the films^[8].

III. RESULTS AND ANALYSES

Stoichiometric zinc oxide materials (O / Zn composition ratio is 1:1) are nearly insulated , whereas the prepared zinc oxide films are n-type semiconductors. Non-stoichiometric zinc oxide films with a heavy number of zinc atoms are always produced because of the lost of oxygen atoms . It cause a defect energy level E_D between the forbidden bands, and IR-reflecting properties of the films exhibiting. It's known that there are two facts that affect IR-reflecting properties of zinc oxide films, the free carrier concentration N and the carrier mobility $\mu^{[2-3]}$. While carrier concentration N declining, IR-reflecting properties of ZnOx films turn bad. The enhancement of carrier concentration N just means the production of a heavy number of zinc atoms, thus causing the decreasing of carrier mobility μ and the increasing of the number of the scattering centres in the films and boundaries. Just for this reason, IR-reflecting properties of zinc oxide films become worse. O / Zn composition ratios seemed to play an important role during our preparations^[4], and bore relations to oxygen flow , substrate temperature , annealing time and evaporation rate . Table 1. shows the properties of ZnOx films prepared by e-beam evaporation technique.

Sample	Technical condition		Thickness(Å)	O / Zn composition ratio analyzed by XPS
	Temperature of substrate (°C)	Annealing time (h)		
Z1	350	5	3700	0.90
Z2	300	5	4000	0.86
Z3	240	5	4500	0.78
Z4	190	5	4900	0.75
Z5	150	5	5400	0.66
Z6	70	5	7000	0.52

TABLE 1. Properties of ZnOx films prepared by e-beam evaporation technique

A typical X-ray photoelectron spectrum of the oxygen $1S_{1/2}$ peak is shown in Fig.1 . Fig.1(1) . Shows the XPS analysis of oxygen of sample Z1 without annealing , and Fig.1(2). shows the XPS analysis of oxygen $1S_{1/2}$ of post-annealing sample Z1 at 350°C.

It's found that the absorbed oxygen was shown by XPS to be in two states , one corresponding to O^{-2} in zinc oxide films , the other being chemisorbed oxygen . The effect of temperature was also determined in the range of 70°C -350°C . The fraction of zinc in the Zn^{+2} valence state after five hours was found to increase nearly linerly with temperature with ZnOx formation at 350°C .

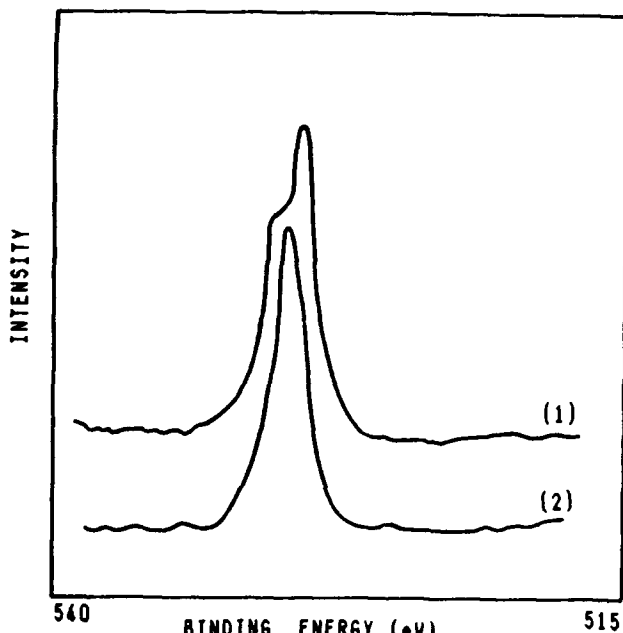


Fig.1. (1) shows the XPS analysis of $O_{1s1/2}$ of sample Z1 without annealing.

(2) shows the XPS analysis of $O_{1s1/2}$ of post-annealing sample Z1 at 350°C

As shown in Fig.2. it was noted that various temperatures of substrates have effects on the structural properties of non-stoichiometric zinc oxide films. By using XRD method, we found that XRD pattern strongly correlated with the deposition temperature. At relatively low deposition temperature, from 70°C–240°C, the (002) peak was always strongly dominant, exhibiting a strongly preferred orientation of the c-axis perpendicular to the substrate surface, while the (101) peak, the dominant line for the powder diffraction pattern of ZnO, could not be found. It's explained that the grains with (002) orientation diminish in size while the grains with (101) orientation increase in size with the deposition temperature^[1].

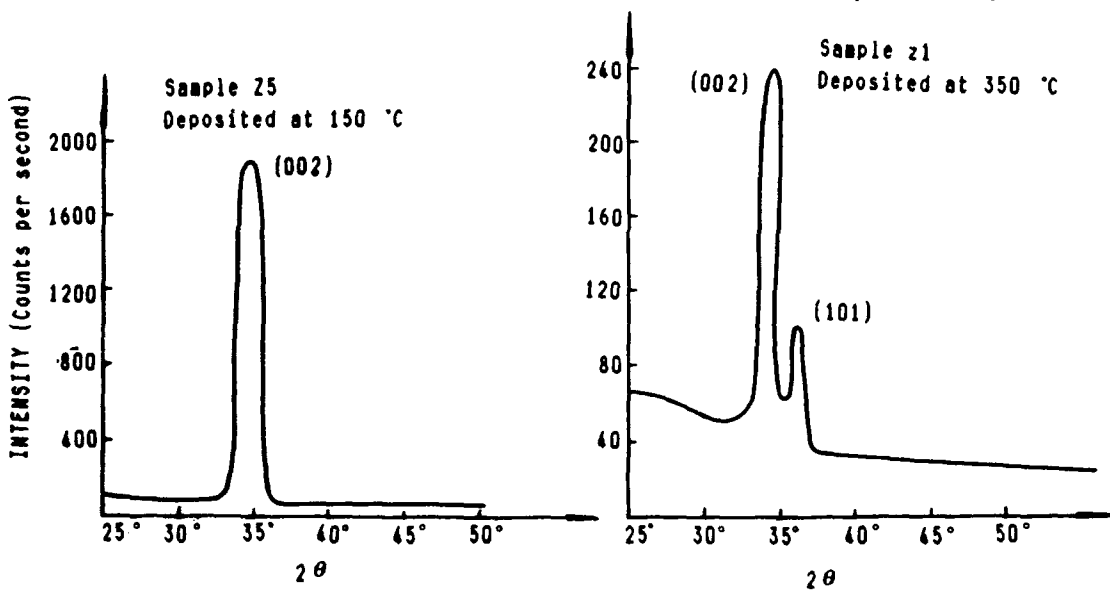


Fig.2. X-ray diffraction spectrum (XRD) of zinc oxide films deposited at about 150°C and 350°C

IV. CONCLUSIONS

The influence of the temperatures of substrates on the structural properties of non-stoichiometric zinc oxide films prepared by e-beam evaporation technique has been investigated. The microstructure of films observed by using XPS and XRD methods suggest that the improvement of these properties of the ZnOx films is related to the improvement of the crystallinity. The orientations of the films are determined by the deposition temperature. A highly preferred orientation with c-axis perpendicular to the substrate is always observed for low temperature deposition. Post-deposition heat treatment was found to remove the stress of the films.

V. REFERENCES

- 1 W.S.LAU and S.J.FONASH, J.Electronic Materials, Vol.16, No.3, 1987. 141-149
- 2 T.MINAMI, H.SATO, T.SONODA, H.NANTO and S.TAKATA, Thin Solid Films, Vol.171, 1989. 307-311
- 3 T.MINAMI, H.NANTO and S.TAKATA, Thin Solid Films, Vol.124, 1985. 43-47
- 4 D.Z.DAI, F.R.ZHU and H.S.TANG, Acta Energiae Solaris Sinica (China), Vol.8, No.2, 1987. 168-172
- 5 G.E.HAMMER and R.M.SHEMENSKI, J.Vac. Sci. Technol. A, Vol.1, No.2, 1983. 1026-1028
- 6 W.S.LAU, J.Vac. Sci. Technol. A, Vol.6, No.3, 1988. 2015-2019
- 7 Z.C.JIN, I.HAMBERG and C.G.GRANQVIST, J.Appl. Phys., Vol.64, No.10, 1988, 5117-5131
- 8 M.J.BRETT, J.Materials Science, Vol.22, 1987. 3611-3614
- 9 I.PETROV and V.ORLINOV, Thin Solid Films, Vol.123, 1985. 55-67

Scanning Scattering Microscope: A Novel Optical
Technique for Imaging Surface Microtopography

Denes Marton[†] and Joseph Fine

Surface Science Division

National Institute of Standards and Technology

Gaithersburg, MD 20899

[†]Now at the Chemistry Department, University of Houston

Telephone: 301-975-2545

The Scanning Scattering Microscope (SSM) [1] can produce two-dimensional, high resolution micrographs of very small surface features and surface microtopography; this optical technique is very sensitive to surface roughness, surface and near-surface damage, and individual surface defects. Its present lateral resolution of about 5 μm is augmented by an extremely high sensitivity to surface roughness of about 2 nm.

This microscope is based on the concept that rougher surfaces scatter more light into off-specular directions than do smoother surfaces [2,3]. This concept has previously been applied in the so-called total integrated scattering (TIS) method where it is used to obtain average surface roughness measurements of relatively large surface regions ($\sim 1\text{mm}^2$). With this TIS method almost all of the off-specularly scattered light is collected by means of a hemispherical mirror and detected. The information content of the off-specularly scattered light is quite different from that of other surface profiling and imaging techniques such as stylus techniques, scanning tunnelling microscopy, scanning electron microscopy, and numerous scanning optical microscopies.

Scattered light is characterized by the r.m.s. roughness of the surface, subject to certain limitations associated with the wavelength of the probe light beam. The SSM not only takes advantage of the sensitivity of the total integrated scattered light measurement but combines it with a microfocused, scanned light beam. The light intensity detected at each point of the surface being scanned is used to construct a two-dimensional point-by-point micrograph of surface features. An enhanced sensitivity to very subtle roughness features is obtained by collecting virtually all of the scattered light while high lateral resolution of surface features results from using a scanned, microfocused light beam. The SSM image is one of surface microroughness rather than of the actual height of surface features. Since light scattering is related also to the reflectivity of the surface, the SSM micrograph can be affected by changes in surface composition and therefore results in a technique capable of providing materials contrast, as well as topographic contrast.

The SSM micrograph can be quantified using light scattering theory in the smooth surface limit. To a first approximation, the rms surface roughness, R_q , can be obtained [3] so:

$$R_q = \frac{\lambda}{4\pi} \sqrt{I/I_o}$$

where λ is the wavelength of the light, I is the intensity of the off-specularly scattered light, and I_o is the intensity of the specularly reflected light. Standards can also be used to quantify the roughness scale associated with these micrographs.

In addition to having a very high sensitivity for surface microroughness, the large working distance (many cm) of the SSM is one of its

major advantages. A properly configured instrument could be used, in-situ, to monitor the progress of thin-film fabrication procedures as well as various types of surface processing. The SSM has been used, for instance, to determine microtopography changes during the initial stages of ion-beam sputter erosion of metal surfaces under ultra-high vacuum conditions [4].

Micrographs have been obtained of what appear to be very smooth Ge surfaces (microroughness of about 5 nm); on such surfaces it has been possible to observe lateral differences in roughness structure with the SSM. Images of this type of microroughness will be presented as well as images obtained of polished Si wafers, integrated circuit line-width patterns, abrasive scratches on thin-film layers, and surface roughness produced by ion beam sputtering of multilayered thin-film materials.

This Scanning Scattering Microscope represents a new type of optical surface imaging technique. It combines a very high sensitivity for surface roughness with high lateral resolution in an instrument whose working distance from the specimen is many cm. This combination of large working distance with a non-contacting probe may give the SSM a unique capability for in-situ process monitoring of nanometer scale surface micro-topography.

References

1. J. Fine and D. Marton, United States Patent Number 4,954,722 issued Sept. 4, 1990.
2. T. V. Vorburger and E. C. Teague, Precision Eng. (1981) 61.
3. J. M. Bennett, Optical Eng. 24 (1985) 380.
4. D. Marton and J. Fine, Thin Solid Films 185 (1990) 79.

Formation of Submicrometer Carbonaceous Islands During SEM Examination of Thin GaAs Layers on Si Substrates

G.W. Turner and P.M. Nitishin
Lincoln Laboratory, Massachusetts Institute of Technology
Lexington, Massachusetts 02173-9108

Abstract

Carbonaceous islands with controllable diameters up to $\sim 2500 \text{ \AA}$ have been formed during SEM examination of very thin GaAs layers deposited by molecular beam epitaxy on Si substrates.

Summary

In the course of investigating the initial stages of GaAs growth on Si substrates by molecular beam epitaxy (MBE), we have discovered an electron-beam-induced growth process that can occur during scanning electron microscope (SEM) examination of samples with a sufficiently thin deposit of GaAs. When such a sample is transferred from the MBE system to the SEM with only a brief exposure to air, a circular island forms at any location on the surface where the SEM electron beam is allowed to dwell. The diameter of such islands increases from about 500 to 2500 \AA as the dwell time is increased from about 1 min to over 10 min. Carbon was the only element detected when the islands were analyzed by an Auger microprobe after surface contamination was removed by sputtering.

The GaAs-on-Si growth runs were performed in a Varian GEN II modular MBE system equipped with a load-lock and ultrahigh-vacuum (UHV) buffer chamber. The Si substrates were commercial 75-mm wafers, misoriented $\sim 4^\circ$ from (100) toward $\langle 110 \rangle$. The substrates were prepared in the standard fashion for GaAs-on-Si growth, with an RCA-style *ex situ* clean followed by an *in situ* thermal oxide desorption step performed in the growth chamber at 800°C . The temperature was then reduced to 600°C , and an As prelayer was deposited for ~ 1 min from an As₄ source with a beam-equivalent pressure of 5×10^{-6} Torr. The Ga shutter was then opened for either 1 or 12 min while maintaining the same As₄ flux. The GaAs deposition rate was $\sim 40 \text{ \AA/min}$ (~ 0.25 monolayer/s). A typical island-like RHEED pattern was observed soon after the Ga shutter

was opened. After growth was terminated, the sample was annealed for 5 minutes at $\sim 650^{\circ}\text{C}$ under an As_4 ambient. The growth temperature of 600°C , which is much higher than the value of $\sim 400^{\circ}\text{C}$ typically used for the initial stages of GaAs-on-Si growth by MBE, was chosen in order to permit comparison of our results with the SEM observations of Akiyama [1] on GaAs-on-Si islands formed during growth by metalorganic chemical vapor deposition at $\sim 600^{\circ}\text{C}$.

The GaAs-on-Si wafers were kept under vacuum in the MBE buffer chamber until just before being transferred to the SEM. After being removed from the MBE system, they were cleaved in air to the desired size, then immediately loaded into the SEM chamber without deposition of contrast enhancement layers. The SEM, an AMRAY 1400 instrument, was operated with a chamber vacuum of $\sim 2 \times 10^{-7}$ Torr, voltages of 20 to 30 kV, and sample currents ranging from 0.08 to 1.08 nA. A variety of magnifications and sample tilt angles were employed in order to optimize the contrast in the SEM micrographs.

The first SEM observations were made on a sample with a GaAs deposit, obtained by growth for 1 min, that had an average thickness of approximately 40 \AA and consisted of islands with diameters on the order of 200 \AA . After initially focusing the SEM, we found that the regions of the surface that had received a large electron dose during focusing showed enhanced secondary electron emission when the sample was imaged at reduced magnification. In contrast, exposure to the electron beam of an SEM often reduces the secondary electron emission as a result of the decomposition and redeposition of background hydrocarbons [2]. Even more strikingly, imaging the sample after the beam had been allowed to dwell in spot mode at one point on the Si surface revealed the presence of a new island in addition to the GaAs islands. Figure 1 shows two micrographs of the same region, taken before and after three circular islands had been formed by allowing the electron beam to dwell at three different locations for 5 min each at a current of 0.4 nA. (Islands were not formed at substantially higher or lower beam currents.) A denuded zone is clearly visible around each island, indicating that some type of beam/surface interaction has occurred. Figure 2 is a micrograph showing islands increasing in diameter from 500 to 2500 \AA that

were formed by allowing the electron beam to dwell at six locations for times increasing from 0.5 to 12 min.

In some cases when the SEM was operated in spot mode to cause island formation, elongated "wires" rather than circular islands were formed because the electron beam drifted due to the instability of the SEM. Figure 3 shows several of these wires, which are about 1 μm long and a few hundred angstroms wide. By intentionally moving the beam during an exposure, we have formed similar wires up to 4 μm long. From the width of these wires as a function of scan rate, together with the diameter of the islands formed when the electron beam was stationary, it appears that the islands form very quickly upon exposure to the beam but do not grow beyond about 2500 \AA in diameter.

To investigate the chemical composition of the islands, a dense array was formed on one region of the Si surface, as shown in Fig. 4. The sample was then removed from the SEM and transferred as rapidly as possible to a scanning Auger microprobe with a lateral spatial resolution of $\sim 0.1 \mu\text{m}$. After the sample was sputtered with Ar ions to remove surface contamination, C was the only element detected in the region of the islands, while Ga, As, and Si (but not C) were detected away from the islands.

We also observed the formation of electron-beam-grown islands on another GaAs-on-Si wafer that was subjected to the same procedures for GaAs deposition (including exposure to the Ga flux for 1 min), transfer from the MBE system to the SEM, and treatment in the SEM. In contrast, islands were not formed on a wafer that was similarly treated, except that the GaAs layer was deposited by exposure to the Ga flux for 12 min, for an average thickness of 480 \AA . Furthermore, island formation was not observed when the original wafer with the thin GaAs layer was returned to the SEM after it had been stored in a dry box for several weeks.

In conclusion, we have observed a novel electron-beam-induced process that results in the formation of carbonaceous islands during SEM examination of Si substrates on which GaAs has been deposited by MBE at $\sim 600^\circ\text{C}$. A similar phenomenon might influence the results obtained when SEM examination is used to study the initial stages of GaAs growth on Si by MBE at the

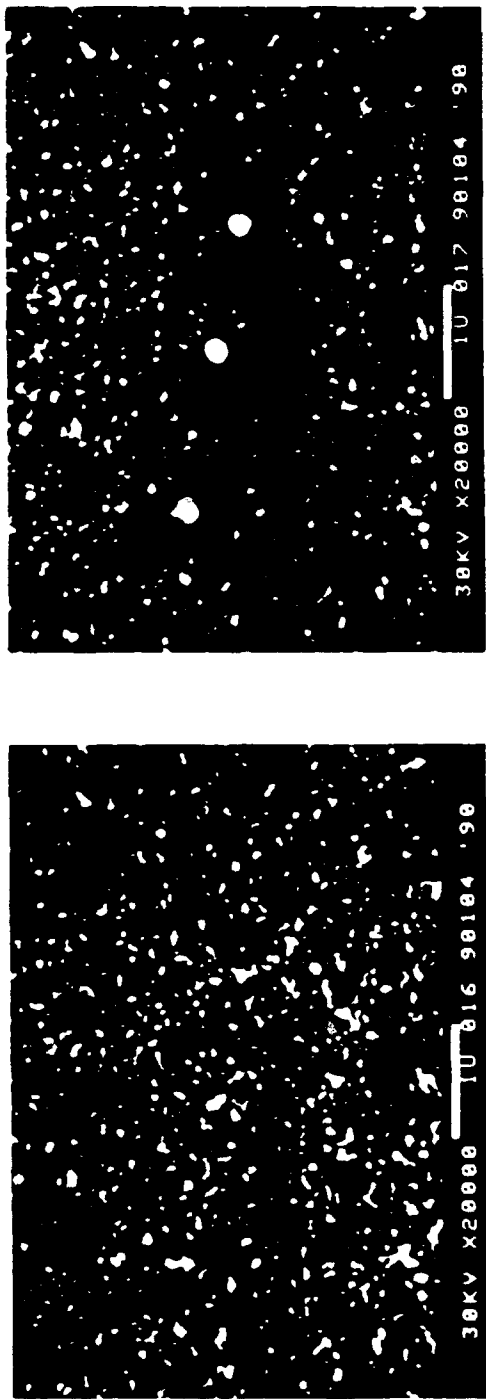
usual temperature of ~ 400°C. Additional experiments are needed to obtain a better understanding of the mechanism of island formation and the properties of the islands.

We would like to thank M.K. Connors for his assistance in sample preparation, M.C. Finn for the Auger analysis, and A.J. Strauss and B-Y. Tsaur for helpful discussions. This work was sponsored by the Defense Advanced Research Projects Agency and the Department of the Air Force.

REFERENCES

- [1] M. Akiyama, T. Ueda, and S. Ononzawa, Mater. Res. Soc. Symp. Proc., Vol. 166 (Materials Research Society, Pittsburgh, 1988), p. 79.
- [2] M. A. Hayat, *Introduction to Biological Scanning Electron Microscopy* (University Park Press, Baltimore 1978), p. 55.

DEMOCRATISATION OF ISLAND FORMATION
WITH DENUDED ZONE



AFTER (5 Minutes x3)

BEFORE



Fig. 1

EFFECT OF BEAM EXPOSURE TIME ON ISLAND SIZE

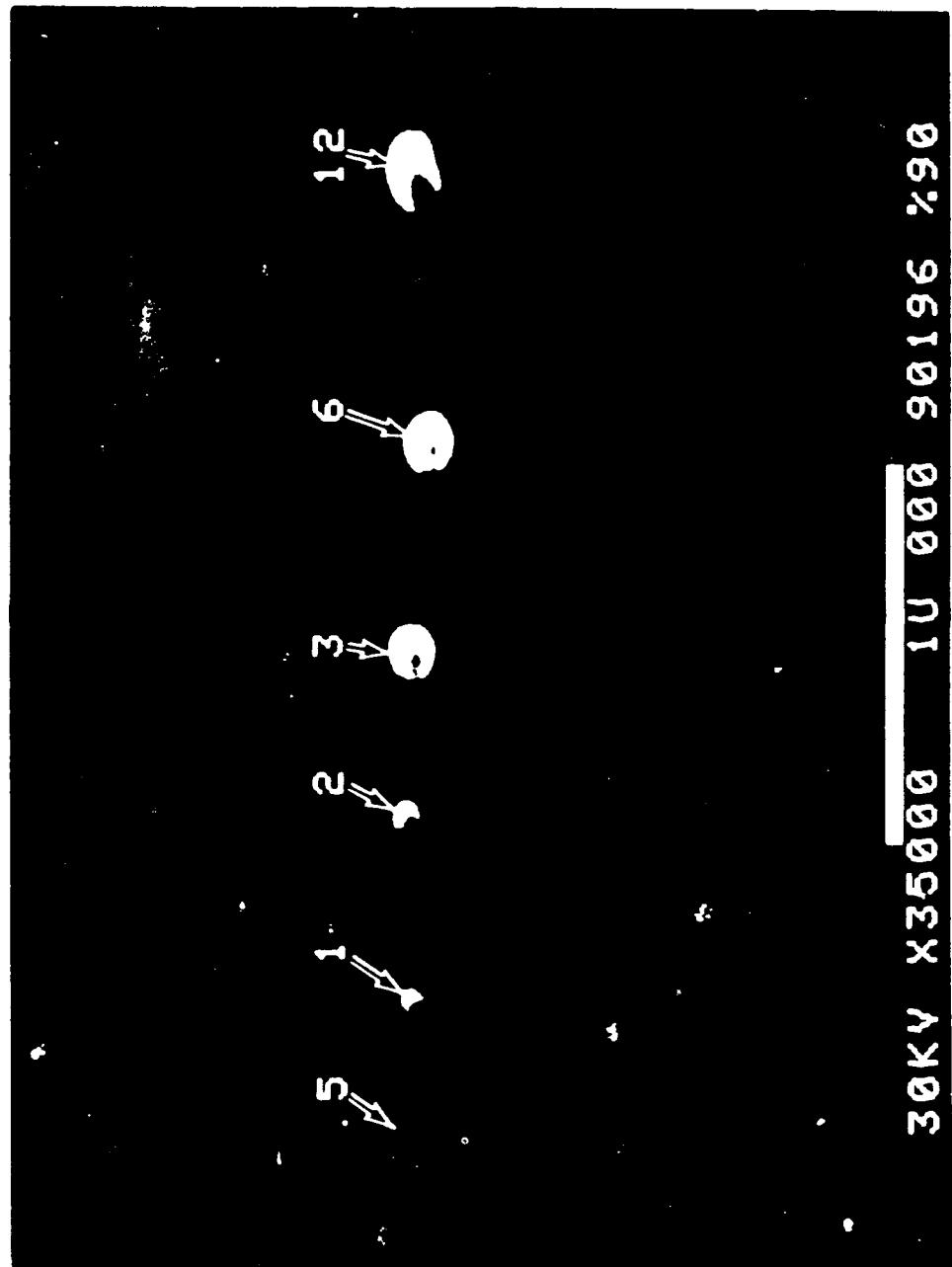


Fig. 2

FORMATION OF "WIRE" STRUCTURES NEAR ISLANDS

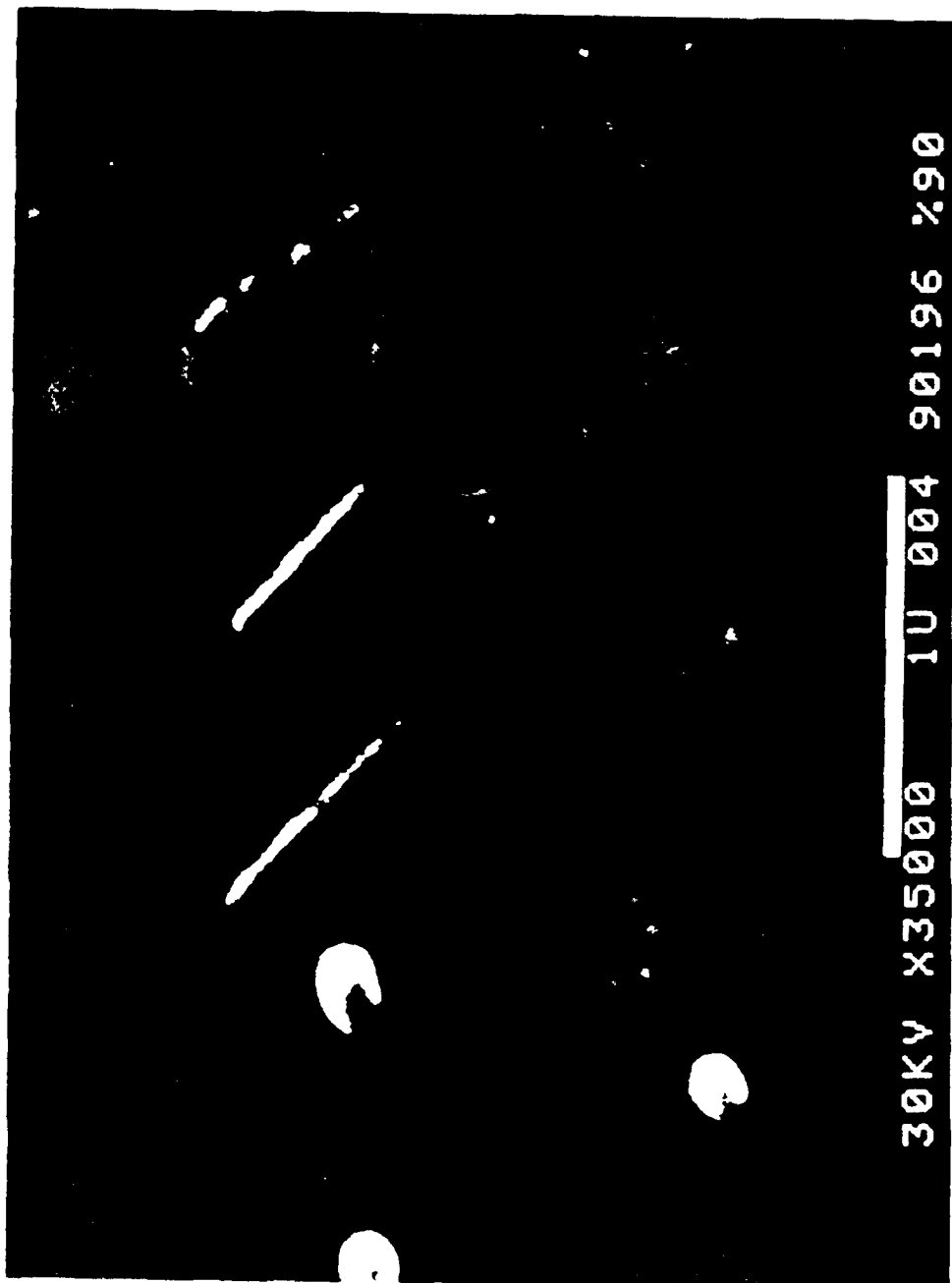


Fig. 3

FORMATION OF ARRAY OF ISLANDS
BY ELECTRON BEAM

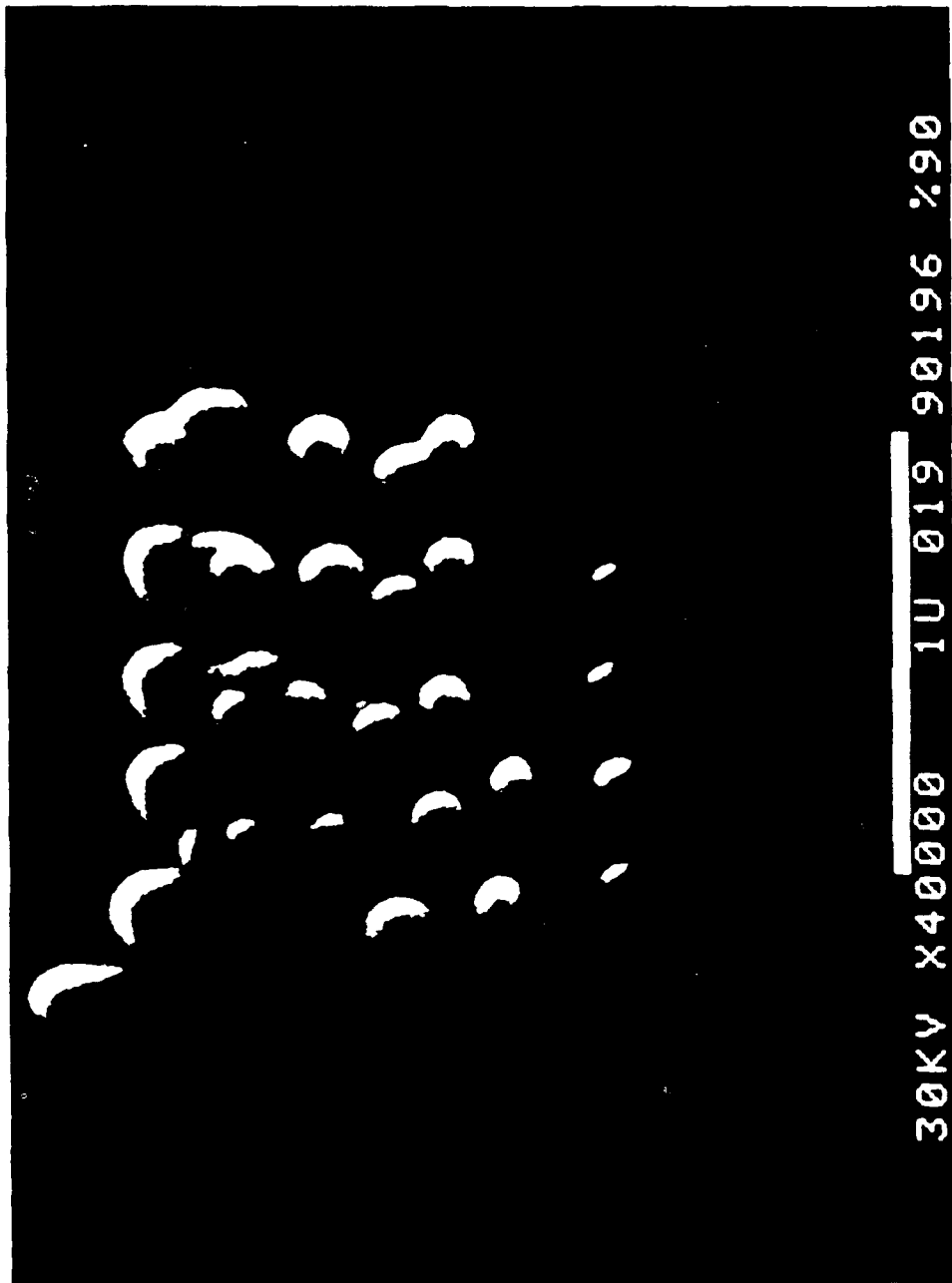


Fig. 4

Excitonic Mechanism of Photon-Stimulated Desorption of Excited Alkali Atoms from Alkali Halides

Patrick H. Bunton

Department of Physics, Box 4608

Austin Peay State University, Clarksville, TN 37044

Telephone 615-648-6241, Telefax 615-648-7475

Richard F. Haglund, Jr.,⁽¹⁾ Dengfa Liu⁽²⁾ and Norman H. Tolk⁽¹⁾

⁽¹⁾Department of Physics and Astronomy and ⁽²⁾ Department of Chemistry

Vanderbilt University, Nashville, TN 37235

615-322-2828, Telefax 615-343-7623

The mechanism leading to photon-stimulated desorption (PSD) of excited atoms from the surfaces of alkali halides has been a subject of controversy since it was first discussed a decade ago [1]. We have recently carried out a systematic experimental study of PSD from alkali halides under both valence-band [2] and core-level [3] excitation. Our data demonstrate that the desorption yields for excited alkali atoms track the excitonic optical response of these crystals even at photon energies below the bulk band gap. Secondary electron measurements, taken simultaneously, implicate the formation of excess metal in the time and dose dependence of PSD yields. These results suggest a unified picture of PSD in which the ion motion initiating desorption is pictured as the decay of a localized, highly deformed vibrational mode of the crystal. Plausible mechanisms for creation of the excited atomic state include relaxation of excited *F*-centers and resonant neutralization into the excited state on metallic microclusters.

The photon source for these experiments was the Aladdin facility of the Synchrotron Radiation Center (SRC) at the University of Wisconsin. Bending-magnet radiation from the 800-MeV electron storage ring was dispersed by a six-meter toroidal-grating monochromator (TGM) or a Seya-Namioka (SN) monochromator and focused onto a sample at normal incidence. Useable photon flux - in the range of 10^{10} photons·s⁻¹ - was available from 5 eV to 30 eV on the Seya, while the TGM has significant flux from 40 to 150 eV. Al and Sn filters were used to block visible light and higher-order light transmitted by the gratings.

Samples were single alkali halide crystals cleaved in air and inserted immediately into an ultra-high vacuum chamber with a base pressure generally in the range of $\sim 10^{-10}$ Torr. The samples were typically under vacuum within about an hour after being cleaved in air. The vacuum system was baked for several hours after sample insertion at 200° C; samples were then cleaned by heating the target assembly for a few hours at 300 to 400° C. A number of studies, cited in Ref. [3], have shown that this procedure yields a stable, reproducible surface.

The experimental apparatus is described in detail in Reference [3]. Fluorescence from excited desorbing alkali atoms was detected in an 0.3 meter Czerny-Turner monochromator with a photomultiplier (PMT) operated in pulse counting mode. Amplified PMT pulses exceeding the threshold of a discriminator were counted and stored in an Apple microcomputer. Secondary electrons were collected by a biased rectangular stainless-steel collector plate positioned close to the target. The collector current monitored by a picoammeter was fed to the analog-to-digital converter channel of a Hewlett-Packard 7090A plotter and the data likewise stored in the computer.

Figure 1 shows an excitation function of excited sodium desorption yield from NaCl taken with an aluminum filter transmitting photons of energies up to about 85 eV with a significant roll-off in flux above about 73 eV. The sharp peak in the NaCl spectrum at 33.5 eV is due to the Na^+ (2p) core exciton [3]. The data have an apparent threshold near the 2p core level; however, the signal does not vanish below the 2p core exciton formation energy, either because of higher order light or absorption by the Cl^- (3s) band.

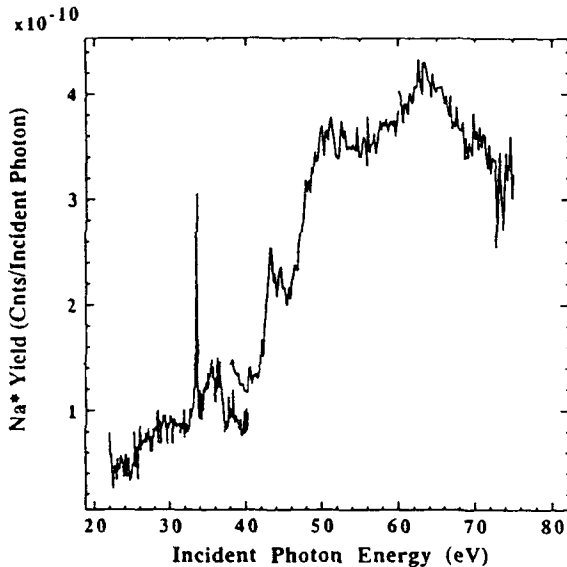


Figure 1. Excitation function showing the yield of Na^* from NaCl under irradiation by uv photons in the energy range 20-70 eV.

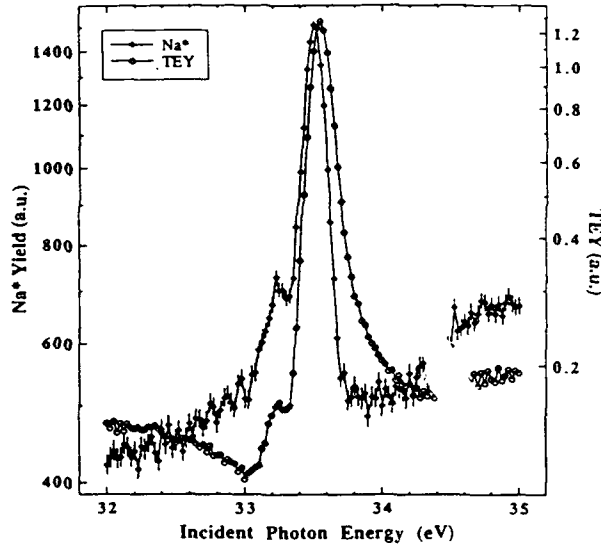


Figure 2. PSD excitation function for the Na^* and total electron yields in the vicinity of the 33.45 eV core exciton of Na.

Figure 2 shows the Na 2p core-exciton lineshapes of the Na^* and the electron yields from NaCl. Evidently the electronic environment that yields the excited sodium atoms is similar to that which yields the electrons, if it differs at all. The total electron yield has the Fano lineshape characteristic of interfering processes. In the L(exciton)-V process the electron and hole recombine and an electron is ejected from the valence band; in the L(exciton)-VV process the core hole is filled by an electron from the valence band and a second electron is ejected from the valence band. The L(exciton)-V decay has initial and final states indistinguishable from those of direct valence-band photoemission; this results in an asymmetric (Fano) lineshape due to interference between these two processes.

The lack of interference structure in the exciton lineshape in the Na^* yield shows that the interatomic L(exciton)-VV decay is more likely to cause desorption while the electron yield has contributions due to interatomic Auger decay, recombination of the exciton, and direct photoemission from the valence band. This is usually taken as evidence that a localized two-hole state is necessary for desorption. However, it may also mean that if a single hole were sufficient for desorption, the interatomic L(exciton)-VV process would still produce two holes per excitation thereby potentially doubling its contribution to the desorption yield.

These excited atom and secondary electron excitation functions generally follow the excitonic features of the optical response of alkali halides [4]. This characteristic has been paid relatively little attention until now; the desorption mechanism has generally been held to result from the specific character of the core-level excitation in maximally covalent insulators, and in particular from the tendency for two holes localized on a single anion to have a relatively long

lifetime. That interpretation must now be re-examined in light of our recent observation of *valence*-band PSD of excited atoms from both LiF and KCl surfaces.

Figure 3 shows an excitation function for LiF from the band-gap to about 25 eV, still well below the lowest core level - the F(2p) - identified in earlier studies. The general excitonic character of the spectrum bears a striking resemblance both to uv absorption and reflection spectra in this same energy range, as discussed in detail in Ref. [2].

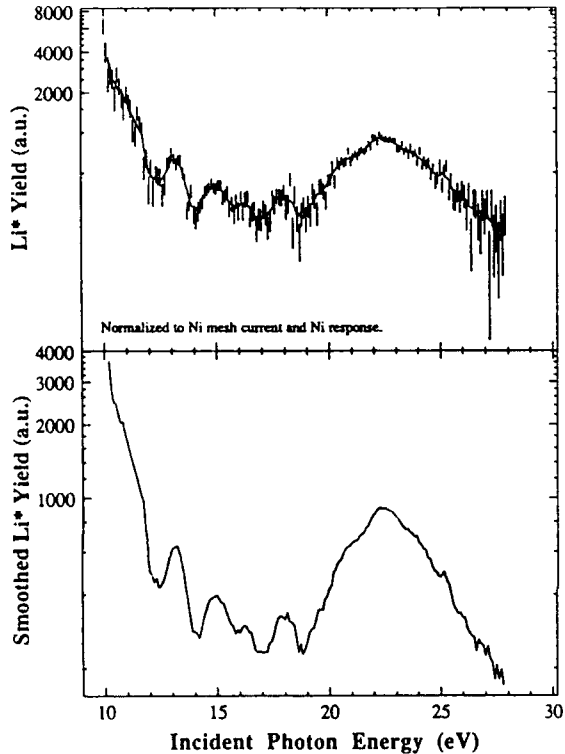


Figure 3. PSD excitation function of Li^* from LiF starting from below the bandgap energy to approximately 25 eV. Upper curve, raw data; lower curve, smoothed.

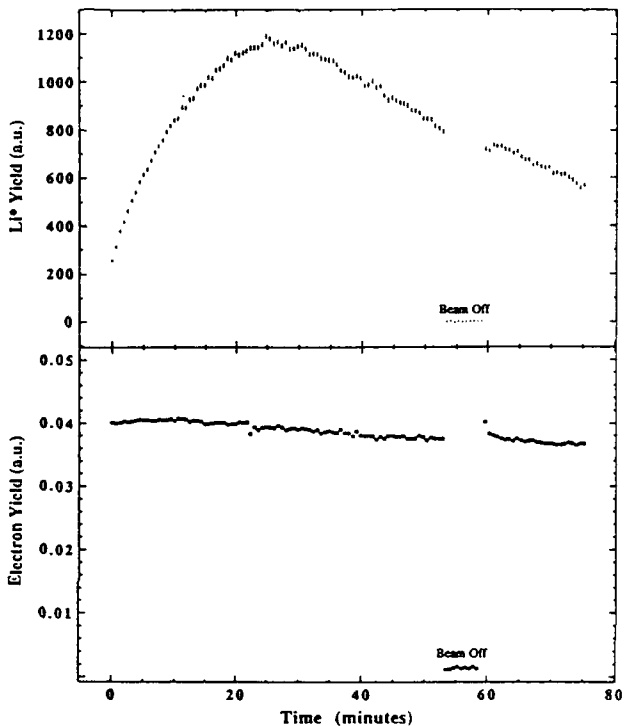


Figure 4. Simultaneous measurement of Li^* yield from PSD of LiF (upper curve) and secondary electron current as a function of irradiation time (lower) at 61.9 eV.

Figure 4 shows the time evolution of the Li^* yield and the total electron yield from LiF for an incident photon energy of 61.9 eV for a sample at room temperature. The steady-state secondary electron yield is significantly smaller than that for the bare LiF surface, indicating the onset of metallization. Similar data were acquired for different temperatures at energies below the lowest core level for LiF. These data clearly implicate the formation of excess metal in PSD of excited alkali atoms through the formation of thin patches and eventually three-dimensional islands of metal on the surfaces. Our data indicate that there is apparently both an optimum metal concentration and an optimum patch size for desorption of excited alkalis.

Any proposed model for PSD of excited atoms must deal with two questions: (1) What is the driving force for ion motion? and (2) What is the origin of the excited electronic state in desorbing atoms? In studies of PSD by core-level excitation, the source of ion motion has been identified as inter-atomic Auger decay into the core holes created by the absorption of the ultraviolet photon. In this Knotek-Feibelman (K-F) [5] or Auger-stimulated desorption (ASD) process [6], ion motion is driven by Coulomb distortion of the lattice following reversal of the Madelung potential. The model makes no prediction about excited atoms.

Both core-level excitation and valence-band excitation produce valence holes, the former through the L(exciton)-VV process. In fact, the valence holes may be the immediate precursors to desorption of excited atoms. Support for this idea comes from recent calculations by Bickham and Sievers [7] showing that excitations with energies of the same order as those required to create *F*-centers in alkali halides can produce long-lived vibrational states at surfaces. In this model, localization of vibrational energy occurs because of the anharmonicity caused both by the creation of an exciton and by the asymmetric interatomic surface potentials.

An *F*-center created by valence-band light could be excited due to scattering of secondary electrons or fluorescence. The strong coupling of an excited *F*-center to the lattice could initiate ion motion and also provide the electron needed for neutralization of a departing ion. Since excited *F*-center lifetimes decrease with increasing temperature, this would also be consistent with the observed change in excited alkali-atom yields. Of course, changes in the surface metallization with temperature might still affect the time and temperature dependence of the excited atom yield by changing the Fermi level relative to the energy of the excited atomic state.

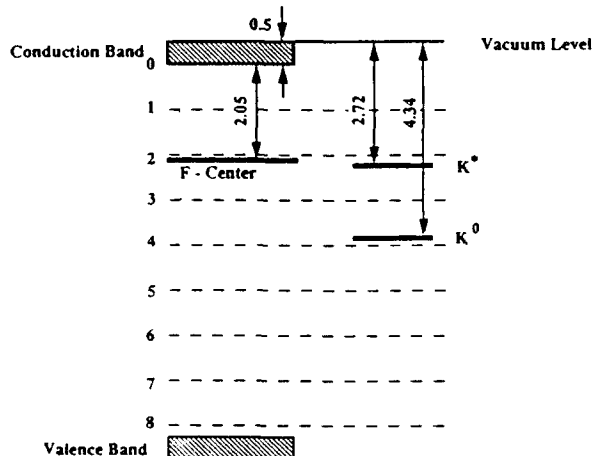


Figure 5. Band diagram for KCl.

An excited *F*-center in KCl has about the right energy to neutralize a potassium ion into the first excited state of the neutral. Figure 5 (left) shows an approximate band diagram for KCl including an *F*-center. The ground state *F*-center is almost resonant with an excited neutral alkali atom. The thermal ionization energy of the *F*-center calculated by Itoh, Stoneham and Harker [8] was used to locate the *F*-center below the conduction band. The ionization limit of the atom was made coincident with the vacuum level of KCl. These methods are approximate, of course, since both the lattice distortion and the surface will alter the band structure dynamically.

This research was sponsored in part by the University Research Initiative of the Air Force Office of Scientific Research (Contract F49620-86-C-0125). PHB was supported by NASA (training grant NGT - 501260. The SRC is supported by the National Science Foundation.

References

- [1] N.H. Tolk, M.M. Traum, J.S. Kraus, T.R. Pian, W.E. Collins, N.G. Stoffel, and G. Margaritondo, Phys. Rev. Lett. **49**, 812 (1982).
- [2] P. H. Bunton, R. F. Haglund, Jr., D. Liu and N. H. Tolk, submitted to Phys. Rev. B.
- [3] P. H. Bunton, R. F. Haglund, Jr., D. Liu and N. H. Tolk, Surf. Sci., to be published.
- [4] S. Pantelides, Phys. Rev. B **11** (1975) 2391.
- [5] M. L. Knotek and P. J. Feibelman, Phys. Rev. Lett. **40**, 965 (1978); P. J. Feibelman and M. L. Knotek, Phys. Rev. B **18**, 6531 (1978).
- [6] C. C. Parks, D. A. Shi, *et al* and G. Loubriel, Phys. Rev. B **29** (1984) 4709.
- [7] S. R. Bickham and A. J. Sievers, submitted to Physical Review B.
- [8] N. Itoh, A. M. Stoneham, and A. H. Harker, Surf. Sci. 217 (1989) 573; J. J. Markham, *F - Centers in Alkali Halides* (Academic Press, NY, 1966), p. 123.

Wednesday, February 13, 1991

Nanoscale Structure and Lithography

WD 8:00pm-9:15pm
Anasazi South

Phaedon Avouris, *Presider*
IBM T. J. Watson Research Center



SCANNING TUNNELING MICROSCOPY STUDIES OF SILICON
MOLECULAR BEAM EPITAXY

M. G. Lagally and Y.-W. Mo

University of Wisconsin-Madison

Madison, WI 53706

608-263-2078

Introduction

It has been recognized since the beginning of serious studies in surface science that kinetic processes underpin a whole range of surface phenomena, including, for example, phase transformations and ordering, epitaxial growth, and surface chemical behavior. However, with few exceptions, available techniques have not lent themselves well to obtaining a truly microscopic view of such kinetic processes. Because of its atomic resolution on the one hand, and the achievable wide field of view on the other (i.e., large dynamic range in resolution) scanning tunneling microscopy (STM) does afford this opportunity. In this talk, we briefly review the types of surface kinetics measurements that can be made using STM. It should be pointed out that the use of STM for studies of kinetics is one of the more recent applications of what is itself still a very young field; hence much remains to be accomplished. We have concentrated our investigations on the initial stages of molecular beam epitaxy of Si and Ge on Si(001) and will use this surface in our examples.

The theoretical framework for investigating surface kinetic processes has been in hand for a long time, and has, in some cases, been developed to a considerable degree. Consider the simplest case: the homoepitaxial growth of a material on itself (A-on-A). Atoms arrive from the vapor phase at a surface. To remain on the surface ("accommodate") they must give up their heat of condensation through one or a series of inelastic collisions. Once bound in the holding potential of the surface, an atom will migrate (surface

self-diffusion) until it finds another of its kind, either at the edge of a terrace or another freely diffusing atom. If it becomes incorporated into the edge of an existing island or terrace, we speak of "lateral accommodation" with a certain probability (the "lateral accommodation coefficient"). If it finds another freely migrating atom, a stable nucleus may form, which will grow with the addition of another atom. (In some situations, a stable nucleus may require more atoms). Nucleation is thus the first stage, followed subsequently by 2-D growth, and eventually by "coarsening" (or "ripening"). Two-dimensional growth involves the lateral sticking coefficient of an atom at an edge. This kinetic parameter is quite important but is often assumed, by implication, to equal one for all situations. The two-dimensional coarsening process, the elimination of small islands at the expense of large ones, driven by a desire of the system to eliminate boundary energy to reduce its total free energy, involves, in addition to migration, a "lateral desorption" process, in which diffusible species are created at the edges of islands. As more than one layer become involved in the growth, additional processes involving transport over steps, both up and down, become important in the growth kinetics. We thus have a series of kinetic parameters that can be categorized in two groups: those that involve adatoms interacting with a bare terrace and those that involve adatom interactions with steps. The latter category is obviously much larger.

The most important microscopic quantity involved in the formation of stable nuclei and their growth is the diffusion coefficient for monomers on the surface at the surface temperature, consisting of an activation energy, E_{migr} , and a preexponential factor, D_0 , that involves the usual quantities of attempt frequency, geometric factors, and an entropy term. The transfer of the heat of condensation of the arriving atom to the lattice may influence the measurement of E_{migr} over a particular (low) temperature range. The diffusion may be anisotropic if the symmetry of the substrate is low. In addition, there may be a separate diffusion coefficient for dimers and for large clusters. Examples of the measurement of the diffusion coefficient for Si/Si(001) and its anisotropy will be shown.⁽¹⁾

While there is a flux of atoms onto the surface from the source, the shape of 2-D ordered structures (islands) that form depends on the competition between kinetic parameters (sticking coefficient for adatoms at edges) and thermodynamic parameters (desire to minimize the free energy by forming an equilibrium shape). Thus in general, there may be "growth shapes" that differ from equilibrium shapes because of kinetic constraints. These are easily observed in STM of Si and Ge deposited on Si(001).^(2,3)

When the flux of atoms arriving from the source is turned off, islands will grow until the mean supersaturation is eliminated. The net flux to and from each island reaches zero as the island establishes its local lateral equilibrium vapor pressure. Because of fluctuations in their initial formation and growth, there will be a size distribution of islands. The free energy of an island determines its local vapor pressure; smaller islands will have a greater boundary free energy (more unsaturated edge bonds relative to the island perimeter), therefore be less stable, and hence have a larger lateral vapor pressure. The difference in concentrations due to differing vapor pressures at large and small islands leads to a further ordering mechanism, "coarsening" or "ripening", which is driven by the difference in boundary free energy of islands of different sizes. Annealing to allow the system to coarsen results in an island shape change. Differences in growth shapes and equilibrium shapes can be investigated by studying the coarsening process using STM. The growth law for coarsening and a measure of the activation energy for lateral desorption off the edges of islands have been obtained for Si/Si(001).

On a stepped surface, a similar desire to reach equilibrium produces steps that have a characteristic density of kinks. By counting these, the edge and kink energies can be determined.⁽⁴⁾

Finally, transport over steps is an essential ingredient in epitaxial growth. Transport may be both "upward" or "downward", but in order to have "smooth" growth, the latter must dominate. The conventional assumption is that there is no transport "upward", but this need

not be true. When the substrate symmetry forces different types of steps on the surface (as in Si(001)), each step type may behave differently with regard to its effect as a barrier for transport "up" or "down". This effect is illustrated for Si diffusion on Si(001).

In summary, Si epitaxy on Si(001) is not only technologically important, it is a system that involves all the major microscopic kinetic mechanisms of growth and, because of its symmetry, anisotropies in them as well. With the proper design of experiments, STM allows a disentanglement of these mechanisms and their individual quantitative investigation.

This research has been supported by ONR, Chemistry Program.

References

1. Y.-W. Mo and M. G. Lagally, *Surface Sci*, submitted.
2. Y.-W. Mo, B. S. Swartzentruber, R. Kariotis, M. B. Webb, and M. G. Lagally, *Phys. Rev. Letters* 63, 2393 (1989); M. G. Lagally, Y.-W. Mo, R. Kariotis, B. S. Swartzentruber, and M. B. Webb in Kinetics of Ordering and Growth at Surfaces, ed. M. G. Lagally, Plenum, New York (1990).
3. Y.-W. Mo and M. G. Lagally, *J. Cryst. Growth*, in press; Y.-W. Mo, D. E. Savage, B. S. Swartzentruber, and M. G. Lagally, *Phys. Rev. Letters* 65, 1020 (1990).
4. B. S. Swartzentruber, Y.-W. Mo, R. Kariotis, M. G. Lagally, and M. B. Webb, *Phys. Rev. Letters* 65, 1993 (1990).

Nanolithography

R. Fabian Pease

Stanford University

Stanford, CA 94305-4055

Our ability of fashion patterns with features below 100nm is beginning to be put to good use for the microfabrication of devices and even circuits. Achieving economic throughput along with the precision required for sub 100-nm features is an enormous challenge.

Ahn, C. C. – WC3
 Atwater, H. A. – MA3, WC3
 Auvert, Geoffroy – TuC2
 Avouris, Phaedon – MB2, WD

Becker, Christopher H. – WB1
 Behm, R. J. – MB4, WA1
 Bermudez, V. M. – MB3
 Block, Jochen H. – TuB4
 Bozso, Ferenc – MA1, MB2
 Buntin, S. A. – TuB1
 Bunton, Patrick H. – WC9

Cavanagh, R. R. – TuB1
 Chen, Rui-yu – WC6
 Coon, P. A. – TuB2
 Cross, J. B. – MB3

Dirks, Joachim – TuB4
 Drachs, Wolfgang – TuB4

Ehrlich, Daniel J. – MB

Farr, J. D. – MB3
 Fine, Joseph – WC7
 Freedman, Andrew – WC4

George, Steven M. – TuB2, WC, WC1
 Goldenberg, S. S. – WA2
 Greene, J. E. – MA2

Haase, G. – TuA3
 Haglund, Jr., Richard F. – MC3, WC9
 Hall, Richard B. – TuB, WB3
 Hamza, A. V. – TuB3
 Hartmann, E. – MB4
 Hattori, Ken – MC3
 Haynes, D. R. – WC1
 Haynes, T. E. – WC5
 Hess, Peter – TuC1
 Hirose, M. – MC5, WB
 Hoffbauer, Mark A. – MB3, WB2
 Hoffmann, Patrik – WA3
 Hoffmann, R. – MB2
 Houle, Frances A. – MA, TuA2

Irvine, Stuart J. C. – TuA
 Ito, Takaishi – WB4
 Itoh, Noriaki – MC3

Jin, Zhong-Kao – TuA1

Kabler, M. N. – WA2
 King, D. S. – TuB1

Koch, F. – MB4

Lagally, M. G. – WD1
 Lecohier, Baudouin – WA3
 Li, Yu-Lin – TuA1
 Liberman, V. – TuA3
 Liu, Dengfa – WC9
 Long, J. P. – WA2
 Lu, Ping-He – TuA1
 Ludeke, R. – WA4
 Lyo, I.-W. – MB2

Mackey, K. J. – WC2
 Marton, Denes – WC7
 Mayer, Thomas – PdP
 McVeigh, Victoria J. – WB2
 Miragliotta, J. – WB3
 Miyazaki, S. – MC5
 Mo, Y.-W. – WD1
 Moro, Lorenza – WB1
 Mouncey, Simon P. – WB1

Nagasawa, Y. – MC5
 Nakai, Yasuo – MC3
 Nakayama, Noriaki – WB4
 Nara, Yasuo – WB4
 Nikzad, S. – WC3
 Nishizawa, Jun-ichi – MB1
 Nitishin, P. M. – WC8

Osgood, Jr., Richard M. – MC4, TuA3, TuC

Paulsen-Boaz, Carlotta – TuA4
 Pease, R. Fabian – WD2
 Philippoz, Jean-Michel – WA3
 Phillips, J. – MC4
 Polizzotti, R. S. – WB3
 Prietsch, M. – WA4

Qin, Qi-Zong – TuA1
 Quiniou, B. – MC4

Rabinowitz, P. – WB3
 Rhodin, Thor – TuA4, WA
 Richter, L. J. – TuB1
 Rodway, D. C. – WC2

Samavar, A. – WA4
 Sanche, Léon – MC2
 Schildbach, M. A. – TuB3
 Schubert, B. – MB2
 Schwarz, W. – MC4
 Shih, M. C. – TuA3
 Smith, P. C. – WC2
 Solka, Herbert – WA3
 Stinespring, Charter D. – WC4

Stuke, Michael - MC
Sugita, Yoshihiro - WB4

Tanaka, T. - MC5
Tokmakoff, A. - WC1
Tolk, Norman H. - WC9
Tsai, C. J. - MA3
Turner, G. W. - WC8

Van den Bergh, Hubert - WA3
Vere, A. W. - WC2
Vreeland, T. - MA3

Wang, Qi-he - WC6
White, J. M. - MC1
Widmer, Marcel - WA3
Wise, M. L. - TuB2
Wu, Z. - MC4

Yang, Q. - MC4
Yuan, Chang-sheng - WC6

Zhang, Zhuang-Jian - TuA1
Zheng, Qi-Ke - TuA1
Zuerlein, Michael J. - WB2
Zuhr, R. A. - WC5